Des polymérisations classiques en solution aux polymérisations radio-induites contrôlées en milieu confiné

Marie-Claude Clochard

To cite this version:

Marie-Claude Clochard. Des polymérisations classiques en solution aux polymérisations radio-induites contrôlées en milieu confiné. Polymères. Université Pierre et Marie Curie - Paris VI, 2013. tel-00823555

HAL Id: tel-00823555
https://theses.hal.science/tel-00823555

Submitted on 17 May 2013

Habilitation à Diriger des Recherches

Des polymérisations classiques en solution aux polymérisations radio-induites contrôlées en milieu confiné

Marie-Claude Dubois-Clochard

Université Pierre et Marie Curie, Paris VI
Spécialité:Science des Polymères

présentée le 25 avril 2013

Table des matières

0.1 Introduction 5

I 9

1 Curriculum vitae 11
1.1 Etat Civil 12
1.2 Cursus 12
1.3 Encadrement d'étudiants 13
1.3.1 Thèses 13
1.3.2 Post-doctorants 14
1.3.3 Stagiaires niveau IUT 14
1.4 Participations à des jurys de thèse 14
1.5 Prix et Distinctions 15
1.6 Publications 15
1.6.1 Articles 15
1.6.2 Articles de Proceedings 17
1.6.3 Chapitre de livre 17
1.6.4 Brevets 17
1.7 Conférences 18
1.7.1 Communications orales sur invitation 18
1.7.2 Organisation de congrès 19
1.8 Missions d'expertises 19
1.8.1 Enseignement - activités de formation 19
1.8.2 Expertises AIEA 19

II 21

2 Activités de recherche 23
2.1 Energie / Environnement 24
2.1.1 Détergent/dispersants pour carburants et lubrifiants 24

2.1.2 Assemblage Membrane-Electrode pour Pile à combustible 34
2.1.3 Capteurs de métaux toxiques pour le contrôle qualité de l'eau 51
2.2 Santé 58
2.2.1 Polymères dégradables 58
2.2.2 Polymères biocompatibles non-dégradables 61
2.3 Nanotechnologies et perspectives 65
2.3.1 Template synthesis 65
2.3.2 Couplage de l'effet piezoélectrique avec des nanofils magnétostrictifs : vers des capteurs de pression 66
2.3.3 Perspectives du projet à 4 ans et plus 82
2.4 Annexe 92
2.4.1 J. Appl. Phys. (2011) 93
2.4.2 Anal. Meth. (2011) 101
2.4.3 Pharm. Res. (2011) 111
2.4.4 Phys. Rev. Lett. (2010) 124
2.4.5 J. Pow. Sources (2010) 129
2.4.6 Polymer (2004) 139
2.4.7 Langmuir (2001) 152

0.1 Introduction

"La science des polymères est vraiment née le jour où quelques chimistes obstinés ont réussi à établir la nature covalente de l'agencement des unités monomères en chaînes macromoléculaires. Ils se sont appuyés, pour cela, sur des arguments physiques, jetant les bases d'une science située, dès son origine, aux frontières de la chimie, de la physico-chimie et de la physique." Cette citation de Jean-Marie Lehn, prix nobel de Chimie 1987, tirée de la préface du livre "Chimie et Physico-chimie des polymères" de Michel Fontanille et Yves Gnanou, définit une science pluridisciplinaire dédiée à des objets multifonctionnels d'une grande modernité. Leur impact sur la vie quotidienne est considérable, même si le grand public ne le conçoit qu'à travers le prisme réducteur des polymères " de commodités".
Même si les polymères sont des matériaux concrets, ils n'en sont pas moins des objets d'intérêt en Recherche fondamentale. Ainsi les concepts de la chimie et de la physique des polymères ont été couronnés par l'attribution de plusieurs prix Nobel : H. Staudinger (1953), K. Ziegler et G. Natta (1963), P. Flory (1974), R. B. Merrifield (1984), P.-G. de Gennes (1991), A. J. Heeger , A. G. MacDiarmid et H. Shirakawa (2000), et, plus récemment, Yves Chauvin (2005).

Mon engouement pour la science des polymères a débuté en 1992 alors que je suivais les cours de licence du professeur Philippe Guérin à l'Université Paris Descartes. Cet homme avait un dynamisme contagieux et m'a montré l'incroyable versatilité des matières polymères. Mon bagage de chimie organique acquis à la faculté de Pharmacie et de Médecine de Paris V prenait soudain un sens. Toutes les réactions de la chimie organique ne semblaient pas trouver de frontière à s'appliquer sur ces matériaux. Cela ouvre toujours, à l'heure actuelle, d'innombrables possibilités pour répondre aux nombreuses demandes sociétales dans divers domaines en transformant la matière organique vers des objets macromoléculaires fonctionnels. Notamment, j'aurais développé avec lui durant ma maîtrise et mon DEA (master I et II) la synthèse de polymères biodégradables pour des applications médicales dans le Laboratoire des BioPolymères du CNRS de Thiais.

Le travail de Recherche, que j'ai mené depuis mon master jusqu'à aujourd'hui (18 ans) dans différents laboratoires (IFP, SOP University of London, LSI-CEA/Ecole Polytechnique), m'a permis d'aborder la chimie macromoléculaire sous de nombreux aspects suivant les types de polymérisations, les milieux, les propriétés physico-chimiques des matériaux d'intérêt... Ce travail de Recherche m'a permis d'appréhender différents systèmes de l'échelle macroscopique à l'échelle nanométrique. La fabrication de nouveaux matériaux a toujours été poussée par une envie de Recherche Appliquée (Santé, Energie, Environnement). Cette orientation a également suscité une empathie pour les mesures physiques des objets synthétisés et mon implication aujourd'hui vers la physique, au sein du Laboratoire des Solides Irradiés à l'Ecole Polytechnique, me mène progressivement à étudier l'objet macromoléculaire synthétisé dans un environnement contraint à l'échelle nanométrique.

Au cours de mon cursus professionnel, différents types de polymérisation ont été abordés :

- Polymérisation anionique par ouverture de cycle de β-butyrolactone en milieu organique ;
- Polymérisation cationique de la 2-methyloxazoline en milieu organique ;
- Copolymérisation radicalaire de PolyIsoButène modifié et d'anhydride maléique en milieu organique puis transformation en succinimide (synthèse d'architecture supramoléculaire) ;
- Polycondensation en milieu aqueux pour la synthèse de polymères pH-dégradables ;
- Polymérisation radicalaire radio-induite en milieu aqueux à l'interface solide-liquide ;(électrons, ions lourds rapides et gammas) : post-irradiation et irradiation *in-situ* ;
- Polymérisation radicalaire en nanoémulsion de difluorure de vynilidène VDF ;
- Polymérisation radicalaire en milieu confiné à l'interface solide-liquide ;
- Polymérisation radicalaire vivante en milieu confiné à l'interface solide-liquide.

Les résultats marquants ont été :

- l'établissement d'isothermes d'adsorption de type bi-langmuir à l'interface solide-liquide organique pour des macromolécules tensioactives à faible concentration, et, à forte concentration, un comportement particulier de réorganisation de ces mêmes macromolécules, non pas en couches alternées, mais sous forme d'hémicelles inverses
- la synthèse d'un polymère pH-dégradable innovant permettant une dégradation hydrolytique en passant de pH 7.4 (Sang) à pH 5.5 (Lysosome intracellulaire) en vue de délivrer des toxines dans les cellules tumorales (Santé)
- la démonstration de l'effet coopératif solvant/polymère en croissance pour la pénétration du greffage induit par irradiation dans des films fluoropolymères
- la synthèse de membranes polymères nanoporeuses à traces attaquées bi-fonctionnelles ayant une fonctionnalité dans les pores et une autre en surface. Cette membrane, après transformation en électrode par simple métallisation aura fait l'objet de projets de valorisation en vue d'une création de start-up et/ou de transfert de technologie pour le développement d'un détecteur de traces métaux lourds dans l'eau traitée (Environnement). Dans la même thématique, la fonctionnalisation directe des traces dans les films de polymères irradiés aux ions lourds rapides du GANIL[1] a permis de développer de nouvelles membranes conductrices de protons pour les piles à combustible (Energie)
- l'observation non-décrite d'effets coopératifs sur la mobilité des ions dans un milieu confiné créé par un nanopore cylindrique unique dans une membrane fine de fluoropolymère. L'effet accélérateur ou deccélérateur de la mobilité des ions confinés dans le pore aux parois chargées semble dépendre uniquement de la nature chimique des

---

[1] Grand Accélérateur d'Ions Lourds

ions et de leur concentration.

Afin de permettre de juger de la pertinence de cette demande d'habilitation à diriger des recherches, la première partie de ce mémoire va faire l'état des lieux sur mon curriculum vitae et une deuxième partie développera mes activités de recherche. En fin de mémoire, se dessinera un projet recherche pour les 4 ans à venir.

Première partie

Chapitre 1

Curriculum vitae

1.1 Etat Civil

Nom : Dubois
Nom marital : Clochard
Prénom : Marie-Claude
Date de naissance : 23/01/1971
Nationalité : française
Civilité : mariée, 3 enfants.

1.2 Cursus

Depuis le 19 novembre 1998, je suis diplômée d'un doctorat ès Sciences spécialité "Chimie et Physico-Chimie des Polymères". Ce diplôme a été délivré par l'Université Pierre et Marie Curie avec les félicitations du jury.

Poste actuel

2006-aujourd'hui	**Chercheur CEA** de la Direction des Sciences de la matière -IRAMIS- Membre du groupe XPnano du Laboratoire des Solides Irradiés à l'Ecole Polytechnique (France)
2007-aujourd'hui	Expert AIEA (Agence Internationale à l'Energie Atomique) dans le domaine du greffage radio-induit dans les polymères
2006-aujourd'hui	Membre du Steering committee de la conférence Internationnale IRaP (Ionizing RAdiation of Polymers)

Expériences professionnelles

2002-2006	**Post-doctorat** au Laboratoire des Solides Irradiés CEA-DSM/IRAMIS Etude des effets d'irradiation et greffage radio-induit dans les polymères solides.
1998-2001	**Post-doctorat** au *Center for Polymers Therapeutics* The School of Pharmacy, University of London, Angleterre.
1995-1998	**Doctorat** de Chimie et Physico-chimie des Polymères à l'Institut Français du Pétrole, IFP, Rueil-Malmaison, France Dispersants en milieu organique : Synthèse et étude physico-chimique de dispersants pour carburants et lubrifiants.

Projets

2011-2013	**Projet ECOSISTEM-CAPTÔT** -suite du projet AIEA 14622- Actuellement soutenu par le programme de valorisation TECHNOSANTE du CEA vers la création d'entreprise et/ou le transfert de technologie. Développement de capteurs de métaux lourds dans les eaux. Financement CEA.
2007-2010	**Projet AIEA 14622** pour le développement de nouvelles membranes et adsorbants par greffage radio-induit pour des applications industrielles et environnementales. Financements : Triangle de la Physique, l'Ecole Polytechnique et OSEO.
2006-2012	**Projet AMECEA** du programme transversal NTE CEA DSM-DRT sur la fabrication d'assemblages Membranes-Electrode pour Piles à Combustible. Financement CEA.
2009-2012	**Projet PIEZOMAG** du programme REI Ministère de la Défense (DGA) sur l'étude des effets magnétostrictifs de nanofils de Nickel moulés dans les nanopores d'une membrane en PVDF piezoélectrique. Financements : DGA et Triangle de la Physique.
2006-2012	**Projet Nanovectorisation et Imagerie médicale** - Nanoparticules de PVDF pur et composite radiogreffées et fonctionnalisées Collaboration initiale avec l'Université de Bordeaux II (thèse CEA 2006-2009) - Collaborations avec Politecnico di Torino (Italie) et l'Université de Tokyo (Japon)
2004-2007	**ACI nanoscience** sur la fonctionnalisation de membranes à traces attaquées obtenues par révélation chimique après irradiation aux ions lourds rapides Consortium de 5 partenaires. Reprise de la coordination du projet initialement assurée par le Dr. N. Betz de 2004-2005. Financement ACI (ex-ANR)

1.3 Encadrement d'étudiants

1.3.1 Thèses

2004-2008	**Olivia Cuscito** "Elaboration de membranes PVDF par attaque de traces et fonctionnalisation spécifique des nanopores" Ecole Polytechnique soutenue le 19/03/2008
2006-2009	**Stéphanie Deshayes** "Synthèse de nanoparticules spécifiques pour le ciblage et l'imagerie de l'angiogenèse tumorale" Université de

	Bordeaux 1 soutenue le 16/12/2009
2007-2011	**Christophe Tasserit** "Transport d'ions et d'objets dans des nanopores" Ecole Polytechnique soutenue le 15/03/2011

1.3.2 Post-doctorants

2004-2006	**Thomas Berthelot** - projet Transverse NTE pile à combustible type PEMFC avec CEA-LITEN et INAC
2009-2011	**Nicolas Bizière** - projet DGA sur magnétostriction d'un nanofil de Nickel induite par polymère piezoélectrique
2009-2013	**Haad Bessbousse** - projet IAEA 14622 financé par RTRA valorisation sur nanocapteur de métaux lourds dans l'eau + CDD CEA valorisation programme Transverse pour la Santé (création d'une Start-up ou transfert de technologie)
2010-2011	**Mohamed El-Jouad** - projet DGA (suite de Nicolas Bizière cf au-dessus)
2010-2012	**Enrico Gallino** - projet Transverse NTE pile à combustible type PEMFC avec CEA-LITEN et INAC

1.3.3 Stagiaires niveau IUT

2003-2004	**A. Lafon** "Méthode de dosage par titration acide-base sur polymère PVDF radiogreffé"
2008-2009	**M. Al-Subaïe** - Projet ASSENSOR
2009 (3 mois)	**V. Lerose** - Projet IAEA 14622
2011 (3 mois)	**V. Lemee** - Projet ECOSISTEM
2012 (3 mois)	**V. Lemee** - Projet CAPTÔT
2012 (3 mois)	**B. Godin** - Projet CAPTÔT
2012 (3 mois)	**H. Mekdad** - Projet REPLIPORE

1.4 Participations à des jurys de thèse

6 déc. 2007	Examinateur de la thèse de **S. Sirijarukul** "Elaboration de membranes à traces en poly(éthylènetéréphtalate) ayant un gradient linéaire de taille de pore et une porosité constante"-Université Montpellier 2-
19 mar. 2008	Co-directeur de la thèse de **O. Cuscito** "Elaboration de membranes PVDF par attaque de traces et fonctionnalisation spécifique des nanopores" - Ecole Polytechnique, Ecole Doctorale Science des Matériaux

16 déc. 2009	Co-directeur de la thèse de **S. Deshayes** "Synthèse de nanoparticules spécifiques pour le ciblage et l'imagerie de l'angigenèse tumorale" - Université de Bordeaux 1, Ecole Doctorale des Sciences Chimiques
3 mar. 2011	Co-directeur de la thèse de **C. Tasserit** "Transport d'ions et d'objets dans des nanopores" - Ecole Polytechnique, Ecole Doctorale Science Physique
30 mar. 2012	Examinateur de la thèse de **F. Roussel** "Elaboration et étude des propriétés électriques d'un matériau composite nanotubes de carbone alignés - époxy" - Ecole Polytechnique, Ecole Doctorale Science Physique

1.5 Prix et Distinctions

2012	**Prix Pollutec** de l'équipe projet CAPTÔT sur le développement du capteur de métaux lourds dans les eaux
2012	**Prix OSEO** d'aide à la création d'entreprise du projet ECOSISTEM porteur de projet : Haad Bessbousse - sur le développement du capteur de métaux lourds dans les eaux
2002	**Prix Le Foulon de la Lande** de la fondation de France obtenue pour l'étude du radiogreffage dans le PVDF pour une application biomédicale dans le cadre des maladies infantiles

1.6 Publications

Dans ce paragraphe, les publications sont répertoriées suivant les articles dans des journaux à comité de lecture, les articles de proceedings, les chapitres de livre et brevets. Le facteur H est de 8.

1.6.1 Articles

1. Bizere N. ; Clochard M.-C. ; Chung P.D. ; Viret M. ; Wegrowe J.-E. "Magnetoresistance measured on magnetic nanoconstrictions : the role of structural defects" J. of Appl. Phys. 2012 (submitted)
2. Barsbay M. ; Güven O. ; Wade T.L. ; Clochard M.-C. "Functionalized membrane electrodes (FMEs) by RAFT-mediated radical polymerization inside synthetic nanochannels" J. of Memb. Sci. 2012 (submitted)
3. Clochard M.-C. "La pile à combustible, une solution vers des véhicules propres" FlashX, La revue scientifique de l'Ecole Polytechnique 2012, 14, 13-17

4. Bizière, N ; Lassalle Ballier, R ; Clochard, M.C. ; Viret, M. ; Wegrowe, J.E. "Synthesis and magnetic reversal of bi-conical Ni nanostructures." Journal of Applied Physics 2011, 110, 6, 063906 DOI : 10.1063/1.3638072
5. Deshayes, S. ; Maurizot, V. ; Clochard, M.-C. ; Baudin, C. ; Berthelot, T. ; Esnouf, S. ; Lairez, D. ; Moenner, M. ; Deleris, G. Pharmaceutical Research, 2011 28, 1631-1642.
6. Bessbousse, H. ; Nandhakumar, I. ; Decker, M. ; Barsbay, M. ; Cuscito, O. ; Lairez, D. ; Clochard, M.-C. ; Wade, T. L. Analytical Methods, 2011 3, 1351-1359.
7. Tasserit, C. ; Koutsioubas, A. ; Lairez, D. ; Zalczer, G. ; Clochard, M. C. Physical Review Letters, 2010 105.
8. Deshayes, S. ; Maurizot, V. ; Clochard, M.-C. ; Berthelot, T. ; Baudin, C. ; Deleris, G. Radiation Physics and Chemistry, 2010 79, 208-213.
9. Clochard, M. C. ; Berthelot, T. ; Baudin, C. ; Betz, N. ; Balanzat, E. ; Gebel, G. ; Morin, A. Journal Of Power Sources, 2010 195, 223-231.
10. Clochard, M. C. ; Cuscito, T. ; Berthelot, T. ; Betz, N. ; Bittencourt, C. ; Pireaux, J. J. ; Goncalves, M. ; Gionnet, K. ; Deleris, G. Reactive and Functional Polymers 2008, 68, 77-90.
11. Cuscito, O. ; Clochard, M. C. ; Esnouf, S. ; Betz, N. ; Lairez, D. Nuclear Instruments and Methods In Physics Research Section B-Beam Interactions With Materials And Atoms 2007, 265, 309-313.
12. Berthelot, T. ; Baudin, C. ; Balanzat, E. ; Clochard, M. C. Nuclear Instruments and Methods In Physics Research Section B-Beam Interactions With Materials And Atoms 2007, 265, 320-324.
13. Clochard, M. C. ; Wade, T. L. ; Wegrowe, J. E. ; Balanzat, E. Nuclear Instruments and Methods In Physics Research Section B-Beam Interactions With Materials And Atoms 2007, 265, 325-329.
14. Clochard, M. C. ; Baudin, C. ; Betz, N. ; Le Moel, A. ; Bittencourt, C. ; Houssiau, L. ; Pireaux, J. J. ; Caldemaison, D. Reactive and Functional Polymers 2006, 66, 1296-1305.
15. Betz, N. ; Clochard, M. C. ; Goncalves, M. ; Bittencourt, C. ; Pireaux, J. J. ; Gionnet, K. ; Deleris, G. ; Le Moel, A. Nuclear Instruments and Methods in Physics Research, Section B (Beam Interactions with Materials and Atoms) 2005, 236.
16. Clochard, M. C. ; Betz, N. ; Goncalves, M. ; Bittencourt, C. ; Pireaux, J. J. ; Gionnet, K. ; Deleris, G. ; Le Moel, A. Nuclear Instruments and Methods In Physics Research Section B-Beam Interactions With Materials And Atoms 2005, 236, 208-215.
17. Clochard, M. C. ; Begue, J. ; Lafon, A. ; Caldemaison, D. ; Bittencourt, C. ; Pireaux, J. J. ; Betz, N. Polymer 2004, 45, 8683-8694.
18. Dubois-Clochard, M. C. ; Durand, J. P. ; Delfort, B. ; Gateau, P. ; Barre, L. ; Blanchard, I. ; Chevalier, Y. ; Gallo, R. Langmuir 2001, 17, 5901-5910.

19. Zloh, M. ; Dinand, E. ; Brocchini, S. ; Clochard, M. Internet Journal Of Chemistry 2001, 4, art. no.-9.
20. Godwin, A. ; Bolina, K. ; Clochard, M. ; Dinand, E. ; Rankin, S. ; Simic, S. ; Brocchini, S. Journal Of Pharmacy And Pharmacology 2001, 53, 1175-1184.
21. Clochard, M. C. D. ; Rankin, S. ; Brocchini, S. Macromolecular Rapid Communications 2000, 21, 853-859.

1.6.2 Articles de Proceedings

22. Clochard M.-C. ; El Jouad M. ; Biziere N. ; Chung P.D. ; Drouhin H.-J. ; Balanzat E. ; Lairez D. ; Viret M. ; Wegrowe J.-E. "Magnetic nanoconstrictions made from Nickel electrodeposition in polymeric bi-conical tracks : magneto-transport behaviour" Rad. Phys. Chem. 2012 (submitted)
23. Gallino, E. ; Clochard, M.-C. ; Balanzat, E. ; Gebel, G. ; Morin, A. Proceedings of the 2011 MRS Fall Meeting 2012
24. Sandana, V. E. ; Rogers, D. J. ; Teherani, F. H. ; McClintock, R. ; Razeghi, M. ; Drouhin, H. J. ; Clochard, M. C. ; Sallet, V. ; Garry, G. ; Fayoud, F. In Zinc Oxide Materials And Devices Iii, 2008 ; Vol. 6895, pp Z8950-Z8950.
25. Simic, S. ; Clochard, M. C. ; Brocchini, S. Abstracts Of Papers Of The American Chemical Society 2001, 221, U426-U427.
26. Clochard, M. C. D. ; Brocchini, S. Abstracts Of Papers Of The American Chemical Society 2000, 219, U443-U443.
27. Chevalier, Y. ; Dubois-Clochard, M. C. ; Durand, J. P. ; Delfort, B. ; Gateau, P. ; Barre, L. ; Frot, D. ; Briolant, Y. ; Blanchard, I. ; Gallo, R. In Trends In Colloid And Interface Science Xv, 2001 ; Vol. 118, pp 110-114.

1.6.3 Chapitre de livre

28. Pivin J.-C. ; Clochard M.-C. "Ion Tracks in Polymers" du livre "Synthesis and engineering of nanostructures by energetic ions" Nanotechnology Science and Technology series Nova Science publishers Inc. 2011 chap.13, 223-231 ISBN 978-1-61668-209-5

1.6.4 Brevets

29. M-Cl. Dubois-Clochard and S. Brocchini, "pH-degradable polymer" EP 99307041.6 (dépôt 03-09-1999) étendu à l'international en 2002 WO 0017515A1 [US6828412(B1)]
30. M-C. Clochard, T. Berthelot, C. Baudin, "Procédé d'élaboration de Membranes Conductrices de Protons de Pile à Combustible par Radiogreffage" CEA French patent (BD 1727) FR 0757875 ext PCT WO/2008/062726 (dépôt 26-09-2007)

31. T. Berthelot, M-C Clochard, "Membranes Conductrices de Protons pour Pile à Combustibles présentant un gradient de protons et Procédés de Préparation desdites Membranes" CEA French patent (BD 10047) FR 0757873 ext PCT WO/2009/103925 (dépôt 26-09-2007)
32. T. Wade, M-C Clochard "Method and device using nanoporous membrane for detecting and quantifying heavy metal ions in a fluid" CEA-X-CNRS European patent EP08305237 (dépôt 06-06-2008)
33. J-E Wegrowe, M-C Clochard, D. Lairez, T.Wade "Capteurs par assemblage de nanofils" CEA-X-CNRS French patent FR 09 51042 étendu PCT 18/08/2011 (dépôt 18-02-2009)
34. T. Berthelot, M-C Clochard, "Membranes Conductrices de Protons pour Pile à Combustible et Procédés de Préparation desdites Membranes" BD11266 French patent FR0955854 ext PCT WO/2010/062512 (dépôt 18-06-2009)
35. T.Wade, M-C Clochard "Nano-valve device comprising nanoporous membrane" CEA-X-CNRS French Patent FR09056967 European patent EP09305252 étendu PCT 06/12/2010 (dépôt 20-03-2009)
36. M-C Clochard, N. Mezailles, H. Bessbousse, T. Wade "nanosensor for capturing charged molecules by using in situ stripping voltammetry" CEA-X-CNRS European patent EP11305112 (dépôt 04-02-2011)
37. M-C Clochard, H. Bessbousse, T. Wade, E. Gallino "Membranes nanostructurées et leur utilisation" CEA-X-CNRS French Patent FR 1153977 (dépôt 09-05-2011)
38. M. Barsbay, O. Güven, H. Bessbousse, M-C Clochard, T. Wade "Method for preparing a functionalized nanoporous track-etched PVDF membrane with RAFT polymerization" EP11306648.4 (dépôt 13-12-2011)
39. E. Gallino, M-C Clochard, A. Morin, G. Gébel "Suspension aqueuse comprenant des particules de catalyseur métallique et des particules de polymère spécifique utilisable pour la fabrication de couche active d'électrode" CEA-X-CNRS FR1252533 (dépôt 21-03-12)

1.7 Conférences

1.7.1 Communications orales sur invitation

- IRaP2012, 10th meeting on Ionizing Radiation Polymers, 13-19 oct. 2012 Cracovie, Pologne - Conférence invitée "Bi-conical Ni nanostructures by template synthesis in track-etched membranes : an original tool for spintronics"

- CAARI, Conference on the Application of Accelerators in Research and Industry, 8-13 août 2010, Fort Worth, Texas, USA - Conférence invitée "Ion Track Membranes"

- IRaP2010, 9th meeting on Ionizing Radiation Polymers, 25-29 sept. 2010, Washington, USA - Conférence invitée "Ion track Membrane for Fuel Cell application"

- IRAP2008, 8th meeting on Ionizing Radiation Polymers, 12-17 oct. 2008, Angra dos Reis, Brésil - Conférence invitée "Functionalized nanoporous track-etched polymer membranes : synthesis and purposes"

- Séminaire « Membranes polymères track-etch nanoporeuses fonctionnalisées : fabrication et applications" 6 déc. 2007, Institut Européen des Membranes, Montpellier, France

1.7.2 Organisation de congrès

- Membre organisateur d'IRAP en 2008 (Brésil), en 2010 (Washington) et en 2012 (Cracovie)conférence internationale bi-annuelle - prochain IRaP à l'automne 2014 en Corée-du-Sud.

- 2nd RMC meeting of the coordinated research project (CRP) on "nano-scale radiation engineering of advanced materials for potential biomedical applications" 15-19 nov. 2010, Observatoire de Paris (co-organisateur de ce workshop de l'IAEA : 20 experts de 15 pays différents)

1.8 Missions d'expertises

1.8.1 Enseignement - activités de formation

J'ai effectué très peu d'activité d'enseignement. J'ai dispensé deux cours de 2h sur la fabrication de membranes polymères à traces attaquées et leurs utilisations à l'Université d'Hacettepe à Ankara en Turquie (8-12 nov. 2010) dans le cadre des missions d'expertise de l'AIEA.

Mes activités en tant que personnel formateur sont principalement dans l'encadrement des étudiants dans le laboratoire ainsi que la formation continue de tout personnel souhaitant utiliser le microscope électronique à balayage à effet de champ (FESEM). Depuis son acquisition, il y a 4 ans par 3 laboratoires de l'Ecole Polytechnique dont le LSI, j'ai formé une vingtaine de personnes à son utilisation.

1.8.2 Expertises AIEA

En tant que personnel CEA, l'AIEA m'a contactée à plusieurs reprises pour effectuer des semaines d'expertise autour d'un sujet d'actualité et de préoccupation pour des pays

en voie de développement. Le but de ces échanges (table ronde d'environ 15-20 personnes représentant en général une moyenne de 14 pays) est d'échanger les équipements, les technologies et les échanges de chercheurs. Cette réflexion est suivie sur 3 ans dans différents lieux pour promouvoir les relations internationales entre pays développés et pays en émergence et donne lieu à un document technique publié aux éditions de l'AIEA.
Ces rencontres se concrêtisent par un projet appelé Coordinated Research Project (CRP)

. 1er Coordinated Research Project pour faire le point de l'état d'avancement dans le domaine suivant : "Development of novel absorbents and membranes by radiation-induced grafting for selective separation purposes".

- Vienna, Austriche, 1st CRP (18-24 nov. 2007)
- Aargau, Suisse, 2nd CRP (14-19 jun. 2009)
- Budapest, Hongrie, 3rd CRP (6-10 dec. 2010)

. 2ème Coordinated Research Project pour faire le point de l'état d'avancement dans le domaine suivant : "Nano-scale radiation engineering of advanced materials for potential biomedical applications" . Membre organisateur du 2nd meeting (1er meeting a eu lieu à Vienne au siège de l'IAEA) :

- Observatoire de Paris, France, 2nd CRP (15-19 nov. 2010)
- Cracovie, Pologne, 3rd CRP (8-12 oct. 2012)

. Déplacement à Vienne au siège de l'AIEA pour une discussion à 5 (France, Pologne, Italie, USA, India) pour la préparation d'un booklet AIEA sur les polymères irradiés et les nanotechnologies (14-19 Mar. 2010).

. Mission d'enseignement payée par l'AIEA à l'Université d'Hacettepe, Ankara, Turquie (8-11 nov. 2010)

Deuxième partie

Chapitre 2

Activités de recherche

L'articulation de ce deuxième chapitre suit les domaines d'application traités dans lesquels interviennent les différentes polymérisations listées dans l'introduction. La synthèse de polymères fonctionnels est à la base des études abordées et, dans l'ordre chronologique de mes activités de recherche, les polymérisations classiques en solution ont fait place aux polymérisations contrôlées en milieu confiné. Cependant, l'innovation ne touche pas ici la recherche de nouveaux mécanismes de polymérisation ou de nouvelles réactions de chimie organique mais porte sur le développement de nouveaux objets aux propriétés physico-chimiques originales. Trois domaines d'application se détachent de mes différentes activités de Recherche : L'Energie-Environnement, la Santé et les Nanotechnologies.

2.1 Energie / Environnement

2.1.1 Détergent/dispersants pour carburants et lubrifiants

Ce travail (Réfs. [1] et [2]) a été effectué dans le cadre de mon doctorat à l'Institut Français du Pétrole sous la direction de Jean-Pierre Durand et Patrick Gateau, Ingénieurs IFP, d'Yves Chevalier, Directeur de Recherche CNRS au LMOPS à Lyon et du Professeur Roger Gallo de l'ENSSPICAM à Marseille.

2.1.1.1 Problématique

Dans la formulation des huiles lubrifiantes et des carburants, de nombreux additifs sont utilisés pour en améliorer les caractéristiques et satisfaire à l'exigence croissante du cahier des charges. Ainsi les essences peuvent contenir des additifs détergents-dispersants, des désactivateurs de métaux, des inhibiteurs de corrosion, des biocides, etc... Les carburants Diesel contiennent également des détergents-dispersants mais aussi d'autres additifs spécifiques tels que des additifs améliorant l'indice de cétane, des additifs de tenue au froid et des anti-odeurs. La formulation des huiles lubrifiantes est encore plus complexe et fait notamment appel à des additifs de viscosité, abaisseurs de point d'écoulement, anti-usure, extrême pression, antioxydants, détergents et neutralisants, dispersants, antirouille et anticorrosion, antimousse, modificateurs de frottement,...

L'encrassement des différents organes du circuit d'alimentation ou du moteur lui-même d'un véhicule automobile se traduit par des perturbations de fonctionnement touchant l'aisance de conduite, la consommation de carburant et les émissions de polluants.

Pour remédier à ces problèmes, les additifs détergents-dispersants sont utilisés dans les carburants pour empêcher ou réduire l'adhésion des dépôts insolubles sur des surfaces métalliques. Ces additifs possèdent une structure de tensioactif polymère. Ils sont parfois associés à une huile porteuse dans les carburants type Essence. Dans les lubrifiants, les dispersants maintiennent en suspension les matières insolubles résultant de la thermoxydation et de la contamination par les suies de combustion. Ils évitent ainsi leur agglomération et contribuent, notamment dans les lubrifiants Diesel, à contrôler l'épaississement des huiles en service.

Dans les deux cas, les dispersants utilisés sont des copolymères amphiphiles dont l'action résulte de deux composantes : l'adsorption assurée par la partie polaire et l'établissement d'une barrière stérique autour des particules insolubles (stabilité colloïdale) ou des surfaces métalliques du moteur assuré par la partie lipophile.

2.1.1.2 Synthèse

Dans la classe des additifs détergent-dispersants sans cendre pour carburant et lubrifiant couramment utilisés, la partie hydrophobe est composée d'une chaine macromoléculaire de

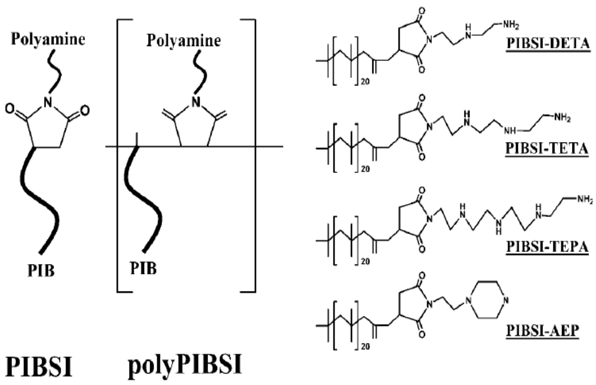

FIGURE 2.1 – *Formules chimiques semi-développées des dispersants sans cendre pour carburants et lubrifiants synthétisés - la partie hydrophobe est à base de polyisobutène PIB de masse 1000g/mol, la partie hydrophile est à base de polyamines : DETA : Diéthylènetriamine, TETA : Triéthylènetétramine, TEPA : Tétraéthylènepentamine, AEP : Aminoéthylpipérazine*

polyisobutène de masse moléculaire d'environ 1000 g/mol, choisi pour ne pas former de dépôt lors de sa dégradation thermique, et la partie polaire est à base d'amines. La formule classique est composée des deux blocs et est notée PIBSI (polyisobuténylsuccinimide). Deux architectures ont été synthétisées au cours de cette étude, l'une étant l'unité macromonomère (PIBSI) de l'autre, poly(PIBSI) (Fig. 2.1).
Cette architecture supramoléculaire a été référée comme polymères "peignes" dans les articles - *voir annexe : article dans Langmuir 2001* -. Différentes longueurs de chaînes polyamines ont été testées pour comparer l'activité détergente des deux structures.

2.1.1.2.1 **"ène" synthèse de structure di-block à partir de chaines macromoléculaires**

Le mécanisme réactionnel est décrit dans la Fig. 2.2. Plusieurs oligomères de polyéthylènamines ont été ajoutés *via* l'anhydride (Fig. 2.1). Non montré dans ce mémoire, une polymérisation cationique de la 2-méthyloxazoline en milieu organique a été également effectuée pour tester des polyamines linéaires de grande taille. Si leur synthèse s'est bien déroulée avec des polyéthylènimines de degré de polymérisation (dp) égal à 20 (valeur éva-

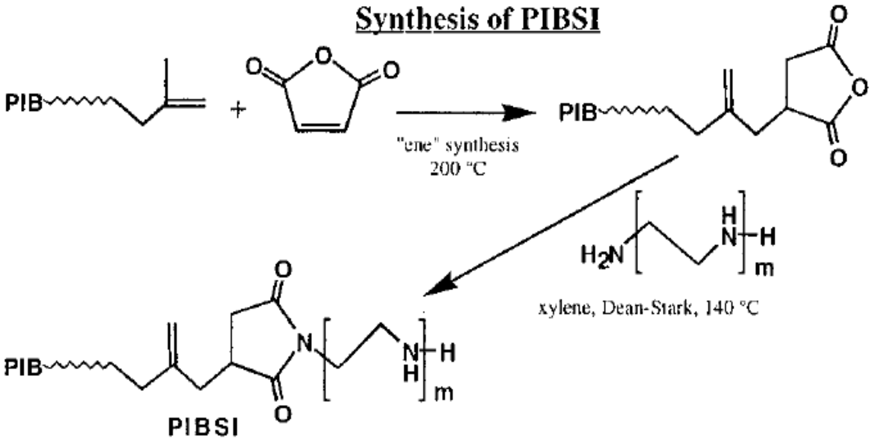

FIGURE 2.2 –

luée par RMN ^{13}C et ^{1}H, confirmée par tonométrie ou osmométrie à pression de vapeur VPO), leur polymérisation avec un PIB terminé par un époxyde a obtenu un rendement faible 18% malgré l'ajout d'un groupe hydroxyle pour accélérer la réaction amine-époxyde. La purification s'est avéré inefficace par précipitation fractionnée et leur utilisation n'a pas été exploitée.

2.1.1.2.2 **polymérisation radicalaire de la structure di-block pour une architecture supramoléculaire**

Le mécanisme réactionnel est décrit dans la Fig. 2.3. L'initiateur utilisé est le tertiobutylperoxybenzoate TBPB. Le PIBSI devient ici le macromonomère d'un polymère ayant une architecture peigne de grande taille noté poly(PIBSI).

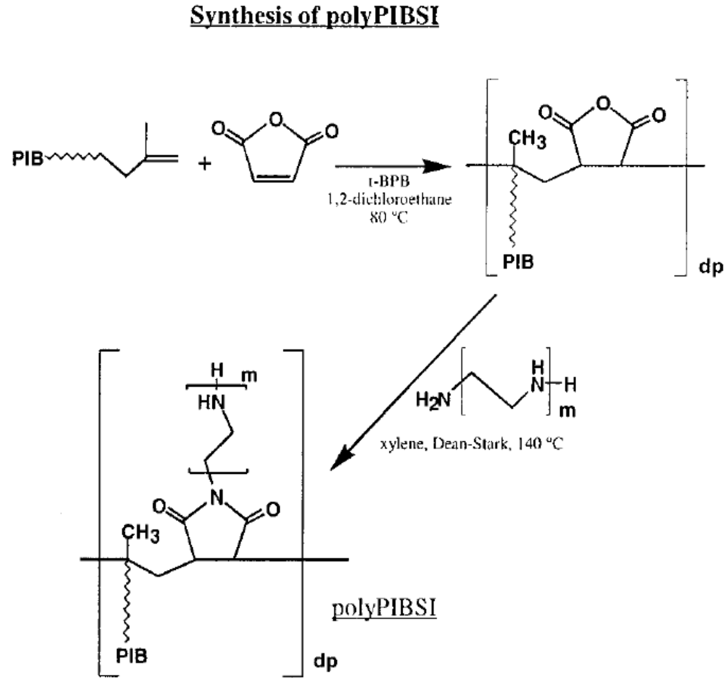
Synthesis of polyPIBSI
PIB
+
t-BPB
1,2-dichloroethane
80 °C
CH3
PIB
dp
H2N
H
N-H
m
xylene, Dean-Stark, 140 °C
H
m
HN
N
O
O
CH3
PIB
dp
polyPIBSI

Figure 2.3 –

La polymérisation radicalaire n'étant pas contrôlée, l'indice de polymolécularité obtenu par Chromatographie d'Exclusion Stérique a été très large (> 5). Grâce à une séparation par précipitation fractionnée dans un mélange de solvants xylène/acétone, des lots de polyPIBSA anhydride de dp[1]=9, 13.5 et 18 avec un indice de polymolécularité moyen de 1,15 ont été recueillis. Une synthèse de 10L de solution a été lancée dans un réacteur semi-industriel pour obtenir suffisamment de polyPIBSA dans les trois gammes de masses afin de tester durant les trois ans de projet des produits provenant d'un même lot. Les polyPIBSI ont été obtenus à partir des polyPIBSA par réaction d'acylation entre l'anhydride succinique terminal du PIBSA et une amine I provenant de polyamines linéaires (DETA : Diéthylènetriamine, TETA : Triéthylènetétramine, TEPA : Tétraéthylènepentamine) et cyclique (AEP : Aminoéthylpipérazine).

2.1.1.3 **Adsorption des dispersants de type polyisobutenylsuccinimides à l'interface solide-hydrocarbure**

Le mécanisme d'action des polymères tensioactifs de type PIBSI et polyPIBSI de têtes polaires de longueurs différentes, linéaires et cycliques, a été étudié en examinant les processus d'adsorption et de désorption de ces polymères à l'interface d'un noir de carbone oxydé (modèle des particules insolubles dans un moteur)/hydrocarbure ainsi que poudre d'aluminium(modèle de la paroi du moteur)/hydrocarbure. Les résultats discutés et publiés portent seulement sur l'interface noir de carbone/hydrocarbure - *voir article Langmuir 2001 en annexe* - .
Les isothermes d'adsorption ont été établis à l'aide d'une méthode spectrophotométrique UV-Visible indirecte. L'allure générale des isothermes et la difficulté à les modéliser par une équation simple de type Langmuir mais plutôt bi-Langmuir (Eq. 2.1) rendent compte de la complexité du phénomène d'adsorption à l'interface noir de carbone/xylène (Fig. 2.4).

$$\Gamma = \frac{\Gamma_1 K_1 C}{1 + K_1 C} + \frac{\Gamma_2 K_2 C}{1 + K_2 C} \tag{2.1}$$

L'adsorption s'effectue par interaction acido-basique des blocs polyamines avec les sites acides de surface présents sur les particules de noir de carbone. La densité de surface de la totalité des acides estimée par titration est de 2 μmol/m^2. Une fraction de ces acidités de 0.9 μmol/m^2 est attribuée aux acides forts (méthode de titration ref. [3]).

Les isothermes présentent une pente initiale forte justifiant l'adsorption langmuirienne. Elles montrent clairement deux régimes (Fig. 2.4) : un accroissement rapide de la quantité adsorbée (Γ) à faible concentration et faible recouvrement de la surface ($\Gamma < 0.5$ μmol/m^2),

---

[1] Remarque : dp = 1 correspond au PIBSI.

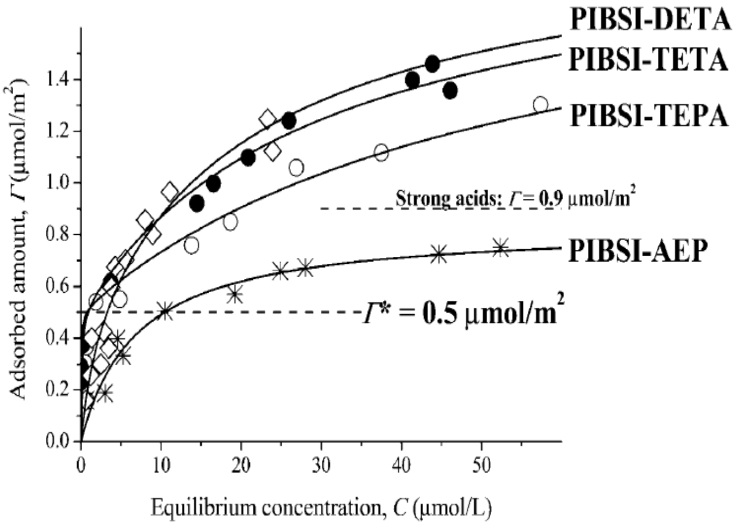

Figure 2.4 – *Isothermes d'adsorption de PIBSI à l'interface xylène/noir de carbone REGAL400R à 20°C : PIBSI-AEP (étoiles) ; PIBSI-DETA (losanges) ; PIBSI-TETA (ronds pleins) ; PIBSI-TEPA (ronds vides). La ligne continue représente le meilleur ajustement de l'Eq.2.1.*

suivi d'une augmentation moins abrupte de Γ vers l'établissement d'un plateau de saturation. L'asymptote de ce plateau a été fixée à 2 μmol/m^2 (quantité totale des sites acides) pour tous les ajustements de courbes. La pente initiale illustre la forte affinité des têtes polaires aminées pour la surface oxydée des noirs de carbone. Le second régime correspondant à une adsorption plus faible a été attribuée aux interactions latérales entre les queues de polyisobutène en accord avec l'illustration donnée par Alexander-De Gennes des polymères adsorbés par leurs fins de chaînes [4]. En régime dilué, appelé "régime champignon", les interactions latérales sont négligeables et l'adsorption est similaire aux petites molécules. A des taux de recouvrements plus importants, le "régime brosse" commence. A ce moment, les interactions latérales gênent l'adsorption et les queues polymères s'étirent. La transition du "régime champignon" au "régime brosse" est atteint quand les pelotes statistiques, formées par les chaines polymères libres de leur mouvement ($R_G = 10$ Å), recouvrent toute la surface :

$$\Gamma^* = \frac{1}{\pi\, R^2{}_G\, N_A} = 0.5\mu\text{mol} \cdot \text{m}^{-2} \tag{2.2}$$

Cette valeur correspond par ailleurs au changement de pente des isothermes. L'ajustement des courbes prend donc en compte $\Gamma_1 = 0.5$ μmol/m^2 et $\Gamma_2 = 1.5$ μmol/m^2. Les valeurs des ajustements sont données dans le tableau suivant :

	PIBSI-AEP	PIBSI-DETA	PIBSI-TETA	PIBSI-TEPA
type of isotherm	Langmuir	di-Langmuir	di-Langmuir	di-Langmuir
Γ_1 (μmol/m^2)	0.84	0.5	0.5	0.5
K_1 (m^3.mol^{-1})	140	500	11000	30000
Γ_2 (μmol/m^2)		1.5	1.5	1.5
K_2 (m^3.mol^{-1})		44	33	18
Γ_{max} (μmol/m^2)	0.84	2.0	2.0	2.0

La PIBSI-AEP est différente des autres PIBSI car la tête polaire ici est cyclique et l'affinité est moins forte. Comme attendu, une chaîne polyamine plus longue conduit à une adsorption plus forte du fait de l'accroche multiple sur plusieurs sites acides. Quand la concentration augmente et que l'on passe en régime "brosse", les sites acides forts sont déjà pris et il ne reste que l'adsorption sur des sites acides faibles. La réorganisation de la couche est moins favorable à des têtes polaires encombrantes ; c'est la raison pour laquelle à régime moins dilué l'adsorption est défavorisée pour les polyamines longues alors que l'inverse s'opère dans le régime dilué.

Dans le cas des polyPIBSI, la constante d'affinité K_1 devient infinie (Fig. 2.5) et l'Eq.

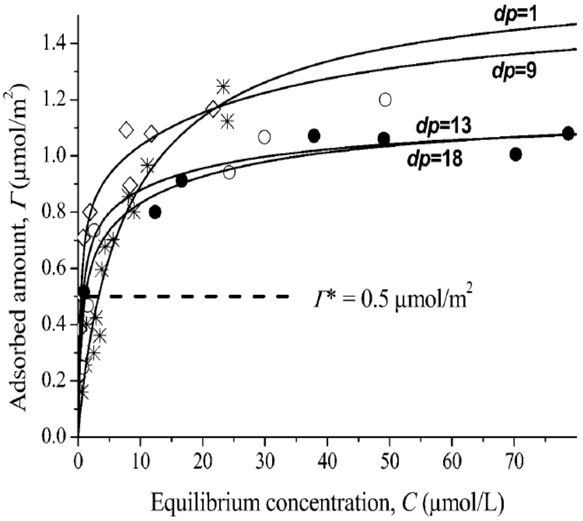

FIGURE 2.5 – *Isothermes d'adsorption de la PIBSI-DETA (dp=1) et des poly(PIBSI-DETA) sur des particules de noir de carbone oxydées*

2.1 devient :

$$\Gamma = \Gamma_1 + \frac{\Gamma_2 \, K_2 \, C}{1 + K_2 \, C} \tag{2.3}$$

Une étude calorimétrique a montré que la réaction d'adsorption était fortement exothermique avec une enthalpie négative suivie d'une variation d'entropie négative. La variation de l'énergie de Gibbs résultante est faible et négative ; $\Delta_{ads}G_M$ est d'un facteur 10 plus faible que $\Delta_{ads}H_M$. Par conséquent, l'adsorption est d'origine enthalpique et la valeur modérée de $\Delta_{ads}G_M$ résulte de la compensation enthalpie-entropie.

2.1.1.4 **Structure de la couche adsorbée**

La structure de la couche adsorbée a été mesurée par Diffusion des Neutrons aux Petits Angles (DNPA) après une annulation de contraste possible dans un mélange heptane hydrogéné / heptane deutéré (3.5 :96.5). L'intensité diffusée décroit en q^{-2} montrant que l'épaisseur de la couche est fine. Faisant l'hypothèse d'une couche homogène, l'intensité diffusée est :

$$I(q) \propto q^{-2}exp(-q^{-2}h^{-2}/12) \tag{2.4}$$

L'épaisseur mesurée a été de 30 Å, significativement plus importante que l'épaisseur en "régime champignon" ($2R_G$=20 Å) et plus petite que celle de la chaîne de PIB de masse 1000 g/mol complètement étirée (40 Å).

2.1.1.5 **Stabilité colloïdale des suspensions de noir de carbone**

L'adsorption des dérivés PIBSI apporte une stabilisation stérique de la suspension de noir de carbone grâce aux chaines PIB tournées vers le solvant. La stabilité colloïdale a été évaluée par des mesures de cinétique d'agrégation en utilisant la diffusion de lumière en milieu noir. Cela a été possible grâce à l'utilisation d'un appareil développé à IFP par le Dr. D. Frot, permettant de travailler en rétrodiffusion et en mode quasi-élastique. Des suspensions relativement concentrées (1-5 wt%) ont pu être ainsi étudiées. Cette expérience permet d'avoir accès aux rayons hydrodynamiques des particules résolus en temps (Fig. 2.6).

Plus rapide est l'agrégation, plus basse est la densité de particules par agrégat et plus basse est la dimension fractale d_f. Les cinétiques pour une réaction limitée par la diffusion (Diffusion Limited Colloid Aggregation DLCA) répondent à R_H=A t^{1/d_f} aux temps longs [5].

La présence de polymère tensioactif s'est avérée efficace puisqu'il permet de stabiliser totalement les suspensions colloïdales de noirs de carbone. Lorsque sa concentration décroît, en régime intermédiaire les cinétiques d'agrégation suivent une loi DLCA avec d_f=2.1. De plus, la contenance minimale en polymère requise pour une stabilisation efficace correspond à une quantité adsorbée de l'ordre de 0.8-0.9 μmol/m^2 quel que soit le polymère (excepté pour le PIBSI-AEP) ; cela correspond au "régime brosse" vu précédemment. Il est à noter que si le PIBSI-AEP est moins efficace, son polymère, le poly(PIBSI-AEP) le devient.
La stabilité colloïdale a également été étudiée à plus forte concentration en noir de carbone par des mesures rhéologiques sur des suspensions à 40wt%. Les suspensions à faible teneur en polymère présentent un caractère visco-élastique. Passé les concentrations pour lesquelles la quantité adsorbée $\Gamma > 0.9 \mu$mol/m^2, la viscosité chute (5-10 mPa.s) et les suspensions adoptent un régime newtonien.

2.1.1.6 **Réarrangement de la couche adsorbée en milieu concentré**

Si on examine ce qu'il se passe au delà du "régime brosse" en milieu très concentré en polymère tensioactif (C>70-80 mmol/m^3), une soudaine augmentation de la quantité de polymère adsorbé est observée (Fig. 2.7). Un accroissement non négligeable de l'enthalpie a également été observé pour cette gamme de concentration [Ref. [1]].

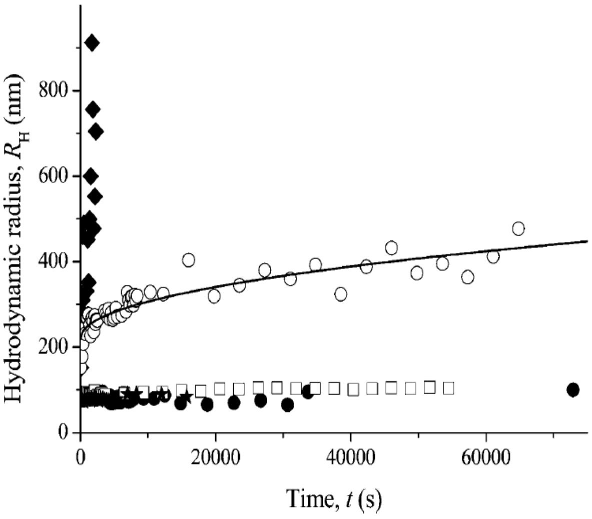

FIGURE 2.6 – *Cinétiques d'agrégation de suspensions de noir de carbone stabilisées avec des quantités variables de PIBSI-TETA-noir de carbone : 1/16 (losanges) ; 1/8 (ronds vides) ; 1/4 (ronds pleins) ; 1 (étoiles). La ligne solide est pour* $d_f = 2.1$

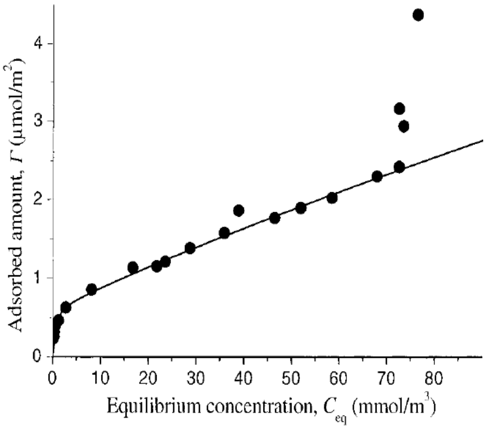

FIGURE 2.7 – *Isothermes d'adsorption de PIBSI-TETA à l'interface xylène/noir de carbone REGAL400R à 60°C. La ligne continue représente le meilleur fit de l'Eq.2.1.*

Du fait que les noirs de carbone analysés ne présentaient pas de microporosité (résultats de l'analyse BET), ce phénomène ne peut pas être attribué à une condensation dans le solide. Un réarrangement en multicouches n'a pas été validé par diffusion des rayons X aux petits angles. La seule hypothèse qui reste est une réorganisation à l'interface solide/hydrocarbure sous forme d'**hémi-micelles inverses**.

2.1.2 Assemblage Membrane-Electrode pour Pile à combustible

Ce travail (Réfs. [7], [6] et [8]) a été effectué dans le cadre de mon poste au Laboratoire des Solides Irradiés. Ce projet de Recherche Appliquée a été initié en 2006 et accepté en 2007 pour financement par le programme transverse Nouvelles Technologies à l'Energie géré par le CEA Grenoble. Le financement de ce projet de 5 ans s'est arrêté en septembre 2012. Il a généré un portefeuille de 5 brevets.
Une proposition ANR MATETPRO est prévue au prochain appel à projet 2013 en collaboration avec une équipe du CEA-LITEN et CEA-INAC ainsi que deux industriels, ARKEMA et une PME, ERAS-Labo.

2.1.2.1.1 Membranes Polymères Electrolytes

Les énergies alternatives sont aujourd'hui une réalité et leur développement est devenu une priorité dans les objectifs de la Recherche française (Grenelle de l'Environnement). Pour l'Automobile, deux technologies sont aujourd'hui en plein essor pour le remplacement du moteur à explosion : la batterie lithium et la pile à combustible.
Dans les deux cas, des prototypes sont à l'essai et les grands constructeurs automobiles (Peugeot, Renault, Nissan, Toyota) ont déjà fait fonctionner certains de leurs modèles avec ces deux types de technologies. La batterie touche un marché plus proche que la pile à combustible car la production d'électricité n'est pas un souci et son acheminement non plus. La pile à combustible, quant à elle, a besoin d'hydrogène pour fonctionner ; il faut donc pouvoir en produire en grande quantité (projet d'un réacteur nucléaire franco-américain pour l'hydrolyse de l'eau haute température) et inventer de nouvelles pompes pour la stocker. Le marché visé est à l'horizon des 20 ans à venir.

La batterie manque cependant d'autonomie et un temps de recharge d'en moyenne de $\frac{1}{2}$ h est nécessaire. Un plein d'essence ne prend pas plus de 8min ! Aussi certains constructeurs pensent à des batteries que l'on pourrait changer comme des valisettes chez les distributeurs classiques pour éviter les temps de recharge. D'autres pensent à une technologie mixte pile à combustible/batterie, la pile servant uniquement à recharger la batterie.

Bref, toute l'inventivité des ingénieurs et des chercheurs se met à la disposition du meilleur dispositif qui pourra un jour remplacer le moteur à explosion pour limiter la dépense en énergie fossile et l'émission de CO_2.

Comment marche une pile à combustible ?

Le principe de la pile à combustible (Fig. 2.8) a été inventé en 1839 par William Grove. Il s'agit tout simplement de la réaction inverse de l'électrolyse de l'eau : $2H_2 + O_2 \rightarrow 2H_2O$.

Il faut donc une anode où l'atome d'hydrogène va se dismuter au contact du catalyseur (en général des grains de platine) selon la réaction suivante :

Anode (oxydation) - carburant : $2H_2 \rightarrow 4H^+ + 4\ e^-$ (0V)

Les deux électrons sont transmis dans le circuit électrique *via* des éléments carbonés conducteurs également présents dans la composition de l'anode. Il y a donc création d'électricité. Les protons sont eux véhiculés vers la membrane échangeuse de protons. Cette membrane peut être en matériaux divers mais **pour l'application automobile, seules les membranes polymères fines et élastiques semblent appropriées. On appelle ce type de pile des piles à combustible à membrane polymère électrolyte (Polymer Mem-**

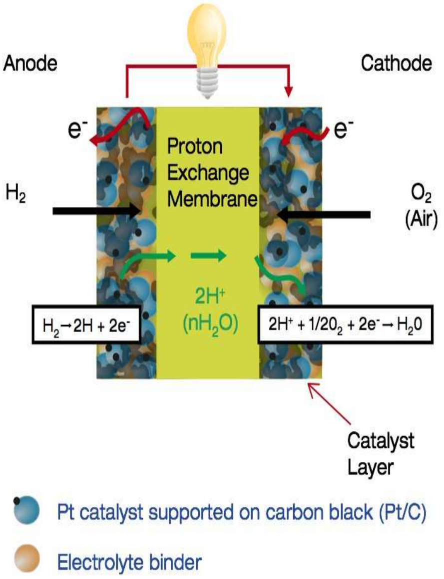

Figure 2.8 – *Schéma montrant le fonctionnement d'une pile à combustible*

brane Fuel Cell ou PEMFC en anglais). Le polymère constituant la membrane se comporte comme un électrolyte solide et est capable d'acheminer les protons de l'anode à la cathode. A la cathode, les protons se recombinent avec l'oxygène de l'air au contact d'un catalyseur (classiquement du platine là encore) selon :

Cathode (réduction) - comburant : $O_2 + 4\ H^+ + 4\ e^- \rightarrow 2\ H_2$O (1,23V)

Le bilan énergétique est donc de 1,23V au maximum. Si on enlève la contribution des résistances du dispositif, on arrive à 0.9 V entre l'anode et la cathode. Lorsqu'on demande du courant à la pile en fonctionnement, la pile va tendre à maintenir cette différence de potentiel. C'est sa faculté à maintenir constante une différence de potentiel la plus haute possible par rapport à la valeur théorique qui fait qu'une membrane est performante ou non pour cette application. On évalue donc les performances d'une pile à combustible non seulement au courant que l'on tire mais aussi par rapport à sa conductivité protonique en réalisant des **courbes dites de polarisation** avec, en ordonnée, la différence de potentiel entre l'anode et la cathode et, en abscisse, la densité de courant (en A/cm^2).

Verrous technologiques à lever

La membrane de référence est une membrane polymère perfluorée sulfonée du fabricant Dupont-De Nemours, le Nafion. L'acide sulfonique est un acide fort ; ce qui signifie que

FIGURE 2.9 – *Exemple d'un stack de piles à combustible permettant le fonctionnement d'une voiture*

sa constante de dissociation est élevée. Il favorise donc la conduction protonique. D'autres fabricants, comme Dow Chemical, commercialisent des variantes de membranes perfluorées sulfonées pour essayer de prendre une part du marché. Néanmoins, la formulation du Nafion fait de cette membrane, la membrane reine dans le domaine des piles à combustible.
Et pourtant, elle a ses limites malgré sa robustesse (5000 h de fonctionnement en milieu acide et oxydant). En effet, sa température de fusion basse interdit de monter trop haut en température de fonctionnement, aux environs de 60-70°C. C'est un problème au niveau des catalyseurs platine qui s'empoisonnent par du monoxyde de carbone à cette température. L'efficacité des catalyseurs est diminuée et la dismutation de l'hydrogène n'est donc pas optimum. De plus, le Nafion a besoin de beaucoup d'eau pour fonctionner, jusqu'à 40% en poids, et, si en mode stationnaire, sa durabilité est forte, en mode cyclique arrêt-démarrage, sa durabilité est nettement affectée par ces cycliques de gonflement et dégonflement liés à la quantité d'eau demandée. Le Nafion est également cher à fabriquer et cela s'ajoute au prix du platine ! Il est donc intéressant de chercher si d'autres types de membranes ne pourraient pas satisfaire davantage au cahier des charges pour l'application automobile ou, tout du moins, pour une même performance, diminuer le prix. Le prix est un paramètre important pour qu'une technologie puisse voir le jour. Pour fabriquer une pile à combustible qui permette de délivrer l'énergie nécessaire pour une voiture, il faut empiler des minipiles les unes aux autres pour créer ce que l'on appelle un "stack" (Fig. 2.9) et pour cela, il faut compter jusqu'à 10m^2 de membrane...

L'objectif est l'étude des membranes polymères électrolytes à base de films fluorés de Poly(Difluorure de vinylidène) (PVDF) nano-structurés linéairement par irradiation aux ions lourds comme alternative au Nafion.

2.1.2.1 Introduction aux Polymères Irradiés

Les polymères irradiés étudiés ici sont sous forme de films fins (de l'ordre de la dizaine de micromètres) et/ou de nanoparticules sphériques. Ces polymères sont soumis à une irradiation par une particule chargée en mouvement. Cette dernière perd son énergie au cours des interactions avec les atomes et les molécules du milieu qu'elle traverse. L'interaction particule-matière donne lieu à des processus physiquement différents : le transfert de quantité de mouvement aux atomes-cibles (par des chocs élastiques), l'excitation-ionisation de la cible (chocs inélastiques), la production de photons, et diverses réactions nucléaires.
Grandeurs caractéristiques des rayonnements ionisants :
. La fluence, notée ici n, est le nombre de particules ionisantes par unité de surface. Elle est reliée au flux Φ, et au temps d'exposition t_e par la relation :

$$n = \int_0^{t_e} \Phi \, \mathrm{d}t \tag{2.5}$$

. La dose absorbée exprime la quantité d'énergie absorbée par un échantillon par unité de masse. Elle est notée D et son unité est le Gray (Gy). La dose absorbée correspond à la quantité d'énergie moyenne E absorbée par la cible par unité de masse. Elle est reliée à la fluence et au pouvoir d'arrêt électronique massique exprimé en MeVcm^2/mg par la relation :

$$D = 1.6 \cdot 10^{-7} \cdot n \frac{dE}{dx} \tag{2.6}$$

. Le débit de dose $\dot{D}$= dD/dt (en Gy.s^{-1}) est la variation de la dose absorbée par unité de temps.

. La longueur du parcours R d'une particule chargée dans la matière peut être calculée à partir de l'expression suivante :

$$R = \int_0^{E} (\frac{dE}{dx})^{-1} \, \mathrm{d}E \tag{2.7}$$

Elle dépend de la masse et de l'énergie du projectile, de la composition atomique et de la densité du matériau cible.

2.1.2.1.2 Irradiation par des électrons

Les électrons peuvent interagir avec la matière au moyen de collisions élastiques et inélastiques (ionisations, excitations). Cependant, lorsque l'énergie des électrons est de quelques

MeV, les interactions par collisions inélastiques sont prépondérantes. Par contraste avec un ion, un électron transporte une charge constante et possède une masse très faible. De ce fait, l'énergie transmise est faible mais suffisante pour que l'électron incident, entré en collision avec un électron des atomes cibles, lui cède une partie de son énergie cinétique et soit dévié de sa trajectoire initiale. L'électron cible (appelé électron secondaire) est ainsi éjecté et peut à son tour induire l'ionisation d'un nouvel atome. Cette réaction en cascade se poursuit jusqu'à ce que l'énergie des électrons ne soit plus suffisante pour entraîner de nouvelles ionisations. **Le dépôt d'énergie est homogène dans l'épaisseur du film polymère**. Les défauts résultants dans le poly(difluorure de vinylidène) PVDF qui sera le polymère étudié ici sont principalement des lacunes électroniques formant des radicaux capables - nous le verrons par la suite- d'initier des polymérisations radicalaires en présence de monomères vinyliques [9]- *voir article Polymer 2004 en annexe* -.

2.1.2.1 **Irradiations par des ions lourds : Interactions ions-matière**

La technique du bombardement ionique nécessite des accélérateurs d'ions couvrant une large gamme d'énergie, de flux et d'angle d'incidence. Cette technique présente comme caractéristiques :

1. une distribution aléatoire des ions sur la cible ;
2. une distribution radiale de l'énergie autour de la trajectoire de l'ion dans un rayon d'environ 10nm.

Elle concerne des matériaux de nature très variée. Le passage d'un ion accéléré entraîne la formation d'une zone endommagée rectiligne appelée **traces latentes**. Spohr [10] décrit de façon simplifiée la formation des traces latentes cylindriques dans la matière condensée. **Le dépôt d'énergie est ici hétérogène par rapport à une irradiation aux électrons**.

Le passage de particules chargées dans la matière fait intervenir différents types d'interactions avec les atomes du milieu traversé :

- collisions inélastiques et élastiques avec les électrons atomiques (collisions de type électronique). C'est le mécanisme prépondérant qui conduit à l'ionisation et/ou l'excitation du milieu traversé. Elles sont prédominantes pour des ions ayant une énergie supérieure à quelques dizaines de keV par unité de masse atomique (uma) ;
- collisions inélastiques avec un noyau (collisions de type nucléaire). La particule est déviée par les forces coulombiennes et son ralentissement se manifeste par l'émission d'un rayonnement de freinage (Bremsstrahlung). Elle peut aussi céder de l'énergie au noyau et amener celui-ci dans un état excité. C'est l'excitation coulombienne du noyau ;
- collisions élastiques avec les noyaux. La particule incidente est diffusée sans rayonner

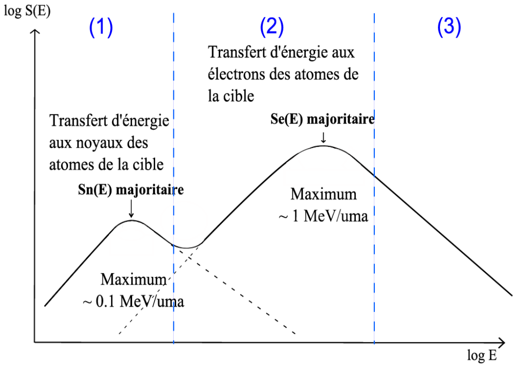

FIGURE 2.10 – *Evolution du pouvoir d'arrêt en fonction de l'énergie de l'ion incident d'après [10]*

ni exciter les noyaux. Ce processus est majoritaire pour des énergies de quelques keV/uma.

Une particule se déplaçant dans un milieu va perdre son énergie par une combinaison de chocs élastiques et inélastiques. En première approximation, le pouvoir d'arrêt des ions est la somme des pertes d'énergie nucléaire et électronique. Le pouvoir d'arrêt peut être calculé par la relation suivante :

$$S(E) = -(\frac{dE}{dx}) = S_n + S_e = \frac{4\pi Z_1^2 e^4 Z_2}{m_0 v^2} \cdot ln(\frac{2m_0 v^2}{I}) \tag{2.8}$$

Avec, Z_1 (Z_2) le numéro atomique de la particule incidente (de la cible), v la vitesse de l'ion incident, e et m_0 la charge et la masse de l'électron et I le potentiel d'ionisation. **Le pouvoir d'arrêt électronique Se est prépondérant aux hautes énergies, ce qui sera le cas dans cette étude**. La Fig. 2.10 représente les variations du pouvoir d'arrêt en fonction de la vitesse de l'ion incident. La forme générale de ces courbes est valable quels que soient l'ion et le matériau. Dans cette courbe, on distingue trois régions différentes. La zone (1) est dominée par l'arrêt nucléaire. Cette contribution nucléaire est d'autant plus importante que l'ion est lourd. **La zone (2) est dominée par l'arrêt électronique.** La zone (3) dite de Bethe-Bloch est la zone où le pouvoir d'arrêt décroît quand l'énergie augmente.

Pour la suite, nous nous situons dans la gamme d'énergie de la zone 2. Lors d'une irradiation par des ions lourds, l'inhomogénéité du dépôt d'énergie et plus précisément celle de la répartition des radicaux formés, va conduire à un greffage radio-induit hétérogène et localisé dans les traces laissées par les ions.

2.1.2.1.2 **Radiogreffage dans les traces latentes créées par les ions lors de l'irradiation**

Le terme radio-greffage ou greffage radio-induit est utilisé lorsque la réaction de greffage est initiée par des radicaux créés préalablement par un rayonnement ionisant. De nombreux paramètres influent sur le radio-greffage :

- les paramètres propres à l'irradiation : dose absorbée, débit de dose et nature du rayonnement
- les paramètres propres aux conditions de greffage : nature du matériau, épaisseur du film, crystallinité, nature du monomère, concentration du monomère, température de réaction, temps de réaction, atmosphère, ajout de solvant, ajout d'inhibiteur d'homopolymérisation, ajout d'agent de transfert...

Le taux de greffage est déterminé par pesée : Y = $\frac{m_f - m_i}{m_i}$ avec m_f, la masse du film après greffage et m_i, la masse initiale.

En présence d'un monomère vinylique tel que le styrène, un film mince (10 μm d'épaisseur) de PVDF de phase crystalline β préalablement irradiés aux ions $^{78}Kr^{38+}$ (10MeV/uma) initie à 60°C la polymérisation radicalaire du styrène dans les traces latentes laissées par les ions. La phase crystalline β est obtenue par bi-étirage du film mince extrudé de PVDF de phase α ; le polymère obtenu voit sa crystallinité augmenter (40wt%) et ses crystallites s'orientent perpendiculairement à la direction d'étirement.
La Fig. 2.11 montre les étapes de fabrication de cette membrane ainsi qu'une image de Microscopie Electronique à Balayage de la coupe de la membrane de PVDF radiogreffée polystyrène (PS) dopée aux ions Césium pour augmenter le contraste PS/PVDF. La Fig.2.12 est une photo montrant la membrane de PVDF radiogreffée par du PS. Cette photo permet de montrer le contraste entre la partie irradiée et greffée blanche irisée et la partie non irradiée transparente.

Le PS est ensuite sulfoné par chlorosulfonation (polystyrène sulfoné noté PSSA). La réaction de substitution électrophile en présence d'acide chlorosulfonique additionne des groupements -SO_3H sur le cycle benzènique du PS greffé dans un premier temps, puis -

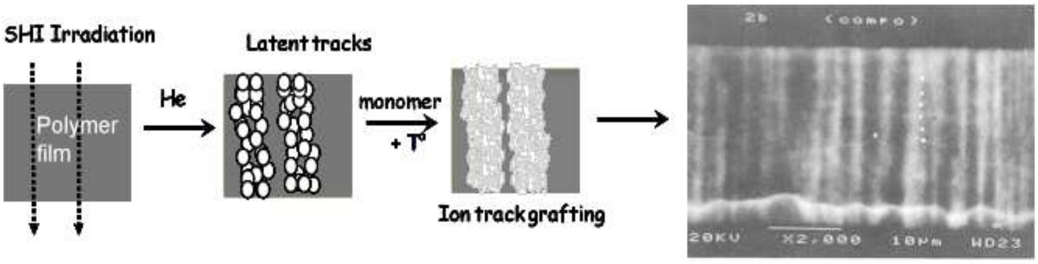

Polymer matrix PVDF 25µm; Irradiation: $_{78}Kr^{31+}$ 10 MeV/uma, 5.10^7 ions/cm^2; monomer: PS, 60°C, Yw = 1.7%

FIGURE 2.11 – *Fabrication d'une membrane polymère radiogreffée dans les traces latentes après irradiation aux ions lourds rapides du GANIL*

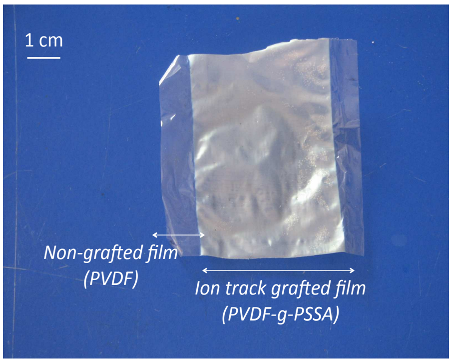

FIGURE 2.12 – *Photo d'une membrane PVDF-g-PSSA radiogreffée dans les traces latentes après irradiation aux ions lourds rapides du GANIL*

SO_2Cl sous l'activation du milieu acide fort en excès. La réaction ne s'arrête donc pas à l'acide sulfonique. Une hydrolyse en milieu basique est nécessaire pour déplacer l'équilibre de la réaction et l'arrêter à l'addition du groupement -SO_3H. La caractérisation de la fonctionnalisation des membranes est suivie par FTIR (Fig. 2.13), XPS et RMN HRMAS - *voir article [7] en annexe*-.

Les acides sulfoniques sont les meilleurs transporteurs de protons dans les polymères fluorés pour l'application pile à combustible. L'originalité de ces membranes est la création des canaux de conductions rectilignes et le renfort mécanique apporté par les zones non greffées qui vont limiter la prise d'eau et donc augmenter la durabilité de cette membrane dans la pile.

2.1.2.1.3 **Transport de protons**

L'efficacité de la fonctionnalisation des membranes polymères est d'abord testée *ex situ* entre deux électrodes en milieu humide afin de vérifier la conduction protonique (Fig. 2.14).

Il est intéressant de noter que la conduction nécessite un taux de greffage suffisant pour les membranes radiogreffées aux rayonnements γ alors que pour les ions, il n'existe pas de taux de greffage seuil. Cela s'explique par le fait que dans le cas des rayonnements γ, l'irradiation mène à un dépôt d'énergie homogène comme dans le cas des électrons et, par conséquent, le radiogreffage commence par les surfaces du film polymère irradié et se propage ensuite vers l'intérieur de la matrice polymère [9]. Il faut donc atteindre un certain taux de greffage pour que les fronts de greffage se rejoignent et que la conduction puisse s'établir.

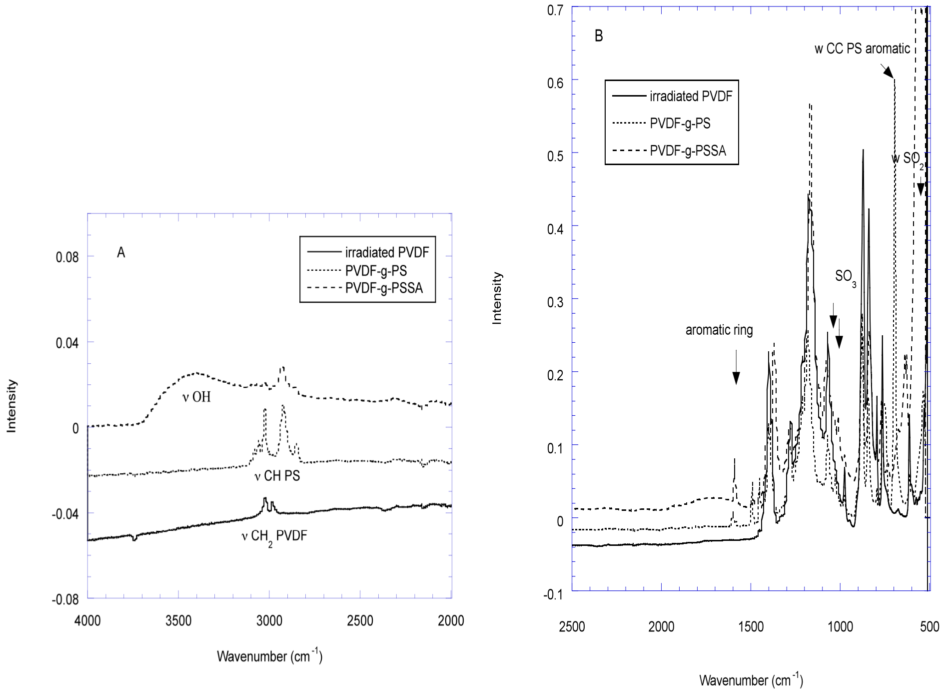

FIGURE 2.13 – *FTIR de membranes de PVDF, PVDF-g-PS et PVDF-g)PSSA préalablement irradiées aux ions* $^{78}Kr^{38+}$ *(10MeV/uma) à une fluence de* 10^{10} *ions/*cm^2

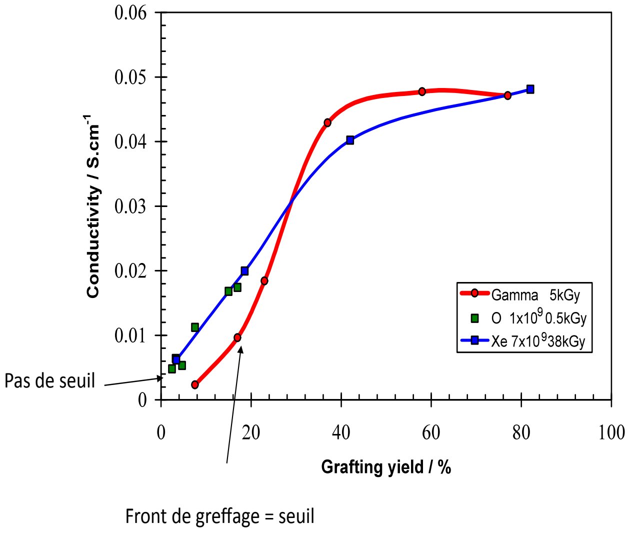

FIGURE 2.14 – *Mesures de conductivité ex situ effectuées au CEA-INAC avec un dispositif deux électrodes de Hg placées de part et d'autre des membranes mouillées. Ces mesures représentent une comparaison entre membranes de PVDF radiogreffées PSSA à différents taux de greffage en utilisant des rayonnements* γ *et des ions*

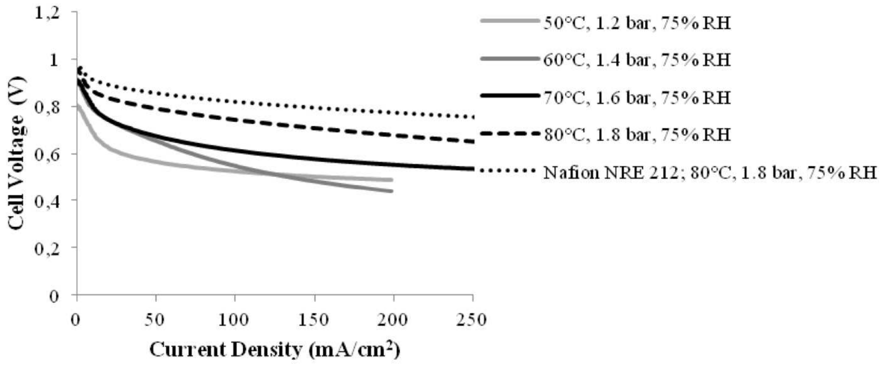

FIGURE 2.15 – *Courbes de polarisation obtenues entre 50°C et 80°C pour la membrane de PVDF-g-PSSA (taux de greffage = 140%) - Tests en pile alimentée en gaz* H_2 *et* O_2 *purs*

Le problème d'un taux de greffage important est que les propriétés mécaniques des membranes résultantes en sont fortement affectées. Leur durabilité en pile devient très faible. Il est donc très intéressant de pouvoir assurer une conduction protonique à faible taux de greffage ; ceci est un avantage pour l'irradiation aux ions.

Les performances des membranes sont finalement testées *in situ* dans une monopile en fonctionnement sur les bancs de test du CEA-LITEN. La reproductibilité des résultats obtenus sur une membrane en PVDF-g-PSSA a été montrée (Fig. 2.15), la conductivité est importante de l'ordre de 30 mS/cm et la densité de courant à 500 mV peut être délivrée sur trois jours à un ampère par cm^2. Ces résultats sont tout à fait comparables au Nafion dans les mêmes conditions. La robustesse des membranes lors du montage en pile est également un atout pour l'application industrielle. Une publication parue début 2010 dans Journal of Power sources - *voir annexe* - compile les résultats obtenus.
Par contre, des tests de durabilité ont montré que le taux de greffage trop important limite la durée de vie à 70h.

Le but en 2011 a donc été de renforcer la tenue mécanique sans décroître le taux de greffage par trace, responsable de la bonne conductivité. Pour cela, il suffit de diminuer la

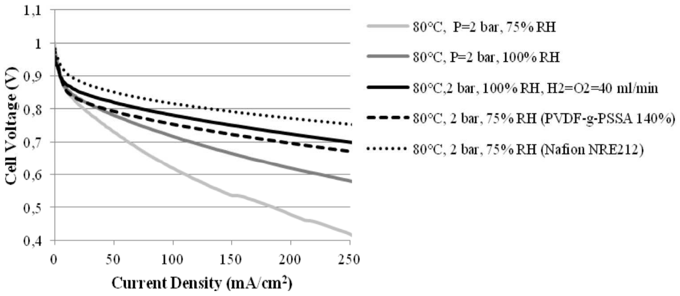

FIGURE 2.16 – *Comparaison des courbes de polarisation obtenues à 80°C pour la membrane de PVDF-g-PSSA (10^{10} ions/cm^2, taux de greffage = 140 wt %), la membrane de PVDF-g-PSSA (10^8 ions/cm^2, taux de greffage = 40 wt %) et le Nafion NRE212 - Tests en pile alimentée en gaz H_2 et O_2 purs*

fluence sans changer les conditions de greffage. La fluence initiale était très élevée de l'ordre de 10^{10} traces/cm^2. On a abaissé cette fluence de deux ordres de grandeur et, malgré cela, en jouant sur les débits d'entrée des gaz H_2 et O_2, les performances en test en pile ont été préservées (Fig. 2.16). Ce résultat montre un fort effet de la structuration en nanocanaux sur les propriétés de conduction de ce nouveau type de membrane pour l'application pile à combustible. Une présentation orale a été retenue au MRS à Boston fin novembre 2011[8]. Il reste à faire des tests de durabilité mais là, la tenue mécanique est nettement améliorée, ce qui nous rend optimiste.

La fonctionnalité polystyrène sulfonée est intéressante du fait de sa haute conductivité protonique, mais nous savons également qu'elle est fragile en condition de pile car il a été reporté dans la littérature qu'au bout d'un certain temps, il y a désulfonation. Nous avons déjà observé par XPS une désulfonation sur une semaine de test. Il faut donc penser également à d'autres types de fonctionnalités. Le polyacide acrylique sulfoné avait été testé en 2010 lors d'un stage court Ecole Polytechnique et un de mes post-doctorant, Enrico Gallino, a répété des tests en pile en 2011. Les deux types d'acidité, carboxylique et sulfonique allaient dans le sens des canaux protoniques multi-acides ce qui ouvrait le champ d'investigation à la création de gradient de protons à l'intérieur des canaux de conduction.

Malheureusement, le résultat est que l'acide carboxylique freine la conduction protonique au détriment de l'acide sulfonique. Par conséquent, la stratégie actuelle n'est plus sur les multi-acides.

2.1.2.2 **Electrodes**

L'amélioration de l'interface membrane-électrode est devenue une priorité dans ce projet en 2012 car elle reste une interrogation sur la compréhension des spectres de spectroscopie d'impédance enregistrés au cours des tests en pile. En effet, on observe, dans des conditions sévères de test en pile, la présence de deux hémisphères au lieu d'une seule révélant plusieurs mécanismes de transport et pouvant être le témoin d'un problème d'interface (Fig. 2.17).

Il ne s'agit donc plus de s'intéresser à la membrane seule mais d'appréhender l'ensemble du système c'est-à-dire l'Assemblage Membrane-Electrode ou AME. Cette amélioration passe par la mise en place d'un AME particulier, dans lequel on change la composition de l'électrode pour assurer une continuité chimique entre la phase active et la membrane. Cela revient à la réalisation d'un AME 100% technologie CEA protégé par un brevet.

2.1.2.2.1 **Point Triple**

Le point dit "triple" se situe au niveau des particules carbonées-grains de platine-électrolyte composant la phase active de l'électrode. Quand l'hydrogène se dismute sur les grains de platine, les électrons doivent être acheminés jusqu'aux plaques polaires collectrices de courant et les protons sont pris en charge par l'électrolyte environnant pour être conduits jusqu'à la Membrane Polymère Electrolyte (PEM). Jusqu'à présent, seules des suspensions de Nafion sont utilisées comme électrolyte dans les électrodes de piles à combustible type PEM. Il est donc important quand il s'agit de tester une membrane autre que Nafion d'assurer une continuité chimique dans le mode de transport des protons.

2.1.2.2.2 **Nanoparticules de PVDF radiogreffées**

L'idée (Schéma Fig. 2.18) est de remplacer le Nafion présent sous forme de suspension colloïdale dans un mélange eau/alcool dans les suspensions de particules carbonées platinées (encres) par des nanoparticules de PVDF radiogreffées par les mêmes entités conductrices de protons que la membrane polymère étudiée.

L'obtention de nanoparticules de PVDF radiogreffée ayant déjà été étudiée dans le cadre d'une thèse que j'ai co-dirigé sur la nanovectorisation pour des applications biomédicales [11] [12] (voir section 2.2.2), le remplacement du Nafion par une suspension de nanoparticules de PVDF n'a été qu'une question de formulation d'encres. Le résultat est montré Fig. 2.19.

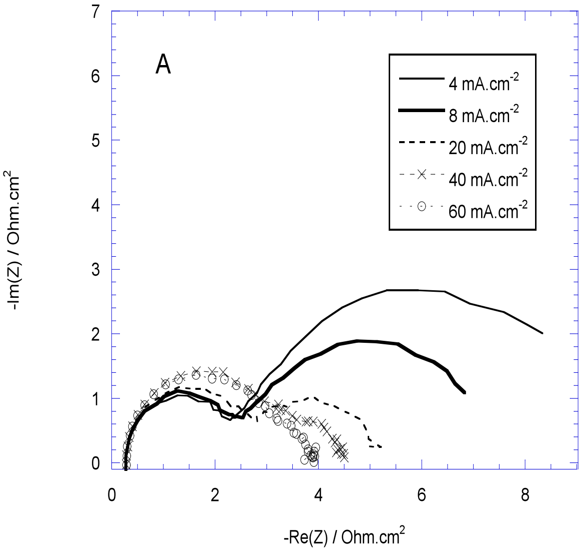

FIGURE 2.17 – *Exemple de courbes de spectroscopie d'impédance enregistrées au début d'un test en pile sur une membrane de PVDF-g-PSSA (10^{10} ions/cm^2, taux de greffage = 140 wt %) pour des conditions particulières de faible température et pression en atmosphère peu humide : 50°C, 2 bars, 35% RH (Relative Humidity)*

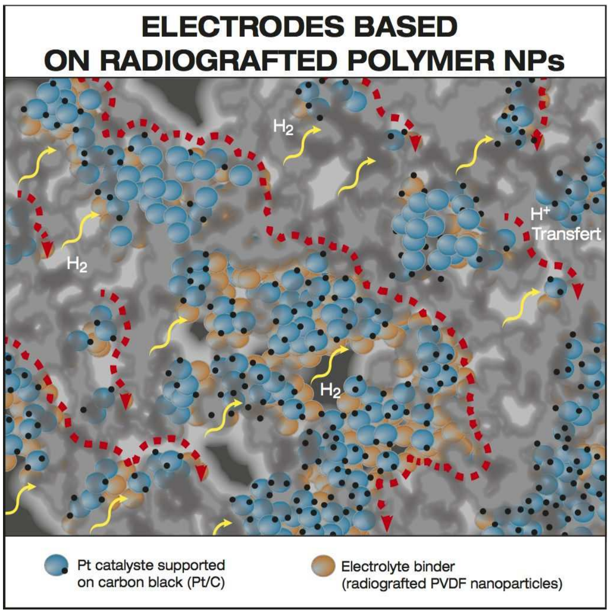

FIGURE 2.18 – *Schéma de la composition d'une électrode comportant des nanoparticules de PVDF fonctionnalisées remplaçant la suspension colloïdale de Nafion*

L'originalité a été de changer les conditions de greffage *in situ* sous rayonnement γ pour s'adapter à une nouvelle fonctionnalité en radiogreffant dans les traces non plus le styrène mais le monomère AMPS[2] .

Les courbes de polarisation obtenues sur des membranes Nafion montrent que ce nouveau type d'encre mérite d'être developpé (Fig. 2.20). En effet, ces courbes de polarisation ont été obtenues à très faible taux d'humidité relative (RH 20%), à des taux où le Nafion n'est pas très performant afin de tester ces nouvelles encres dans des conditions non favorables[3]. Et les résultats montrent que la phase active reste efficace quel que soit le procédé de déposition à température ambiante ou à chaud sur les membranes ici en Nafion.

---

[2] 2-acrylamido-2-propane sulfonic acid

[3] Remarque : les résultats avec l'air comme comburant au lieu de l'oxygène pur sont classiquement moins bons et permettent d'être encore plus descriminants

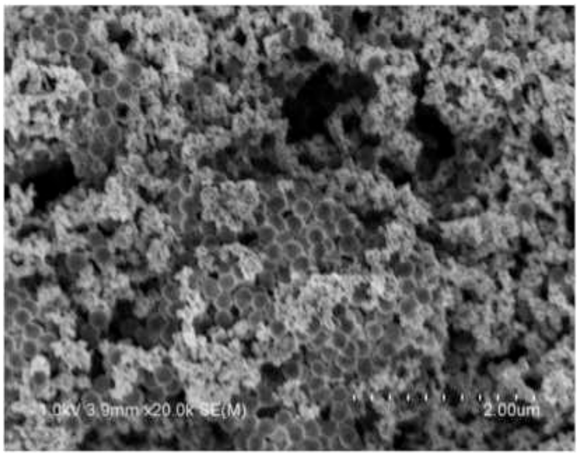

FIGURE 2.19 – *Image FESEM de la nouvelle encre composée des nanoparticules de PVDF-g-AMPS (diamètre 220 nm) et de particules carbones platinées et testée en condition de pile au CEA-LITEN à Grenoble*

2.1.3 Capteurs de métaux toxiques pour le contrôle qualité de l'eau

Ce travail [13] a été effectué dans le cadre de mon poste au Laboratoire des Solides Irradiés et fait suite à la thèse de doctorat d'Olivia Cuscito [14] que j'ai co-encadrée entre 2004-2007. Ce projet de Recherche, actuellement en voie de transfert de technologie, a été initié en 2008 et accepté en 2009 pour financement par le RTRA, Ile de France, dans la catégorie valorisation ; puis, un soutien OSEO a pris le relais et, actuellement, ce projet est soutenu par programme transverse TECHNOSANTE géré par le CEA Saclay jusqu'en mars 2013. Il a généré un portefeuille de 5 brevets et a reçu deux prix : le prix OSEO à d'aide à la création d'Entreprise 2012 et le prix Pollutec 2012.

2.1.3.1 Radiogreffage dans les traces attaquées des membranes nanoporeuses de PVDF

Les films polymères soumis aux rayonnements ionisants présentent différents types de défauts occasionnés lors de l'irradiation : scission de chaînes, dégagement de gaz suivant la nature chimique des polymères, réticulations, formation d'espèces radicalaires... Si le polymère est semi-crystallin, les radicaux vont se trouver piégés dans les crystallites et leur durée de vie peut être très importante si les conditions de stockage post-irradiation préservent à la fois de l'oxygène de l'air et de températures trop élevées. C'est ainsi que le greffage

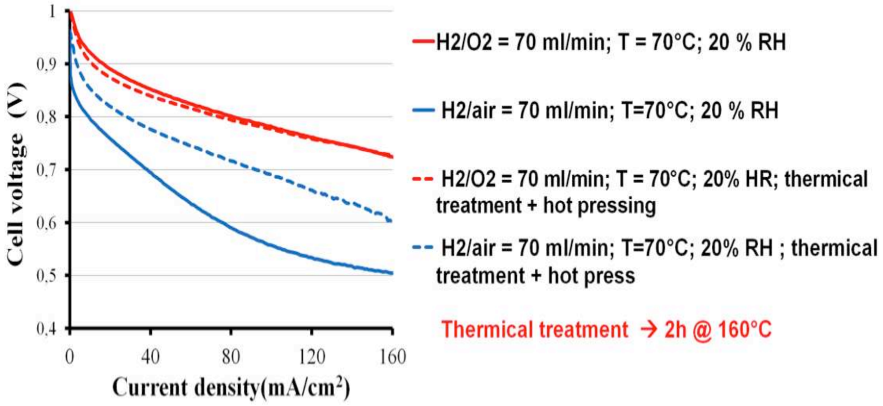

FIGURE 2.20 – *Courbes de polarisation obtenues à très faible taux d'humidité relative (RH 20%) avec des électrodes contenant des nanoparticules de PVDF-g-AMPS (diamètre 220 nm)*

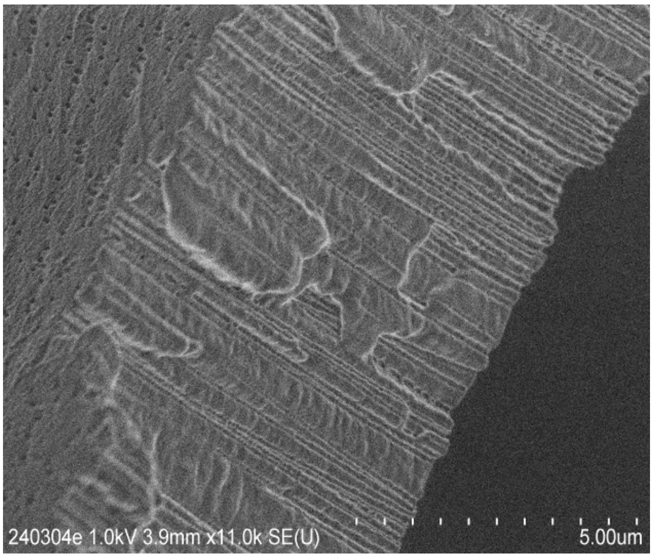

FIGURE 2.21 – *Image FESEM de la tranche d'une membrane β-PVDF à traces attaquées - solution d'attaque = KOH 10N,* $KMnO_4$ *0.25N, 65°C, temps d'attaque = 30min*

radio-induit par polymérisation radicalaire en présence d'un monomère vinylique peut se faire dans les traces latentes laissées par des ions lourds rapides comme vu précédemment pour l'application pile à combustible ou dans des travaux antérieurs publiés sur des films de PVDF irradiés aux électrons [15] [16] et [17]. Ici, il s'agit du même principe mais les traces ont été préalablement révélées par attaque chimique. **Une étude RPE a montré contre toute attente que des radicaux étaient encore présents sur la paroi des nanocanaux, même après une exposition à 65°C dans une solution fortement oxydante.**

2.1.3.1.1 Révélation des traces latentes créées lors de l'irradiation aux ions lourds accélérés

Les traces latentes laissées par le passage de l'ion-projectile dans le film polymère après irradiation aux ions lourds rapides du GANIL peuvent se révéler sous l'action d'une base forte. L'énergie cinétique des ions incidents permet de traverser complètement les 10 μm d'épaisseur des films de β-PVDF étudiés. Ainsi, après révélation chimique, chaque trace donne naissance à un pore débouchant de part et d'autre de la membrane polymère ainsi formée (Fig. 2.21). Le rapport d'aspect est important ; il s'agit en fait de nanocanaux plutôt que de nanopores. Le diamètre de la trace est proportionnel au temps d'attaque chimique (Fig. 2.22). Ce diamètre peut être aussi petit que 10 nm et aller à quelques microns.

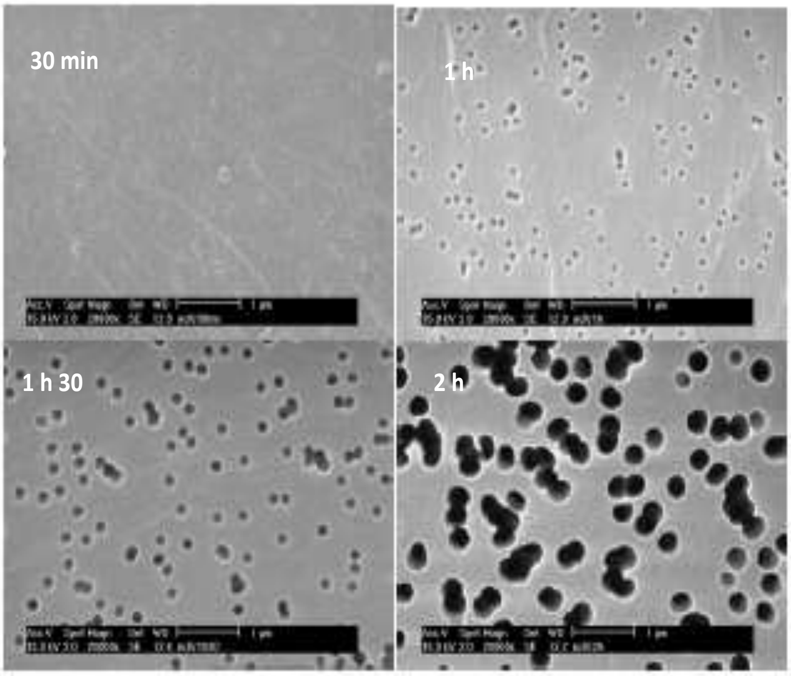

FIGURE 2.22 – *Images MEB de même grandissement (X 20 000) de la surface de membranes β-PVDF à traces attaquées en fonction du temps d'attaque chimique - solution d'attaque = KOH 10N, $KMnO_4$ 0.25N, 65°C*

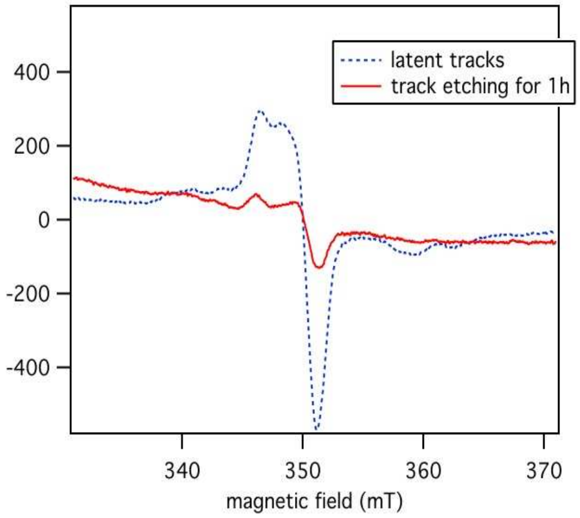

FIGURE 2.23 – *RPE de membranes β-PVDF à traces non-attaquées et attaquées- solution d'attaque = KOH 10N,* $KMnO_4$ *0.25N, 65°C, temps d'attaque = 1h*

2.1.3.1.2 **Persistance des radicaux après révélation chimique des traces**

Si le diamètre de la trace attaquée est submicronique, alors des défauts de type radicalaires sont toujours présents comme le montre la Fig. 2.23.

Une étude RPE complète a été effectuée durant la thèse d'Olivia Cuscito [14] et approfondie ensuite [13]. La décroissance radicalaire en fonction du diamètre varie en $1/r^2$ où r est le rayon du nanopore. Pour des temps d'attaques de traces supérieurs à 40 min (environ 80 nm de diamètre), la quantité de radicaux n'est plus suffisante pour initier une polymérisation. De plus, la polymérisation radicalaire est initiée par les radicaux alkyles et, après un certain temps de contact avec la solution d'attaque contenant un oxydant puissant, le $KMnO_4$, les radicaux résiduels sont en grande majorité des radicaux peroxyles.

2.1.3.1.3 **Création de membranes polymères nanoporeuses bifonctionnelles**

Pour des diamètres de pores de l'ordre de 50 nm, les radicaux alkyles sont majoritaires. Ces radicaux initient la polymérisation radicalaire d'un monomère vinylique à l'intérieur des pores. De l'acide acrylique a ainsi été polymérisé avec succès [14]. Pour prouver que le greffage se localisait dans les pores et non sur la surface, un traitement des oxydes de surface par de l'éthylène diamine a permis de remplacer toutes les acidités par des fonctions

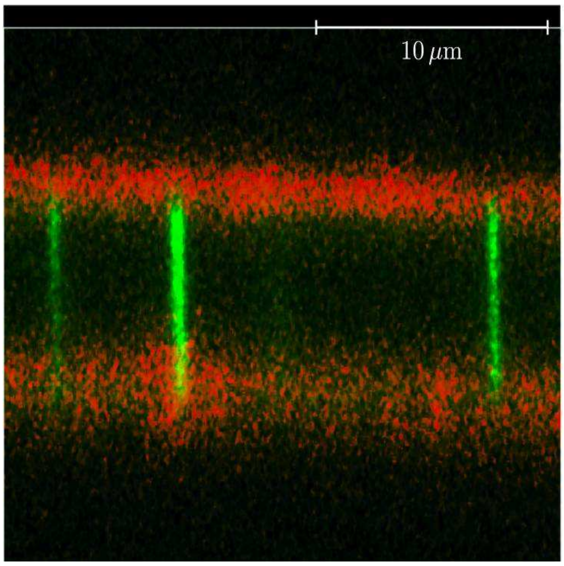

Figure 2.24 – *Images de Microscopie Confocale à Balayage Laser d'une membrane nanoporeuse de PVDF-g-PAA modifiée en surface par couplage des oxydations de surface avec l'éthylenediamine avant greffage radio-induit dans les pores. Les images sont enregistrées suivant le plan-xz (section) et subissent une reconstruction des séries de tranches xy. L'axe z a été réajusté en tenant compte de l'indice de réfraction du PVDF. Rouge : Fluoresceine isothiocyanate marqueur des groupes fonctionnels aminés, i.e. oxydation de surface. Vert : Alexa Fluor R hydrazide, marqueur des groupes acides carboxyliques, i.e. poly(acide acrylique)*

amines I ; le radiogreffage de l'acide acrylique a ensuite eu lieu. Le double marquage de cette membrane s'est déroulé par réaction de couplage en présence d'une carbodiimide soluble dans l'eau, l'EDC, avec deux sondes fluorescentes : l'Alexa Fluor hydrazide pour les acides carboxyliques et la Fluorescéine isothiocyanate pour les amines. Le résultat de ce double marquage est montré dans la Fig. 2.24.

2.1.3.1.4 **Transformation des membranes polymères nanoporeuses en capteurs de métaux lourds**

Le poly(acide acrylique) (PAA) est un polyélectrolyte qui capte par simple interaction électrostatique tous types d'ions bivalents. Ces ions appelés "ions lourds" dans le jargon des personnes travaillant dans la pollution de l'eau sont souvent toxiques pour l'Environnement et l'Homme.

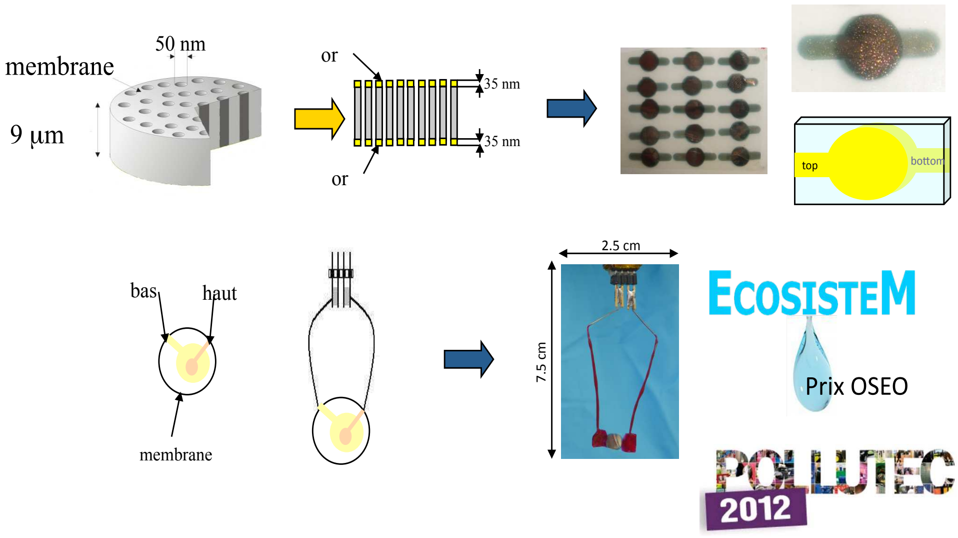

FIGURE 2.25 – *Projet ECOSISTEM - Fabrication des petits capteurs écologiques pour la détection de traces de métaux toxiques dans l'eau*

L'invention a été de transformer ces membranes en électrode pour pouvoir procéder à une analyse électrochimique du contenu des pores fonctionnalisés par du PAA. Pour se faire (Fig. 2.25), il suffit de métalliser la surface des membranes de PVDF fonctionnalisées avec une couche d'or suffisamment fine (environ 25 nm) sans obturer les pores (choisis pour cette application de 50 nm de diamètre).

Après contactage à un potentiostat portable et application d'un potentiel négatif pour électrodéposer les ions piégés dans la membrane sur la surface d'or servant d'électrode de travail, il est possible de faire une analyse dite de voltammétrie à redissolution anodique ou ASV en anglais (Anodic Stripping Voltammérie) en balayant la tension vers des potentiels

positifs (Fig 2.26).
Par intégration des signaux, la détection de métaux lourds à l'état de trace (ppb et subppb) est possible.

Le projet se nomme ECOSISTEM[4] et propose une solution respectueuse de l'Environnement « Green Tech » pour l'analyse de la qualité de l'eau sous la forme d'un capteur propre, portable et facile d'emploi. La cible d'ECOSISTEM est la détection des métaux lourds dangereux pour la santé, comme par exemple le plomb, le cadmium ou le mercure. Les capteurs ECOSISTEM sont adaptés aux besoins du client, simples ou multi-paramètres. En effet, différents types de monomères vinyliques peuvent être polymérisés radicalairement à l'intérieur des nanocanaux apportant des fonctionnalités variables pouvant ainsi ne détecter qu'un ion d'intérêt parmi d'autres. ECOSISTEM se démarque de la concurrence par son extrême sensibilité et offre la possibilité de réaliser des mesures directement dans le site sans prélever d'échantillons.

Aujourd'hui, ECOSISTEM propose un kit contenant le démonstrateur ECOSISTEM avec le système de mesure existant sur le marché (exemple : Palm Sens). A long terme, le projet proposera aussi l'appareillage de mesure propre et adapté aux capteurs ECOSISTEM.

2.2 Santé

2.2.1 Polymères dégradables

2.2.1.1 Polymères biorésorbables par l'organisme

Durant ma maîtrise et mon DEA (master I et II), j'ai abordé la synthèse de polymères biodégradables pour des applications médicales dans le Laboratoire des BioPolymères du CNRS de Thiais.
La polymérisation anionique par ouverture de cycle de β-butyrolactone en milieu organique permet d'obtenir des polyesters de haute masse molaire jusqu'à 1 000 000 g/mol. L'amorceur était le benzoate de tétramethyl ammonium (10^{-3} éq.). Le poly(β-acide malique) (PMLA) obtenu s'hydrolysait en acide malique qui est un constituant du cycle de Krebs. L'objectif poursuivi a été la synthèse chimique de terpolymères dérivés du PMLA et la modification chimique de ces terpolymères afin de répondre aux exigences inter-réactionnelles entre le polymère et les facteurs de croissance ainsi qu'à la compatibilité avec le milieu biologique. Ainsi les synthèses de poly(malate de benzyle - *co* - malate de butyle - *co* - malate d'allyle) et de poly(malate de benzyle - *co* - malate de butyle - *co* - malate de 3-methyl-3-butène) ont été effectuées et suivies de modifications chimiques pour l'interaction avec un facteur

---

[4] projets dérivés ASSENSOR et CAPTÔT

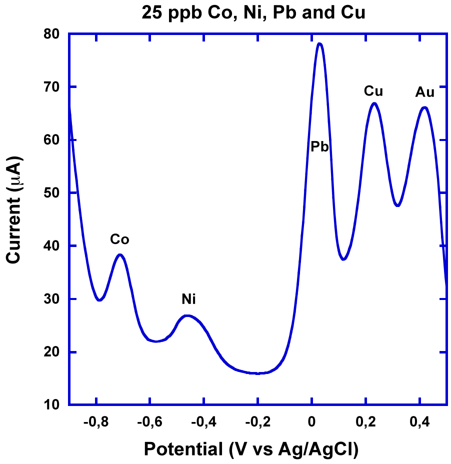

Figure 2.26 – *Analyse ASV par le capteur à base de membranes PVDF à traces attaquées fonctonnalisées (technologie ECOSISTEM) d'une solution aqueuse contenant 4 ions différents à l'état de trace*

de croissance permettant la cicatrisation musculaire et cutanée. Ces polymères étaient destinés à entrer dans la composition d'un médicament en tant que régulateur du relargage du facteur de croissance dans le corps humain.
Les étapes de purification par chromatographie polaire de phase normale et inversée ainsi que les nombreuses caractérisations RMN ^{1}H et ^{1}3C ont été très riches d'enseignement pour la suite de ma carrière.

2.2.1.2 Polymères pH-dégradables pour la délivrance de médicaments

Après un doctorat dans les détergents/dispersants pour carburant et lubrifiant à l'IFP (voir section 2.1.1), je suis partie en Angleterre pour un post-doctorat à l'Ecole de Pharmacie de l'Université de Londres (1998-2001) où j'ai repris mes activités de polymériste dans le domaine de la Santé abordée durant mon master. La mission qu'il m'était confiée par le Dr. Stephen Brocchini (à l'époque sous la direction du Professeur Ruth Duncan) a été de mettre au point la synthèse d'un polymère pH-dégradable pour la délivrance de toxines dans les cellules tumorales.
Ce travail a donné lieu à un brevet et trois papiers [18] [19] [20].

L'idée repose sur l'effet EPR (Enhanced Permeation Retention) qui suggère une rétention plus importante des molécules de fortes masses au voisinage des tumeurs. Cette accumulation liée à la taille est provoquée par la mauvaise croissance des vaisseaux sanguins autour de la tumeur. Notamment la vascularisation est irrégulière formant des constrictions qui freinent le passage des plus grandes molécules. Leur temps de présence à ces endroits devient donc plus long qu'ailleurs. De plus, le gainage endothélial est peu efficace et les macromolécules diffusent à l'extérieur entrant en contact avec les cellules tumorales. Celles-ci font pénétrer les macromolécules en leur intérieur par invagination de leur membrane (phénomène de pinocytose). Les macromolécules se retrouvent ainsi dans des lysosomes à l'intérieur des cellules tumorales. Le milieu intra-lysosomal est à un pH acide de l'ordre de 5. L'idée est donc de **synthétiser des polymères ayant des toxines greffées stables au pH du sang (7.4) et pouvant se dégrader à pH 5**. Les toxines type Taxol ou Doxorubicine ne sont pas actives si elles sont greffées sur un polymère.
Le polymère synthétisé doit avoir une taille supérieure au filtre du rein (40 000 daltons) mais ses produits de dégradation doivent pouvoir être éliminés facilement.
La synthèse polymère que j'ai mise au point (protégée par un brevet) est une simple polycondensation de macromonomères de PEG (de taille très inférieure à 40 000 daltons et préalablement modifiés à ses extrémités) avec des éléments *cis*-aconitiques stables à pH neutre et qui se clivent à pH acide par cyclisation.

2.2.2 Polymères biocompatibles non-dégradables

Dans le cadre de mon travail au LSI, cette thématique "Santé" s'est poursuivie ; j'ai obtenu un prix Le Foulon de Lalande, décerné par l'Institut de France, pour travailler avec le Dr Natacha Betz au CEA de Saclay sur le thème des maladies infantiles. En collaboration avec le professeur Gérard Déléris de l'Université de Bordeaux 2, nous avons étudié l'immobilisation, par radiogreffage sur des films de PVDF, de peptides cycliques interagissant avec des facteurs de croissance endothéliaux (VEGF : Vascular Endothelial Growth Factor). Ces facteurs de croissance interviennent pour la croissance de nouveaux vaisseaux sanguins (Angiogenèse). Lorsqu'une tumeur se développe, elle a besoin de sang pour grossir et demande à l'organisme de sur-exprimer les VEGF. Les récepteurs VEGF sont à ce moment localisés en grand nombre autour de la tumeur en croissance. Les peptides cycliques synthétisés par l'équipe du professeur G. Déléris sont des inhibiteurs de VEGF, notés CBO-P11. Le CBO-P11 se fixe sur les récepteurs de VEGF et empêche la réaction biochimique de se mettre en place. L'angiogenèse est inhibée et la tumeur meurt par manque de nutrition. Les thérapies anti-angiogéniques sont en tests cliniques depuis quelques années mais il y a un manque de suivi thérapeutique efficace. Par conséquent, le développement de nanovecteurs anti-angiogéniques pour l'imagerie médicale intéresse fortement les médecins.

Le fait d'immobiliser des agents de ciblage et des sondes pour l'IRM sur un même nanovecteur comporte plusieurs avantages tels qu'une durée de vie plus longue de l'agent de ciblage dans l'organisme, l'action de l'effet EPR sur des particules de rayon hydrodynamique plus large que les petites molécules, le suivi efficace des agents de ciblage, une meilleure élimination de ces agents par l'organisme.

Le PVDF est un polymère fluoré inscrit à la Pharmacopée et a reçu sa nomination de polymère biocompatible par la FDA. **L'utilisation de rayonnements ionisants pour le greffage de molécules biologiques permet d'éviter une chimie de surface utilisant des produits ou sous-produits toxiques.**

Les immobiliser dans un premier temps sur un film de PVDF a permis de mettre au point les réactions de radiogreffages mises en jeu [15] [16] [17] et dans un deuxième temps de les appliquer sur des suspensions colloïdales de nanoparticules de PVDF [12] [11].

2.2.2.1. Nanovecteurs pour l'imagerie médicale et le traitement tumoral

Cette application a nécessité une polymérisation radicalaire en nanoémulsion du monomère gazeux VDF afin d'obtenir un latex de nanoparticules de PVDF (Fig. 2.27). Les conditions opératoires avaient déjà été mises au point par Bezrukov et al. [21]. Le montage sous pression a été reproduit au laboratoire et continue de fonctionner avec succès. Une fois les nanoparticules de PVDF synthétisées, une modification de leur surface a nécessité plusieurs étapes de synthèses chimiques pour leur conférer les propriétés de ciblage tumoral (immobilisation du cyclopeptide inhibiteur du VEGF, CBO-P11) et d'imagerie par l'accrochage de différents marqueurs tels que des sondes fluorescentes ou bien des agents de

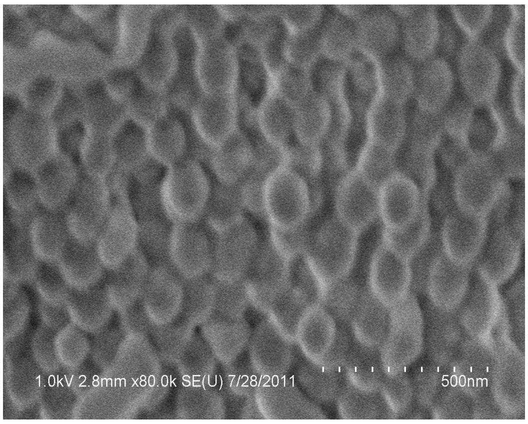

Figure 2.27 – *Image FESEM des nanoparticules de PVDF obtenues par polymérisation par nanoémulsion avec le montage du LSI*

contraste permettant le transfert de polarisation en IRM.
L'astuce est de créer une plateforme sur laquelle l'immobilisation de différentes molécules est facilitée. Une première et très fine couche d'accroche "universelle" est formée par irradiation γ polymérisant radicalairement *in situ* de l'acide acrylique. Les acides carboxyliques sont ensuite modifiés de manière à obtenir une surface couverte de fonctions azotures -N_3. Ainsi toute molécule ayant un alcyne vrai en bout se lie par simple cycloaddition 1,3-dipolaire de Huisgen, appelée communément *"click" chemistry.* Les étapes de synthèse sont décrites dans la Fig. 2.28 et ont été mises au point par Stéphanie Deshayes durant sa thèse que j'ai eue en co-direction avec le professeur Déléris (2006-2009) - *voir article Pharm. Res. en annexe* -.

Un résultat de fluorescence avec une sonde de fluorescence CyTE777-Lys(CBO-P11)-propargyl amide pour l'application à l'imagerie médicale est montré Fig. 2.29. Les spectres de fluorescence, enregistrés dans l'eau avec une concentration en sonde de 2μM, ont révélé un maximum d'absorption à 783 nm et un maximum d'émission à 809 nm. Les spectres restent similaires avant et après greffage sur les nanoparticules qui ne présentent donc pas d'impact notoire sur les propriétés de fluorescence des marqueurs. La même conclusion a pu être faite en immobilisant de la coumarine.

Les tests de cytotoxicité n'ont pas montré de danger pour les cellules.

Pour le traitement tumoral, des collaborations sont actuellement en cours (Prof. Marco Sangermano de Politecnico di Torino en Italie et Prof. Kataoka de l'Université de Tokyo au Japon) afin d'incorporer des nanoparticules d'or pleines et creuses dans les nanoparticules de PVDF pour ajouter à ces vecteurs des propriétés photothermiques.

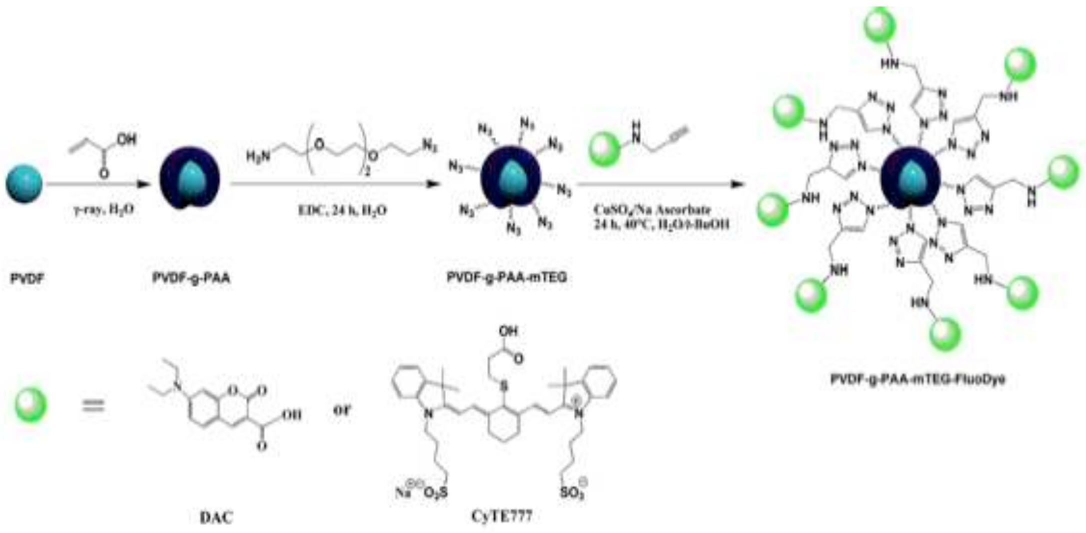

FIGURE 2.28 – *Schéma réactionnel des étapes de fonctionnalisation des nanoparticules de PVDF après irradiation aux gammas*

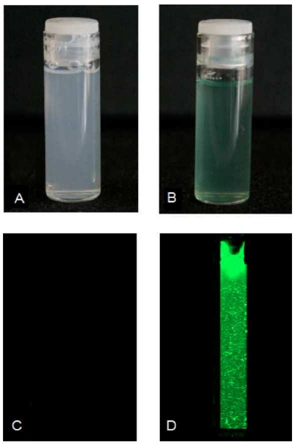

Figure 2.29 – *Images visibles (en haut) et de fluorescence (en bas) des nanoparticules de PVDF (à gauche) et de PVDF-g-PAA-mTEG-CyTE777 (àdroite). A/ PVDF NPs ; B/ PVDF-g-PAA-mTEG-CyTE777 NPs. C/ et D/ mesures correspondantes sur équipement Odyssey à 800 nm*

2.2.2.2. Membranes 'single' nanopore pour suivre le repliement des protéines

Un autre volet du domaine de la Santé a été entrepris durant la thèse de Christophe Tasserit que j'ai co-encadrée avec Didier Lairez, chercheur CEA au Laboratoire Léon Brillouin (2008-2011). Ce sujet traitait de la translocation de protéines à travers un nanopore synthétique unique. Le nanopore a été synthétisé par la technique d'attaque de trace après une irradiation ion unique sur films polymères minces de polycarbonate et polyimide. Cette expérience a pu se faire grâce à la collaboration avec le Dr. Emmanuel Balanzat du CIMAP au GANIL.
Ce sujet difficile a mené à une étude du bruit dans un nanocanal unique. Suivant les électrolytes, le passage non pas de molécules mais d'ions est déjà problématique suivant les charges en présence sur les parois. Un très beau papier a été publié à PRL fin 2010 [22] - *voir annexe* -. Cette publication rend compte de l'observation non-décrite d'effets coopératifs sur la mobilité des ions dans un milieu confiné créé par un nanopore cylindrique unique dans une membrane fine de fluoropolymère. **L'effet accélérateur ou deccélérateur de la mobilité des ions confinés dans le pore aux parois chargées semble dépendre uniquement de la nature chimique des ions et leur concentration.**

2.3 Nanotechnologies et perspectives

Depuis l'automne 2010, avec d'autres chercheurs du Laboratoire des Solides irradiés nous avons regroupé nos compétences sous le groupe XPnano (Physique et physico-chimie des nano-objets) dirigé par le professeur Henri-Jean Drouhin, chercheur DGA et polytechnicien très engagé dans l'enseignement à Polytechnique. Depuis, mes activités de recherche s'enrichissent de mesures physiques et trouvent de nouveaux intérêts dans les nanotechnologies.

2.3.1 Template synthesis

Les membranes polymères à traces attaquées multiples ou trace unique intéressent les physiciens travaillant sur le transport électronique dans des nanostructures. En effet, l'électrodéposition d'ions métalliques dans les nanopores permet de créer des nanofils (Fig.2.30). Cette technique est connue sous le nom de "template synthesis".
Le moulage de nano-fils métalliques [23] [24] [25] et non-métalliques [26] [27] prend actuellement une place significative dans mes activités de Recherche.

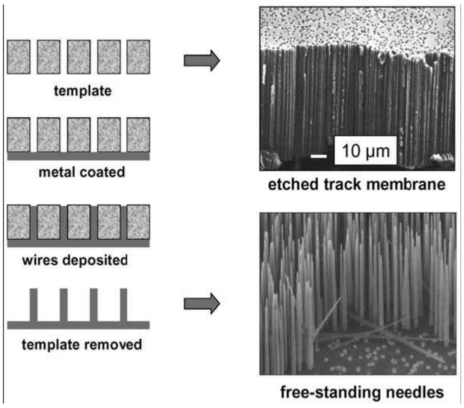

FIGURE 2.30 – *Etapes de préparation des nanofils métalliques par électrodéposition dans des membranes polymères à traces attaquées, méthode dite de "Template Synthesis"*

2.3.2 Couplage de l'effet piezoélectrique avec des nanofils magnétostrictifs : vers des capteurs de pression

Dans le cadre du projet PIEZOMAG financé par le DGA et le RTRA (2009-2012), l'étude a porté sur l'interactivité d'une membrane polymère piezoélectrique à traces attaquées et électrodéposée par du Nickel en collaboration avec le Professeur Jean-Eric Wegrowe (collègue LSI, Professeur de Mécanique Quantique à l'Ecole Polytechnique).
Ce projet est une étude de faisabilité pour la conception de nanocapteurs de pression reposant sur la fabrication de nanostructures magnétiques par voie électrochimique dans un nanomoule en polymères irradiés (« ion track technology »). L'idée de base consiste à exploiter les propriétés magnétoélastiques de nanofils ferromagnétique (Ni, CoTb), afin de mesurer à l'échelle nanométrique la réponse de l'aimantation à une contrainte mécanique. L'état de l'aimantation des nanofils est mesuré par le biais de la magnétorésistance.

2.3.2.1 Electrodeposition et contact d'un nanofil métallique unique

Le contact d'un nanofil unique de Nickel se fait pendant l'étape d'électrodéposition. Une épaisse couche d'or recouvrant les pores sur une face de la membrane polymère sert d'électrode de travail où les ions vont se réduire et former le nanofil ; une autre couche d'or mais beaucoup plus fine n'obstruant pas les pores, est également déposée par métallisation (évaporateur cathodique) sur l'autre côté. La membrane de PVDF nanoporeuse ainsi dorée est contactée à ses surfaces et immergée dans un bain électrolytique contenant des sels de Nickel. Une différence de potentiel de -1V est ensuite appliquée entre la couche épaisse d'or et le bain réduisant les sels de Nickel dans les traces. Les nanofils ne croissent pas à la même

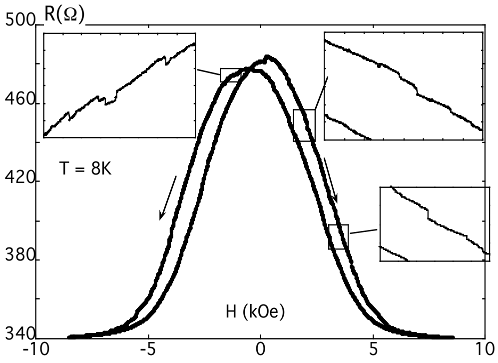

FIGURE 2.31 – *GMR effect in a single Cu/Co multilayer wire tiré de [28] mesuré à un angle de 90° entre le champ magnétique et l'axe du nanofil*

vitesse et quand le premier nanofil arrive sur la deuxième surface dorée, il se contacte et l'électrodéposition est stoppée.

2.3.2.2 **Mesure AMR**

Le Nickel étant magnétique, ses domaines magnétiques se trouvent contraints dans une structure nanoscopique tel que le nanofil. Si on mesure la résistance de ce nanofil de Ni sous champ magnétique formant un angle perpendiculaire à l'axe du nanofil, on obtient une courbe en cloche, signature de son anisotropie magnétique ou AMR (Anisotropic Magneto-Resistance) [28]. Ce signal représente en général 1% de la résistance totale. Il peut être exarcerbé dans le cas de nanofils en multicouche, on parle de Giant Magneto Resistance (GMR) (Fig. 2.31).
Ces études fondamentales sur les effets de magnétorésistance après contact d'un nanofil unique magnétique ont trouvé des applications concrêtes puisque cette technologie se retrouve dans les têtes de lecture de CDs et les mémoires RAM des ordinateurs (Prix Nobel A. Fert 2007).

Notre approche consiste à appliquer une tension mécanique sur ce nanofil par le biais de la déformation plastique de la membrane nanoporeuse en β-PVDF piezoélectrique et de mesurer son effet sur le signal d'AMR. Pour que la déformation plastique du PVDF puisse atteindre le nanofil, il a fallu dessiner des masques pour la lithogravure (Fig. 2.32). Cette lithogravure sur matériau souple a été difficile à mettre en oeuvre et a nécessité l'adaptation des procédures en salle blanche grâce à une collaboration avec le SPEC, service du CEA situé à l'Orme-des-merisiers près de l'Ecole Polytechnique. La membrane nanoporeuse

est donc recouverte d'une épaisse couche d'or (500 nm) ; une couche de résine positive est ensuite appliquée et chauffée pour réaliser sa réticulation, puis le masque est aligné sur la membrane et insolé par des UVs. La résine qui se trouve sous le motif chromé du masque en verre reste réticulée alors que celle qui a été insolée est dégradée. Une première révélation permet donc d'enlever la résine insolée. Une deuxième révélation au KI permet ensuite de graver l'or qui se trouve à nu dans les parties où la résine a été éliminée. Le résultat de cette gravure d'or sur membrane mince de PVDF nanoporeuse est montrée sur la Fig. 2.33. L'image FESEM d'une tranche de la membrane de PVDF nanoporeuse dorée et gravée par lithogravure permet de mieux se rendre compte des étapes successives (Fig. 2.34).
L'électrodéposition a lieu au niveau des 50 lignes fines de 20 μm de largeur et de 600 μm de long. Ces lignes fines sont intercalées par des lignes plus larges que l'on nomme "capacités" par extension de langage et par le biais desquelles une tension est appliquée.

2.3.2.3 **Effet magnétostrictif sur un nanofil de Nickel unique cylindrique**

L'effet de la contrainte mécanique exercée par la membrane sur un nanofil unique de Ni a été finalement mis en évidence tout récemment en juillet 2012. Cet effet est de l'ordre de 12% pour une tension de 30V appliquée sur la membrane (Fig.2.35). Cette amplitude est comparable à l'effet obtenu sur un ensemble macroscopique de nanofils dans la membrane PVDF par le groupe de Louvain, effectué à 200V [29] .

Les courbes présentées sur la Fig.2.35 sont les résultats de moyennes prises sur cinq cycles d'hystérésis (5 allers-retours de la rampe de champ magnétique de -1.6 T à 1.6 T et retour à -1.6T). Ces résultats vont nous permettre de quantifier précisément les effets de la contrainte magnétostrictive (en direction et intensité). Cependant, l'étude en fonction de l'angle a été limitée par l'amplitude du bruit, toujours très élevé du fait de la tension appliquée à la membrane (Fig.2.36). Il s'agit d'un effet électrostatique de charge partielle de la membrane et de courant de fuite. Ce problème, qui n'est pas systématique pour les tensions faibles (20 à 30 V), n'a pas été résolu pour les tensions supérieures. Il semble que cela soit lié au fait que le PVDF piézoélectrique soit un mauvais isolant électrique dans la gamme de sensibilité des mesures effectuées dans ce projet. Une autre matrice polymère électrostimulable peut être envisagée (voir section 2.3.2.1).
De plus, un effet de mémoire est observé après application de la tension sur la membrane. Cet effet est probablement dû à un effet de charge électrique, en liaison avec le bruit électrostatique. Ces deux problèmes restent aujourd'hui les points faibles les plus délicats à régler pour l'étude quantitative des résultats des mesures de l'effet piézoélectrique.

Deux scénarios sont testés pour l'interprétation des données. En effet, au delà de l'effet

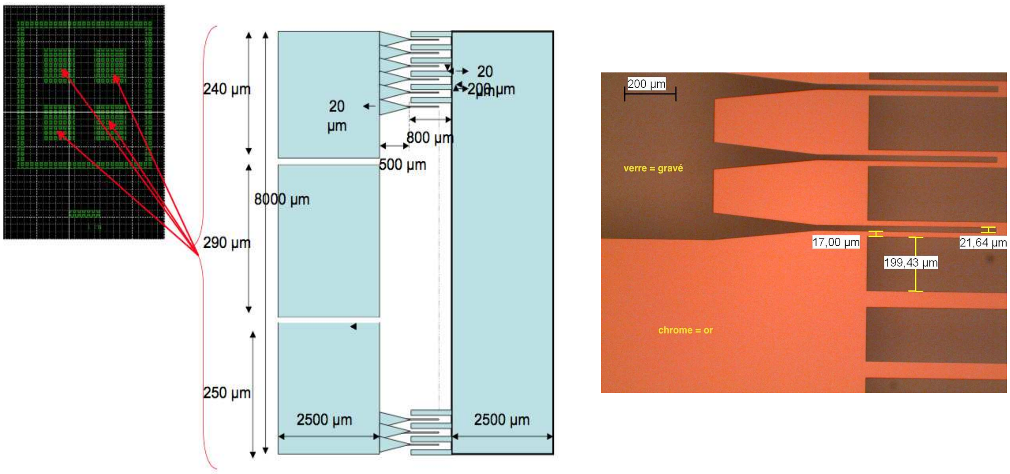

FIGURE 2.32 – *Masque « interdigité ». (a) le schéma du masque, (b) photo prise avec le microscopie optique. Le masque est en verre et le motif est la partie chromée sur cette plaque de verre. La partie supérieure montre trois lignes avec l'électrode de contact à gauche et les capacités entre les lignes à droite.*

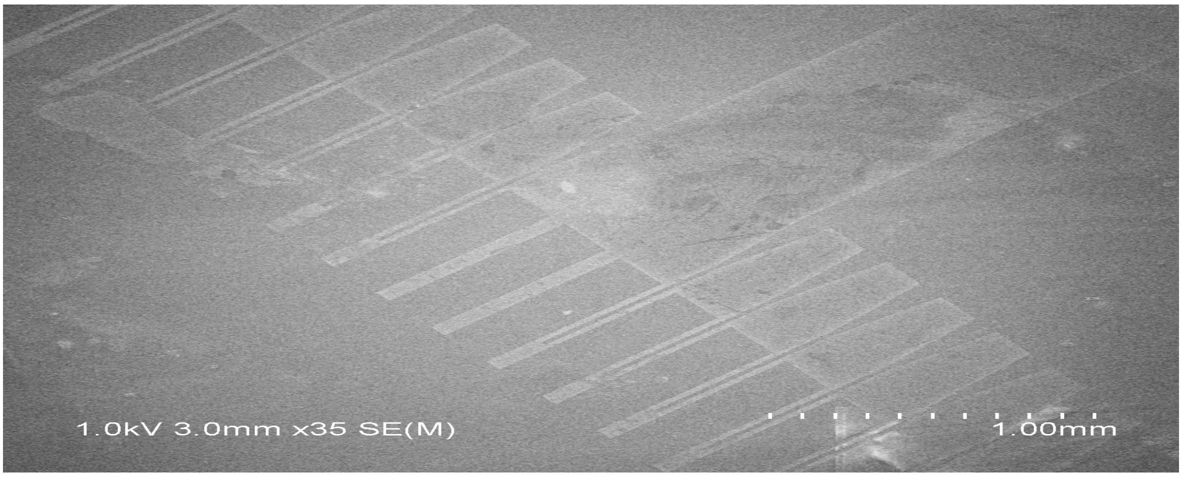

Figure 2.33 – *Impression du Masque « interdigité » sur la membrane nanoporeuse de β-PVDF.*

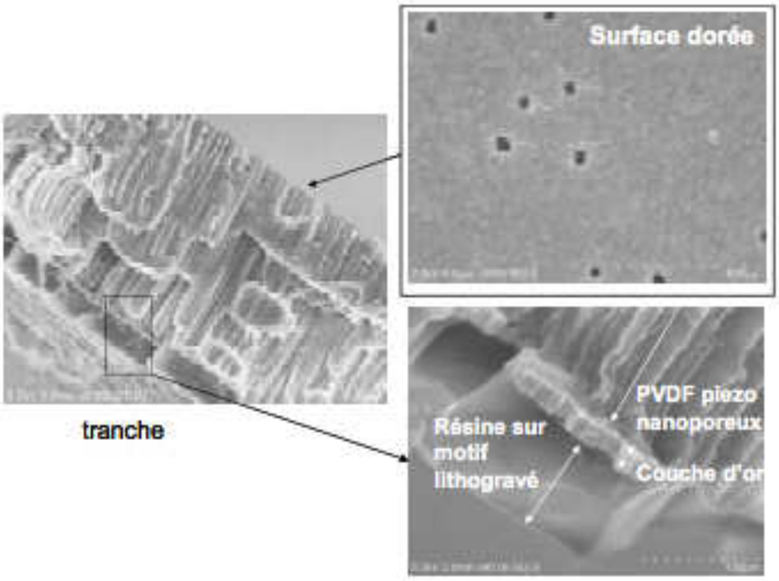

FIGURE 2.34 – *Images FESEM de la tranche cryofracturée d'une membrane en β-PVDF piezoélectrique de 10µm d'épaisseur (diamètre des pores 80nm) métallisé à l'or (en encadré : image FESEM de la surface montrant que la couche d'or est suffisamment fine pour ne pas obstruer les nanopores) et gravé à ses surfaces par lithographie*

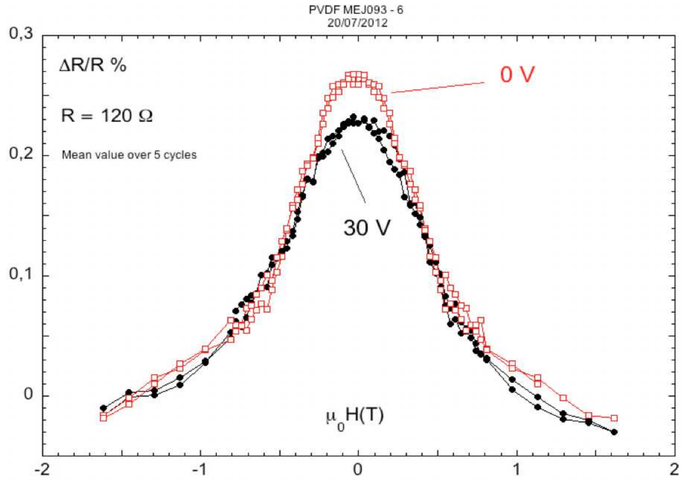

Figure 2.35 – *Courbes de magnétorésistance d'anisotropie en fonction du champ magnétique. Les courbes de résistance décrivent la rotation de l'aimantation en fonction du champ magnétique appliqué avec (point noirs) et sans (carrés rouges) la contrainte mécanique.*

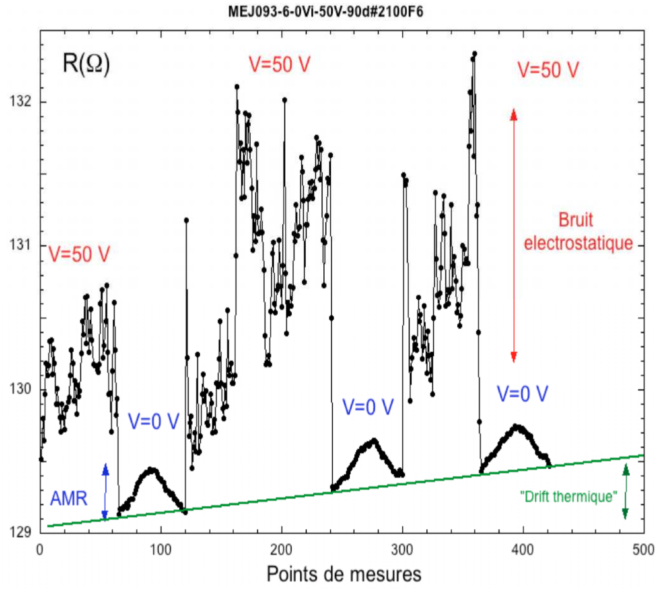

FIGURE 2.36 – *Succession de demi-rampes en champ magnétique (de -1.2 T à 1.2T) au cours du temps. Le signal de magnétorésistance à 0 V (demi-cycles de référence) est bien visible. L'effet du bruit électrostatique géant est immédiat lorsque 50V sont appliqués sur la membrane. La droite en bas est un décalage thermique.*

purement magnétoélastique attendu en réponse à la sollicitation mécanique de la membrane, l'hypothèse d'un effet de modification élastique du contact électrique n'est pas rejeté. Ces deux hypothèses peuvent être distinguées par l'application sur les données du modèle de Stoner-Wohlfarth avec un terme supplémentaire de magnétostriction [30] [31] [32] [33] [34].

L'effet de l'application d'une tension sur le polymère piézoélectrique est donc bien visible sur le profil de la courbe représentée en Fig.2.35. Cependant, cet effet n'est pas celui attendu à priori pour un effet magnétostrictif (inverse) en réponse à la contrainte piézoélectrique. En effet, la largeur du cycle (i.e. l'anisotropie) est peu modifiée, et l'amplitude change significativement. La différence avec les effets thermo-mécaniques montrés sur la Fig.2.37 est très nette. Dans le dernier cas, c'est bien l'anisotropie (ou la coercivité de façon plus générale) qui est modifiée.

Dans le modèle le plus simple (du type Stoner-Wohlfarth), si on ajoute l'effet d'une contrainte magnétoélastique sur le nanofil dans une direction, cela provoque un décalage du profil de la même façon que lorsqu'un champ magnétique local est ajouté au champ appliqué. La Fig.2.38 montre l'effet d'une contrainte appliquée en 0z. Par conséquent, l'effet observé est inattendu et semble très spécifique. Ce profil ne ressemble pas aux effets thermo-mécaniques mesurés systématiquement sur ces objets. Cela nous incite à développer une autre interprétation reposant sur un effet élastique de la contrainte mécanique sur le nanocontact, ce qui est susceptible de modifier les propriétés de magnétorésistance.

2.3.2.4 **Effet magnétostrictif sur un nanofil de Nickel unique biconique**

Dans le cadre de l'étude de nanostructuration menée au laboratoire depuis 2003, des chercheurs LSI ont mis au point un procédé pour réduire au maximum le diamètre des nanofils cylindriques jusqu'à 5 nm dans des alumines nanoporeuses [34].

Afin d'éviter les problèmes qu'ils avaient rencontrés, liés aux résistances très grandes dans ce type de configuration, la solution est de réaliser des nanofils biconiques par un choix judicieux de polymère - *voir article JAP 2011 en annexe* -. La partie la plus étroite de la structure étant celle dont la résistance est la plus grande, il est ainsi possible de travailler sur une constriction de quelques nm de long et d'un à deux ordres de grandeur plus étroite (de 5 à 0.5 nm) que les structures étudiées jusque là dans le cadre de ce projet.
Si en premier lieu, nous avons étudié des nanofils dans une matrice polymère à base de Polyéthylènetéréphtalate (PET) [25], le copolymère poly(VDF-co-TrFE) s'est révélé être un meilleur candidat pour la fabrication de bicônes. Non seulement, il est électrostimulable comme le PVDF ; mais aussi, il possède un ratio d'environ 10 entre la vitesse d'attaque longitudinale (V_t) des zones d'endommagement (ou traces laissées par le bombardement des

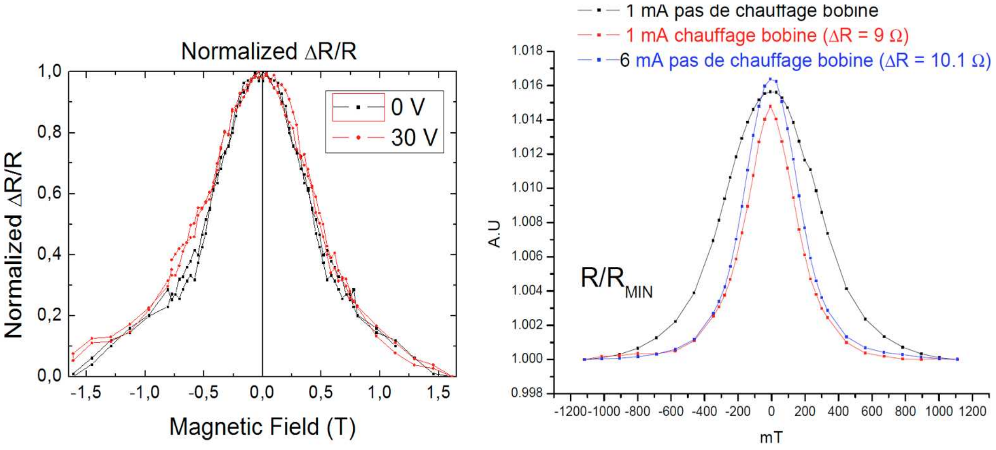

FIGURE 2.37 – *Gauche) Profils de magnétorésistance d'anisotropie de la Figure 1 normalisés en H=0 avec (point noirs) et sans (carrés rouges) la contrainte mécanique. Droite) pour comparaison, les effets des contraintes thermo-mécaniques (non-normalisés) en chauffant la membrane entière (avec une bobine résistive) et en chauffant le nanofil seul par effet joule en injectant un fort courant (6mA).*

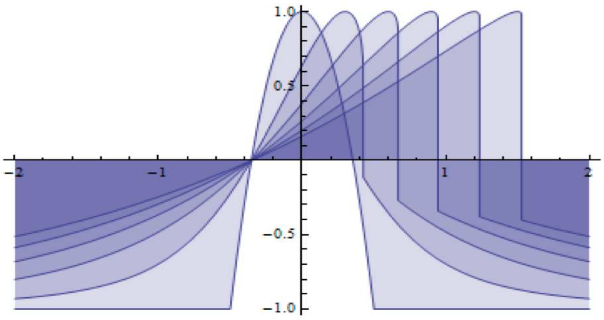

Figure 2.38 – *Magnétorésistance calculée en fonction du champ magnétique extérieur. Modélisation des états quasi-statiques (modèle de Stoner-Wohlfarth) avec un terme de magnétostriction le long de la direction Oz. La discontinuité à droite est due au saut irréversible d'une branche du cycle à l'autre. Une contrainte isotrope produit un élargissement du cycle (anisotropie plus grande), comparable aux effets thermo-mécaniques présentés Fig. 2.37*

ions) et la vitesse d'attaque radiale (V_b) dans la matrice polymère favorisant la création de pores biconiques (Fig. 2.39). En hydrolysant simultanément les deux côtés de la membrane, on peut réaliser des bicônes de taille et symétrie contrôlées (Fig. 2.40).

La caractérisation de la constriction se fait par MEB à effet de champ en extrapolant deux valeurs de diamètre prise sur la cryofracture de la membrane polymère ou sur les répliques métalliques des traces selon la formule suivante :

$$\beta = 2.arctan(\frac{x_1 - x_2}{2d}) \tag{2.9}$$

Cette formule a été établie lors d'un précédent travail de l'équipe sur les attaques asymétriques avec la mise en place d'une cellule à deux compartiments séparés par le film polymère irradié [23].
L'intérêt d'une telle cellule est de suivre l'attaque jusqu'à l'ouverture du pore par conductimétrie [22] et/ou pH métrie [23]. Lors d'une attaque asymétrique, une solution acide neutralise la solution d'attaque à base de soude ou de potasse afin de stopper la réaction d'attaque dès l'ouverture du pore. La Fig.2.41 montre l'influence de l'énergie d'irradiation sur la vitesse d'attaque V_b et la monodispersité obtenue sur le diamètre des pores ouverts en face dite de sortie. Ce protocole de suivi est adaptable aux constrictions biconiques.

Dans l'étude, nous focalisons sur les plus petites constrictions possibles. Le traitement

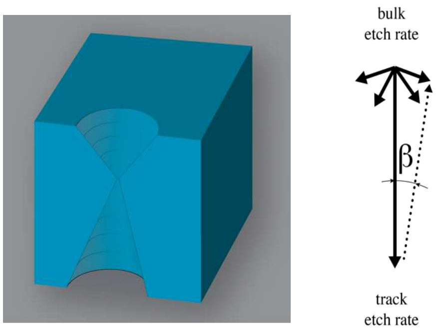

FIGURE 2.39 – *Attaque de traces considérant un régime constant pour* v_t *et* v_b *et* $sin\beta = v_b/v_t$

UV permet de sensibiliser encore plus les traces latentes et donc, d'augmenter V_t. La conicité peut être modifiée afin d'obtenir un panel de géométries biconiques aux constrictions variables. Un exemple de faible conicité est présenté sur la Fig.2.42 à comparer avec la Fig.2.40.

L'étude des mesures physiques sur de tels objets a permis de comprendre dans les grandes lignes les effets d'une contrainte mécanique qui s'applique sur une nanoconstriction. Par ce biais, un capteur de pression nanoscopique a été réalisé sans passer par les mesures de magnétorésistance (mais de la résistance seule).

La Fig.2.43 montre deux profils de résistance en fonction de l'amplitude d'un champ magnétique orienté perpendiculairement à l'axe du bicone. La Fig.2.43 (gauche) correspond à une constriction moyenne large (de l'ordre de 10 nm) avec beaucoup de nanofils en parallèle et la Fig.2.43 (droite) correspond à une constriction très étroite (de l'ordre de 1 nm). La Fig.2.44 montre un exemple des profils typiques obtenus pour la constriction la plus étroite à angle fixe du champ appliqué. Le profil AMR de la Fig.2.43 (gauche) est assez standard pour une large constriction et s'explique par le déplacement d'une paroi de domaine magnétique de part et d'autre de la constriction. Une étude extensive de ce type d'échantillons a été réalisée, avec une publication dans J. App. Phys. (avec les simulations numériques pour la description des états magnétiques au voisinage de la constriction) - *voir article en annexe* -. Au contraire, les profils de la Fig.2.43 (droite) et de la Fig.2.44 ne peuvent pas être interprétés par un effet de l'AMR, quelles que soient les configurations magnétiques considérées. En effet, la résistance des états d'aimantation à saturation le long du fil ou perpendiculaire au fil est incompatible avec celle mesurée en AMR.

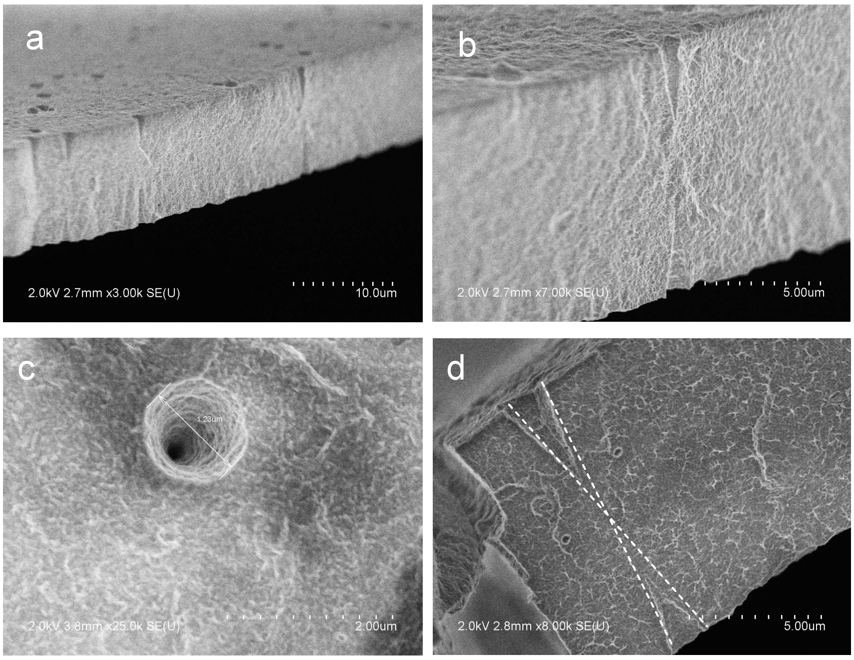

FIGURE 2.40 – *Images FESEM images des traces biconiques obtenues après attaque chimique d'un film de poly(VDF- co -TrFE) préalablement irradié avec des ions* $^{78}Kr^{31+}$ *(accélérés à 10MeV/uma) avec une fluence de* 10^6 *traces.cm*$^{-2}$ *Conditions d'attaque : KOH 10N /* $KMnO_4$ *0.25N 80°C, 1h. a) Vue globale de la tranche cryo-fracturée d'une membrane attaquée de poly(VDF- co -TrFE) membrane ; b)zoom de la tranche focalisé sur une trace biconique ; c) surface ; d) extrapolation pour determiner la taille de la nanoconstriction invisible à cause de la limite de résolution et de la cassure aléatoire*

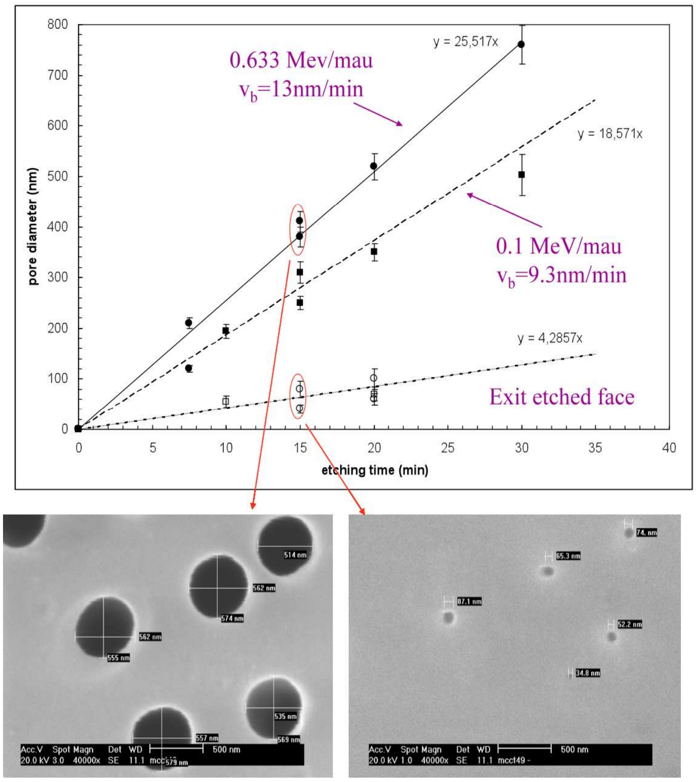

Entry face Exit face

FIGURE 2.41 – *Traces biconiques de faible conicité obtenues dans une membrane en polycarbonate irradiée aux ions* $^{78}Kr^{31+}$ *0.633MeV.mau fluence* 10^8 *ions.cm*$^{-2}$ *et attaquée asymétriquement (face d'entrée et de sortie différente) suit une loi linéaire en fonction du temps d'attaque montrant un contrôle facile de ce type de structure et une monodispersité des diamètres. On note ici l'influence de l'énergie cinétique des ions-projectiles sur la vitesse d'attaque radiale* V_b.

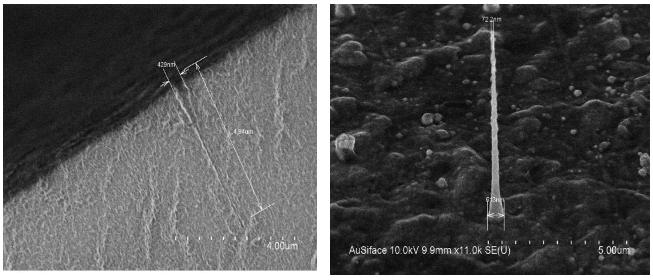

FIGURE 2.42 – *Autre exemple d'une membrane à traces biconiques en poly(VDF- co -TrFE) (gauche) et sa réplique métallique (droite) obtenue par "template synthesis" présentant une conicité faible.*

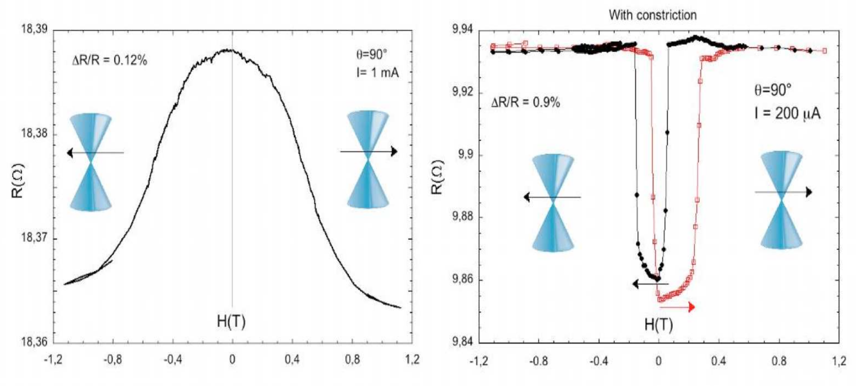

FIGURE 2.43 – *mesure de résistance en fonction du champ magnétique. Gauche : constriction large ; Droite : constriction étroite.*

En comparant ces résultats avec une étude précédente sur des nanoconstrictions granulaires [35], il est possible d'établir l'interprétation suivante. Dans une constriction de section de l'ordre de 1 nm et inférieure, la résistance est définie par le nombre de canaux de conduction en parallèle. Notons au passage que si les canaux étaient balistiques (et ce serait certainement le cas à basse température, ainsi que cela a été vérifié en [35]), la résistance de chaque canal serait d'un quantum de résistance (soit 13 kΩ). En régime diffusif, la résistance est proportionnelle à l'inverse de la section, ce qui conduit à des résistances très importantes (de l'ordre de 10 kΩ). Le fait de mesurer un ensemble de bicônes contactés en parallèles (avec une distribution large sur les sections de constrictions) conduit à une faible résistance, de l'ordre de 10 Ω. **Le scénario envisagé est que la magnétostriction des nanofils de Ni conduit à une variation du volume, qui en retour ouvre ou ferme la constriction.** On passe ainsi d'une bonne conduction à une mauvaise conduction en fonction de l'amplitude et de l'angle du champ magnétique. Ce scénario va être maintenant testé sur des bicônes non-ferromagnétiques (Cu, Au, Ag) déposés dans les membranes copolymères poly(VDF- *co* -TrFE) piezoélectriques.

Nous espérons ainsi reproduire le même type de signaux en appliquant une tension sur la membrane piézoélectrique comme nous savons le faire à présent à partir du motif lithogravé utilisant le masque interdigité (Fig. 2.33).

2.3.3 Perspectives du projet à 4 ans et plus

A l'issue de trois années d'une étude intensive pour arriver à la réalisation des objectifs du projet PIEZOMAG, nous concluons sur la difficulté qu'il y a à mesurer directement les effets magnétostrictifs à l'échelle nanométrique, et à fortiori à la réalisation pratique du nanocapteur. L'objectif initial du projet a été finalement atteint, mais dans des conditions beaucoup moins favorables qu'initialement prévues. Au-delà des difficultés techniques liées à la nanofabrication, les raisons de ce succès en demi-teinte proviennent en grande partie d'une surestimation des effets des contraintes mécaniques sur les nanofils (magnetoélasticité « inverse »).

L'espoir de mesurer un signal magnétique géant en réponse à une sollicitation mécanique à l'échelle d'un nanofil était à l'origine de ce projet. Cet espoir reposait sur une étude des effets des contraintes thermo-mécaniques (dilation et constriction de la membrane) sur l'aimantation. **Cette étude a révélé que l'échelle à laquelle les effets sont significatifs est plus proche de l'échelle nanométrique et sub-nanométrique que l'échelle de la dizaine de nanomètre.** Cette conclusion s'impose après avoir mesuré un grand nombre de nanofils de morphologies différentes, et en particulier des nanoconstrictions obtenues dans des matrices de copolymères poly(VDF- *co* -TrFE) nanoporeuses. La différence

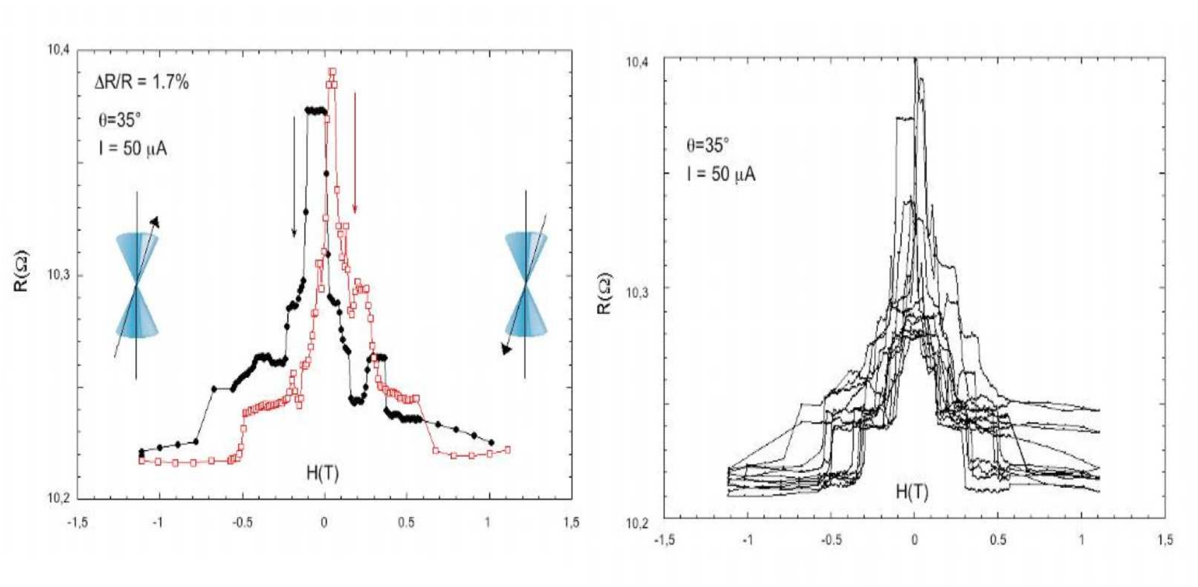

FIGURE 2.44 – *Profil de résistance en fonction de l'amplitude du champ magnétique H pour un angle de 15° par rapport à l'axe du bicône. La figure de droite montre la reproductibilité sur 6 cycles d'hystéris.*

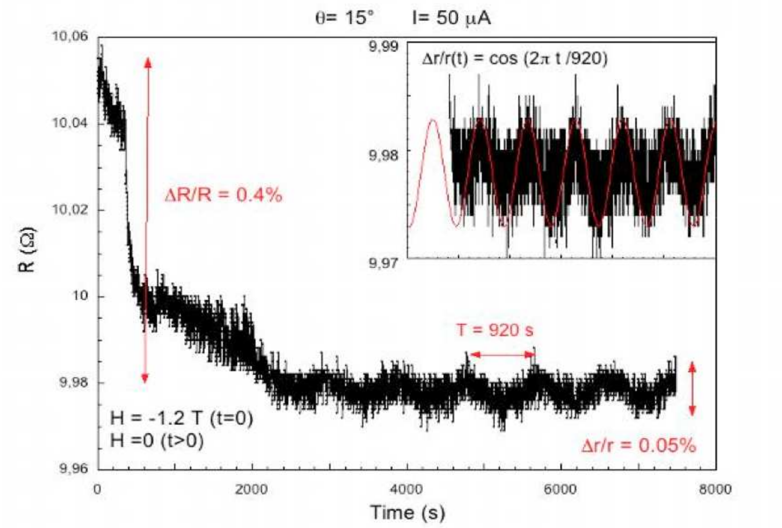

FIGURE 2.45 – *Dépendance du temps sur les états magnétiques (après-effet magnétique) à $\theta = 15°$. Au temps t=0, le champ magnétique passe de H=-1.2 T à H=0. Différents mécanismes de relaxation prennent place. Encadré : zoom sur les oscillations avec un ajustement cosinus.*

considérable de l'amplitude des signaux observés entre un effet thermo-mécanique et effet électro-mécanique (e.g. piézoélectrique) n'est pas encore élucidée. L'analyse et la modélisation des résultats acquis pendant la durée du projet est en cours (ex. Fig.2.45 issue d'un article soumis à J. Appl. Phys. en déc. 2012 où l'on observe que les phénomènes de sauts de résistance sous impulsion magnétique s'accompagnent de relaxations).

Cependant, nous pouvons d'ores et déjà conclure que l'avenir des capteurs de pression à l'échelle nanométrique repose sur la maîtrise de la fabrication de nano-objets inférieurs à 10 nm. Nous avons donc orienté la fin de cette étude et le développement à venir du projet nanocapteur sur l'élaboration de nanoconstrictions ou de nanofils multiparois comportant une paroi extrêmement fine ($<$ 10nm) constituée en matériau magnétostrictif.

Cette dernière option est tout à fait novatrice et fait l'objet des efforts de nanofabrication pour les 4 ans à venir.

Partant de l'expérience acquise au LSI en bombardement d'ions rapides de films minces

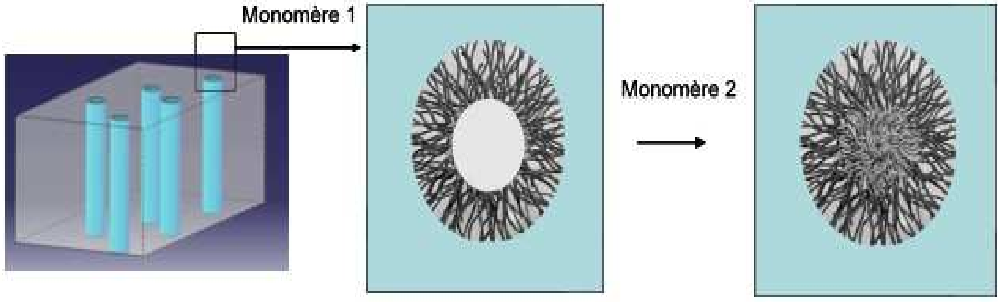

FIGURE 2.46 – *Schéma représentant un agrandissement de l'intérieur d'un nanopore cylindrique dans une membrane à traces attaquées radiogreffé par polymérisation radicalaire de type RAFT avec un monomère 1, puis copolymérisé avec un monomère 2 sur les greffons par la même technique de polymérisation radicalaire contrôlée*

de polymères et du résultat remarquable concernant la rémanence de radicaux sur la paroi des nanopores révélés après ce bombardement ionique, **le projet ouvre une perspective nouvelle sur la création de nanofils métalliques multi-parois dont la composition et les tailles seraient assistées suivant la fonctionnalité et l'organisation des polymères et/ou copolymères radiogreffés dans le nanopore.** Ce projet s'appuie sur un type de polymérisation radicalaire contrôlée en plein essor : le procédé RAFT (Reverse Addition-Fragmentation Transfer).

Après révélation des traces latentes laissées par les ions lourds rapides, le radiogreffage par polymérisation radicalaire est initié par les radicaux résiduels présents sur les parois. En dorant une face du film polymère attaqué, il est possible de faire croître par électrodéposition des nanofils métalliques avec un fort rapport d'aspect (diamètre nanométrique sur une longueur micrométrique), cette technique est connue sous le terme de "template synthesis" (voir section 2.3.1).
Cependant, le " template synthesis " seul ne permet pas de faire des nanofils multi-parois métalliques qui ouvriraient davantage le champ d'investigation dans ce domaine. Grâce à la polymérisation radicalaire vivante utilisant le mécanisme RAFT en milieu confiné, il est possible de contrôler la longueur des chaînes de polymère en croissance et donc d'arrêter la polymérisation à une distance déterminée de la paroi des nanopores dans les membranes à traces attaquées (Fig. 2.46 avec monomère 1).

Une étude menée en collaboration avec l'Université d'Ankara a montré qu'il était possible de maîtriser la longueur des chaînes de PAA en croissance dans les nanopores par polymérisation radicalaire contrôlée de type RAFT (Fig. 2.47) - *article soumis en décembre 2012 à Journal of Membrane Science [36]* -.

Si le polymère radiogreffé est un polyélectrolyte classique de type polyacide acrylique, la simple adsorption d'ions métalliques par effet électrostatique va permettre de concentrer ces ions dans la couche polymère comme nous l'avons vu dans l'application du capteur ECOSISTEM (section 2.1.3).
La réduction de ces ions est ensuite possible par deux méthodes : soit l'addition d'un agent réducteur dans le milieu, soit une irradiation aux électrons (cf ref [37]) . La création d'un nanotube métallique devient alors envisageable. Ce nano-objet sera déjà un succès si j'arrive à l'obtenir par cette technique. L'épaisseur de la paroi devrait être dépendante de la longueur des chaînes du polyélectrolyte radiogreffé dans les traces. Le contact de ces nanotubes de Ni ou de TbCo aux parois très fines ($<$ 10 nm) permettront les mesures AMR.

Un autre atout de la polymérisation radicalaire de type RAFT est que cette polymérisation est dite « vivante », c'est-à-dire que les fins de chaînes du polymère en croissance sont toujours actives, il est donc possible de faire des copolymères à blocs avec l'addition d'un 2ème monomère (Fig. 2.46 avec monomère 2).
Des ions différents peuvent ainsi être piégés suivant leur affinité avec les blocs de polymères aux différentes fonctionnalités dans le nanopore. Après réduction des ions métalliques, des nanotubes multi-parois de métaux différents pourraient être créés selon le schéma 2.48.
On peut ensuite finir le remplissage du lumen résiduel par électrodéposition (Fig. 2.49). Il serait intéressant ainsi de fabriquer des couches successives de Cu/Co pour être dans la configuration perpendiculaire des nanofils étudiés pour la GMR.

Une fois de tels nano-objets créés dans une matrice polymère électrostimulable et contactés, les mesures physiques d'AMR pourront être comparées aux bicônes. L'amplitude des effets devrait encore être améliorée. La compréhension des phénomènes ne sera pas pour autant complète et ce projet s'ouvre sur une recherche à très long terme.

Que ce soit des structures biconiques ou des nanofils multicouches déjà en cours d'étude, la reproductibilité de ces nano-objets reste le souci majeur quand on étudie l'objet unique. En effet, à ces échelles, l'erreur est souvent de l'ordre de grandeur de l'objet à étudier. L'emploi d'une matrice bien calibrée avec des nanopores monodisperses, une fonctionnalisation contrôlée avec des longueurs de chaînes de polymères bien définies devrait minimiser les écarts d'une nanostructure à une autre. C'est en tous cas ma motivation dans ce projet. Je suis consciente de la difficulté d'aboutir mais la maîtrise de cette technicité est stimulante et sera à n'importe quel degré une avancée.

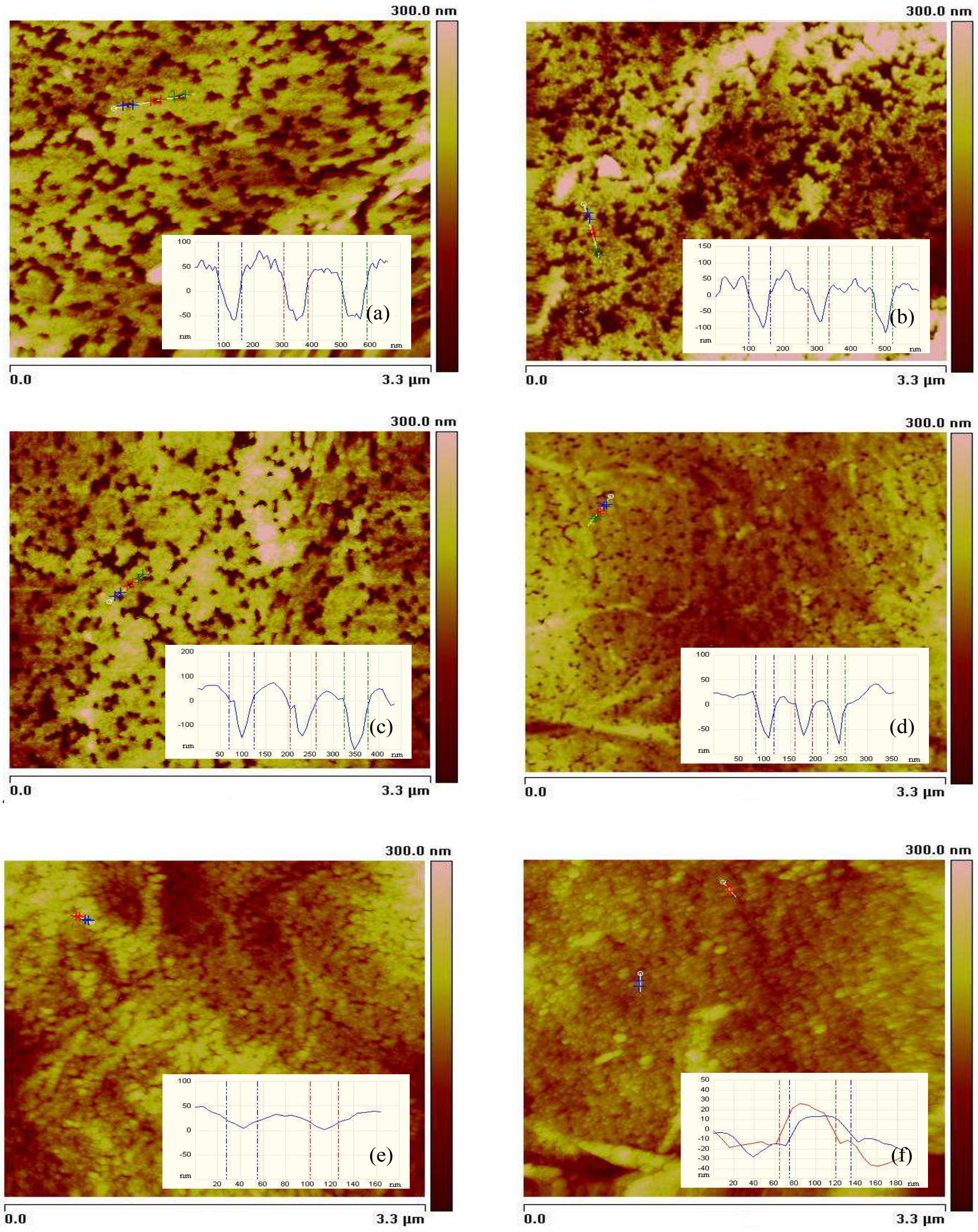

Figure 2.47 – *Images et profils AFM de membranes à traces attaquées de PVDF-g-PAA radiogreffées par polymérisation radicalaire contrôlée de type RAFT à différent taux de greffages. a) PVDF nanoporeux; b) PVDF-g-PAA à 8wt%; c) PVDF-g-PAA à 14wt%; d) PVDF-g-PAA à 31wt%; e) PVDF-g-PAA à 43wt%; f) PVDF-g-PAA à 63wt%*

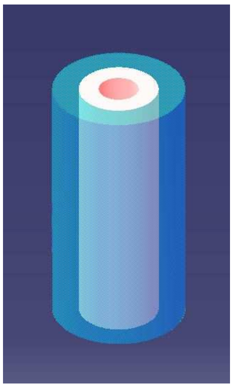

FIGURE 2.48 – *Schéma d'un nanotube multi-parois*

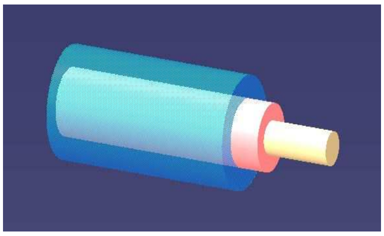

FIGURE 2.49 – *Schéma d'un nanofil multi-parois*

Bibliographie

[1] Dubois-Clochard, M. C. ; Durand, J. P. ; Delfort, B. ; Gateau, P. ; Barre, L. ; Blanchard, I. ; Chevalier, Y. ; Gallo, R. Langmuir 2001, 17, 5901-5910.

[2] Chevalier, Y. ; Dubois-Clochard, M. C. ; Durand, J. P. ; Delfort, B. ; Gateau, P. ; Barre, L. ; Frot, D. ; Briolant, Y. ; Blanchard, I. ; Gallo, R. In Trends In Colloid And Interface Science Xv, 2001 ; Vol. 118, pp 110-114.

[3] a) H.P. Boehm, E. Diehl, W. Heck, Rev. Gen. Caout. 1964, 41, 461 ; b) H.P. Boehm, E. Diehl, W. Heck,R. Sappock. Angew. Chem. 1964 3, 669 ; c)a) H.P. Boehm, E. Diehl, W. Heck, Proc. Carbon Conf. 1966, 369

[4] a) S. Alexander, J. Phys. 1977, 38, 983 ; b) P-G. De Gennes, Macromolecules 1890, 13, 1069 ; c) P-G. De Gennes, Adv. Colloid Interface Sci. 1987, 27, 189.

[5] D.A. Weitz, J.S. Huang, M.Y. Lin, J. Sung, Phys. Rev. Lett. 1985, 54, 1416

[6] Clochard M.-C. "La pile à combustible, une solution vers des véhicules propres" FlashX, La revus scientifique de l'Ecole Polytechnique 2012, 14, 13-17

[7] Clochard, M. C. ; Berthelot, T. ; Baudin, C. ; Betz, N. ; Balanzat, E. ; Gebel, G. ; Morin, A. Journal Of Power Sources, 2010 195, 223-231.

[8] Gallino, E. ; Clochard, M.-C. ; Balanzat, E. ; Gebel, G. ; Morin, A. Proceedings of the 2011 MRS Fall Meeting 2012

[9] Clochard, M. C. ; Begue, J. ; Lafon, A. ; Caldemaison, D. ; Bittencourt, C. ; Pireaux, J. J. ; Betz, N. Polymer 2004, 45, 8683-8694.

[10] R. Spohr, K. Bethge, "Ion Tracks and microtechnology : principles and applications. Vieweg, 1990.

[11] Deshayes, S. ; Maurizot, V. ; Clochard, M.-C. ; Berthelot, T. ; Baudin, C. ; Deleris, G. Radiation Physics and Chemistry, 2010 79, 208-213.

[12] Deshayes, S. ; Maurizot, V. ; Clochard, M.-C. ; Baudin, C. ; Berthelot, T. ; Esnouf, S. ; Lairez, D. ; Moenner, M. ; Deleris, G. Pharmaceutical Research, 2011 28, 1631-1642.

[13] Bessbousse, H. ; Nandhakumar, I. ; Decker, M. ; Barsbay, M. ; Cuscito, O. ; Lairez, D. ; Clochard, M.-C. ; Wade, T. L. Analytical Methods, 2011 3, 1351-1359.

[14] Cuscito, O. ; Clochard, M. C. ; Esnouf, S. ; Betz, N. ; Lairez, D. Nuclear Instruments and Methods In Physics Research Section B-Beam Interactions With Materials And Atoms 2007, 265, 309-313.

[15] Clochard, M. C. ; Betz, N. ; Goncalves, M. ; Bittencourt, C. ; Pireaux, J. J. ; Gionnet, K. ; Deleris, G. ; Le Moel, A. Nuclear Instruments and Methods In Physics Research Section B-Beam Interactions With Materials And Atoms 2005, 236, 208-215.

[16] Betz, N. ; Clochard, M. C. ; Goncalves, M. ; Bittencourt, C. ; Pireaux, J. J. ; Gionnet, K. ; Deleris, G. ; Le Moel, A. Nuclear Instruments and Methods in Physics Research, Section B (Beam Interactions with Materials and Atoms) 2005, 236.

[17] Clochard, M. C. ; Cuscito, T. ; Berthelot, T. ; Betz, N. ; Bittencourt, C. ; Pireaux, J. J. ; Goncalves, M. ; Gionnet, K. ; Deleris, G. Reactive and Functional Polymers 2008, 68, 77-90.

[18] Clochard, M. C. D. ; Rankin, S. ; Brocchini, S. Macromolecular Rapid Communications 2000, 21, 853-859.

[19] Godwin, A. ; Bolina, K. ; Clochard, M. ; Dinand, E. ; Rankin, S. ; Simic, S. ; Brocchini, S. Journal Of Pharmacy And Pharmacology 2001, 53, 1175-1184.

[20] Zloh, M. ; Dinand, E. ; Brocchini, S. ; Clochard, M. Internet Journal Of Chemistry 2001, 4, art. no.-9.

[21] S. M. Bezrukov and M. Winterhalter, Phys. Rev. Lett. 85, 202 (2000)

[22] Tasserit, C. ; Koutsioubas, A. ; Lairez, D. ; Zalczer, G. ; Clochard, M. C. Physical Review Letters, 2010 105.

[23] Clochard, M. C. ; Wade, T. L. ; Wegrowe, J. E. ; Balanzat, E. Nuclear Instruments and Methods In Physics Research Section B-Beam Interactions With Materials And Atoms 2007, 265, 325-329.

[24] Biziere N. ; Clochard M.-C. ; Chung P.D. ; Viret M. ; Wegrowe J.-E. "Magnetoresistance measured on magnetic nanoconstrictions : the role of structural defects" J. of Appl. Phys. 2012 (submitted)

[25] Bizière, N ; Lassalle Ballier, R ; Clochard, M.C. ; Viret, M. ; Wegrowe, J.E. "Synthesis and magnetic reversal of bi-conical Ni nanostructures." Journal of Applied Physics 2011, 110, 6, 063906 DOI : 10.1063/1.3638072

[26] Berthelot, T. ; Baudin, C. ; Balanzat, E. ; Clochard, M. C. Nuclear Instruments and Methods In Physics Research Section B-Beam Interactions With Materials And Atoms 2007, 265, 320-324.

[27] Clochard, M. C. ; Baudin, C. ; Betz, N. ; Le Moel, A. ; Bittencourt, C. ; Houssiau, L. ; Pireaux, J. J. ; Caldemaison, D. Reactive and Functional Polymers 2006, 66, 1296-1305.

[28] J.-E. Wegrowe et al., Phys. Rev. Lett. 82, 3681 (1999)

[29] L. Piraux, G. Hamoir, M.-W. Lee, E. Ferain, A. M. Jonas, I. Huynen, and J. De La Torre Medina : «Template Approach for Novel Magnetic ?Ferroelectric Nanocomposites» Applied Physics Express 4 (2011) 115001

[30] N. Tiercelin, Y. Dusch, A. Klimov, S. Giordano, V. Preobrazhensky, and Philippe Pernod, « Room temperature magnetoelectric memory cell using stress-mediated magnetoelastic switching in nanostructured multilayer »Applied Physics Letters 99, 192507 (2011).

[31] S. Yoichi ; N. Takayuki ; B. Frederic ; et al. « Induction of coherent magnetization switching in a few atomic layers of FeCo using voltage pulses » NATURE MATERIALS 11, 39-43 (2012)

[32] Lei Na ; Park S. ; Lecoeur Ph., Ravolosona D., C. Chappert, O. Stelmakhovych, and V. Holy. « Magnetization reversal assisted by the inverse piezoelectric effect in Co-Fe-B/ferroelectric multilayers », Pys. Rev. B 84, 012404 (2011).

[33] K. Roy, S. Bandyopadhyay, and J. Atulasimha, « Hybrid spintronics and straintronics : A magnetictechnology for ultra low energy computing and signal processing » Appl. Phys. Lett. 99, 063108 (2011).

[34] TL Wade and JE Wegrowe, «Template synthesis of nanomaterials», European Physical Journal - Applied Physics 29, 1, 3-22 (2005)

[35] J.-E. Wegrowe, T. Wade, X. Hoffer, L. Gravier, J.-M. Bonard, and J. Ph. Ansermet "Magnetoresistance of nanocontacts with constrained magnetic walls" Phys. Rev. B 67, 214414 (2003)

[36] Barsbay M. ; Güven O. ; Bessbouss H. ;Wade T.L. ; Clochard M.-C. "Functionalized membrane electrodes (FMEs) by RAFT-mediated radical polymerization inside synthetic nanochannels" J. of Memb. Sci. 2012 (submitted)

[37] G. R. Dey, A. K. El Omar, J. A. Jacob, M. Mostafavi, J. Belloni "Mechanism of Trivalent Gold Reduction and Reactivity of Transient Divalent and Monovalent Gold Ions Studied by Gamma and Pulse Radiolysis" J. Phys. Chem. A 2011, 115, 383-391

2.4 Annexe

Cet annexe comprend une sélection de sept publications permettant de mieux suivre le parcours et reprennent les principaux résultats et thématiques discutés dans ce manuscrit :

- Nanotechnologies et perspectives (Bizière et al.)
- Capteurs écologiques pour l'analyse des métaux toxiques dans l'eau (Bessbousse et al.)
- Santé (Deshayes et al.)
- Recherche fondamentale d'un nanocanal unique (Tasserit et al)
- Energie/Environnement : Pile à combustible (Clochard et al)
- Recherche fondamentale en greffage radio-induit (Clochard et al)
- Energie/Environnement : Dispersants sans cendre pour carburant et lubrifiant (Dubois-Clochard et al)

2.4.1 J. Appl. Phys. (2011)

AIP Journal of Applied Physics

Synthesis and magnetic reversal of bi-conical Ni nanostructures

N. Biziere, R. Lassalle Ballier, M. C. Clochard, M. Viret, T. L. Wade et al.

Citation: J. Appl. Phys. **110**, 063906 (2011); doi: 10.1063/1.3638072

View online: http://dx.doi.org/10.1063/1.3638072

View Table of Contents: http://jap.aip.org/resource/1/JAPIAU/v110/i6

Published by the American Institute of Physics.

JOURNAL OF APPLIED PHYSICS **110**, 063906 (2011)

Synthesis and magnetic reversal of bi-conical Ni nanostructures

N. Biziere,[1,2,a)] R. Lassalle Ballier,[3] M. C. Clochard,[1] M. Viret,[3] T. L. Wade,[1] E. Balanzat,[4] and J. E. Wegrowe[1]
[1]*Laboratoire des Solides Irradiés, CEA/CNRS/Ecole Polytechnique, Ecole Polytechnique, 91128 Palaiseau Cedex, France*
[2]*CEMES-CNRS, 29 Rue Jeanne Marvig, 31055 Toulouse, France*
[3]*Service de Physique de l'Etat Condensé, DSM/IRAMIS/SPEC, CEA Saclay URA CNRS 2464, 91191 Gif-Sur-Yvette Cedex, France*
[4]*CIMAP, Unité Mixte CEA-CNRS-ENSICAEN, F-14070 Caen Cedex 5, France*

(Received 27 May 2011; accepted 5 August 2011; published online 20 September 2011)

Template synthesis in polyethylene terephthalate (PET) membranes has been used to grow hour glass shaped nickel nanowires with a constriction in the range of tens of nanometers at the center. Anisotropic magnetoresistance measurements have been performed on a single nanowire to follow magnetization reversal of the structure. The results are explained via 3D micromagnetic simulations showing the appearance of a complex vortex state close to the constriction whose propagation depends on the angle between the cone axis and the applied field. The interest of this original growth process for spintronics is discussed. © *2011 American Institute of Physics*. [doi:10.1063/1.3638072]

I. INTRODUCTION

In the field of spintronics, magnetic nanowires are being intensively studied. Particular attention has been paid to the interplay between an electrical current or a magnetic field and a domain wall (DW). This is highly motivated by the technological potential of DWs for magnetic data storage,[1] logic gates,[2] and magnetic sensor[3] applications. For example, it has been shown that a high density spin polarized current can exert a torque on the spins of a DW via the so-called spin transfer torque (STT) and induce the motion of the DW.[4–8] Reciprocally, the nonlinear profile of the DW affects the transport properties and contributes to the magnetoresistance.[9–11] While several theories have been proposed to explain the microscopic origin of STT in DW (Refs. 12–14) or DW magnetoresistance,[15,16] some fundamental questions still remain unclear.

In order to better understand these effects, a number of experiments have been performed on patterned nanostructures with constrictions down to a few nanometers. Indeed, confinement acts as an artificial pinning site for DWs (Refs. 17 and 18) through the local modification of the magnetostatic energy. As a first approximation, the constriction can then be modeled as a pinning potential well whose amplitude and profile depend on the shape and size of the constriction and on the DW configuration. The DW can then be considered as a quasi-particle, with mass and inertia, moving in this potential well under an external force (electrical current or magnetic field). However, beside a precise knowledge of the sample geometry, it is fundamentally important to know the structure of the domain wall at the constriction (Bloch, Néel, vortex…) to get a complete description of the system. This point generally requires micromagnetic simulations or advanced imaging techniques such as MFM, Lorentz microscopy, or polarized X-ray photoemission. The shape of the nanostructure will also influence the maximum velocity at which a DW can propagate in a strip (referred to as the walker limit) and also the amplitude of the so-called intrinsic pinning.[19] Interestingly, DWs are massless in cylindrical nanowires with a suppression of the walker limit leading to very high DWs velocities.[20] This is due to the symmetry of the nanowire that prevents a modification of the internal structure of the DW during its displacement, in opposition to the case of flat strips. In this context, it is then particularly interesting to develop new techniques to grow magnetic nanostructures with original shapes and symmetries and to understand their magnetic configurations that are most often non-linear for sub-micron sizes.

In this paper, we propose to study the micromagnetic states of a single nickel nanowire with a bi-conical symmetry. One unique feature of this geometry is the possibility to get a constriction of a few tens of nanometers with a cylindrical symmetry. It has been achieved by developing an original technique based upon template synthesis in a specific matrix. The magnetic states of the nanostructure are probed via the anisotropic magnetoresistance (AMR) of the wire and explained using 3D micromagnetic simulations. We show that magnetization reversal occurs through the nucleation of a complex vortex like a state whose propagation through the constriction depends on the direction of the applied field. Moreover, AMR measurements indicate that small inhomogeneities help to trap this DW close to the constriction.

II. MATERIALS AND METHODS

Swift heavy ions (SHI) irradiations were performed using SME beam line at the GANIL (Cyclotron accelerator at Caen, France). 16 μm thick poly(ethylene terephthalate) (PET) films (from GoodFellow, kindly donated by CIMAP laboratory) were irradiated with Kr^{31+} ions of 10 Mev/amu

---

[a)] Electronic mail: nicolas.biziere@cemes.fr.

under helium atmosphere with fluences of 5.10^6 and 5.10^8 ions/cm^2. During SHI, ions induce a continuous trail of excitations and ionizations leading to the formation of specific cylindrical damage zones called latent tracks all along their trajectory through the thickness of PET film. The final heterogeneous solid is then formed of latent tracks (or highly damaged zones) and pristine areas. The latent tracks are more fragile than the non-irradiated bulk.

PET membrane ion tracks were then revealed by symmetrical chemical etching in 2 N NaOH at 80 °C. The conical shape of the pores is ensured by the velocity anisotropy of the hydrolysis reaction between the damage zone created during the ion bombardment and the polymer bulk. For the samples of interest here, the hydrolysis velocity of the membrane in the direction perpendicular to the surface is about 10 times faster than in the direction parallel to the surface leading to cone shaped etch tracks. This ratio is highly dependent on the NaOH concentration, temperature, and ion kinetic energy. As the dissolution by hydrolysis is performed on each side of the PET, a constriction is realized when two growing cones meet. The diameter of the constriction is mainly controlled by the time the membrane spends in the NaOH solution. All samples presented below have been grown in PET etched for 7.5 mn. Figure 1(a) shows the Field Emission Scanning Electron Microscopy (FESEM) image of the cross-section of the resulted bi-conical tracks. The flexibility of the track etching technique allows the synthesis of a wide variety of cone-shaped tracks with different constriction sizes.

Electrodeposition is then used to fill the pores with Ni. A piece of PET for which one side has been sputtered with a 150 nm gold layer is immersed into an aqueous electrolytic solution composed of $NiSO_4$ and H_3BO_4. The electric potential between the golden surface of the PET (working electrode) and an Ag/AgCl reference electrode is set to -1.000 Vs. The electrodeposition is stopped when a large sheet of Ni has grown on top of the PET. As shown by previous studies about cylindrical and cigar shaped tracks,[21] the current versus time plots during electrodeposition should reflect the pore geometry. The black curve in Fig. 2 corresponds to the electrodeposition current versus time plot for a PET membrane with a pore density of 5.10^8/cm^2. Since the electrodeposition current density is proportional to area, it is large at the beginning of the electrodeposition (about 47 mA/cm^2), corresponding the conical openings of the membranes. The current density then decreases as the nickel deposit approaches the 50 to 100 nm constriction in the middle of the membrane (about 16 mA/cm^2 at 680 s). Finally the current density increases as the deposition proceeds to the conical openings at the other side and then surface growth outside the pores. For comparison, nickel nanowires were deposited in 6 micron thick 30 nm pore diameter polycarbonate filters (Poretics) using the same electrodeposition conditions, (see Fig. 2, gray curve). The nominal interior pore diameter of the filters is about 60 nm depending on the measurement technique [see Ref. 21]. It is interesting to note that the current density for constriction is similar to that for the electrodeposition in the filter, 12–15 mA/cm^2. The pore density for the filter is $3*10^8$/cm^2 and $5*10^8$/cm^2 for the bi-cone membrane while deposition area is 9 cm^2 for filter and 6 cm^2 for the bi-cone membrane resulting in $2.7*10^9$ pores for the filter and $3.0*10^9$ for the bi-cone membrane.

To characterize the shape of the nanowires, electrodeposition in PET membrane with a pore density of 5.10^6 has been realized. Once Ni nanowires have been grown as explained above, the membrane is left in NaOH until it is completely dissolved. Ni nanowires attached to the large Ni plate can then be observed. However because of their weight, they break at the constriction during the dissolution of the membrane. Figure 1(b) is a FESEM electron microscopy image of one half of a Ni nanowire. We can clearly observe the conical shape of the wire thus validating our method. The size of the constriction for this wire is below 100 nm and the cone aperture is about 5°. We have observed on a few nanowires that the diameter at the break can range from 50 to 100 nm and that the cone angles ranges between 4 and 6°. We also observe roughness on the lateral surface of the cone that we estimate to be about 1% of the diameter.

III. AMR MEASUREMENTS

In order to measure the magnetoresistance of Ni nanowires, electrodeposition is performed in 5.10^6/cm^2 pore density PET membranes with 150 nm of gold sputtered on both

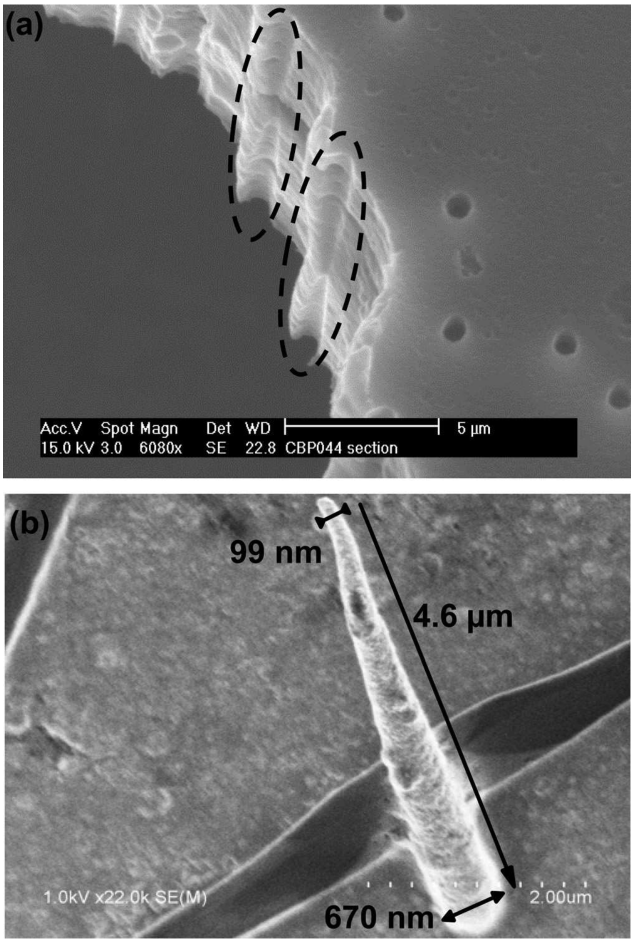

FIG. 1. (a) Electron microscopy image of the cone trace in the PET after freeze fracturing. The dotted circle is a guide to the eye to localize the cone shaped trace. (b) Electron microscopy image of half of a Ni nanowire after dissolution of the PET matrix.

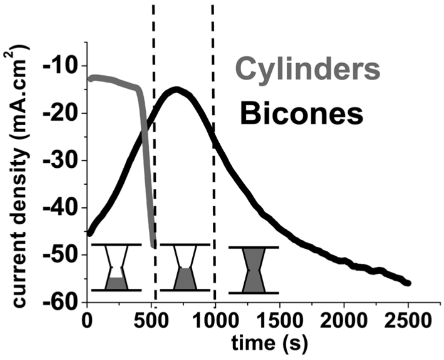

FIG. 2. Electrochemical reduction current density as a function of time for the potentiostatic plating of Ni (-1.000 V) in cylindrical pores (gray curve) and in bi-conical pores (black curve). The schematics display three different stages of the growth process corresponding to the black curve. In region I, metal wires (filled) are before the constriction, the current decreases following the surface decrease. In region II, the metal filling is at the constriction of bi-conical tracks, minimum of current intensity, and minimum exposed surface to electrolyte. In region III, growth continues to larger surfaces up to the whole membrane surface.

sides. The electrical contact on a single nanowire is ensured by *in situ* recording of the current in the electrolytic cell. Indeed, when a first nanowire reaches the top surface, it short cuts the top and bottom gold layers and induces a sharp increase of the current in the cell. Details about the growth procedure are given elsewhere.[22]

Figure 3 shows the resistance of a Ni nanowire as a function of the applied magnetic field amplitude H_0 and for different angles θ between H_0 and the nanowire axis. The field is scanned from negative to positive saturation and then back. The AMR ratio, defined by $R_{//}$-$R_{\perp}/R_{//}$ measured at saturation, is about 0.55%, which is around half of the AMR ratio that has been measured on Ni cylindrical nanowires electrodeposited in commercial polycarbonate membrane[23] (between 1 and 1.5%). The difference is due to the contact resistance between the gold layers on top of the PET and the nanowire. Because the cone angle is very small, we can consider, as a first approximation, that the current lines are parallel in the cone. The cone resistance can then be estimated to lie between 8 and 10 Ω for this sample. However, because of the cone shape, the main contribution (more than 80%) to this resistance comes mainly from the constriction and a small part on each side (few hundred of nanometers). The total resistance of the different nanowires (cone + contact resistances) we have measured range between 20 and 35 Ω, a span that can be accounted for by the difference in the contact resistance, the cone angle, and the size of the constriction. This shows that despite measurement geometry in a two point contact, we are sensitive to the AMR of the constriction.

We observe in Fig. 3 that for $\theta = 0°$, the AMR slightly increases when the field amplitude decreases. This can be accounted for the uncertainty of θ. We estimate it to be up to a few degrees due to the fact that the membrane is not perfectly flat at the surface of the sample holder and to the uncertainty on the orientation of the latter in our electromagnet. The cone shape of the wire can also explain the slight increase of the AMR. Indeed, when H_0 decreases the spins at the edge of the cone tend to align parallel to the surface and therefore to the current lines.

AMR measurements reveal different magnetic states at remanence as a function of θ. More particularly, there is a clear difference between a field applied almost parallel or almost perpendicular to the cone axis. In the latter case, the magnetic state within the constriction is non-uniform with spins aligned mainly perpendicular to the cone axis.

To get a better understanding of what happens in the vicinity of the magnetic switching, we performed magnetoresistance (MR) measurements on another sample while sweeping the field in small steps of 1 mT. The results obtained for $\theta = 0$ and 50° are presented in Fig. 4. Similar results have been obtained on other samples. Each curve is an average of over 10 scans. For convenience, both MR measurements have been normalized by the value of the resistance at saturation. While the shape of both MR cycles exhibits some differences, especially when H_0 changes its sign, some similarities can be observed. In both cases the resistance decreases before H_0 reaches zero. This is proof that the magnetic state at remanence is non-uniform for both orientations of the applied field. The resistance decrease is consistent with an AMR signature of spins, which tend to align

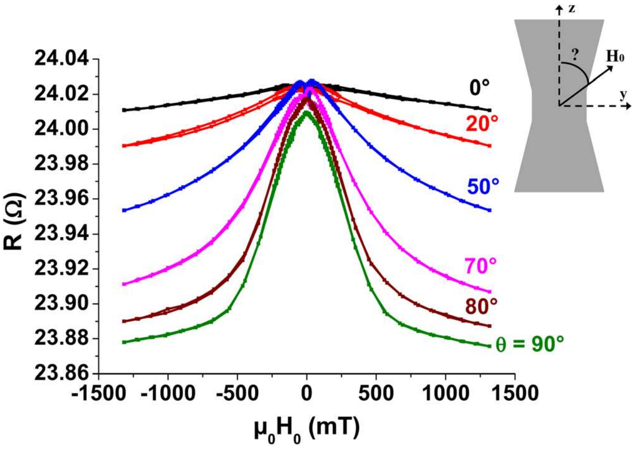

FIG. 3. (Color online) (a) MR of a single Ni nanowire as a function of the applied field H_0. Values correspond to the relative angle between H_0 and the cone axis.

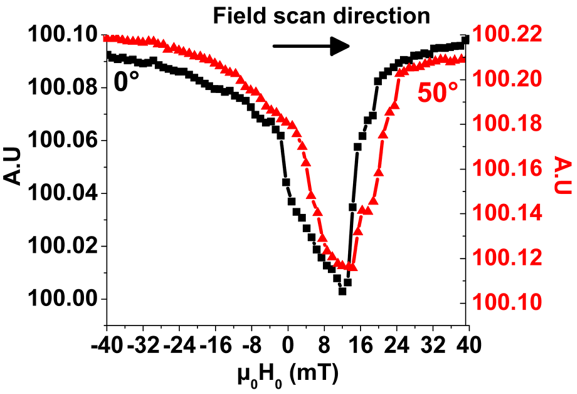

FIG. 4. (Color online) Magnetoresistance of a Ni nanowire as a function of H_0 for $\theta = 0°$ (squares) and 50° (triangles). The resistance has been normalized by the value at negative saturation for convenience.

perpendicularly to the cone axis. Then a sharp decrease of the resistance is observed at $\mu_0H_0 = 0$ and 3 mT for $\theta = 0$ and 55°, respectively. As confirmed by the simulations (see below), we assume that this step in the resistance corresponds to the nucleation of a DW in the vicinity of the constriction. This is followed, on a field range of about 10 mT, by a slight decrease of the resistance. This can be accounted for by a small propagation of the DW. Finally, over a last range of fields of less than 10 mT and beginning at the coercive field Hc, (defined as the field for which the resistance is the lowest), the resistance increases back to its value at negative field. We note here that the difference in the switching field from one scan to another is less than 10% for both field orientations. The steps observed in this field range is a typical feature of a magnetic switching ensured by a propagating DW through the constriction hopping from one pinning site to another. It is also interesting to notice that despite the difference in θ, the values of the switching field are very similar for each orientation. This point confirms that the magnetization reversal occurs through a nucleation/propagation process instead of a coherent rotation of the spins in the constriction as one could expect from the shape anisotropy of the nanowire.

IV. MICROMAGNETIC MODELING

The 3D micromagnetic OOMMF freeware program[24] has been used to simulate the magnetic states of the cone. For obvious calculation consumption time, real samples could not be entirely simulated. Instead, the simulated wire length is taken to be 4.2 μm long, with a cone angle of 2.5°. The constriction is defined as a 100 nm long cylinder with a radius of 50 nm. On one side of the cone, we have simulated a "mushroom shaped" Ni contact. This mushroom grows at the top of the Ni nanowire during electrodeposition when the wire reaches the surface. It can be a few hundreds of nanometers up to >1 μm high depending on the sample (see Refs. 21 and 23 for more details). Here we have simulated a mushroom with a diameter of 200 nm. The parameters used for the simulations are $\mathrm{Ms} = 4.10^5$ A/m, $\mathrm{A} = 9.10^{-12}$ J/m. Crystalline anisotropy has been neglected because the electrodeposited Ni grows with a polycrystalline structure. The cell is a cube of 125 nm^3. Field steps have been limited to 4.5 mT in the vicinity of the switching field in order to remain within reasonable calculation times. As a first approximation the AMR of the cone can be described as the average value of the square of magnetization in the direction z of the cone axis. Figure 5 shows the result of the simulation of $\langle \mathrm{Mz} \rangle^2$ as a function of the applied field for $\theta = 0$ and 45°. We can see that the shape is in quite good agreement with the experiments. More particularly two major features are reproduced. The first is the decrease of $\langle \mathrm{Mz} \rangle^2$ before the field is reversed. The second is that both switching fields are quite close for both orientations of the magnetic field.

Figure 6 shows the equilibrium magnetic states calculated at the points denoted I, II, III, and IV in Fig. 5 ($\theta = 0°$). The arrows represent magnetization vectors in the xy plane for different z values. Starting from the negative saturation, two vortices appear in the mushroom and at the bottom of the cone thus decreasing the magnetostatic energy. The vortex in the mushroom is created around –100 mT while that at the bottom of the cone appears around −90 mT (figure not shown). We observe that the cores of the two vortices point toward the direction of the applied field (-z). However the chirality of the two vortices is opposite. We assume that the chirality of the bottom vortex is induced by the small stray field coming from the mushroom such as to close the magnetic flux outside the cone.

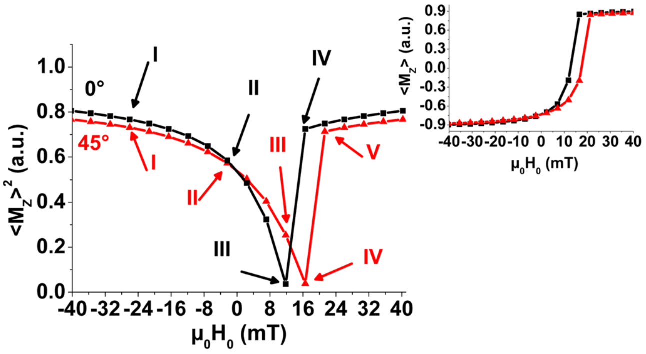

FIG. 5 (Color online) Square of the average Mz component of the magnetization of the cone for $\theta = 0°$ (squares) and 45° (triangles). Inset: Average Mz component of the magnetization for $\theta = 0°$ (squares) and 45° (triangles).

When decreasing the amplitude of the applied field, the vortices at top and bottom of the nanowire propagate toward the constriction (points I, II, and III) until Hc is reached. However, at point III the vortices stop at a distance of less than 1 μm from the center of the constriction in which the spins still point to the –z direction. This indicates that the cost in exchange energy to create a vortex at the center of

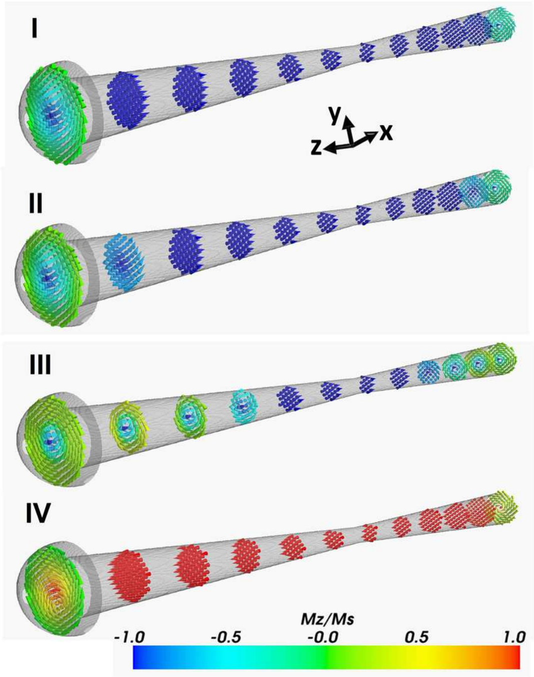

FIG. 6. (Color online) Magnetization of the cone in the xy plane at different z values. The field is applied parallel to the z axis (cone axis). The cone is preliminary saturated in the –z direction. The different images refer to the equilibrium magnetic states denoted I, II, III, and IV in Fig. 4.

the cone would be too important and that the shape anisotropy dominates. When increasing the field from III to IV the magnetization reverses in the cone. Only the vortices at the top and bottom remain but we can see that if the chirality has been conserved the core direction has been inversed to decrease the Zeeman energy. More details about the dynamic of the switching are presented below.

A similar behavior is observed for $\theta = 45°$ (field applied in the yz plane) in Fig. 7. However we observe that the chirality of the top and bottom vortices is the same at point I. This is due to the y component of the applied field, which favors a domain with a majority of spins in the –y direction when the vortex nucleate. Once again, the vortices propagate toward the constriction until the field reaches Hc for which the spins at the center of the cone are aligned in the –z direction. Unlike the case $\theta = 0°$, we observe that when the vortex propagates, the vortex core is not aligned with the axis of the cone, i.e., along the z axis, but spirals around it. We explain this fact by the competition between the Zeeman and magnetostatic energies. Indeed, at zero field the vortex core is located in the middle of the xy plane as could be expected. Then when the field is reversed, the +y component of the applied field induces a displacement of the vortex core toward the edge of the cone. However, because of the cone shape, this would push the core's magnetization to point out of the cone and induce a stray field. To allow for the magnetic flux to stay in the cone and to minimize the Zeeman energy, the vortex core spirals around the z axis so that most of the spins can rotate in the y and z directions. One important feature revealed by these simulations is that magnetic states with vortices of similar chirality on each side of the constriction are more stable.

To explain the dynamics of the switching we present in Fig. 8 some snapshots of the magnetization for $\theta = 0°$ starting from point III and before it reaches the equilibrium position of point IV. Similarly to the case at $\theta = 45°$, we observe that the vortex core begins to spiral around the z axis to minimize the Zeeman energy. We emphasize here that this spiral is an unstable state unlike at point III for $\theta = 45°$. Then in a small zone in each side of the cone, we observe a flip of the vortex core to allow for the spins to align in the direction of the applied field. Then this domain grows and pushes away the vortices toward the top and bottom of the structure. We can notice that the spins flip first in the top part of the cone for which the vortex has entered the furthest in the cone. At this step a uniform domain with the spins aligned in the opposite direction of the field is trapped in the constriction. The vortices act as a head-to-head and a tail-to-tail domain wall as schematically shown by the arrows. Finally the switching is achieved when the two vortices coming from each part of the cone annihilate in the constriction.

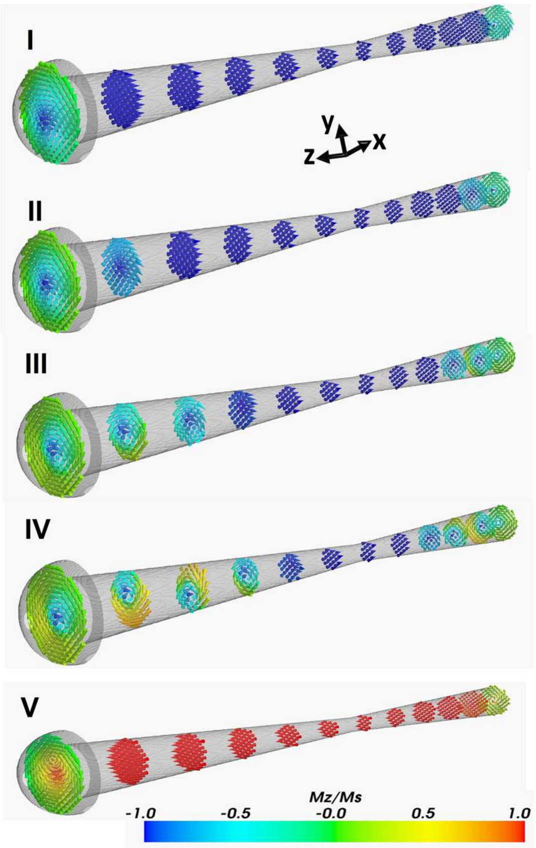

FIG. 7. (Color online) Magnetization of the cone in the xy plane at different z values. The field is applied at 45° from the z axis in the yz plane. The cone is preliminary saturated with a negative field with respect to the axis orientation. The different images refer to the equilibrium magnetic states denoted I, II, III, IV, and V in Fig. 4.

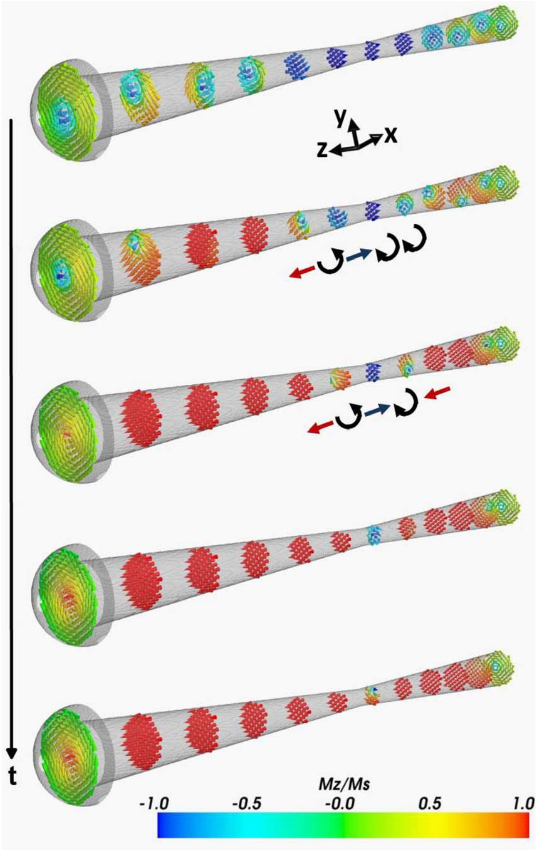

FIG. 8. (Color online) Snapshots of the magnetization in the xy plane at different z values during switching for $\theta = 0°$. Arrows are a schematic of the magnetization in the vicinity of the constriction.

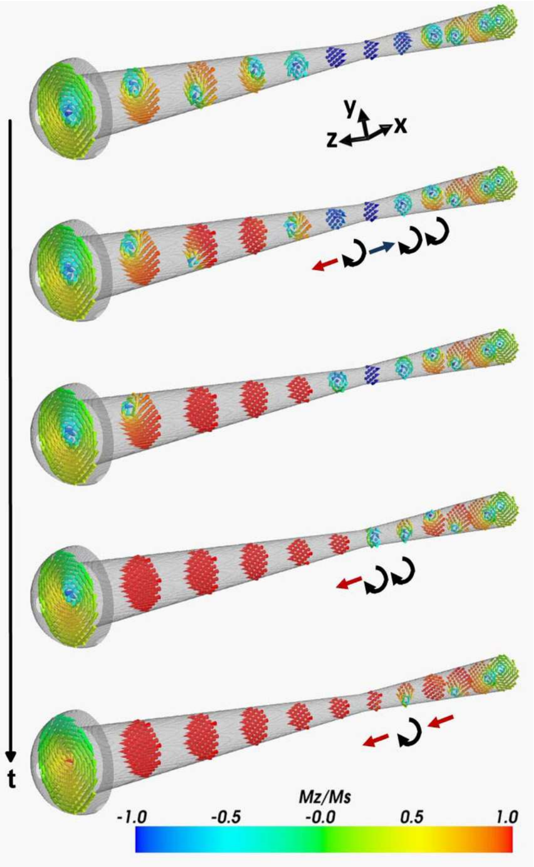

FIG. 9. (Color online) Snapshots of the magnetization in the xy plane for different z values during switching for $\theta = 45°$. Arrows are a schematic of the magnetization in the vicinity of the constriction.

The situation for $\theta = 45°$ is slightly different as can be observed in Fig. 9. Indeed the magnetization flips only in the part of the cone with the mushroom. Then we see that the vortex can propagate easily through the constriction. The reason is that the magnetic domain with spins aligned in the –z direction is not held on each side by two domains with spins in the +z direction and so it does not prevent the vortex to enter the constriction.

It is interesting to compare the magnetic simulations with the AMR experiments. Indeed, simulations performed on an ideal system with no roughness highlight that the vortices propagate through the constriction without being trapped. While it is difficult to know the exact diameter of the constriction and the cone angle of the sample we measured, we can assume that micromagnetic mechanisms of switching are most likely equivalent for similar cone angles and similar constriction diameters. Then we can assume that the steps observed in the AMR in Fig. 3 for $H_0 < Hc$ correspond to local roughness induced pinning of the vortex while propagating toward the constriction. More interestingly, we can assume that the steps observed when passing Hc correspond to the pinning of the vortex in the vicinity of the constriction. Then this system becomes very interesting for spintronic studies since one can trap a head to head or tail to tail vortex domain wall in a constriction with cylindrical symmetry.

V. CONCLUSIONS

We have developed an original method based upon template synthesis in a PET matrix to grow bi-conical Ni nanowires with a constriction of a few tens of nanometers. The micromagnetic states of a single nanowire have been studied through AMR and micromagnetic modeling during magnetization reversal. Simulations have revealed a complex vortex like state whose propagation through the constriction depends on the relative angle between the applied field and the cone axis. While simulations predict no pinning of the vortex in the constriction, our magnetoresistance measurements provide evidence that small inhomogeneities allow the trapping of head-to-head or tail-to-tail domain walls in the vicinity of the constriction.

[1] S. S. P. Parkin, M. Hayashi, and L. Thomas, Science **320**, 190 (2008).
[2] J. Jaworowicz, N. Vernier, J. Ferre, A. Maziewski, D. Stanescu, D. Ravelosona, A. S. Jacqueline, C. Chappert, B. Rodmacq, and B. Dieny, Nanotechnology **20**, 215401 (2009).
[3] G. A. Wang, Y. Masuda, T. Kato, and S. Iwata, J. Phys. D: Appl. Phys. **43**, 455001 (2010).
[4] S. Emori and G. S. D. Beach, Appl. Phys. Lett. **98**, 132508 (2011).
[5] X. Jiang, L. Thomas, R. Moriya, and S. S. P. Parkin, Nano Lett. **11**, 96 (2011).
[6] J.-Y. Chauleau, R. Weil, A. Thiaville, and J. Miltat, Phys. Rev. B **82**, 214414 (2010).
[7] X. Waintal and M. Viret, Europhys. Lett. **65**, 427 (2004).
[8] J. Heinen, O. Boulle, K. Rousseau, G. Malinowski, M. Kläui, H. J. M. Swagten, B. Koopmans, C. Ulysse, and G. Faini, Appl. Phys. Lett. **96**, 202510 (2010).
[9] A. K. Patra, A. von Bieren, S. Krzyk, J. Rhensius, L. J. Heyderman, R. Hoffmann, and M. Kläui, Phys. Rev. B **82**, 134447 (2010).
[10] C. H. Marrows, Adv. Phys. **54**, 585 (2005).
[11] J. L. Prieto, M. G. Blamire, and J. E. Evetts, Phys. Rev. Lett. **90**, 027201 (2003).
[12] G. Tatara and H. Kohno, Phys. Rev. Lett. **92**, 086601 (2004).
[13] A. Vanhaverbeke and M. Viret, Phys. Rev. B **75**, 024411 (2007).
[14] L. Berger, Phys. Rev. B **80**, 144427 (2009).
[15] L. Berger, Phys. Rev. B **75**, 174401 (2007).
[16] M. Viret, D. Vignoles, D. Cole, J. M. D. Coey, W. Allen, D. S. Daniel, and J. F. Gregg, Phys. Rev. B **53**, 8464 (1996); P. M. Levy and S. Zhang, Phys. Rev. Lett. **79**, 5110 (1997).
[17] J.-S. Kim, O. Boulle, S. Verstoep, L. Heyne, J. Rhensius, M. Kläui, L. J. Heyderman, F. Kronast, R. Mattheis, C. Ulysse, and G. Faini, Phys. Rev. B **82**, 104427 (2010).
[18] A. Bisig, J. Rhensius, M. Kammerer, M. Curcic, H. Stoll, G. Schütz, B. Van Waeyenberge, K. W. Chou, T. Tyliszczak, L. J. Heyderman, S. Krzyk, A. von Bieren, and M. Kläui, Appl. Phys. Lett. **96**, 152506 (2010).
[19] T. Koyam, Nature Mater. **10**, 194 (2011).
[20] M. Yan, A. Kakay, S. Gliga, and R. Hertel, Phys. Rev. Lett. **104**, 057201 (2010).
[21] C. Schönenberger, B. M. I. van der Zande, L. G. J. Fokkink, M. Henny, C. Schmid, M. Krüger, A. Bachtold, R. Huber, H. Birk, and U. Staufer, J. Phys. Chem. B **101**, 5497 (1997).
[22] J. E. Wegrowe, Q. A. Nguyen, and T. L. Wade, IEEE Trans. Mag. **46**, 3 (2010).
[23] J.-E. Wegrowe, Q. A. Nguyen, M. Al-Barki, J.-F. Dayen, T. L. Wade, and H.-J. Drouhin, Phys. Rev. B **73**, 134422 (2006).
[24] M. J. Donahue and D. G. Porter, OOMMF User's Guide, http://math.nist.gov/oommf.

2.4.2 Anal. Meth. (2011)

Analytical
Methods

Cite this: *Anal. Methods*, 2011, **3**, 1351

www.rsc.org/methods

PAPER

Functionalized nanoporous track-etched β-PVDF membrane electrodes for lead(II) determination by square wave anodic stripping voltammetry

Haad Bessbousse,[a] Iris Nandhakumar,[b] Maxime Decker,[a] Murat Barsbay,[c] Olivia Cuscito,[a] Didier Lairez,[d] Marie-Claude Clochard*[a] and Travis. L. Wade*[a]

Received 21st January 2011, Accepted 24th March 2011
DOI: 10.1039/c1ay05038a

Track-etched functionalized nanoporous β-PVDF membrane electrodes, or functionalized membrane electrodes (FMEs), are electrodes made from track-etched, poly(acrylic acid) (PAA) functionalized nanoporous β-poly(vinylidene fluoride) (β-PVDF) membranes with thin porous Au films sputtered on each side as electrodes. In order to form the β-PVDF nanoporous membranes, β-PVDF films are irradiated by swift heavy ions. After irradiation, radical tracks are left in the membranes. Etching removes some of the radical tracks revealing nanopores. The remaining radicals initiate radio grafting of PAA from the pore walls of the nanoporous β-PVDF. PAA is a cation exchange polymer that adsorbs metal ions, such as Pb^{2+}, from aqueous solutions thus concentrating the ions into the membrane. After a calibrated time, the FME is transferred to an electrochemical cell for analysis. A negative potential is applied to the Au film of the FME for a set time to reduce the adsorbed ions onto the Au film working electrode. Square-wave anodic stripping voltammetry was performed on the FME to determine the Pb^{2+} ion concentration in the original solution based on calibration. The zero current intercept of the calibration for Pb^{2+} is 0.13 ppb (μg L^{-1}) and three times the sample blank deviation (3S/N) is 0.050 ppb.

Introduction

The maximum level of Pb^{2+} in potable water established by the World Health Organisation (WHO) is 10.0 ppb (10 μg L^{-1}).[1] Reliable quantification of this low concentration is difficult and expensive. Also, the analysis equipment for inductively coupled plasma mass spectroscopy (ICP-MS) and atomic absorption spectroscopy (AAS) are not portable. Samples have to be sent to a centralised lab. This typically involves a 24 hour turn around time which means that pollution events can be missed, or detected too late.

Electrochemical analysis techniques, such as anodic stripping voltammetry (ASV), are inexpensive, rapid, and portable. The electrode of choice for measuring trace levels of toxic metal ions by ASV has been the dropping mercury electrodes (DMEs).[2] DMEs and mercury film electrodes are very sensitive (limits of detection (LOD) of 10^{-3} ppb for lead(II)), due to their high capacity to preconcentrate ions for analysis by reduction, insensitivity to dissolved oxygen, and their low charging capacitance.[3–6] The problem with mercury is that it is unacceptable for environmental applications because of its toxicity. Also, DMEs are expensive and difficult to use. Currently, there is interest in finding replacement electrodes for DMEs and mercury films.[7]

A new industry, based on thick-film screen-printed electrodes (SPEs), has evolved to exploit the growing interest in environmental sensors and to replace mercury electrodes.[8–10] Unmodified, screen-printed electrodes are cheap and disposable but the quoted LODs are barely able to measure the required low concentration levels.[8–13] Extra steps of modification are needed to improve the LODs for screen printed electrodes.[14,15]

Mercury free Au electrodes have demonstrated good performances for the detection of Ag^+ and As^{3+} traces by ASV.[16–22] However, lead(II) LODs are higher whatever the mercury free electrodes.[8–10] The lowest Pb^{2+} LOD is 0.020 ppb using bismuth-films on glassy carbon electrodes modified with calixarene.[23] Low Pb^{2+} LODs (<0.1 ppb) have been also obtained with silver rotating disk electrodes, and carbon electrodes that were modified with poly(pyrrole-malonic acid), and *in situ* electrodeposited bismuth modified gold or carbon paste electrodes.[24–26]

This paper describes a new mercury free electrode. The new electrode is based on track-etched poly(acrylic acid) (PAA) functionalized nanoporous β-poly(vinylidene fluoride) (β-PVDF) membranes with porous gold conductive layers on each side (Fig. 1). The grafted PAA inside the pores is a good complexion agent for some heavy metal ions. It acts as a sponge

---

[a] *Laboratoire des Solides Irradiés, CEA-CNRS-Ecole Polytechnique, 91128 Palaiseau, France. E-mail: marie-claude.clochard@polytechnique.edu; travis.wade@polytechnique.edu; Fax: +33 (0)169334554*
[b] *School of Chemistry, University of Southampton, University Road, Southampton, S017 1BJ, UK*
[c] *Hacettepe University, Department of Chemistry, Polymer Chemistry Division, 06800 Beytepe, Ankara, Turkey*
[d] *Laboratoire Léon Brillouin, CEA-CNRS UMR 12, CEA-Saclay, 91191 Gif-sur-Yvette, France*

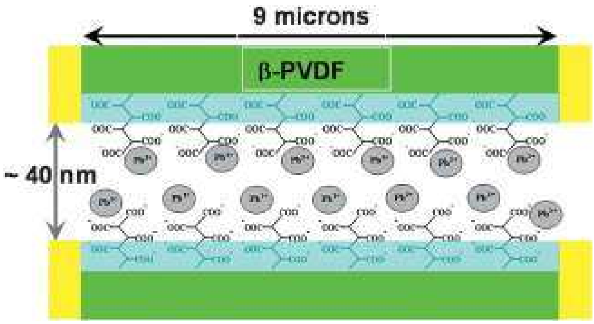

Fig. 1 Diagram of a single nanopore from a gold coated 9 micron thick PAA functionalized radio-track etched β-PVDF membrane (FME) after absorbing Pb^{2+} ions from polluted water. The β-PVDF membrane is shown as green and the $–RCOO^-$ as blue zones represents the PAA gel that is radio grafted into the 40 nm diameter nanopores of the membrane. The 35–40 nm thick gold coating is shown as yellow. The grey balls represent absorbed Pb^{2+} ions.

to pre-concentrate the ions prior to ASV analysis. Unlike DMEs and SPEs, pre-concentration is done at open circuit.

The present paper describes: elaboration of functionalized nanoporous membrane by swift heavy ion irradiation, chemical revealing, and radical grafting. Characterization by EPR allows us to draw the radical profile inside the tracks. XPS gives information about grafting coverage and CSLM images show grafting confinement within the membrane pores. FESEM and AFM are used to study the pore morphology. Next, these functionalized membranes are transformed into electrodes namely FMEs by sputtering a fine layer of gold. We will use ASV to optimize the analysis conditions and plot a calibration curve for Pb^{2+} in water.

Experimental

Materials

β-Poly(vinylidene fluoride) (β-PVDF) films of 9 μm thickness were provided by PiezoTech SA. Toluene, potassium hydroxide, potassium permanganate, potassium disulfite, acrylic acid (AA), Mohr's salt ($(NH_4)_2Fe(SO_4)_2\cdot 6H_2O$), sulfuric acid, $C_8H_{17}N_3\cdot HCl$ (EDC), phosphate buffer saline (PBS), *t*BuOK (C_4H_9OK 95%) were purchased from Sigma-Aldrich. Alexa Fluor R 488 hydrazide ($C_{21}H_{15}N_4NaO_{10}S_2$) was purchased from Invitrogen.

Irradiation

Prior to the swift heavy ion irradiation β-PVDF films were toluene-extracted for 24 h. The irradiation was performed at the GANIL irradiation centre (Caen, France). Films were irradiated with Kr ions (10.37 Mev amu^{-1}, fluence 10^7 to 10^{10} cm^{-2}) in a He atmosphere. The irradiated films were stored at −20 °C in a N_2 atmosphere until chemical etching and radio grafting.

Chemical etching

β-PVDF irradiated films were chemically etched using permanganate solution (0.25 M) in a highly alkaline medium (KOH, 10 M) at 65 °C for 30 min. After etching the obtained membranes were washed in potassium disulfite solution (15%) and de-ionized water. The KOH solution is very corrosive and should only be handled in a fume hood wearing protective clothing, gloves, and safety glasses. The used KOH solution should be disposed of as corrosive waste.

Radio-grafting

Etched β-PVDF films were immersed at room temperature into a radio grafting solution containing AA and Mohr's salt (0.25%, w/w) in a purgeable glass tube and then connected to a Schlenk line. After 15 min of N_2 bubbling at room temperature, the glass tube was sealed and put into a thermostatted water bath at 60 °C for 1 h. The radio grafted film was washed with water and then Soxhlet extracted in boiling water for 24 hours in order to extract free homopolymer. The membrane was dried at 50 °C under vacuum overnight. The acrylic acid solution is very corrosive and should only be handled in a fume hood wearing protective clothing, gloves, and safety glasses. The used acrylic acid solution should be disposed of as corrosive waste.

Field-Emission Scanning Electron Microscopy (FESEM)

FESEM micrographs were acquired with a Hitachi S-4800 microscope.

Infra-red spectroscopy

FTIR spectra of PVDF were obtained with a Nicolet Magna-IR 750 spectrometer equipped with a DGTS detector. Spectra were recorded in Attenuated Total Reflexion (ATR) mode using a diamond-crystal with single reflection. Spectra were collected by cumulating 32 scans at a resolution of 2 cm^{-1}.

Confocal Scanning Laser Microscopy (CSLM)

Measurements were performed with a Leica TCS-SP2 using an Ar laser (488 nm). Samples were observed in water with a 40× dry objective of numerical aperture 0.85.

Electron Paramagnetic Resonance (EPR)

EPR spectra were recorded at the X band (9.4 GHz) on a Brüker ER-200D spectrometer.

Atomic Force Microscopy (AFM)

AFM images were acquired by tapping mode in air on a Multimode AFM system equipped with a Nanoscope III controller.

Solutions

The Pb^{2+} solutions were diluted from 1.000 μg mL^{-1} AAS calibration standards (Alfa Aesar) or from $PbCO_3$ powder 99% (VWR). The electrolyte for the voltammetry measurements was 0.1 M sodium acetate (Sigma-Aldrich). All solutions were made with 18 Mohm deionised water (Aquadem Veolia). 100 ml polypropylene containers (VWR) were used for dilution and analysis to avoid the loss of Pb^{2+} due to surface adsorption on glass.[27] The Pb^{2+} solutions are poisonous so gloves should be worn when handling and the solutions should be disposed of as toxic waste.

Connections

The functionalized membranes were metalized by gold sputtering on both sides by a K550 gold sputter (EMITECH) with a sputtering current of 40 mA in an argon atmosphere of 10^{-2} mbar through a mask with 0.4 cm diameter holes for 3 minutes. Under these conditions the gold sputtering rate is 12 nm per minute. Gold sputtering targets were purchased from NewMet (New Metals & Chemicals Ltd). The metalized sides were then connected to 0.5 mm diameter stainless steel wires with silver paste (FERRO, CDS Electronique). The connections were water proofed with hot wax and fingernail polish.

Voltammetry

The voltammetry and other electrochemical measurements were performed in a three-compartment electrochemical cell controlled by a PalmSens potentiostat (PalmSens) or a BiStat 3200 (Uniscan). Ag/AgCl (3 M KCl) reference electrodes (METROHM) were used for all measurements.

Results and discussion

The synthesis of functionalized radio grafted β-PVDF membranes was developed at the Laboratoire des Solides Irradies (LSI).[28–34] β-PVDF is a very durable material with chemical and mechanical properties similar to Teflon and is nontoxic. β-PVDF polymer films are first bombarded by swift heavy ions, Fig. 2a, and the tracks formed along the ion passage are revealed under alkaline chemical treatment, Fig. 2b and c. After etching times of less than one hour, the radical residues within the nanopore walls were sufficient for radio grafting.[32] This is due to the remarkable property of β-PVDF favouring the radical stability by trapping them inside its crystalline areas.[35,36] PAA can then be selectively radio grafted into the pore walls, confirmed by confocal laser imaging, Fig. 2d. The obtained nanoporous polymer membranes do not need to undergo subsequent e-beam irradiation to increase radicals in the polymer bulk for submicron pore diameters.

When a heavy ion crosses the PVDF film, it deposits an important quantity of energy all along the latent track. This energy per mass unit (dose) forms a radial distribution from the ion trajectory. The energy transferred to the electrons of the polymer atoms by ion irradiation generates: defects (cross-links, chain scissions, double bonds); the creation of new active species (radicals), and gas release. The main defects in PVDF have been established by FTIR,[37–39] DSC, and X-ray diffraction.[40] The rapid diffusion of radicals may be related to either individual diffusion of small radical species or cooperative modes of lone electron diffusion.[41] The radical migration, initiated by the ion dose deposition, is localized in a cylinder centred around the ion trajectory with a radius roughly equal to 1 µm. EPR spectra recorded under vacuum[36] show the presence of various alkyl radicals ($R^{\cdot}$): end chain radicals ($CF_2–H_2C^{\cdot}$) or ($CH_2–F_2C^{\cdot}$) and middle chain radicals ($CF_2–HC^{\cdot}–CF_2$) or ($CH_2–FC^{\cdot}–CH_2$). As soon as alkyl radicals are in contact with air, they immediately combine with oxygen to form peroxyl radicals ($ROO^{\cdot}$) which are characterized by a loss of hyperfine structure in the EPR signal.

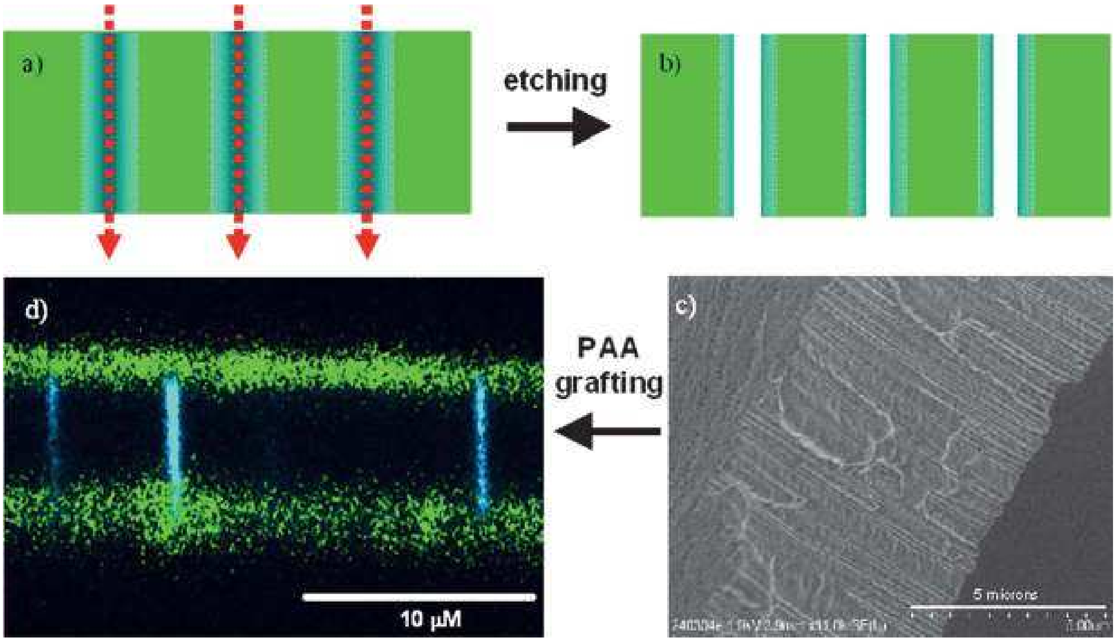

Fig. 2 (a) 9 µm thick β-PVDF films were irradiated with Kr ions (10.37 Mev amu^{-1}, fluence 10^7 cm^{-2}) under a He atmosphere. The dashed red arrows indicate the path of the Kr ions and the black/grey areas indicate the zone of irradiation damage in the film. (b) The ion tracks were revealed under chemical etching. (c) FESEM image of a track etched β-PVDF membrane cross-section with pore diameters of 40 nm and a membrane thickness of 9 µm. (d) Fluorescein isothiocyanate labelling reveals amine groups (green), *i.e.* surface oxidation and Alexa Fluor R hydrazine labelling reveals carboxyl group (blue), *i.e.* PAA.

EPR signals are consequently representative to both alkyl and peroxyl species whatever the accelerated particle.

Fig. 3 shows the evolution of the residual radical fraction and the radio-grafting *versus* etching time. The overall radical fraction $x_a(t)$ displays an exponential decay with a characteristic rate of 0.055 min^{-1}. The presence of a persistent non-decaying radical fraction of 17% is observed. It is the result of a compensative effect between the removal of alkyl radicals by etching and the creation of peroxyl radicals by oxidation in the presence of prolonged contact with $KMnO_4$.

The decrease of the carboxylic acid peak at 1710 cm^{-1} from FTIR for increasing etching times also follows an exponential decay and can be directly related to EPR results.[32] Consequently, the radical distribution profile in a track drives the radical polymerisation.

One hour of etching corresponds to radii of 44 nm. Above this value, the radio-grafting is no longer homogeneous and the degree of grafting becomes very low (<2 wt%) as shown in the right axis of Fig. 3. As alkyl radicals are well-known to be more efficient as initiators in comparison to peroxyl radicals in the radio-grafting process on solid polymers, the results lead to the conclusion that after one hour of etching, alkyl radicals are no longer present.

As the radical concentration decreases with the etching time, longer grafted PAA chains are favoured when the pore size increases but, simultaneously, the density of grafted PAA chains on the pore wall surface becomes very low. For a better coverage of pore walls, it is preferable to have shorter PAA chains and a denser grafted PAA chain layer. A good compromise was to radio-graft pores with radii as less than 25 nm to have sufficient radicals for a good covering of pore walls. This is the reason we have chosen 30 min of etching for the further development of the electrodes.

The etched PVDF membranes are then radiografted in 50% acrylic acid aqueous solutions. Fig. 4 shows the XPS spectra of the surface composition of all atoms linked to C_{1S} onto track-etched PVDF membranes before and after PAA grafting. The C_{1S} ray spectrum of the initial track-etched β-PVDF, Fig. 4a, displays, after peak de-convolution, two typical peaks of the same height and area for CH_2 and CF_2 of the PVDF at 286.5 eV and 291 eV respectively. Two additional peaks at 287.8 eV and 289 eV correspond to surface oxidation peaks. The peak present at 285 eV comes from non-removable PDMS contaminant present in the 9 μm thick β-PVDF. Even a 24 h toluene extraction did not remove these alkyl contaminants coming from grease used during the initial extrusion process. Fig. 4b displays the C_{1S} ray spectrum of a PAA radio grafted PVDF track-etched membrane (PVDF-*g*-PAA). The de-convoluted signals show not only the two peaks of PVDF but also an increase of alkyl C_{1S} contribution as well as a COOH peak. This gives evidence of PAA characteristic peaks at 285 eV, 285.8 eV and 289 eV corresponding to CH_2, CH and COOH respectively, allowing an estimation of the PAA coverage onto the track-etched β-PVDF from peak integrations. Only 34% of the total surface at a fluence of 10^7 tracks cm^{-2} was covered by PAA. It (XPS) indicates grafting heterogeneity on the PVDF-*g*-PAA membrane and it gives us supplementary evidence for the specific localisation of grafted PAA inside the tracks, as is clearly seen in the CSLM image in Fig. 2d, and not on the non-irradiated part of the surface of the PVDF-*g*-PAA membranes.

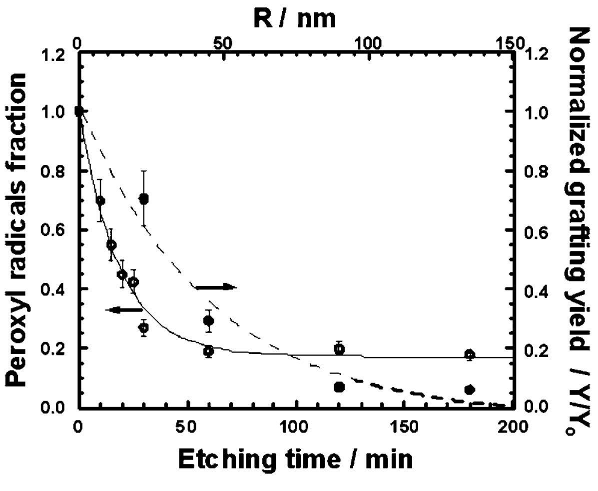

Fig. 3 Decay of peroxyl radical fraction (●) and grafting yield (○) *versus* etching time. The initial grafting yield value was $Y_0 = 8$ wt%. The R scale corresponds to pore radii after an etching time t: $R = 0.8 \times t$.

FESEM and AFM images indicate the change of the pore size and shape after grafting, Fig. 5. For the ungrafted membrane the pore diameter is about 40 nm, Fig. 5a–c, while the diameter of the PAA grafted membrane is about 30 nm, Fig. 5d–f, showing that about 5 nm of PAA is grafted onto the walls of the nanopores.

To transform the functionalized membrane into an electrode, a thin (~36 nm) Au film is sputtered onto each surface to provide a good conductive layer without blocking the pores, Fig. 6 and 7a. From the FESEM micrograph in Fig. 6b it is clearly seen that the pores of the film remain open after sputtering.[42]

Following the Au film sputtering through a mask, Fig. 7a, a 1.5 × 0.6 cm square of membrane is cut out, Fig. 7b and c, and connected to stainless steel wires with silver paste. The contacts are first protected with hot wax and then fingernail polish, Fig. 7d.

A cyclic voltammogram (CV) was performed on a FME in a blank solution (0.1 M sodium acetate, pH 4.5), Fig. 8. In spite of the fact that the gold layer on the β-PVDF membrane is only ~35 nm thick the CV shows the typical profile of a amorphous Au electrode.[43] The CV was performed on the membrane starting at 0.0 V and ramped at a scan rate of 20 mV s^{-1} to +1.2 V where the scan was reversed until the scan was stopped at +0.2 V. The other side of the FME served as the counter electrode. This configuration of the working and the counter electrodes is essentially that of a thin-layer cell.[44]

The reduction peak at 0.62 V in Fig. 8 is the reduction of one monolayer of Au oxide formed at potentials more positive than 0.850 V during the positive scan.[43] Integration of this reduction peak between 0.400 and 0.800 V gives a charge of 75 μC. The charge for the oxidation of a monolayer of gold (111) is 482 μC cm^{-2}.[43] This gives an area of 0.1556 cm^2.

During the immersion of a FME in a sample containing heavy metal ions, the PAA grafted in the membrane complexes some of the metal cations, eqn (1). For example the pK_M of Pb^{2+} in bulk PAA is 4.0 for pHs > 4.0.[45]

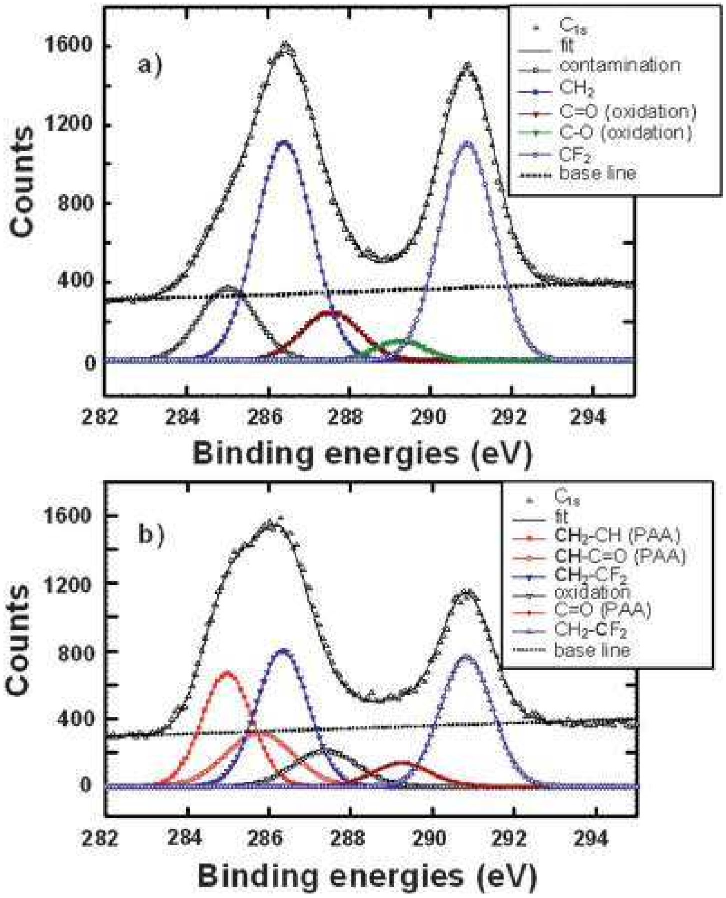

Fig. 4 C_{1S} ray of XPS spectra of (a) track-etched PVDF membrane (fluence 10^7 cm^{-2}) and (b) grafted PAA track-etched PVDF membrane (PVDF-*g*-PAA) (fluence 10^7 cm^{-2}). Etching conditions: 30 min, 65 °C in KOH 10 N and $KMnO_4$ 0.25 N; grafting: AA aqueous solution of 50% at $T = 60$ °C for 1 h.

$$M^{n+} + R\text{–}COO^- \leftrightarrow R\text{–}COO^-M^{n+} \qquad (1)$$

For the electrochemical analysis, the FME is connected to a potentiostat and placed at a negative potential. The negative potential reduces the absorbed metal ions that are very close to the working electrode, from the poly(acrylic acid) in the pores to their metallic state at the Au surface, eqn (2).

$$R\text{–}COO^-M^{n+} + ne^- \rightarrow M(Au) \qquad (2)$$

After the reduction, square wave anodic stripping voltammetry (SW-ASV) analysis is performed in order to oxidize the metal from the working electrode surface and measure the resulting current, eqn (3).

$$M(Au) \rightarrow M^{n+} + ne^- \qquad (3)$$

Fig. 9 shows the SW-ASV analysis of a solution containing 25 ppb of Co^{2+}, 10 ppb of Ni^{2+} and 25 ppb of Pb^{2+} using a frequency of 25 Hz, a step amplitude of 25 mV and a potential increment of 4 mV. Oxidation peaks for Ni and Pb are seen at −0.53 V and −0.05 V respectively. No oxidation peak was observed for Co^{2+} which is more negative than Ni^{2+} and could not be detected in the high background at more negative potentials. This is the subject of ongoing studies, however, the Pb oxidation peak is well defined and we will look at it in greater detail for the remainder of this paper.

The optimisation of the deposition potential, deposition time, and immersion time for Pb^{2+} follows: the deposition potential was determined by immersing a FME in 50 ml of stirred 3 ppb Pb^{2+} sample for 10 minutes followed by SW-ASV. The charge increases with decreasing deposition potential, Fig. 10a. There is a local minimum at −0.9 V. This is likely due to the hydrogen gas bubbles from proton reduction at the FME that could impair Pb^{2+} deposition, eqn (4).

$$2H^+ + 2e^- \rightarrow H_2\,(g) \qquad (4)$$

Also, for potentials more negative than −0.8 V there was a problem with the gold electrode adhesion due to the formation of hydrogen gas bubbles. Therefore, a deposition potential of −0.8 V was used for further studies. The absorption time was determined by immersing a FMS in 50 ml of a 3 ppb Pb^{2+} sample for different times followed by deposition at −0.8 V, Fig. 10b.

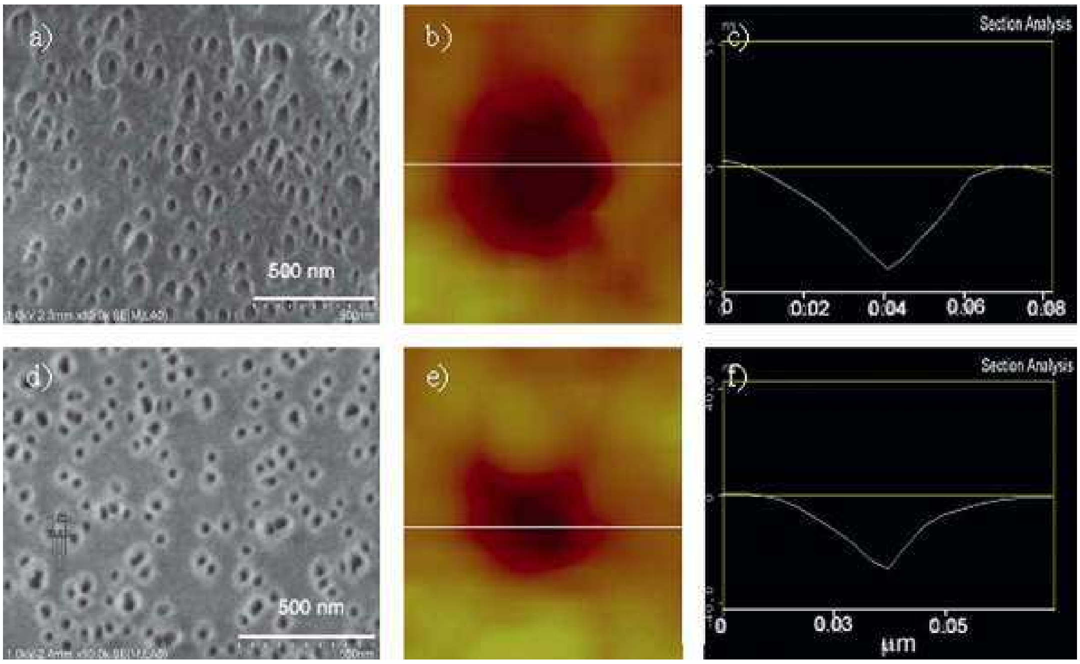

Fig. 5 (a–c) FESEM image, AFM image and AFM line profiles of an ungrafted β-PVDF membrane irradiated with a fluence of 1 × 10^{10} ions per cm^2 and 30 minutes of etching and (d–f) the same membrane after PAA grafting.

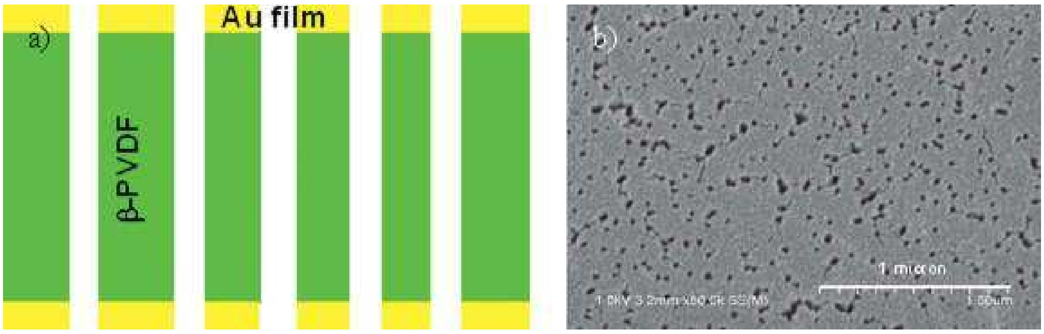

Fig. 6 (a) Scheme of a 9 µm thick functionalized β-PVDF membrane (green) with a 35 nm sputtered gold film (yellow) on each side. (b) FESEM image of a 9 µm thick functionalized β-PVDF membrane with a 35 nm Au film sputtered on the surface.

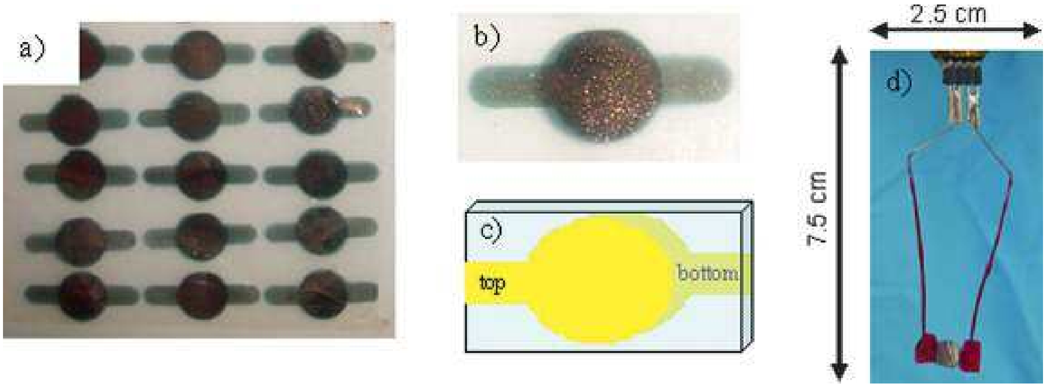

Fig. 7 (a) Image of a 35 nm thick gold layer sputtered on each side of the functionalized β-PVDF membrane through a mask. (b and c) Image and scheme of a metalized membrane cut out from the large surface from image (a). (d) Image of a membrane attached to stainless steel wire leads with silver paste and protected with wax and fingernail polish for connection to a potentiostat.

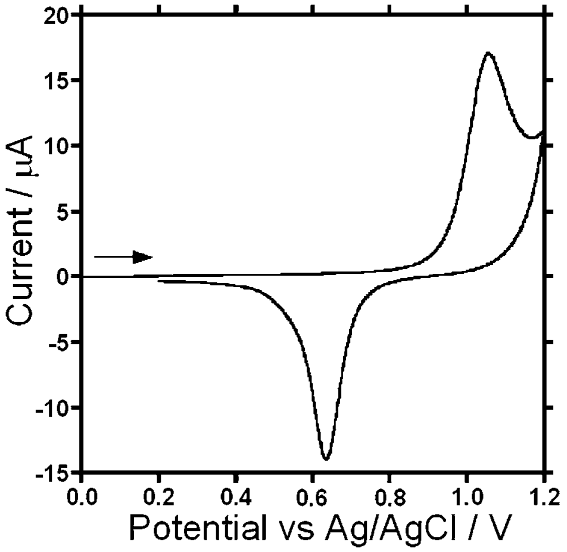

Fig. 8 0.4 cm diameter Au CV in 0.1 M CH_3COONa, pH ≈ 4.5 (scan rate = 20 mV s^{-1}). The arrow indicates the sense of the scan.

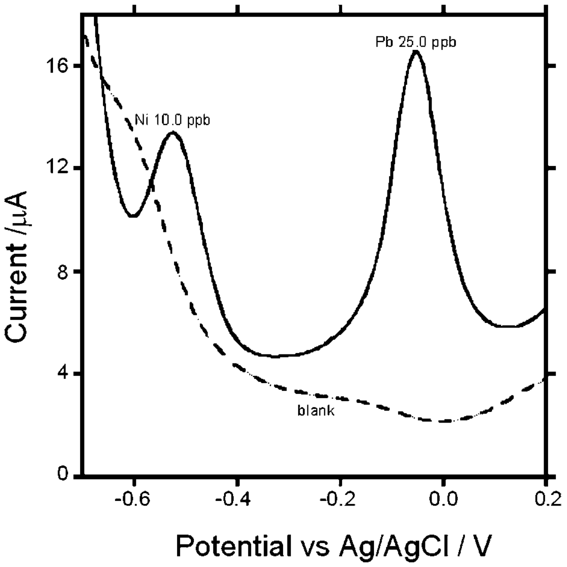

Fig. 9 SW-ASV analysis of FME after immersion in 50 ml of a stirred solution of 25 ppb Co^{2+}, 10 ppb Ni^{2+} and 25 ppb Pb^{2+} for 30 minutes. The curve from a blank analysis is also plotted. The parameters for the SW-ASV analysis were a frequency of 25 Hz, a step amplitude of 25 mV and a potential increment of 4 mV.

After 30 minutes equilibrium is established. Fig. 10c shows the charge *versus* the deposition time. After 100 seconds a plateau is reached so a minimum deposition time of 100 seconds is used for further studies.

Fig. 11 is a plot of superimposed SW-ASV current peaks for different concentrations of Pb^{2+} along with a blank scan. Each curve was obtained using a different FME. At concentrations higher than 3 to 4 ppb current/voltage curves do not increase much in height but become very broad. For this reason the calibration curve was plotted using the peak charge and not the peak current.

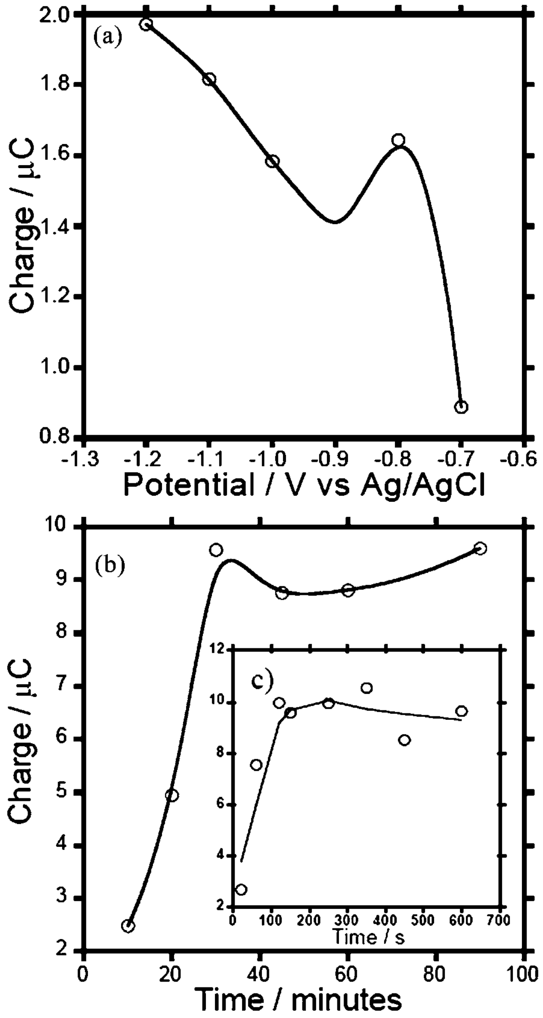

Fig. 10 (a) A plot of oxidation charge from SW-ASV scans of FMEs that were immersed in 50 ml of stirred 3 ppb Pb^{2+} samples for 10 minutes with different deposition potentials. (b) A plot of the charge *versus* immersion time in 50 ml of stirred 3 ppb Pb^{2+} samples using a deposition potential of −0.8 V. (c) A plot of deposition time *versus* charge for a membrane that been immersed in 50 ml of stirred 3 ppb Pb^{2+} samples for 30 minutes with a deposition potential of −0.8 V.

Fig. 11b is a curve of the charges found from Fig. 11a *versus* the concentrations of the solutions measured. Different isotherms were used to fit the curve in Fig. 11b and a Temkin isotherm gave the best fit with a R^2 of 0.98664.[2] The Temkin isotherm indicates that there is a decrease in the heat of adsorptions with increasing lead coverage within the pores.[46] The intercept of the charge *versus* log [Pb^{2+}] plot has a [Pb^{2+}] value of 0.13 ppb. The 3S/N of eight blank scans was 0.05 ppb. Above concentrations of about 4 ppb the current peaks actually decrease until about 12 ppb and the charge increases much more slowly with increasing concentration. At concentrations above 3.6 ppb the measured charge is higher than 10 μC so the pores and the gold near the pores could be saturated with lead and the

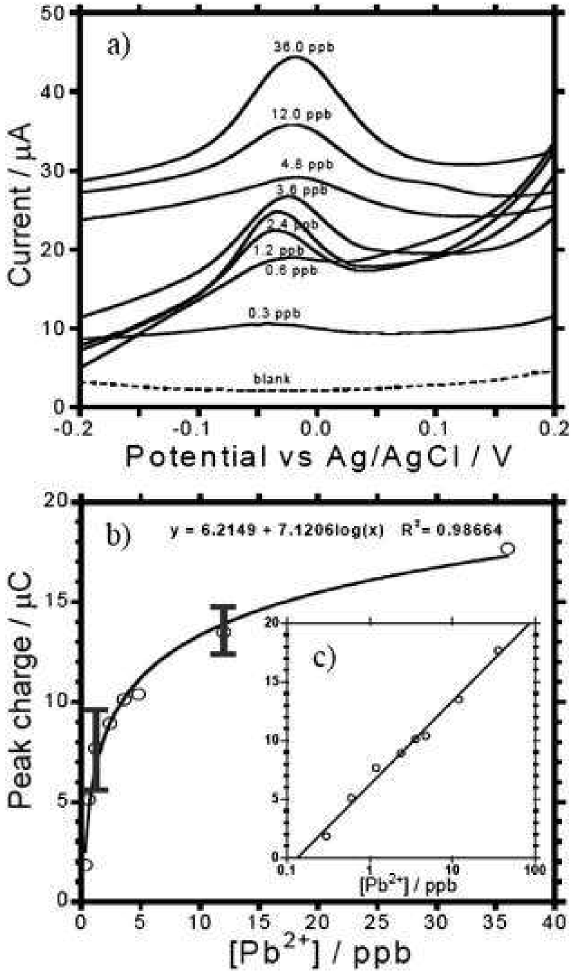

Fig. 11 SW-ASV analysis plots of FMEs after immersion in 50 ml of stirred Pb^{2+} ion solutions for 30 minutes using different concentrations. The curve from a blank analysis is also plotted. (b) A calibration curve for Pb^{2+} ions determined from the peak charges in (a). The error bars for 1 and 12 ppb are also shown. (c) A charge *vs.* log concentration curve.

surface could longer be considered a Au surface. This could also influence the form of the calibration curve.

Preliminary statistical data show that the coefficients of variation for 8 repeated measurements of 1.0 ppb and 12.0 ppb were 40% and 22% respectively. The error intervals are plotted in Fig. 11b. These measurement uncertainties could reflect the variation of the PAA grafting yields which were 10–15%.

Fig. 12 shows the pre-concentration effect of the radio-grafted PAA. The measured SW-ASV charge for PAA grafted membrane is about 3.5 times higher than for the non-grafted pores. The fact that the non-grafted membranes collect the Pb^{2+} ions indicates that the solution is absorbed by capillarity into the 9 micron long nanopores during the adsorption step. The ions are recovered due to the thin-layer electrode configuration of the membrane. Thin-layer electrodes are able to very efficiently recover analytes from solution.[47]

Real waters contain many possible interfering ions. To validate the accuracy of our FME, a SW-ASV measurement was performed using tap water. It showed no indication of Pb^{2+} contamination. When the same tap water sample was spiked with 3 ppb of Pb^{2+}, the recovered charge was 88.5% of the expected charge for 3 ppb. This value is in agreement with the error interval. It shows that there are no significant interference effects.

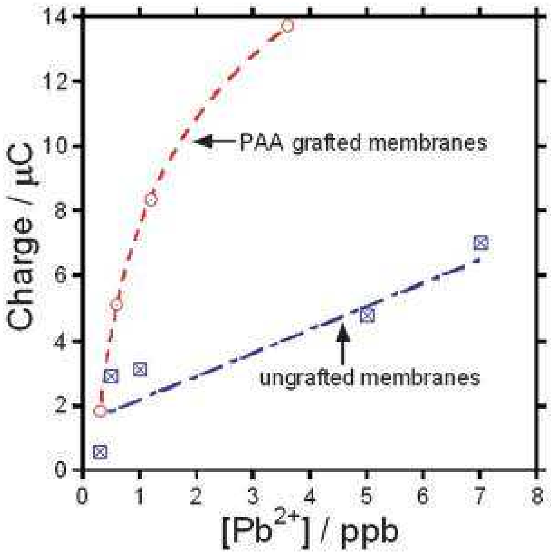

Fig. 12 SW-ASV charge *versus* Pb^{2+} concentration plot for PAA grafted membranes and ungrafted membranes.

Conclusion

We have developed and characterized a new nanoporous thin-layer electrode functionalized with PAA, referred to as a functionalized membrane electrode (FME). The PAA in the electrode can complex and concentrate metal cations from solutions. Using SW-ASV on the FME we were able to detect Ni^{2+} and Pb^{2+} after immersion in a solution containing Co^{2+}, Ni^{2+} and Pb^{2+}. The lack of a signal for Co^{2+} has not been studied but will be addressed in following reports. A very clean reduction peak for Pb^{2+} was seen and the analysis parameters were optimised.

The shape of the calibration curve and the change in the SW-ASV peak shapes for Pb^{2+} follow a Temkin adsorption behaviour. The Temkin isotherm could indicate that there is a decrease in the heat of adsorptions with increasing Pb^{2+} coverage within the PAA coated pores. It means that adsorption is less efficient when Pb^{2+} concentrations increase. However, this effect could also be due to either saturation of the electrode by deposited lead or gold/lead alloy formation.

The FME is sensitive to sub-ppb concentrations of Pb^{2+}. The membrane preparation is done in bulk and is very inexpensive in materials. The most expensive step is the gold sputtering. However, amorphous carbon can also be used. The adsorption is done at open circuit and the SW-ASV analysis is very fast, less than 3 minutes. The ability to preconcentrate the ions at open circuit means that many samples can be collected in parallel and stored for later analysis. We are in the process of functionalizing the β-PVDF membranes with polymers other than PAA to evaluate different ion adsorption efficiencies and selectivities.

Acknowledgements

The research described here has been supported by Triangle de la physique contract 2009-042T and the Department d'Enseignement-Recherche de Physique de l'ECOLE Polytechnique. The authors would also like to acknowledge Dr Emmanuel Balanzat from CIMAP at GANIL for his invaluable assistance for Swift Heavy Ion Irradiation.

References

1 *Guidelines for Drinking-Water Quality*, World Health Organisation, 2008, vol. 1, p. 392.
2 C. M. A. Brett and A. M. O. Brett, *Electrochemistry Principles, Methods, and Applications*, Oxford University Press, Oxford, 1st edn, 2005.
3 J. H. Pei, M. L. Tercier-Waeber and J. Buffle, *Anal. Chem.*, 2000, **72**(1), 161–171.
4 S. Bahrami, S. Abbasi, Y. A. Ghorbani and A. A. Miran-Beigi, *Russ. J. Electrochem.*, 2009, **45**(2), 208–214.
5 E. Fischer and C. M. G. van den Berg, *Anal. Chim. Acta*, 1999, **385**(1–3), 273–280.
6 B. Bas and M. Jakubowska, *Anal. Chim. Acta*, 2008, **615**(1), 39–46.
7 E. A. Hutton, S. B. Hocevar and M. Ogorevc, *Anal. Chim. Acta*, 2005, **537**(1–2), 285–292.
8 S. Laschi, I. Palchetti and M. Mascini, *Sens. Actuators, B*, 2006, **114**(1), 460–465.
9 O. D. Renedo, M. A. Alonso-Lomillo and M. J. A. Martinez, *Talanta*, 2007, **73**(2), 202–219.
10 M. A. G. Rico, M. Olivares-Marin and E. P. Gil, *Talanta*, 2009, **80**(2), 631–635.
11 E. Khaled, H. N. A. Hassan, I. H. I. Habib and R. Metelka, *Int. J. Electrochem. Sci.*, 2010, **5**(2), 158–167.
12 O. D. Renedo and M. J. A. Martinez, *Anal. Chim. Acta*, 2007, **589**(2), 255–260.
13 W. Yantasee, L. A. Deibler, G. E. Fryxell, C. Timchalk and Y. H. Lin, *Electrochem. Commun.*, 2005, **7**(11), 1170–1176.
14 M. Khairy, R. O. Kadara, D. K. Kampouris and C. E. Banks, *Anal. Methods*, 2010, **2**(6), 645–649.
15 R. O. Kadara, N. Jenkinson and C. E. Banks, *Electroanalysis*, 2009, **21**(22), 2410–2414.
16 M. Javanbakht, F. Divsar, A. Badiei, F. Fatollahi, Y. Khaniani, M. R. Ganjali, P. Norouzi, M. Chaloosi and G. M. Ziarani, *Electrochim. Acta*, 2009, **54**(23), 5381–5386.
17 R. Feeney and S. P. Kounaves, *Anal. Chem.*, 2000, **72**(10), 2222–2228.
18 Y. Song and G. M. Swain, *Anal. Chem.*, 2007, **79**(6), 2412–2420.
19 B. K. Jena and C. R. Raj, *Anal. Chem.*, 2008, **80**(13), 4836–4844.
20 X. Dai, O. Nekrassova, M. E. Hyde and R. G. Compton, *Anal. Chem.*, 2004, **76**(19), 5924–5929.
21 E. Majid, S. Hrapovic, Y. L. Liu, K. B. Male and J. H. T. Luong, *Anal. Chem.*, 2006, **78**(3), 762–769.
22 R. I. Stefan-van Staden, S. G. Bairu and J. F. van Staden, *Anal. Methods*, 2010, **2**(6), 650–652.
23 F. Torma, A. Gruen, I. Bitter and K. Toth, *Electroanalysis*, 2009, **21**(17–18), 1961–1969.
24 M. Brand, I. Eshkenazi and E. KirovaEisner, *Anal. Chem.*, 1997, **69**(22), 4660–4664.
25 M. Heitzmann, L. Basaez, F. Brovelli, C. Bucher, D. Limosin, E. Pereira, B. L. Rivas, G. Royal, E. Saint-Aman and J. C. Moutet, *Electroanalysis*, 2005, **17**(21), 1970–1976.
26 L. Baldrianova, I. Svancara, M. Vlcek, A. Economou and S. Sotiropoulos, *Electrochim. Acta*, 2006, **52**(2), 481–490.
27 J. P. Pinheiro and W. Bosker, *Anal. Bioanal. Chem.*, 2004, **380**(7–8), 964–968.
28 N. Betz, A. L. Moel and J.-J. Pireaux, *Nucl. Instrum. Methods Phys. Res., Sect. B*, 2005, **236**, VII–VIII.
29 M. C. Clochard, J. Begue, A. Lafon, D. Caldemaison, C. Bittencourt, J. J. Pireaux and N. Betz, *Polymer*, 2004, **45**(26), 8683–8694.
30 M. C. Clochard, N. Betz, M. Goncalves, C. Bittencourt, J. J. Pireaux, K. Gionnet, G. Deleris and A. Le Moel, *Nucl. Instrum. Methods Phys. Res., Sect. B*, 2005, **236**, 208–215.
31 M. C. Clochard, T. L. Wade, J. E. Wegrowe and E. Balanzat, *Nucl. Instrum. Methods Phys. Res., Sect. B*, 2007, **265**(1), 325–329.
32 O. Cuscito, M. C. Clochard, S. Esnouf, N. Betz and D. Lairez, *Nucl. Instrum. Methods Phys. Res., Sect. B*, 2007, **265**(1), 309–313.
33 M. Grasselli and N. Betz, *Polymer*, 2005, **45**(26), 8683–8694.
34 R. Mazzei, G. G. Bermudez, N. Betz and E. Cabanillas, *Nucl. Instrum. Methods Phys. Res., Sect. B*, 2004, **223**(4), 575–584.
35 C. Aymes-Chodur, N. Betz, M. C. Porte-Durrieu, C. Baquey and A. Le Moel, *Nucl. Instrum. Methods Phys. Res., Sect. B*, 1999, **151**(1–4), 377–385.
36 C. Aymes-Chodur, S. Esnouf and A. Le Moel, *J. Polym. Sci., Part B: Polym. Phys.*, 2001, **39**(13), 1437–1448.
37 E. Balanzat, N. Betz and S. Bouffard, *Nucl. Instrum. Methods Phys. Res., Sect. B*, 1995, **105**(1–4), 46–54.
38 E. Balanzat, S. Bouffard, A. Lemoel and N. Betz, *Nucl. Instrum. Methods Phys. Res., Sect. B*, 1994, **91**(1–4), 140–145.
39 N. Betz, A. Lemoel, E. Balanzat, J. M. Ramillon, J. Lamotte, J. P. Gallas and G. Jaskierowicz, *J. Polym. Sci., Part B: Polym. Phys.*, 1994, **32**(8), 1493–1502.
40 V. Chailley, E. Balanzat and E. Dooryhee, *Nucl. Instrum. Methods Phys. Res., Sect. B*, 1995, **105**(1–4), 110–114.
41 H. Alem, A. S. Duwez, P. Lussis, P. Lipnik, A. M. Jonas and S. Demoustier-Champagne, *J. Membr. Sci.*, 2008, **308**(1–2), 75–86.
42 T. M. McCleskey, D. S. Ehler, J. S. Young, D. R. Pesiri, G. D. Jarvinen and N. N. Sauer, *J. Membr. Sci.*, 2002, **210**(2), 273–278.
43 J. C. Hoogvliet, M. Dijksma, B. Kamp and W. P. van Bennekom, *Anal. Chem.*, 2000, **72**(9), 2016–2021.
44 A. T. Hubbard and F. C. Anson, *Anal. Chem.*, 1966, **38**(1), 58.
45 T. Miyajima, M. Mori and S. Ishiguro, *J. Colloid Interface Sci.*, 1997, **187**(1), 259–266.
46 C. G. Bond, *Catalysis by Metals*, Academic Press Inc., London, 1st edn, 1962, vol. 1, p. 519.
47 J. Zak, M. D. Porter and T. Kuwana, *Anal. Chem.*, 1983, **55**(14), 2219–2222.

2.4.3 Pharm. Res. (2011)

Pharm Res
DOI 10.1007/s11095-011-0398-5

RESEARCH PAPER

"Click" Conjugation of Peptide on the Surface of Polymeric Nanoparticles for Targeting Tumor Angiogenesis

Stéphanie Deshayes • Victor Maurizot • Marie-Claude Clochard • Cécile Baudin • Thomas Berthelot • Stéphane Esnouf • Didier Lairez • Michel Moenner • Gérard Déléris

Received: 1 December 2010 / Accepted: 8 February 2011

ABSTRACT

Purpose Angiogenesis plays a critical role in tumor growth. This phenomena is regulated by numerous mediators such as vascular endothelial growth factor (VEGF). CBO-P11, a cyclo-peptide, has proven to specifically bind to receptors of VEGF and may be used as targeting ligand for tumor angiogenesis. We herein report the design of novel nanoparticles conjugated to CBO-P11 in order to specifically target tumor site.

Methods The conjugation of CBO-P11 on the surface of poly (vinylidene fluoride) (PVDF) nanoparticles was investigated using the copper(I)-catalyzed Huisgen 1,3-dipolar cycloaddition known as "click" reaction. CBO-P11 was modified with a near-infrared cyanine dye bearing an alkyne function, allowing both "click" coupling on azido-modified nanoparticles and fluorescence labelling. Each step of this nanodevice construction was judiciously performed in aqueous solution and successfully characterized. The cytotoxicity of nanoparticles was evaluated in human brain endothelial cell line and their affinity for VEGF receptors was determined *via* fluorescence-based uptake assays on porcine aortic endothelial cell line.

Results Nanoparticles were found to be spherical, dense, monodisperse and stable. No cytotoxicity was observed after four days of incubation, demonstrating the biocompatibility of nanoparticles. Fluorescence highlighted the specific interaction of these functionalized nanoparticles for VEGF receptors, suggesting that the targeting peptide bioactivity was retained.

Conclusions These results demonstrate the potential of these functionalized nanoparticles for targeting tumor angiogenesis and their possible use as multifunctional plateform for cancer treament if coupled with therapeutic agents.

KEY WORDS angiogenesis · "click" chemistry · cyclo-peptide · nanoparticles · PVDF· tumor targeting

ABBREVIATIONS

AA	acrylic acid
ACN	acetonitrile
DCM	dichloromethane
DIEA	diisopropylethylamine
DLS	dynamic light scattering
DMEM	Dulbecco's modified eagle medium
EDC	ethyl-3(3dimethylaminopropyl)carbodiimide
EDTA	ethylenediaminetetraacetic acid
EGM-2	endothelial growth medium
ESI	electrospray ionization
FBS	fetal bovine serum

Electronic supplementary material The online version of this article (doi:10.1007/s11095-011-0398-5) contains supplementary material, which is available to authorized users.

S. Deshayes · V. Maurizot · G. Déléris
CNAB, Chimie Bio-Organique UMR CNRS 5084
Université de Bordeaux 2
33076 Bordeaux, France

S. Deshayes · M.-C. Clochard (✉) · C. Baudin · T. Berthelot
Laboratoire des Solides Irradiés UMR CNRS-CEA 7642
Ecole Polytechnique
28 route de Saclay
91128 Palaiseau, France
e-mail: marie-claude.clochard@polytechnique.edu

S. Esnouf
Laboratoire de Radiolyse, Service de Chimie Moléculaire
UMR CNRS-CEA 3299
91191 Gif-Sur-Yvette, France

D. Lairez
Laboratoire Léon Brillouin UMR CNRS-CEA 12
91191 Gif-Sur-Yvette, France

M. Moenner
Laboratoire des Mécanismes Moléculaires de l'Angiogenèse
INSERM U920 Université de Bordeaux 1
33405 Talence, France

FESEM	field emission scanning electron microscope
FTIR	fourier transform infrared
HCMEC	human brain endothelial cells
HOBt	*N*-hydroxybenzotriazole
HPLC	high-performance liquid chromatography
HUVEC	human umbilical vein endothelial cells
IC_{50}	half-maximal inhibitory concentration
Ip	polydispersity index
MALDI-TOF	matrix-assisted laser desorption/ionization-time of flight
mTEG	modified tetraethyleneglycol
NIR	near-infrared
NMP	*N*-methylpyrrolidone
NMR	nuclear magnetic resonance
PAA	poly(acrylic acid)
PAE	porcine aortic endothelial cells
PBS	phosphate-buffered saline
POA	perfluorooctanoic acid
PVDF	poly(vinylidene fluoride)
Rg	radius of gyration
Rh	hydrodynamic radius
SANS	small-angle neutron scattering
SLS	static light scattering
t-BuOH	*tertio*-butanol
TFA	trifluoroactic acid
THF	tetrahydrofurane
TIS	triisopropylsilane
UV	ultra-violet
VEGF	vascular endothelial growth factor
VEGFR	receptor of VEGF
VF2	vinylidene fluoride
WST-1	4-[3-(4-iodophenyl)-2-(4-nitrophenyl)-2H-5-tetrazolio]-1,3-benzene disulfonate
XPS	X-ray photoelectron spectroscopy

INTRODUCTION

Lack of selectivity in cancer therapies is one of the major limitations of chemotherapies due to their strong side effects. The quest for tumor-specific treatments has led to the development of nanoparticulate drug delivery systems (1). Indeed, polymeric nanoparticles gained considerable attention in recent years because they offer two strategic pathways: passive and active targeting. Passive targeting occurs by passive accumulation of polymeric nanoparticles preferentially in tumor tissues by enhanced permeation and retention effects of malignant vessels compared to healthy vessels (2). On the other hand, nanoparticles which have a high surface area can carry a large number of biological molecules such as ligands that specifically bind to overexpressed receptors in the tumor region; this is named active targeting. Among targeting agents, anti-angiogenic peptides have received intense interest (3). Angiogenesis is the development of new blood vessels from existing ones and plays a critical role in controlling tumor growth and metastasis. Indeed, Folkman hypothesized in 1971 that tumor growth requires the elaboration of vascular network to supply nutrients and oxygen avoiding hypoxia and tumor cell apoptosis (4). Angiogenesis is regulated by a balance of positive and negative mediators. Among them, vascular endothelial growth factor (VEGF) is a key factor in tumor growth; it regulates endothelial cell proliferation, permeability, and survival. VEGF exerts its action *via* binding to two main receptor-type tyrosine kinase: VEGFR-1 (known also as Flt-1) and VEGFR-2 (known also as KDR) (5–7). These receptors are overexpressed on tumor-associated endothelial cells (8–10). Thus, blocking tumor angiogenesis appears to be an attractive target to inhibit specifically tumor growth without damaging normal cells. In our laboratory, we have synthesized a 17-amino acid molecule designated cyclo-peptidic vascular endothelial growth inhibitor (cyclo-VEGI or CBO-P11) encompassing residues 79–93 of VEGF which are involved in the interaction with VEGFR-2 (11). CBO-P11 shows a micromolar affinity for VEGFR-2 and can be used as a tumor targeting agent.

In this paper, we present an elegant strategy for the conjugation of this peptidic ligand on poly(vinylidene fluoride) (PVDF) nanoparticles which could be used as a novel tool for targeting tumor angiogenesis. PVDF was chosen due to its known non-toxicity, biocompatibility, and chemical stability properties (12). Commercially available PVDF devices are in use for medical application. For example, XIENCE V™ utilizes the MULTI-LINK VISION® stent, the antiproliferative drug everolimus, a fluorinated polymer drug carrier, poly(vinylidene fluoride-co-hexafluoropropylene) (PVDF-HFP) and a stent-specific delivery system (13). PVDF is also used for surgical mesh (DynaMesh® for abdominal hernia repair) (14–16). Other applications have been as well reported, such as membranes for osteoblast adhesion (17) or nerve regeneration (18). Although PVDF has been used for biomedical applications, literature lacks reports about the use of PVDF nanoparicles as nanocarrier. PVDF is a hydorphobic polymer, suggesting that it could be coated with a hydrophilic layer to get a core/shell structure and then can be used as drug delivery system. According to an optimized process from a preliminary study (19), nanoparticles were consequently coated with poly(acrylic acid) (PAA), using electron-beam irradiation yielding PVDF-g-PAA nanoparticles.

To achieve the conjugation of CBO-P11 to PVDF-g-PAA nanoparticles without modifying the bioactivity of targeting peptide, we investigated “click” reaction, which has received much attention for preparation of bioconjugated systems due to its high degree of selectivity and stability and its potential use under physiological aqueous conditions (20–22). We have chosen to take advantage of Huisgen 1,3-dipolar cyclo-addition to conjugate alkyne-peptide and azido polymeric nanoparticles (Scheme 1). First, CBO-P11 was coupled with a fluorescent cyanine dye bearing an alkyne function (Scheme 2). Subsequently, carboxylic functions on the surface of PVDF-g-PAA nanoparticles were coupled with an amine-terminated azido spacer arm derived from oligoethylene glycol. This ethylene glycol chain aims to increase the hydrophilicity of nanoparticles and space the future biologically active molecule away from the core of the nanoparticles.

A detailed characterization was performed to assess the morphology of nanoparticles and the grafting location. Furthermore, *in vitro* cytotoxicity and uptake studies were performed on endothelial cells in order to check the biocompatibility of these nanoparticles and the keeping of the peptide affinity for VEGF receptors.

MATERIALS AND METHODS

Materials

The following chemicals were purchased from Sigma-Aldrich (Saint-Quentin Fallavier, France) and used as received: paraffin Wax, potassium persulfate, perfluorooctanoic acid (POA), acrylic acid (AA) stabilized with 200 ppm hydroquinone, propargylamine, piperidine, diisopropylethylamine (DIEA), copper sulfate, sodium ascorbate, trifluoroactic acid (TFA), triisopropylsilane (TIS) and 4-carboxy TEMPO. Vinylidene fluoride (VF2) monomer was provided by Solexis (Yverdon-les-Bains, Switzerland). *N*-hydroxybenzotriazole (HOBt), Ethyl-3(3dimethylaminopropyl)carbodiimide (EDC), phenol and potassium bromide were obtained from Fluka (Saint-Quentin Fallavier, France). The HPLC grade solvents dichloromethane (DCM), tetrahydrofurane (THF) and acetonitrile (ACN) were provided from VWR (Fontenay sous Bois, France). *N*-methylpyrrolidone (NMP) was purchased from Applied Biosystems (Villebon-sur-Yvette, France). *Tertio*-butanol (*t*-BuOH) was purchased from Acros Organics (Geel, Belgium). Fmoc-Lys(Boc)-OH was provided by Novabiochem (Darmstadt, Germany). Thioanisole and ethylenediaminetetraacetic acid (EDTA) were purchased from Alfa Aesar. Endothelial growth medium (EGM-2) Bulletkit was purchased from Cambrex (Walkersville, USA). Human brain endothelial cells (HCMEC) were kindly provided by P.O. Couraud (Institut Cochin, Paris, France) and were grown as previously reported by Weksler *et al.* (23). Porcine aortic endothelial cells stably transfected with VEGFR-2 (PAE) were a gift from Dr. Lena Claesson-Welsh (Ludwig Institute, Uppsala, Sweden). Dulbecco's modified eagle medium (DMEM) was purchased from Invitrogen (Cergy Pontoise, France). 4-[3-(4-iodophenyl)-2-(4-nitrophenyl)-2H-5-tetrazolio]-1,3-benzene disulfonate (WST-1) was provided from Roche Applied Science (Indianapolis, IN, USA).

Synthesis of PVDF Nanoparticles

PVDF nanoparticles were prepared by emulsion polymerization of corresponding monomer (VF2) as previously described (19). Two different syntheses were run in the presence or in the absence of surfactant. Briefly, 3 l of an aqueous solution consisting of paraffin (40 g, 10% in weight of monomer), potassium persulfate initiator (400 mg, 1.5 mmol) and, only for the second synthesis, perfluorooctanoic acid surfactant (10 g, 24 mmol) and potassium hydroxide (1.5 g, 27 mmol) were put in a stirred autoclave under vacuum. The mixture was then heated to 40°C and stirred at 800 rpm. The reactor was fed with VF2 gaseous monomer (400 g, 6.2 mol) to reach desired pressure (100 bars) while the temperature carried on rising up to 80°C.

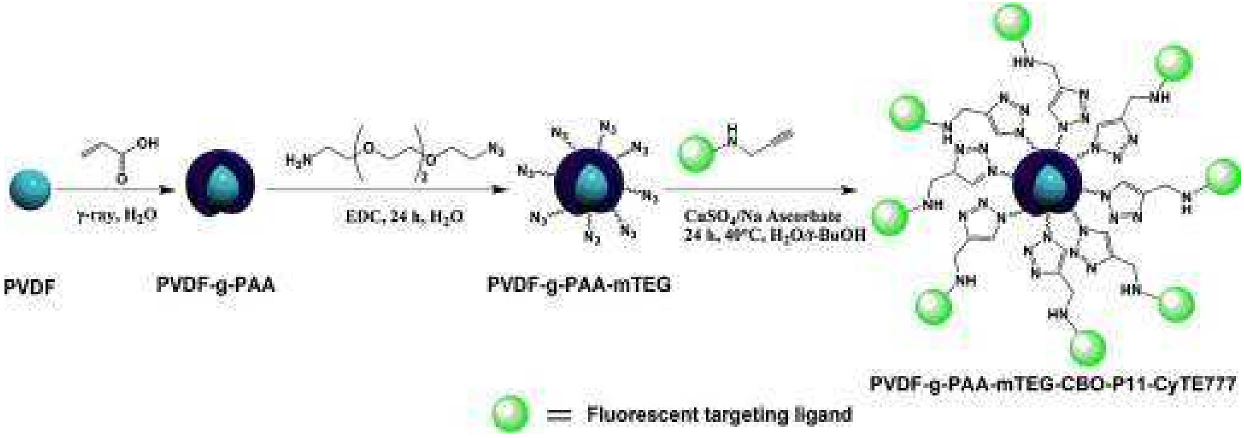

Scheme 1 Functionalization of PVDF nanoparticles. Radio-grafting of PAA, coupling with azido spacer arm (mTEG) and "click" conjugation of fluorescent targeting ligand (CBO-P11-CyTE777).

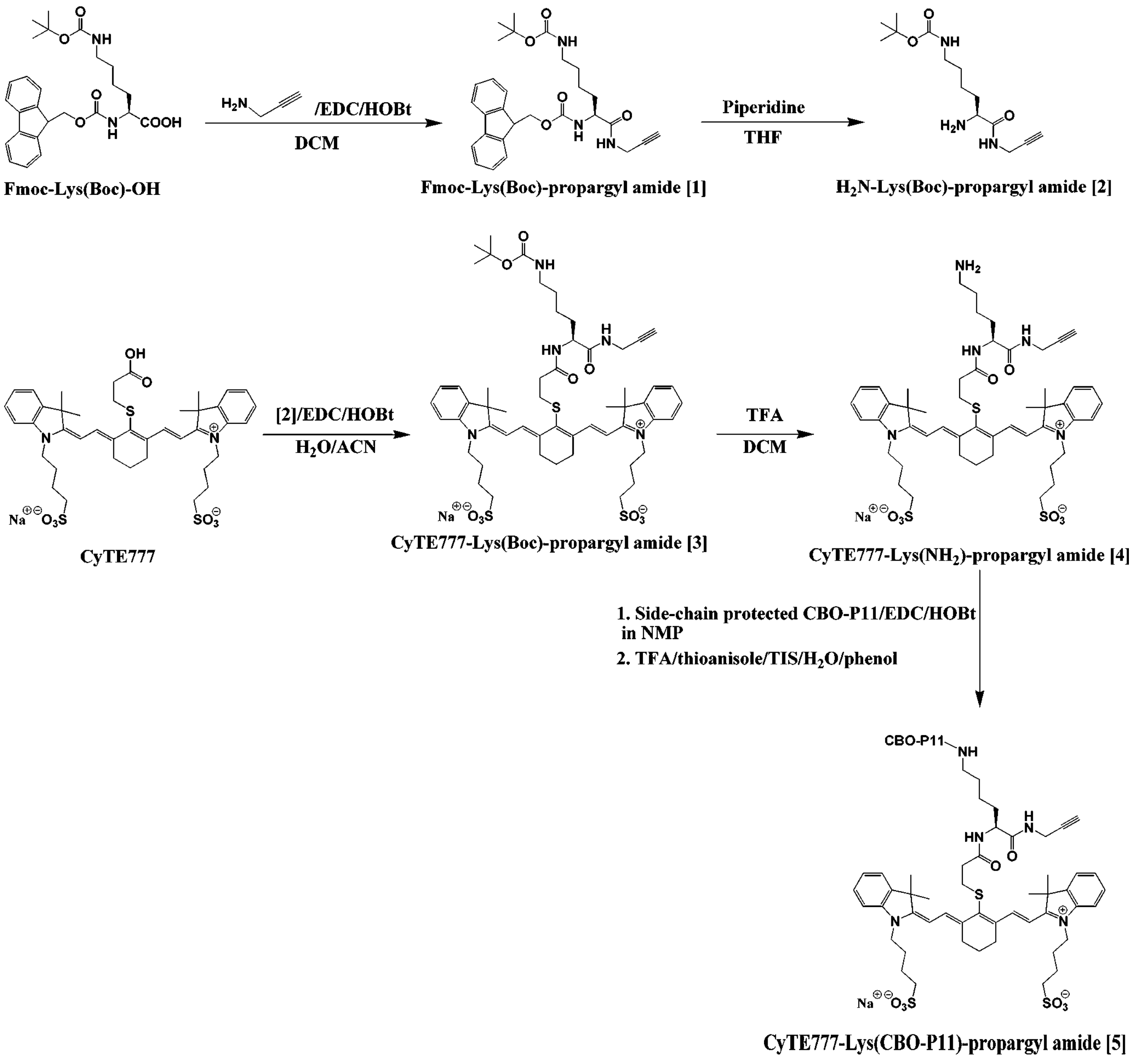

Scheme 2 Synthesis of fluorescent targeting ligand CyTE777-Lys(CBO-P11)-propargyl amide.

When pressure decreased under 80 bars for the first synthesis and 60 bars for the second one, stirring was stopped. After the removal of the supernatant containing paraffin, the latex dispersion made of PVDF nanoparticles in suspension was used without further purification.

In Situ Radiation Grafting of PVDF with Acrylic Acid

PAA grafting onto PVDF nanoparticles was directly achieved upon γ-irradiation of PVDF nanoparticles dispersed (10 mg/ml) in a 2% AA aqueous solution. The irradiation was performed at room temperature under vacuum, using a Gammacell 3000 Elan, MDS Nordion irradiator from a ^{137}Cs source in the 1–10 kGy dose range at 0.33 kGy/h dose rate. Then, the mixture was washed with distilled water by filtration on 0.05μm Millipore membranes to completely remove the homopolymer and the unreacted monomer.

Covalent Coupling of Spacer Arm

The spacer arm noted mTEG was synthesized as described in a previous paper (24). mTEG (10 eq.) was coupled to PVDF-g-PAA nanoparticles (5 mg/ml) *via* an amide bond to the carboxylic acid functions of PAA using EDC (10 eq.) at room temperature for 24 h under mechanical stirring.

Then, the dispersion was purified by dialysis using Spectra/Por membrane (MW: 50,000 Da) for 3 days. The PVDF-g-PAA-mTEG nanoparticles were kept in water to avoid aggregation.

Synthesis of Fmoc-Lys(Boc)-propargyl Amide [1]

To a solution of Fmoc-Lys(Boc)-OH (3.74 g, 8 mmol) in DCM (60 ml), EDC (1.7 ml, 9.6 mmol) and HOBt (1.47 g, 9.6 mmol) were added. The mixture was stirred at room temperature for 30 min. Then, propargylamine (1.1 ml, 16 mmol) was added, and the resulting solution was stirred for 12 h. The crude product dissolved in DCM was washed with 10 ml of 1 M HCl solution. A white precipitate was formed and removed by filtration. The organic phase was washed with water and dried over $\mathrm{MgSO_4}$, and solvent was evaporated under reduced pressure. The solid was rinsed with diethyl ether and dried to give a pale yellow solid (3.56 g, 88%) without further purification. The product was analyzed by reversed-phase HPLC with the following gradient: 30% of eluant B for 5 min and 30%–100% for 10 min; detector: 214 nm, tr=21.8 min and purity=95%. ^{1}H NMR (300 MHz, $\mathrm{CDCl_3}$): $\delta=1.34$–1.55 (m, 4 H, $\mathrm{CH_2C}H_2\mathrm{C}H_2\mathrm{CH_2}$), 1.45 (s, 9 H, $(\mathrm{C}H_3)_3\mathrm{C}$), 1.69 (q, 1 H, $J=7.6$ Hz, $\mathrm{CHC}H_2\mathrm{CH_2}$), 1.86 (q, 1 H, $J=7.6$ Hz, $\mathrm{CHC}H_2\mathrm{CH_2}$), 2.16 (br s, 1 H, $\mathrm{CH_2C{\equiv}C}H$), 3.11 (br s, 2 H, $\mathrm{CH_2C}H_2\mathrm{NH}$), 4.03 (br s, 2 H, $\mathrm{NHC}H_2\mathrm{C{\equiv}CH}$), 4.23 (t, 2 H, $J=5.9$ Hz, $\mathrm{C}H\mathrm{CH_2}$ and $\mathrm{NHC}H\mathrm{CO}$), 4.41 (d, 2 H, $J=5.5$ Hz, $\mathrm{CHC}H_2\mathrm{CO}$), 4.73 (br s, 1 H, $\mathrm{N}H\mathrm{Boc}$), 5.74 (d, 1 H, $J=6.4$ Hz, $\mathrm{N}H\mathrm{Fmoc}$), 6.83 (br s, 1 H, $\mathrm{CON}H\mathrm{CH_2}$), 7.31 (t, 2 H, $J=7.3$ Hz, $\mathrm{CH_{Ar}}$), 7.41 (t, 2 H, $J=7.0$ Hz, $\mathrm{CH_{Ar}}$), 7.59 (t, 2 H, $J=6.7$ Hz, $\mathrm{CH_{Ar}}$) and 7.77 (t, 2 H, $J=7.1$ Hz, $\mathrm{CH_{Ar}}$). ^{13}C NMR (75.5 MHz, $\mathrm{CDCl_3}$): $\delta=22.5$ ($\mathrm{CH_2}C\mathrm{H_2C}H_2$), 28.5 ($(C\mathrm{H_3})_3\mathrm{C}$), 29.2 ($\mathrm{CH_2}C\mathrm{H_2C}H_2$), 29.6 ($\mathrm{NH}C\mathrm{H_2C{\equiv}CH}$), 32.01 ($\mathrm{CH}C\mathrm{H_2CH_2}$), 47.2 ($\mathrm{CH_2}C\mathrm{H_2NH}$), 53.5 ($C\mathrm{HCH_2}$), 54.7 ($\mathrm{NH}C\mathrm{HCO}$), 67.2 ($\mathrm{CH}C\mathrm{H_2CO}$), 71.9 ($\mathrm{CH_2C{\equiv}}C\mathrm{H}$), 75.5 ($\mathrm{CH_2}C\mathrm{{\equiv}CH}$), 79.2 ($(\mathrm{CH_3})_3C$), 120.1 (2 $C\mathrm{H_{Ar}}$), 125.2 (2 $C\mathrm{H_{Ar}}$), 127.1 (2 $C\mathrm{H_{Ar}}$), 127.8 (2 $C\mathrm{H_{Ar}}$), 141.4 (2 C_{Ar}), 143.8 (2 C_{Ar}), 156.5 (COBoc and COFmoc) and 171.7 (NHCO). Mass analysis (MALDI-TOF): m/z 528.1900 (calcd for $\mathrm{C_{29}H_{35}N_3O_5Na}$ [M$^+$] m/z 528.5951).

Synthesis of $\mathrm{H_2N}$-Lys(Boc)-propargyl Amide [2]

Fmoc-Lys(Boc)-propargyl amide (450 mg, 0.89 mmol) was dissolved in 3% piperidine in THF (30 ml). After the mixture was stirred for 5 h at room temperature, solvent was removed under reduced pressure, and the residue was coevaporated three times with toluene. Petroleum ether (10 ml) was added to the crude product, and the supernatant containing the dibenzofulvene-piperidine adduct was removed. The residue was dried under vacuum and was used as is without further purification. Mass analysis (ESI): m/z 284.1968 (calcd for $\mathrm{C_{14}H_{26}N_3O_3}$ [M$^+$] m/z 284.3666).

Synthesis of CyTE777-Lys(Boc)-propargyl Amide [3]

The CyTE777 NIR dye was synthesized as previously reported by Hilderbrand *et al.* (25). To a solution of CyTE777 (180 mg, 0.22 mmol) in a mixture $\mathrm{H_2O}$/ACN (1/1) (30 ml), EDC (47 μl, 0.26 mmol) and HOBt (40 mg, 0.26 mmol) were added. The mixture was stirred at room temperature for 30 min. Then, $\mathrm{H_2N}$-Lys(Boc)-propargyl amide (156 mg, 550 μmol) was added, and the resulting solution was stirred for 5 h. The solvent was removed under reduced pressure, and the residue was used as is without further purification. Mass analysis (ESI): m/z 1084.4526 (calcd for $\mathrm{C_{55}H_{75}N_5O_{10}S_3Na}$ [M$^+$] m/z 1084.4568).

Synthesis of CyTE777-Lys($\mathrm{NH_2}$)-propargyl Amide [4]

CyTE777-Lys(Boc)-propargyl amide (174 mg, 0.16 mmol) was dissolved in a mixture of DCM/TFA (1/1) (6 ml). After the mixture was stirred for 2 h 30 at room temperature, DCM was evaporated under reduced pression. Then, water was added, and the mixture was freeze-dried. The product was purified by preparative HPLC with the following gradient: 0% B for 5 min, increase up to 20% B in 5 min, 20% B for 10 min, increase up to 100% B in 10 min and 100% B for 10 min, $\lambda_{\max}$ of detector: 740 nm, tr= 33.5 min. ACN was evaporated and the aqueous solution was freeze-dried to give a green solid (83 mg, 53%). UV-visible ($\mathrm{H_2O}$): $\lambda_{\max}=782$ nm (49,000 $\mathrm{M^{-1}cm^{-1}}$). ^{1}H NMR (300 MHz, $\mathrm{CD_3OD}$): $\delta=1.28$–1.49 (m, 2 H), 1.56–1.71 (m, 4 H), 1.77 (s, 12 H), 1.86–2.12 (m, 10 H), 2.53 (t, 1 H, $J=2.6$ Hz), 2.55–2.63 (m, 2 H), 2.65–2.80 (m, 2 H), 2.89 (tt, 8 H, $J=7.2$ Hz), 3.08 (t, 2 H, $J=7.0$ Hz), 3.91 (t, 2 H, $J=2.7$ Hz), 4.23 (t, 4 H, $J=7.3$ Hz), 4.88–4.93 (m, 1 H), 6.35 (br s, 2 H), 7.19–7.56 (m, 8 H), 8.90 (br s, 2 H). Mass analysis (ESI): m/z 984.4044 (calcd for $\mathrm{C_{50}H_{67}N_5O_8S_3Na}$ [M$^+$] m/z 984.4088).

Synthesis of CyTE777-Lys(CBO-P11)-propargyl Amide [5]

CBO-P11, cyclo(*D*FPQIMRIKPHQGQHIGE) peptide with protected side chains was synthesized by Fmoc/*t*-butyl batch solid phase synthesis on an Applied Biosystems 433A automated peptide synthesizer as previously described by Zilberberg *et al.* (11). To a solution of side-chain protected CBO-P11 (371 mg, 0.10 mmol) in NMP (4 ml), EDC (47 μl, 0.26 mmol), HOBt (42 mg, 0.26 mmol) and DIEA (66 μl, 0.39 mmol) were added. The mixture was stirred at room temperature for 30 min. Then, CyTE777-Lys($\mathrm{NH_2}$)-propargyl amide (78 mg, 80 μmol) was added, and the resulting solution was stirred for 24 h. After addition of water (20 ml), a precipitate was formed, removed by filtration and dried under vacuum. Then, side-chain peptide protections were removed with a solution of TFA/phenol/water/thioanisole/TIS (10/0.75/0.5/0.5/0.25 v/w/v/v/v). Ten ml of this solution were added to 368 mg of product. The mixture was stirred for 3 h at room temperature. After addition of diethyl ether (30 ml), a white precipitate was formed, removed by filtration and dried under vacuum to give a green solid (283 mg, 92%). The product was analyzed by reversed-phase HPLC with the following gradient: 30% of eluant B for 5 min, 30%–50% for 5 min, 50% for 10 min, 50%–100% for 5 min and 100% for 5 min; detector: 785 nm, tr=26.5 min and purity =90%. UV-visible (H_2O): $\lambda_{max}=787$ nm (56,000 $M^{-1}cm^{-1}$). Mass analysis (MALDI-TOF): *m/z* 2943.10 (calcd for $C_{140}H_{205}N_{33}O_{29}S_4$ [M^+] *m/z* 2942.58).

Conjugation of CyTE777-Lys(CBO-P11)-propargyl Amide to Azido-nanoparticles by "Click" Chemistry

An excess of [5] (2 eq.) was added to a solution of PVDF-g-PAA-mTEG (nanoparticles irradiated at 5 kGy) using copper sulfate (0.5 mM) and sodium ascorbate (1 mM) at 40°C for 24 h in a mixture of H_2O/*t*-BuOH (1/1) (16 ml). Nanoparticles were washed with a 1 mM EDTA solution in order to remove copper catalyst by filtration on 0.05 μm Millipore membranes. Then, nanoparticles were dialyzed using Spectra/Por membrane (MW: 50,000 Da) for 3 days against water to obtain a 1.4 mg/ml PVDF-g-PAA-mTEG-CBO-P11-CyTE777 nanoparticles aqueous suspension. In order to obtain a control sample without targeting peptide, PVDF-g-PAA-mTEG-CyTE777 nanoparticles were synthesized in a similar way using the fluorescent dye [4].

Cytotoxicty Assays

HCMEC were grown on a 0.2% gelatine matrix in EGM-2 at 37°C, 5% CO_2 up to confluence. After trypsinization, cells were washed with DMEM containing 10% FBS by centrifugation (800 rpm for 5 min). One hundred microliters of the cell suspension containing 7.5×10^3 cells were inoculated into each well of 96-well plates, and cells were allowed to settle for one night. Nanoparticles (PVDF, PVDF-g-PAA, PVDF-g-PAA-mTEG and PVDF-g-PAA-mTEG-CBO-P11-CyTE777) were then added at different concentrations (0, 0.1, 0.3, 1.1, 3.3, 11, 33 and 100 μg/ml) to each well. After 2, 3 or 4 days incubation with nanoparticles (except for PVDF-g-PAA-mTEG-CBO-P11-CyTE777, incubation for only 3 days), 5 μl of WST-1 was added to cell medium, and absorbance was determined after 2 h at 440 nm using an ELISA microplate reader (Molecular Devices Corporation). Results were analyzed using the Softmax Pro 4.0 software (Molecular Devices Corporation). The assay was performed in triplicates. Cells were counted using a cell counter (Coulter, Becton Dickinson).

Cell Uptake Assays

Cell uptake experiments were performed using a porcine aortic endothelial (PAE) cell line modified to overexpress VEGFR-2. PAE cells were inoculated into 96-well plates and grown up to confluency on a 0.2% gelatine matrix in EGM-2 at 37°C, 5% CO_2. They were then washed with DMEM and incubated for 45 min at 37°C in the same basal medium. Cells were then cultured in incomplete EGM-2 medium in the presence or absence of 100 ng/ml VEGF for 45 min at 37°C. Nanoparticles (PVDF-g-PAA-mTEG-CyTE777 and PVDF-g-PAA-mTEG-CBO-P11-CyTE777) were added at different fluorophore concentrations (1.4 μM; 466 nM; 155 nM; 52 nM; 17.3 nM; 5.8 nM; 1.9 nM; 640 pM). After a 12-h incubation at 37°C in the presence of nanoparticles, PAE cells were washed three times with PBS, and 96-well plates were analyzed using the Odyssey scanner.

RESULTS AND DISCUSSION

Synthesis and Characterization of PVDF Nanoparticles

Radical polymerization in aqueous emulsion was used to produce PVDF nanoparticles according to a previously described procedure (19). In order to assess the influence of surfactant on the size of these particles, two different batches of PVDF nanoparticles were prepared in the presence or in the absence of perfluorooctanoic acid (POA). Perfluorinated surfactants present a better active surface due to their high acid strength compared to hydrocarbon surfactants and promote micellization at lower concentration (26). The size, morphology and stability of nanoparticles were determined by field emission scanning electron microscopy (FESEM), static light scattering (SLS), dynamic light scattering (DLS) and small-angle neutron scattering (SANS). Table I summarizes data observed by these different techniques. In the absence of POA, the particles were two-fold larger than in the presence of POA. Surfactant stabilized the emulsion and contributed to minimize the size of the nanoparticles. The ratio between the radius of gyration and the hydrodynamic radius (R_g/R_h), which is a characteristic of nanoparticles morphology, was found equal to 0.722 for the synthesis without POA and 0.777 for the synthesis with POA, indicating that the nanoparticles were in both cases dense spheres (theoretically 0.775). Polydispersity index (I_p) of

Table I Gyration and Hydrodynamic Radii (R_g and R_h), Polydispersity Index (I_p) and Zeta Potential (ζ) of PVDF Nanoparticles Synthesized with or Without Surfactant (POA), PVDF-g-PAA, PVDF-g-PAA-mTEG and PVDF-g-PAA-mTEG-CBO-P11-CyTE777 Nanoparticles Determined by FESEM, SLS, SANS and/or DLS

	FESEM	SLS	SANS	DLS		
	R (nm)	R_g (nm)	R (nm)	R_h (nm)	I_p[c]	ζ (mV)
PVDF[a]	110 ± 5	86 ± 4	ND	102 ± 5	0.070 ± 0.008	−43.9 ± 0.3
PVDF[b]	55 ± 5	49 ± 3	61 ± 1	59 ± 4	0.002 ± 0.003	−42.7 ± 0.2
PVDF-g-PAA	58 ± 5	ND	63 ± 5	103 ± 5	0.228 ± 0.041	−57.3 ± 0.2
PVDF-g-PAA-mTEG	58 ± 5	ND	ND	103 ± 5	0.130 ± 0.024	−49.9 ± 0.7
PVDF-g-PAA-mTEG-CBO-P11-CyTE777	60 ± 5	ND	ND	135 ± 9	0.134 ± 0.031	−12.3 ± 4.6

[a] Synthesis without POA; [b] Synthesis with POA; [c] I_p given by Zetasizer (as I_p tends to 0, monodispersity is high); *ND* no determined

particles was calculated by DLS as a measurement of the distribution of size to appreciate the homogeneity of the sample. The very low I_p values indicated that PVDF nanoparticles were monodisperse for both syntheses. In addition, the zeta potential values found by DLS were around −40 mV and indicated stable dispersions in water. In theory, high zeta potential values, being positive or negative, tend to stabilize particle suspension. The electrostatic repulsion between particles with the same electric charge prevents the aggregation of the spheres (27). The negative values of zeta potential (presence or absence of POA) come from initiator sulfonate groups and polymer surface charges. Indeed, PVDF is a dielectric polymer, and electrons are trapped at its surface.

In Situ Radio-Grafting of Poly(Acrylic Acid) (PAA)

Introducing negatively charged hydrophilic groups onto hydrophobic PVDF polymer is necessary to confer biological hemocompatibility to nanoparticles. These functional groups could also be used for the anchoring of biological molecules by covalent binding (28). Acrylic acid (AA) was chosen as the monomer to obtain grafted PVDF-g-PAA polymer, as its radical polymerization is easy to control. Pending carboxylic acid functions could allow subsequent coupling. The lack of reactive functions in PVDF makes the functionalization difficult with usual chemical reactions. Thus, irradiation was used to create free radicals on the surface of the solid and initiate the polymerization of monomer leading to the formation of a grafted polymer. Radiation initiation is one of the cleanest grafting methods available, since molecular initiator or catalysts are not required. In a previous work, we reported the grafting of AA on PVDF nanoparticles after their irradiation (*post*-radio-grafting) (19). However, electron paramagnetic resonance and differential scanning calorimetry studies showed a relative instability of radicals initiated under irradiation in comparison with PVDF films, decreasing the radical amount available for *post*-polymerization of AA. In order to circumvent this problem, PVDF-g-PAA nanoparticles were directly prepared by irradiation of PVDF nanoparticle suspensions *in situ* in a monomer solution. Additionally, this *in situ* method allowed us to keep nanoparticles in suspension, preventing aggregation. Moreover, AA monomers act as radiation protectors and reduce the risk of degradation of the polymer substrate by the radiation itself (29).

In agreement with previous studies (19,30,31), the FTIR spectrum of PVDF-g-PAA (Fig. 1) shows a characteristic absorption band at 1,726 cm^{-1} attributed to the C=O stretching vibration of the carboxylic acid of PAA. The PVDF CH_2 stretching vibrations give absorption bands at

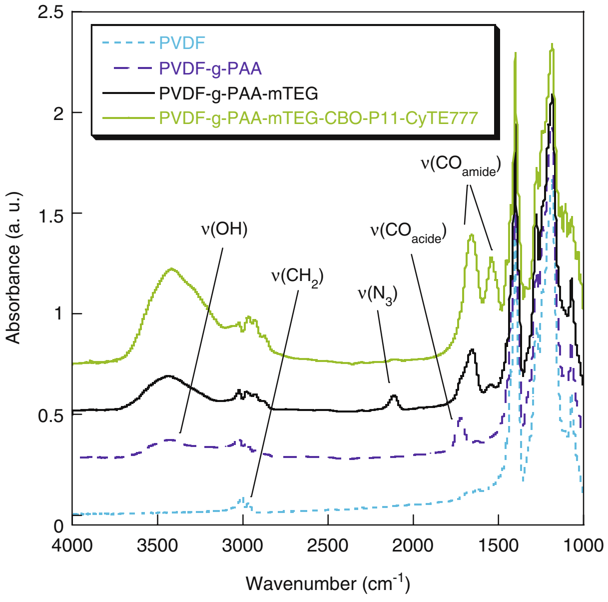

Fig. 1 FTIR transmission spectra of PVDF, PVDF-g-PAA, PVDF-g-PAA-mTEG and PVDF-g-PAA-mTEG-CBO-P11-CyTE777 nanoparticles. PVDF nanoparticles were irradiated at 5 kGy.

3,022 and 2,979 cm^{-1} which are superimposed with the OH vibrations of PAA band in the 2,500–3,500 cm^{-1} region. To estimate the grafting yields by FTIR, a calibration curve was performed by integration of the C=O stretching band from known amounts of a PAA standard in the KBr pellets (see Figure S1 in Electronic Supplementary Material). The yields of PAA grafting increase gradually with irradiation dose in agreement with the evolution of radical concentration (data not shown). Overall grafting yields are low (<7% w/w), and we assume that grafting occurred mainly onto the nanoparticles surface and not in the nanoparticles bulk. Indeed, radiation grafting to polymeric nanoparticles proceeds from the substrate surface, and as the nanoparticles swell, it progressively enters into substrate bulk. This mechanism known as the grafting front mechanism was first described in Chapiro's pioneer work in the early 1960s (32). To check this hypothesis, PVDF-g-PAA nanoparticles were analyzed by a surface technique named X-ray photoelectron spectroscopy (XPS) (see Figure S2 in Electronic Supplementary Material). First, survey spectra confirmed the PAA grafting with the presence of O_{1S} ray at 533 eV. Furthermore, ratios of deconvoluted C_{1S} peaks allowed a grafting yield estimation of 11 mol% over the 8 nm probed thickness. As the grafting yield of the whole nanoparticles was found equal to 2 mol% by FTIR, it consequently suggests an enrichment of PAA at the surface of nanoparticles.

The influence of PAA grafting on the nanoparticles dispersion was investigated by SANS. Scattering intensity per unit volume and total concentration unit of both PVDF and PVDF-g-PAA nanoparticles at different irradiation doses are shown in Fig. 2 (data treatment are shown in Electronic Supplementary Material). At high q, the shape of the spectra was similar, indicating that radiografting did not induce any significant change of the size and shape of nanoparticles. They remained spherical after irradiation in spite of the presence of PAA. Indeed, the grafting yields being low, they have a negligible effect on the nanoparticles morphology. On the opposite at low q, the scattered intensity decreased with the irradiation dose. An increase in repulsive interactions due to the charges of the increasing number of dissociated carboxylic functions is clearly indicated. These repulsive interactions were coroborated by higher negative zeta potential relative to PVDF nanoparticles (Table I), which favours colloidal stability, a very important property for a long blood circulation time.

Coupling of Spacer Arm (mTEG)

To increase the hydrophilicity of the polymer, to allow the coupling of the targeting peptide and improve its accessibility in the future biological environment, a spacer arm was coupled to carboxylic acid functions of PVDF-g-PAA nanoparticles. As a model, a short ethylene glycol was first chosen as spacer. A modified tetraethylene glycol (noted mTEG) with an amine function at one end and an azide function at the other end was prepared (24). The amine function was coupled to the carboxylic acid functions of PAA *via* an amide bond, using a water-soluble carbodiimide (EDC) as coupling agent (Scheme 1). FTIR spectrum of PVDF-g-PAA-mTEG nanoparticles (Fig. 1) shows specific amide bond absorptions (1,643 and 1,572 cm^{-1}), NH amide (3,700–3,130 cm^{-1}), CH_2 ether (2,950–2,840 cm^{-1}), azide stretching vibrations (2,112 cm^{-1}) and decrease of the COOH absorption band, in agreement with the covalent coupling of the amino spacer arm. Furthermore, when PVDF-g-PAA-mTEG nanoparticles were analyzed by XPS (see Figure S3 in Electronic Supplementary Material), a new peak corresponding to N_{1S} of azide and/or amide functions was observed, and the deconvoluted C_{1S} ray signal showed the contribution of both ether and amide functions. These results confirm that the spacer arm was grafted to nanoparticles and not simply adsorbed. The coupling of spacer arm did not modify the size of nanoparticles as shown by FESEM and DLS data in Table I. Furthermore, zeta potential was maintained negative and confers a high stability to the nanoparticle suspensions.

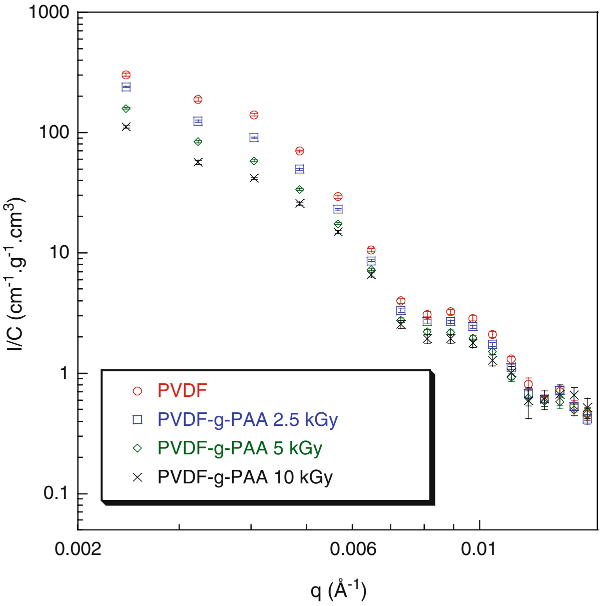

Fig. 2 SANS spectra of PVDF nanoparticles before irradiation and PVDF-g-PAA nanoparticles at different irradiation doses. The spectra were normalized to the concentration of nanoparticles in D_2O.

Synthesis of Fluorescent Alkyne-modified Peptide and "Click" Coupling on Azido Nanoparticles

CBO-P11, a 17-amino acid cyclo-peptide encompassing residues 79–93 of VEGF, was synthesized as previously

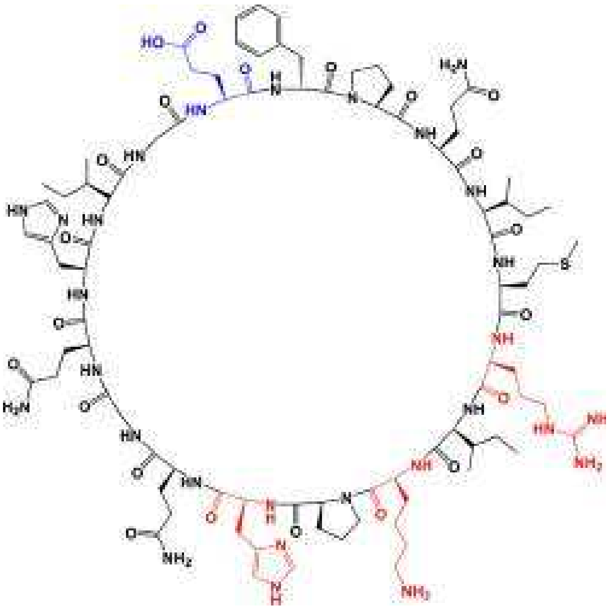

Fig. 3 Chemical structure of CBO-P11. The three basic amino acids essential for the interaction with VEGF receptors are in red. Amino acid which allowed the peptide functionalization is in blue.

described (Fig. 3) (11). CBO-P11 was shown to bind to VEGFR-2 and inhibit VEGF binding with a half-maximal inhibitory concentration (IC_{50}) of 1.3μM. This high affinity makes CBO-P11 a suitable candidate for targeted anti-angiogenic therapy.

The anchoring of CBO-P11 on polymeric nanoparticles required a method allowing to keep the integrity of essential basic amino-acids. The copper(I)-catalyzed Huisgen 1,3-dipolar cycloaddition, named "click" chemistry, has proven to be an easy path to covalently couple azides and acetylenes (33–35). To apply this reaction on the azido nanoparticles, CBO-P11 has been modified with a pendant alkyne moiety. This acetylene was introduced between a fluorescent cyanine dye (CyTE777) (25) and CBO-P11 using lysine as intermediate. The peptide was labelled with a cyanine to detect and locate nanoparticles. Cyanines belong to the family of near infrared (NIR) probes with emissions above 700 nm. The use of NIR dyes shows relevant advantages, such as minimal interfering absorption, inexpensive laser diode excitation, reduced scattering and enhanced tissue penetration depth (36). Thus, Fmoc-Lys(Boc)-OH was modified with an alkyne function from propargylamine *via* EDC-mediated amide coupling. Then, after a consecutive protecting group removal and amide coupling, we obtained CyTE777-Lys(CBO-P11)-propargyl amide (Scheme 2).

Then, the fluorescent alkyne-modified peptide [5] was conjugated to azido-functionalized PVDF-g-PAA-mTEG nanoparticles in a H_2O/t-BuOH solvent system (Scheme 1). The opportunity to perform "click" reaction in aqueous media allowed us to keep nanoparticles in their mother solution and limit the risk of aggregation. Additionally, it avoids the use of toxic solvents, which is crucial for biological applications. After reaction and purification, the fluorescent peptide content was estimated by UV spectroscopy and found equal to 4.3 mol%. FTIR spectra show a decrease of azide band at 2,112 cm^{-1} and an increase of amide bands after reaction (Fig. 1), in agreement with a covalent coupling. Fluorescence spectra (Fig. 4A) show an absorption maximum $\lambda_{exc}=785$ nm and an emission maximum $\lambda_{em}=843$ nm for PVDF-g-PAA-mTEG-CBO-P11-CyTE777 nanoparticles.

Fig. 4 (**A**) Normalized excitation and emission spectra of 2.0μM aqueous solutions of PVDF-g-PAA-mTEG-CBO-P11-CyTE777 nanoparticles. (**B**) Visible images of PVDF nanoparticles (*left top*) and PVDF-g-PAA-mTEG-CBO-P11-CyTE777 nanoparticles (*right bottom*). Fluorescence images of PVDF nanoparticles (*left top*) and PVDF-g-PAA-mTEG-CBO-P11-CyT777 nanoparticles (*right bottom*) recorded in water (1.7 g/ml, i.e. 60μM of CyTE777) by Odyssey at 800 nm.

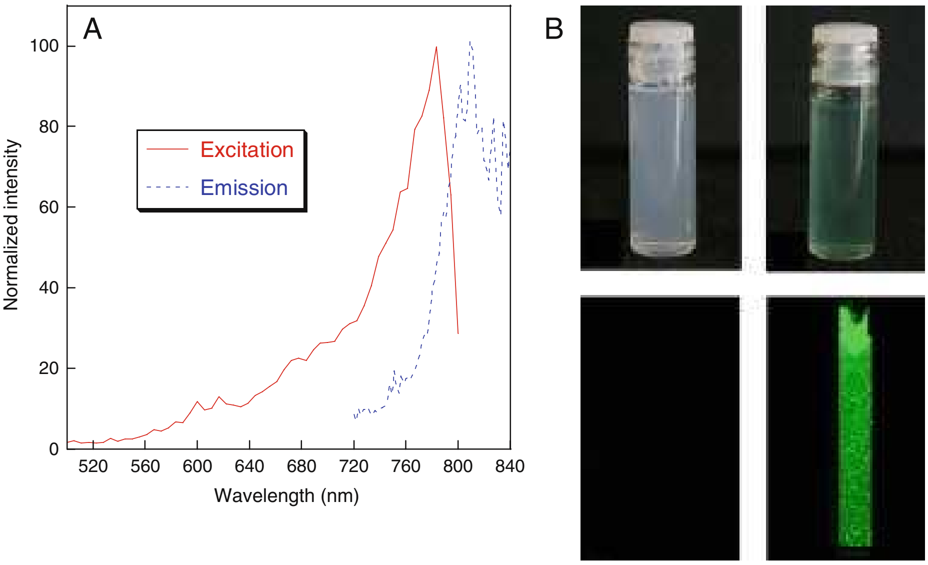

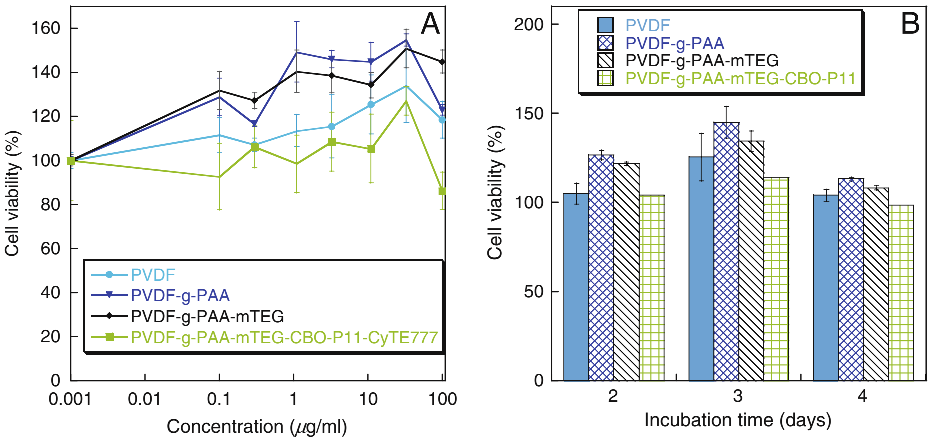

Fig. 5 Cytotoxicity profiles for HCMEC. (**A**) Effect of the nanoparticles on cell viability after a three-day incubation with either PVDF, PVDF-g-PAA, PVDF-g-PAA-mTEG or PVDF-g-PAA-mTEG-CBO-P11-CyTE777. (**B**) Cell viability in time after incubation with 11 µg/ml of nanoparticles.

To demonstrate the potential use of these devices for imaging, fluorescence images of PVDF and PVDF-g-PAA-mTEG-CBO-P11-CyTE777 nanoparticles in water suspension were recorded using a fluorescence scanner (Odyssey) commonly available in biological laboratories (Fig. 4B). The image for labelled nanoparticles (PVDF-g-PAA-mTEG-CBO-P11-CyTE777) shows very bright green color, whereas the image remains dark when nanoparticles are not labelled with fluorescent probe. Nanoparticles did not quench the fluorescence of cyanine after conjugation. The high fluorescence intensity suggests a great potential for an application in medical imaging.

Cytotoxicity Assays

To assess the biocompatibility of functionalized nanoparticles, human brain endothelial cells (HCMEC) were exposed to nanoparticles at different concentrations for 2, 3 or 4 days. Cell viability was then checked by measuring the absorbance of WST-1 reagent on an ELISA plate reader (Fig. 5). WST-1, a modified tetrazolium salt, is reduced to water-soluble formazan in the mitochondria of living cells. This reduction only takes place when mitochondrial reductase enzymes are active, and therefore conversion can be directly related to cell viability (37). Data revealed the absence of toxicity of the nanoparticles, whatever the concentration used, after four days of incubation. Unexpectedly, we observed an increase in WST-1 signal under high concentrations of nanoparticles, suggesting a slight metabolic effect of these compounds on cells. Similar results were obtained using other endothelial cell types from different tissue and animal origins, including porcine aortic endothelial (PAE) cells, and human umbilical vein endothelial cells (HUVEC) (not shown). From these results, functionalized PVDF nanoparticles thus appeared to be biocompatible.

Cell Uptake Assays

In order to check that CBO-P11 kept its binding affinity for VEGF receptors after conjugation on nanoparticles, cell uptake assays were performed on PAE cells which were

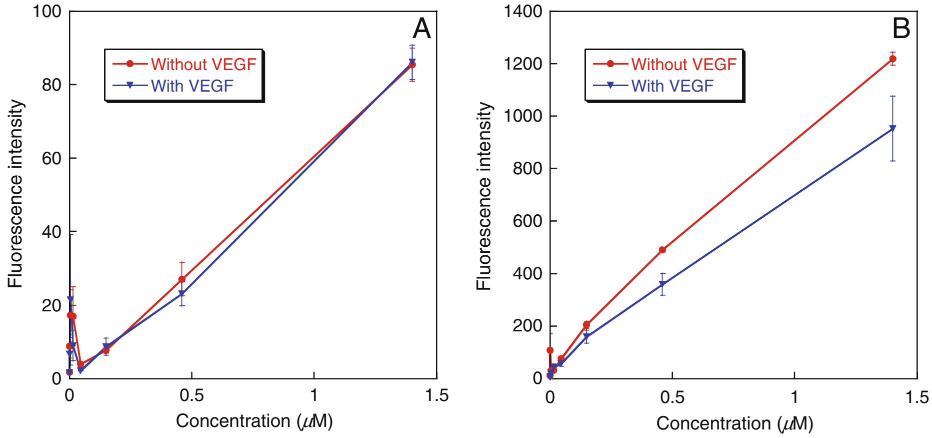

Fig. 6 Fluorescence intensity in PAE cells incubated with (**A**) PVDF-g-PAA-mTEG-CyTE777 nanoparticles and (**B**) PVDF-g-PAA-mTEG-CBO-P11-CyTE777 nanoparticles, with or without 100 ng/ml VEGF.

modified to overexpress VEGFR-2. PAE cells were incubated with fluorescent nanoparticles containing CBO-P11 (PVDF-g-PAA-mTEG-CBO-P11-CyTE777) or with control fluorescent nanoparticles without peptide (PVDF-g-PAA-mTEG-CyTE777). Control cells were also incubated in the presence of an excess (100 ng/ml) of VEGF to block receptors, thus preventing VEGFR-2-mediated uptake of nanoparticles. Fluorescence was quantified at different fluorophore concentrations (Fig. 6). Figure 6A showed a similar uptake profile with or without VEGF for PVDF-g-PAA-mTEG-CyTE777 nanoparticles. In contrast, fluorescence intensity for PVDF-g-PAA-mTEG-**CBO-P11**-CyTE777 nanoparticles was significantly higher (22%) in the absence of VEGF relative to cells incubated with VEGF (Fig. 6B). This indicates that VEGF receptors on the cells were partially responsible for the nanoparticles uptake, suggesting a specific interaction between CBO-P11 and VEGF receptors. Therefore, the anchoring of the VEGF receptor-targeting peptide on the surface of nanoparticles did not impede its binding to VEGF receptors. This indicates that nanoparticles containing CBO-P11 may represent useful vectors for targeting tumor angiogenesis.

CONCLUSION

In this paper, we have developed novel polymeric nanoparticles as a tool for targeting tumor angiogenesis. CBO-P11, a VEGFR-2-specific cylco-peptide, was successfully conjugated on the surface of PVDF nanoparticles using “click” chemistry. The nanoparticles were prepared from monomer of PVDF by radical aqueous emulsion polymerization. They were functionalized by *in situ* radiation grafting of acrylic acid in aqueous solution. This process was chosen to prevent aggregation and optimize the radical polymerization initiation step. Then, a spacer with azide function was coupled to nanoparticles to increase the hydrophilicity of the polymer. In the future, a longer poly (ethylene glycol) spacer will have to be considered to provide a better colloidal stability and to avoid immune system identification (mode “stealth”). CBO-P11 was labelled with an NIR cyanine dye bearing an alkyne function which allowed “click” reaction with azide functions on the periphery of nanoparticles. From SANS, FESEM, SLS and DLS, nanoparticles appeared spherical, dense and monodisperse. SANS data indicated a relative stable dispersion due to electrostatic interactions of PAA grafted onto PVDF nanoparticles. This stability of the nanoparticles should favour a long blood circulation time. IRTF and XPS studies confirmed a grafting on the surface of nanoparticles, making the reactive functions more available. Furthermore, every synthesis step was run in aqueous solution, leaving nanoparticles in a favourable environment for medical application. Cytotoxicity assays revealed the absence of toxicity after incubation of nanoparticles on HCMEC, suggesting the biocompatibility of theses nanodevices. Cell uptake assays showed that nanoparticle-conjugated CBO-P11 retained its binding specificity for VEGFR-2. These results are very encouraging to use these novel nanodevices for targeting tumor vasculature. In addition, the labelling with a cyanine dye may be useful for *in vivo* optical imaging due to the high depth of NIR probes. “Click” chemistry is highly selective and can be broadly applicable to a panel of molecules (therapeutic drugs, imaging agents etc.). As a matter of fact, a combination of these labelled nanoparticles with therapeutic agents to obtain multifunctional system for drug delivery is under study.

ACKNOWLEDGMENTS

We are grateful to François Bauer (Piezotech SA) for the PVDF nanoparticles synthesis. We also thank Dr. Christophe Schatz (Laboratoire de Chimie des Polymères Organiques, UMR CNRS 5629, University of Bordeaux, France) for dynamic light scattering experiments and La Ligue Contre le Cancer for its financial support.

REFERENCES

1. Brigger I, Dubernet C, Couvreur P. Nanoparticles in cancer therapy and diagnosis. Adv Drug Deliv Rev. 2002;54(5):631–51.
2. Matsumura Y, Maeda H. A new concept for macromolecular therapeutics in cancer chemotherapy: mechanism of tumoritropic accumulation of proteins and the antitumor agent Smancs. Cancer Res. 1986;46(12 Part 1):6387–92.
3. Ruoslahti E. Targeting tumor vasculature with homing peptides from phage display. Semin Cancer Biol. 2000;10(6):435–42.
4. Folkman J. Tumor angiogenesis: therapeutic implications. N Engl J Med. 1971;285:1182–6.
5. de Vries C, Escobedo JA, Ueno H, Houck K, Ferrara N, Williams LT. The *fms*-like tyrosine kinase, a receptor for vascular endothelial growth factor. Science. 1992;255(5047):989–91.
6. Terman BI, Dougher-Vermazen M, Carrion ME, Dimitrov D, Armellino DC, Gospodarowicz D, *et al*. Identification of the KDR tyrosine kinase as a receptor for vascular endothelial cell growth factor. Biochem Biophys Res Commun. 1992;187(3):1579–86.
7. Ferrara N, Hillan KJ, Novotny W. Bevacizumab (Avastin), a humanized anti-VEGF monoclonal antibody for cancer therapy. Biochem Biophys Res Commun. 2005;333(2):328–35.
8. Ferrara N. Role of vascular endothelial growth factor in physiologic and pathologic angiogenesis: therapeutic implications. Semin Oncol. 2002;29(6, Supplement 16):10–4.
9. Ferrara N, Davis-Smyth T. The biology of vascular endothelial growth factor. Endocr Rev. 1997;18(1):4–25.
10. Eichhorn ME, Strieth S, Dellian M. Anti-vascular tumor therapy: recent advances, pitfalls and clinical perspectives. Drug Resist Updat. 2004;7(2):125–38.
11. Zilberberg L, Shinkaruk S, Lequin O, Rousseau B, Hagedorn M, Costa F, *et al*. Structure and inhibitory effects on angiogenesis and tumor development of a new vascular endothelial growth inhibitor. J Biol Chem. 2003;278(37):35564–73.

12. Braga FJC, Rogero SO, Couto AA, Marques RFC, Ribeiro AA, Campos JSdC. Characterization of PVDF/HAP composites for medical applications. Mater Res. 2007;10:247–51.
13. Ding N, Pacetti SD, Tang F-W, Gada M, Roorda W. XIENCE V™ stent design and rationale. J Interv Cardiol. 2009;22:S18–27.
14. Klinge U, Klosterhalfen B, Ottinger AP, Junge K, Schumpelick V. PVDF as a new polymer for the construction of surgical meshes. Biomaterials. 2002;23(16):3487–93. doi:10.1016/S0142-9612(02)00070-4.
15. Conze J, Junge K, Weiß C, Anurov M, Oettinger A, Klinge U, *et al.* New polymer for intra-abdominal meshes—PVDF copolymer. J Biomed Mater Res B Appl Biomater. 2008;87B(2):321–8.
16. Berger D. Prevention of parastomal hernias by prophylactic use of a specially designed intraperitoneal onlay mesh (Dynamesh IPST®). Hernia. 2008;12(3):243–6.
17. Klee D, Ademovic Z, Bosserhoff A, Hoecker H, Maziolis G, Erli H-J. Surface modification of poly(vinylidenefluoride) to improve the osteoblast adhesion. Biomaterials. 2003;24(21):3663–70. doi:10.1016/S0142-9612(03)00235-7.
18. Valentini RF, Vargo TG, Gardella Jr JA, Aebischer P. Electrically charged polymeric substrates enhance nerve fibre outgrowth *In vitro*. Biomaterials. 1992;13(3):183–90. doi:10.1016/0142-9612(92)90069-Z.
19. Deshayes S, Maurizot V, Clochard M-C, Berthelot T, Baudin C, Déléris G. Synthesis of specific nanoparticles for targeting tumor angiogenesis using electron-beam irradiation. Radiat Phys Chem. 2010;79(3):208–13.
20. von Maltzahn G, Ren Y, Park J-H, Min D-H, Kotamraju VR, Jayakumar J, *et al.* Tumor cell targeting with "click" nanoparticles. Bioconjug Chem. 2008;19(8):1570–8.
21. Opsteen JA, Brinkhuis RP, Teeuwen RLM, Lowik DWPM, Hest JCMV. "Clickable" polymersomes. Chem Commun. 2007;30:3136–8.
22. Nicolas J, Bensaid F, Desmaele D, Grogna M, Detrembleur C, Andrieux K, *et al.* Synthesis of highly functionalized poly(alkyl cyanoacrylate) nanoparticles by means of click chemistry. Macromolecules. 2008;41(22):8418–28.
23. Weksler BB, Subileau EA, Perriere N, Charneau P, Holloway K, Leveque M, *et al.* Blood-brain barrier-specific properties of a human adult brain endothelial cell line. FASEB J. 2005;19(13):1872–4.
24. Gonçalves M, Estieu-Gionnet K, Berthelot T, Laïn G, Bayle M, Canron X, *et al.* Design, synthesis, and evaluation of original carriers for targeting vascular endothelial growth factor receptor interactions. Pharm Res. 2005;22(8):1411–21. doi:10.1007/s11095-005-5265-9.
25. Hilderbrand SA, Kelly KA, Weissleder R, Tung C-H. Monofunctional near-infrared fluorochromes for imaging applications. Bioconjug Chem. 2005;16(5):1275–81.
26. Moody CA, Field JA. Perfluorinated surfactants and the environmental implications of their use in fire-fighting foams. Environ Sci Technol. 2000;34(18):3864–70.
27. Chansiri G, Lyons RT, Patel MV, Hem SL. Effect of surface charge on the stability of oil/water emulsions during steam sterilization. J Pharm Sci. 1999;88(4):454–8.
28. Steffens GCM, Nothdurft L, Buse G, Thissen H, Höcker H, Klee D. High density binding of proteins and peptides to poly(D, L-lactide) grafted with polyacrylic acid. Biomaterials. 2002;23(16):3523–31.
29. Stannett V. Grafting. Radiat Phys Chem. 1981;18(1–2):215–22.
30. Betz N, Begue J, Gonçalves M, Gionnet K, Déléris G, Le Moël A. Functionalisation of PAA radiation grafted PVDF. Nucl Instrum Methods Phys Res Sect B. 2003;208:434–41.
31. Clochard MC, Begue J, Lafon A, Caldemaison D, Bittencourt C, Pireaux JJ, *et al.* Tailorring bulk and surface grafting of poly(acrylic acid) in electron-irradiated PVDF. Polymer. 2004;45(26):8683–94.
32. Chapiro A. In: Gaylord NG, Adler G, editors. Radiation chemistry of polymeric systems high polymers. New York: Interscience; 1962.
33. Rostovtsev V, Green L, Fokin V, Sharpless K. A stepwise Huisgen cycloaddition process: copper(I)-catalyzed regioselective "ligation" of azides and terminal alkynes. Angew Chem Int Ed. 2002;41(14):2596–9.
34. Perez-Balderas F, Ortega-Munoz M, Morales-Sanfrutos J, Hernandez-Mateo F, Calvo-Flores FG, Calvo-Asin JA, *et al.* Multivalent neoglycoconjugates by regiospecific cycloaddition of alkynes and azides using organic-soluble copper catalysts. Org Lett. 2003;5(11):1951–4.
35. Hiki S, Kataoka K. A facile synthesis of azido-terminated heterobifunctional poly(ethylene glycol)s for "click" conjugation. Bioconjug Chem. 2007;18(6):2191–6.
36. Rao J, Dragulescu-Andrasi A, Yao H. Fluorescence imaging *in vivo*: recent advances. Curr Opin Biotechnol. 2007;18:17–25.
37. Berridge MV, Tan AS, McCoy KD, Wang R. The biochemical and cellular basis of cell proliferation assays that use tetrazolium salts. Biochemica. 1996;4:15–20.

2.4.4 Phys. Rev. Lett. (2010)

Pink Noise of Ionic Conductance through Single Artificial Nanopores Revisited

C. Tasserit,[1,2] A. Koutsioubas,[1] D. Lairez,[1,*] G. Zalczer,[3] and M.-C. Clochard[2]

[1]*Laboratoire Léon Brillouin, CEA/CNRS UMR 12, CEA-Saclay, 91191 Gif-sur-Yvette cedex, France*
[2]*Laboratoire des Solides Irradiés, CEA/CNRS/Ecole Polytechnique, Ecole Polytechnique, 91128 Palaiseau cedex, France*
[3]*Service de Physique de l'Etat Condensé, CEA-Saclay, 91191 Gif-sur-Yvette cedex, France*

(Received 9 July 2010; revised manuscript received 9 September 2010; published 22 December 2010)

We report voltage-clamp measurements through single conical nanopore obtained by chemical etching of a single ion track in polyimide film. Special attention is paid to the pink noise of the ionic current (i.e., $1/f$ noise) measured with different filling liquids. The relative pink-noise amplitude is almost independent of concentration and pH for KCl solutions, but varies strongly using ionic liquids. In particular, we show that depending on the ionic liquid, the transport of charge carriers is strongly facilitated (low noise and higher conductivity than in the bulk) or jammed. These results show that the origin of the pink noise can be ascribed neither to fluctuations of the pore geometry nor to the pore wall charges, but rather to a cooperative effect on ions motion in confined geometry.

DOI: 10.1103/PhysRevLett.105.260602 PACS numbers: 66.10.Ed, 05.40.−a, 61.20.Qg, 87.80.Jg

After the work of the Nobel prize winners Neher and Sakmann for their single ion-channel recordings experiments [1], the first application of their technics for *in vitro* single-molecule manipulation [2] stimulated many hopes for the study of biological macromolecules. The main idea is that individual polymer chain driven electrophoretically through a single nanopore (namely, chain translocation) causes a resistive pulse of the ionic conductance of the channel that can be observed. Noticeable challenging applications of this method are DNA sequencing [3–5] and protein folding-unfolding studies [6]. Initially concerned with biological nanopores (mainly α-hemolysin inserted into lipid bilayer), more recent reports consider artificial nanopores because of their versatility [7]. Two main processes are used to obtain such artificial nanopores: chemical etching of a single ion track in polymer film [8–10] and ion-beam sculpting of silicon nitride [11]. Nanopore sensing of macromolecules in solution is based on an accurate analysis of the electrical ionic current through the nanopore: passing throughout the nanopore, a macromolecule causes fluctuations of the ionic current. Analysis of the time correlation of these fluctuations, i.e., duration and frequency probabilities, is expected to sign the solute [7]. While quite promising, progress in this domain is widely impeded by a low frequency $1/f$ noise (named ''pink noise'') of the power spectral density (PSD) of current observed even for a nanopore filled with a blank sample, i.e., solvent alone. The understanding and reduction of this noise is crucial to make the most of translocation studies [12,13]. Pink noise of the PSD is characteristic of anomalous and slow relaxation of fluctuations. Unfortunately, it is not the signature of a unique and universal elementary mechanism, as many causes can result in the same $1/f$ spectrum [14]. Actually, it is reported in many voltage-clamp studies not only on artificial nanopores but also on biological systems from neural ionic channels [15], membrane-active peptides [16,17] to protein channels [18,19]. A common feature of pink noise encountered in electronic devices but also on ionic current though nanopores, is that the amplitude of the $1/f$ power law of the PSD increases as the square of the average current [20]. This is the signature of conductance fluctuations. Generally speaking, the conductance $G = I/U$ (where I is the current and U the voltage) of an Ohmic system made of a nanopore filled with an ionic solution can be written as the product

$$G = Q^2 C \mu L, \tag{1}$$

where Q is the charge of ions, C their concentration (number per unit volume), μ their effective mobility along the pore axis (averaged velocity per unit force), and L an effective length characteristic of the pore geometry (typically the ratio of the cross section to the length for a cylindrical pore). Straightforwardly from Eq. (1), conductance fluctuations can be either imputed to the pore itself (L) or to the charge transport ($C\mu$). Actually in the literature, both kinds of hypothetical explanations are proposed. Among the first kind, ''channel breathing'' is invoked for protein channel [19] and ''pore wall dandling fragments'' or ''opening-closing'' process [21] are invoked for track-etched nanopores. Whereas the second kind is mainly proposed for silicon nitride nanopores, for which conductance fluctuation are attributed to fluctuations of ion concentration [13] and inspired by the Hooge phenomenological formula [20] obtained for electronic devices. In this case, concentration fluctuations are claimed to be related to the surface charge of the pore wall [22].

In this Letter we address the problem of pink noise measured on conical track-etched single nanopore in polyimide film (Kapton). First we show that for the same level of ionic current, the pink-noise amplitude is considerably decreased using an appropriate ionic liquid as charge carrier, and considerably increased using another one. This result gives strong evidence that the origin of the pink noise cannot be attributed to fluctuations of the pore geometry [L in Eq. (1)] but rather to local fluctuations of the liquid conductivity ($\sigma = Q^2 C\mu$). In addition, we show that these latter fluctuations are independent on the surface charge of the pore wall and cannot be accounted for by the Hooge formula and concentration fluctuations. Thus, our results provide evidence that the pink-noise in such nanopores comes from anomalous cooperative fluctuations of the confined ions motion.

Samples characteristics and preparation.—Single heavy-ion (Kr^{28+}, 10.36 MeV) irradiations of 8 μm thick polyimide foils (Kapton HN) were performed at GANIL (France). Conically shaped single nanopores were prepared by anisotropic chemical etching of these irradiated films. The etching process was performed following Ref. [23] at $T = 328$ K using a two chambers conductivity cell where one chamber is filled with NaOCl etching solution ($p\mathrm{H} = 12.5$), while the other chamber contains 1 M KI neutralizing solution. Across the film a voltage of +1 V (with respect to the grounded neutralizing compartment) is applied for detection of the breakthrough event and also to assist the neutralization of NaOCl upon breakthrough. For conductivity measurements, the ionic liquids used are 1-ethyl-3-methylimidazolium thiocyanate (EMIM-SCN, from Sigma) and 1-butyl-3-methylimidazolium bis(trifluorosulfonyl)imide (BMIM-TFSI, from Solvionic). Their main characteristics are summarized in Table I. They have comparable viscosity and electrical conductivity but the former is fully miscible in water whereas the latter is not. These ionic liquids display large electrochemical windows that prevent electrochemical reaction at the electrodes at our working voltage [24,26]. However, due to the very low ionic current level through a single nanopore, the polarization characteristic time of the electrodes is very long compared to our measurement duration.

Data acquisition and treatment.—Voltage clamp and current amplification were ensured by an Axopatch 200B with a 10 kHz low-pass analog filter setting. The amplified current was digitized with a 16 bit ADC (Iotech Dacqbook) at 250 kHz sampling rate and averaged over 25 samples. PSD was averaged following the periodogram method over at least 50 time segments. Measurements were performed at room temperature under normal atmospheric composition using two Ag/Ag-Cl electrodes of 2 mm diameter and 10 mm in length with the tip of conical nanopore at the ground potential.

TABLE I. Viscosity η and electrical conductivity σ_{bulk} of ionic liquids in the bulk at room temperature (from Refs. [24,25]). σ_{conf} is the electrical conductivity deduced from our measurements of conductance through nanopores.

	η (mPa s)	σ_{bulk} (S/m)	σ_{conf} (S/m)
EMIM-SCN	20	0.20	0.23 ± 0.02
BMIM-TFSI	50	0.38	4.7 ± 0.5

Results.—In Fig. 1, typical current-voltage characteristic curves of a single conical nanopore are plotted for different filling liquids. For KCl solutions (molar conductivity: 73 and 76×10^{-4} $\mathrm{S\,m^2\,mol^{-1}}$ for K^+ and Cl^-, respectively) at $p\mathrm{H} = 7$, the nanopore is highly rectifying. As ionic conductivities of cations and anions are identical, the symmetry breaking can only be due to the electrical charge of the pore wall. Oxidation during chemical etching leads to carboxylic groups on the pore wall which are dissociated at $p\mathrm{H} = 7$. This charged surface is responsible for an ion selectivity leading to this polarity dependent conductance of the pore. At $p\mathrm{H} = 2$, carboxylic groups are fully protonated, the pore wall is neutral, and this effect disappears. At this pH, the variation of the nanopore conductance with KCl concentration (up to 3 M) does not differ significantly from the variation of KCl conductivity in the bulk reported in Ref. [27]. The effective characteristic length L of the pore can thus be determined from the ratio of the conductance G to the conductivity σ of the filling solution: $L = G/\sigma$. The results here reported were obtained using two nanopores of characteristic size $L = (4.0 \pm 0.5)$ nm. For truncated conical pores: $L = \pi r_1 r_2 / l$, where r_1 and r_2 are the radii of the two apertures and l the pore length (film thickness). The largest radius r_1 has been measured by “field emission scanning electron microscopy” imaging of a multipore membrane (10^8 pores cm^{-2}) prepared under the same conditions as single pores and was found to be $r_1 = 0.5$ μm. Single nanopores differ the one from the other mainly by their smaller radius r_2. From the L values one gets $r_2 = (20 \pm 2)$ nm. The conductance measured with ionic liquid compared to KCl solutions allows us to determine the conductivity σ_{conf} of ionic liquids in the nanopore (Table I). For EMIM-SCN (hydrophilic anion), $\sigma_{\mathrm{conf}} \simeq \sigma_{\mathrm{bulk}}$. However, for BMIM-TFSI (hydrophobic anion), one finds $\sigma_{\mathrm{conf}} \gg \sigma_{\mathrm{bulk}}$. Note that recently with similar nanopores filled with BMIM-methyl sulfate and methoxyethoxyethyl sulfate (amphiphilic anion) the opposite behavior is reported ($\sigma_{\mathrm{conf}} \ll \sigma_{\mathrm{bulk}}$) [28]. As regards to the wide variability of ionic liquids properties these discrepancies are not necessarily unexpected and opens a wide field of investigation.

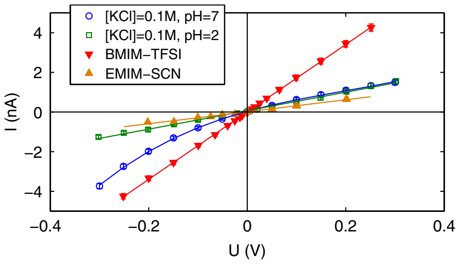

FIG. 1 (color online). Current-voltage characteristic curves measured for single nanopore with different filling liquids. Slopes of straight lines are equal to 3.0 nS (EMIM-SCN), 17 nS (BMIM-TFSI), and 4.7 nS ([KCl] = 0.1 M), respectively.

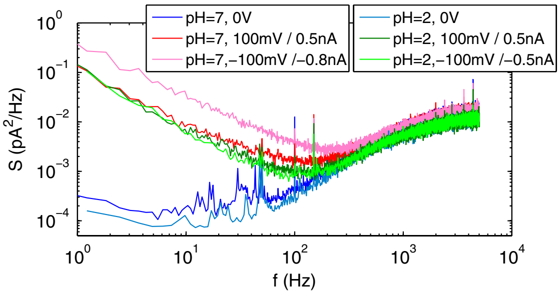

FIG. 2 (color online). Power spectral density S of the ionic current through a single nanopore filled with KCl solutions ($[\mathrm{KCl}] = 0.1$ M) at different pH values and applied voltages.

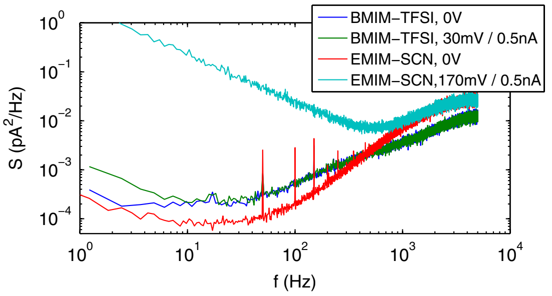

FIG. 3 (color online). Power spectral density S of the ionic current through single nanopore filled with ionic liquid for $I = 0$ and 0.5 nA.

In Fig. 2, typical power spectral density of the current is plotted for KCl solution at $p\mathrm{H} = 2$ and 7 at different voltages. Typical spectra measured for ionic liquids are plotted in Fig. 3. The shape of these spectra can be imputed neither to the electrodes nor to the measurement device [29], it displays two parts. At high frequency the spectra are independent of the voltage and of the pH. This high frequency noise can be attributed to electrochemical equilibrium of functional groups of the pore wall [29] and can be fitted with a polynomial [30]. At low frequency spectra display a $1/f$ noise that increases in amplitude with the current. The whole frequency range was accounted for by fitting the spectra with

$$S = S_1 \frac{1}{f} + a + bf - cf^2 + \cdots . \tag{2}$$

Results found for the pink-noise amplitude S_1 are plotted in Fig. 4. For KCl solutions, whatever the salt concentration, the pH, and the voltage, a single master curve $S_1/I^2 = \mathrm{Cst}$ is found over 6 orders of magnitude. With ionic liquids, the amplitude of the pink noise differs significantly from the KCl solutions master curve. It is increased by a factor 40 with EMIM-SCN but conversely decreased by 2 orders of magnitude with BMIM-TFSI. The origin of this discrepancy is not understood but should be probably related to the effect of confinement on the conductivity already mentioned.

Discussion.—The power spectral density S is the Fourier transform of the autocorrelation that obviously vanishes beyond the longest relaxation time $\tau^* = 1/f^*$. In our case one can write

$$S = t_0 I^2 \frac{\langle \Delta G^2 \rangle}{G^2} \mathcal{F}(f/f^*), \quad \text{with} \begin{cases} \mathcal{F}(x \ll 1) = 1 \\ \mathcal{F}(x \gg 1) = x^{-1} \end{cases} \tag{3}$$

with t_0 the time unit. Unfortunately, we did not succeed in reaching the expected plateau of the PSD at low frequency.

Let us first consider fluctuations of the pore geometry (breathing or dandling fragments) as responsible for the pink noise. $G = \sigma L$, $\langle \Delta G^2 \rangle = \sigma^2 \langle \Delta L^2 \rangle$, and Eq. (3) give

$$S_1 \propto I^2 \frac{\langle \Delta L^2 \rangle}{L^2} f^*. \tag{4}$$

One can reasonably assume that the amplitude $\langle \Delta L^2 \rangle$ of fluctuations of pore geometry is a thermodynamical or static property that only weakly depends on the filling liquid. Only the dynamics of these fluctuations would shift to low frequencies proportionally to the increase of viscosity η, i.e. $f^* \propto \eta^{-1}$. Finally, fluctuations of the pore geometry would lead to $S_1 \propto I^2 \eta^{-1}$. Evidently, our results disagree with this behavior as both ionic liquids have a higher viscosity than KCl solutions but give a pink noise much higher or much lower.

The pink noise is more likely to come from fluctuations of ionic conductivity of the confined liquid, i.e., concentration or mobility fluctuations. Let us consider N independent charge carriers with individual current contributions i: $I = Ni$ and $\langle \Delta I^2 \rangle = N \langle \Delta i^2 \rangle$. If N is proportional to the bulk concentration C then

$$S_1 \propto \frac{I^2}{C} \times \frac{\langle \Delta i^2 \rangle}{i^2}. \tag{5}$$

For independent charge carriers $\langle \Delta i^2 \rangle / i^2$ is independent of C and Eq. (5) gives $S_1 \propto C^{-1}$ (Hooge's formula). This is in contradiction with the master curve (Fig. 4) obtained for KCl concentrations varying by 2 orders of magnitude (i.e., a factor much larger than the "width" of the master curve). This disagreement has been already pointed out [22], and efforts to reconcile experiment and Hooge's formula invoke ion concentrations inside the pore different from the bulk ones due to the charges of the pore wall ($N \not\propto C$). At

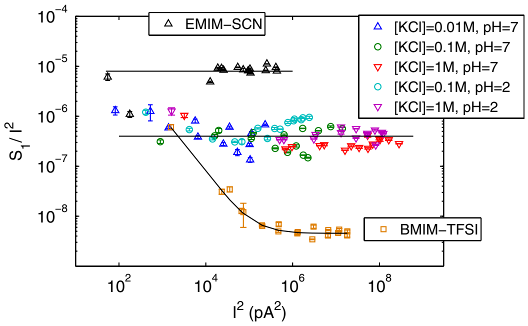

FIG. 4 (color online). Relative pink-noise amplitude S_1/I^2 vs square of the current I^2 for single nanopores with different filling liquids at different voltages. Lines are guides for the eyes.

pH = 2 surface charges are clearly annihilated (Fig. 1 no rectifying effect) but noise data at this pH still remain on the master curve (Fig. 4). This result rules out concentration fluctuations due to pore wall charges as responsible for pink noise but also any mechanism involving individual fluctuations of ions mobility.

On the contrary, our results for KCl solutions give evidence for cooperative effects on ions mobility. These cooperative effects are not observed in the bulk and are due to confinement. For KCl solutions they manifest themselves only on conductivity fluctuations but not on its averaged value that follows (within error bars) the expected concentration dependence. But for ionic liquids, cooperativity is even more evident. Ionic liquids are known to self-organize into liquid crystal-like structure when the side chain of the cation is long enough [31] (e.g., butyl of BMIM vs ethyl of EMIM). More recently, the phase behavior has been found to depend on the external electric field [32,33]. These effects should be responsible for the different conductivity properties of ionic liquids in confined geometry, i.e., facilitated transport (low noise and $\sigma_{\mathrm{conf}} \gg \sigma_{\mathrm{bulk}}$ for BMIM-TFSI) or jammedlike transport (high noise and $\sigma_{\mathrm{conf}} \ll \sigma_{\mathrm{bulk}}$ for EMIM-SCN and BMIM-methyl sulfate and methoxyethoxyethyl sulfate [28]). The noise reduction we have observed with one ionic liquid probably explains success recently reported for nanopore sensing of small molecules [34] or DNA [35] using ionic liquids and is quite promising for future applications in this field. Even if $1/f$ noise of ionic conductance in single nanopores is not yet understood, its origin has to be searched in relation with the slow dynamics of the confined electrolyte that should display jammedlike features [36] such as those encountered for quasi-1D transport [37]. Finally, we think that these noise measurements should be quite interesting not only for the improvement of single-molecule detection but also for the development and improvement of electrical batteries and cells that increasingly use confined geometries.

We thank Jean Le Bideau for enlightening discussions concerning ionic liquids. This work was supported by ANR-06-Nano-003 and ANR-08-Blan-0094-04.

---

*Corresponding author.

[1] E. Neher and B. Sakmann, Nature (London) **260**, 799 (1976).

[2] J. J. Kasianowicz, E. Brandin, D. Branton, and D. W. Deamer, Proc. Natl. Acad. Sci. U.S.A. **93**, 13 770 (1996).

[3] M. Akeson, D. Branton, J. J. Kasianowicz, E. Brandin, and D. W. Deamer, Biophys. J. **77**, 3227 (1999).

[4] A. Meller, L. Nivon, and D. Branton, Phys. Rev. Lett. **86**, 3435 (2001).

[5] J. J. Nakane, M. Akeson, and A. Marziali, J. Phys. Condens. Matter **15**, R1365 (2003).

[6] G. Oukhaled, J. Mathé, A. L. Biance, L. Bacri, J.-M. Betton, D. Lairez, J. Pelta, and L. Auvray, Phys. Rev. Lett. **98**, 158101 (2007).

[7] S. Howorka and Z. Siwy, Chem. Soc. Rev. **38**, 2360 (2009).

[8] Z. Siwy and A. Fuliński, Phys. Rev. Lett. **89**, 198103 (2002).

[9] A. Mara, Z. Siwy, C. Trautmann, J. Wan, and F. Kamme, Nano Lett. **4**, 497 (2004).

[10] C. C. Harrell, Y. Choi, L. P. Horne, L. A. Baker, Z. S. Siwy, and C. R. Martin, Langmuir **22**, 10 837 (2006).

[11] J. Li, D. Stein, C. McMullan, D. Branton, M. J. Aziz, and J. A. Golovchenko, Nature (London) **412**, 166 (2001).

[12] V. Tabard-Cossa, D. Trivedi, M. Wiggin, N. N. Jetha, and A. Marziali, Nanotechnology **18**, 305505 (2007).

[13] R. M. M. Smeets, U. F. Keyser, N. H. Dekker, and C. Dekker, Proc. Natl. Acad. Sci. U.S.A. **105**, 417 (2008).

[14] M. B. Weissman, Rev. Mod. Phys. **60**, 537 (1988).

[15] H. Derksen and A. A. Verveen, Science **151**, 1388 (1966).

[16] R. Sauvé and E. Bamberg, J. Membr. Biol. **43**, 317 (1978).

[17] G. C. Fadda, D. Lairez, and G. Zalczer, Phys. Rev. Lett. **103**, 180601 (2009).

[18] S. Nekolla, C. Andersen, and R. Benz, Biophys. J. **66**, 1388 (1994).

[19] S. M. Bezrukov and M. Winterhalter, Phys. Rev. Lett. **85**, 202 (2000).

[20] F. Hooge, T. Kleinpenning, and K. Vandamme, Rep. Prog. Phys. **44**, 479 (1981).

[21] Z. Siwy and A. Fuliński, Phys. Rev. Lett. **89**, 158101 (2002).

[22] M. R. Powell, I. Vlassiouk, C. Martens, and Z. S. Siwy, Phys. Rev. Lett. **103**, 248104 (2009).

[23] Z. Siwy, P. Apel, D. Dobrev, R. Neumann, R. Spohr, C. Trautmann, and K. Voss, Nucl. Instrum. Methods Phys. Res., Sect. B **208**, 143 (2003).

[24] M. Galinski, A. Lewandowski, and I. Stepniak, Electrochim. Acta **51**, 5567 (2006).

[25] U. Domanska, M. Królikowska, and M. Królikowski, Fluid Phase Equilib. **294**, 72 (2010).

[26] J. Pringle, J. Golding, C. Forsyth, G. Deacon, M. Forsyth, and D. R. MacFarlane, J. Mater. Chem. **12**, 3475 (2002).

[27] M. Della Monica, A. Ceglie, and A. Agostiano, J. Phys. Chem. **88**, 2124 (1984).

[28] M. Davenport, A. Rodriguez, K. J. Shea, and Z. S. Siwy, Nano Lett. **9**, 2125 (2009).

[29] D. P. Hoogerheide, S. Garaj, and J. A. Golovchenko, Phys. Rev. Lett. **102**, 256804 (2009).

[30] R. A. Levis and J. L. Rae, Biophys. J. **65**, 1666 (1993).

[31] K. Binnemans, Chem. Rev. **105**, 4148 (2005).

[32] Y. T. Wang, J. Phys. Chem. B **113**, 11 058 (2009).

[33] G. X. Xie, J. B. Luo, D. Guo, and S. H. Liu, Appl. Phys. Lett. **96**, 043112 (2010).

[34] D. Jayawardhana, J. Crank, Q. Zhao, D. Armstrong, and X. Guan, Anal. Chem. **81**, 460 (2009).

[35] R. S. de Zoysa, D. Jayawardhana, Q. Zhao, D. Wang, D. Armstrong, and X. Guan, J. Phys. Chem. B **113**, 13 332 (2009).

[36] G. Biroli, Nature Phys. **3**, 222 (2007).

[37] T. Nagatani, Rep. Prog. Phys. **65**, 1331 (2002).

2.4.5 J. Pow. Sources (2010)

Journal of Power Sources 195 (2010) 223–231

Contents lists available at ScienceDirect

Journal of Power Sources

journal homepage: www.elsevier.com/locate/jpowsour

Ion track grafting: A way of producing low-cost and highly proton conductive membranes for fuel cell applications

M.-C. Clochard[a,*], T. Berthelot[a], C. Baudin[a], N. Betz[a,1], E. Balanzat[b], G. Gébel[c], A. Morin[d]

[a] Laboratoire des Solide Irradiés, CEA - DSM/IRAMIS – CNRS UMR 7642 - Ecole Polytechnique, F-91128 Palaiseau, France
[b] CIMAP, CEA – CNRS – ENSICAEN BP 5133 F-14040 Caen, France
[c] CEA - DSM/INAC/SPrAM CEA-Grenoble 17 rue des Martyrs, F-38054 GRENOBLE Cedex 9, France
[d] CEA - DRT/LITEN/DTH/LCPEM CEA-Grenoble 17 rue des Martyrs, F-38054 GRENOBLE Cedex 9, France

ARTICLE INFO

Article history:
Received 17 March 2009
Received in revised form 22 May 2009
Accepted 9 July 2009
Available online 18 July 2009

Keywords:
Ion track grafting
Radiografting
Swift heavy ions
Proton conductivity
Polymer electrolyte membrane
Proton exchange membrane fuel cell

ABSTRACT

Proton conductive individual channels through a poly(vinyl di-fluoride) PVDF matrix have been designed using the ion track grafting technique. The styrene molecules were radiografted and further sulfonated leading to sulfonated polystyrene (PSSA) domains within PVDF. The grafting process all along the cylindrical ion tracks creates after functionalisation privileged paths perpendicular to the membrane plane for proton conduction from the anode to the cathode when used in fuel cells. Such ion track grafted PVDF-g-PSSA membranes have low gas permeation properties against H_2 and O_2. A degree of grafting (Y_w) of 140% was chosen to ensure a perfect coverage of PSSA onto PVDF-g-PSSA surface minimizing interfacial ohmic losses with the active layers of the Membrane Electrolyte Assembly (MEA). A three-day fuel cell test has been performed feeding the cell with pure H_2 and O_2, at the anode and cathode side respectively. Temperature has been progressively increased from 50 to 80 °C. Polarisation curves and Electrochemical Impedance Spectroscopy (EIS) at different current densities were used to evaluate the MEA performance. From these last measurements, it has been possible to determine the resistance of the MEA during the fuel cell tests and, thus the membrane conductivity. The proton conductivities of such membranes estimated during fuel cell tests range from 50 mS cm^{-1} to 80 mS cm^{-1} depending on the operating conditions. These values are close to that of perfluorosulfonated membrane such as Nafion® in similar conditions.

1. Introduction

One of the challenges of the twenty first century is to develop efficient low-cost membranes for fuel cell application, notably for the industrialisation of non-pollutant cars. The ideal membrane should satisfy to the following requirements: permeability lower than perfluorosulfonated membrane such as Nafion®, that is to say lower than 5 barrer at 80 °C when fully humidified, high proton conductivity 10^{-2} to 10^{-1} S cm^{-1} at high temperature and low water content, especially above 80 °C, a chemical stability in the fuel cell conditions, especially versus oxidation, reduction, hydrolysis, low dimensional changes upon swelling, a high mechanical stability and a sensitive price. Even the most used polymer electrolyte membranes in fuel cells applications, the Nafion® membranes from Dupont, do not completely fulfil these drastic requirements. Theses membranes consist of a hydrophobic fluorocarbon backbone assuring the mechanical support and hydrophilic sulfonic side chains for proton transfer. Despite some serious inconvenient such as a high cost (ca. US$ 850–800 m^{-2} for *Nafion*-117 sheet membranes [1]), a water swelling shortening the membrane life time and conductivity losses at high temperature, the Nafion® is still the reference today. Presently, only Gore Primea 5710 series membranes are really able to reach its fuel cell test performances and life time [2,3] but it is still a derivative of Nafion®.

Many other type of membranes have already been tested: (i) non-fluorinated membranes [4]: sulfonated copolymers of polystyrene-polybutadiene, polyethersulfone, polyphenylenesulfone [5,6], polyetherketone [4,7–9], polyarylene ethers [10], polyimides [11,12], polybenzimidazole [8,13–15], polyacrylates [16–18], oxadiazole-based polymers [19] and (ii) fluorinated membranes: trifluoroethylene (TFE) copolymers and many radiografted polystyrene or styrene derivatives onto fluorinated polymer such as ethylene tetrafluoethylene (ETFE) or PVDF [20–29]. Some of these new polymers are promising but the two main problems are a lower conductivity and stability in oxidizing conditions compared to Nafion® shortening the life time in fuel cell conditions [30–33].

---

* Corresponding author at: Laboratoire des Solides Irradiés, CEA/DSM/IRAMIS/LSI, Ecole Polytechnique, F-91128 Palaiseau, France. Tel.: +33 1 69 33 45 26; fax: +33 1 69 33 45 54.
E-mail address: marie-claude.clochard@polytechnique.edu (M.-C. Clochard).

[1] Deceased.

0378-7753/$ – see front matter © 2009 Elsevier B.V. All rights reserved.
doi:10.1016/j.jpowsour.2009.07.016

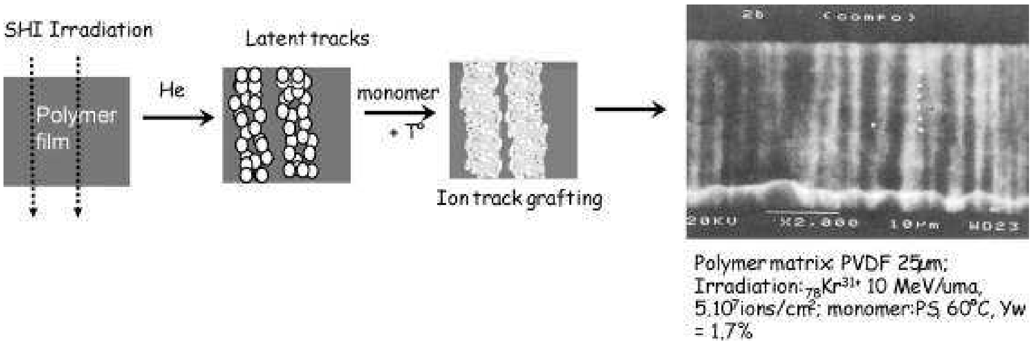

Fig. 1. Scheme of swift heavy irradiation of penetrating ions through a polymeric foil, the latent track formation and the subsequent ion grafting localised inside the latent track. Example: SEM micrograph of the cross-section of an ion-track grafted PVDF-g-PS membrane.

The lower proton conductivity can be compensated increasing the ion content but it is generally at the expense of the mechanical stability in water swollen conditions. Consequently, the trend is to reinforce theses new polymer electrolyte membranes either by adding some crosslinkers or by introducing an inorganic filler to improve the polymer membrane mechanical properties [34–40]. Radiation [41] to graft membranes is widely investigated because of the double effect: (i) functionalisation with proton conductive entities and (ii) creation of a three-dimensional network if the radiation dose is higher than the dose gel of the polymer or if a radiation sensitive crosslinker such as di-vinyl benzene is used during the formulation.

Until now, low ionising radiations such as electrons, γ-rays or X-rays ionising radiations have been used to radiograft homogeneously polymer foils [25,42,43]. The LSI in collaboration with the CIMAP uses a less studied kind of ionising radiation for polymer electrolyte membranes synthesis, swift heavy ions (SHI). Indeed, ions induce all along their trajectory through the solid a continuous trail of excitations and ionisations leading to the formation of a specific cylindrical damage called latent tracks. The final heterogeneous solid is then formed of latent tracks (or highly damaged cylindrical zones) and pristine areas. The latent tracks are radically active and allow the copolymerisation with vinyl monomers. Ion track grafting was first performed by Monnin and Blanford in 1973 [44] for detection of nuclear tracks. Since this pioneer work, a large majority of related publications has been written by N. Betz from the LSI [45–49]. Her unique experience in this field is still pursued today in our team.

The idea [50] was to ensure the mechanical and dimensional stability of the future proton exchange membrane stability by playing with SHI properties allowing to leave some pristine fluorinated polymer parts as a support matrix and to design proton conductive channels by radio-induced track grafting inside this same PVDF matrix (Fig. 1). This SHI processing is a unique way for creating nanocomposite membranes. PVDF is a very appropriate substrate because of its high chemical resistance, its good mechanical properties and its hydrophobic fluorocarbon backbone. The channels consist of high density of proton conductive entities interpenetrated with PVDF chains. All theses proton conductive entities are covalently bound to the PVDF support. The cost of such membranes was estimated by us from catalogue prices at no more than US$ 200 m^{-2} at a small production scale (ion-beam irradiation cost representing only 10% of the membrane price).

The present paper relies on fuel test performances of 40 μm thick PVDF-g-PSSA polymer electrolyte membranes obtained from SHI track grafting. EIS was used in parallel especially to determine the influence of the working parameters, such as outlet gas pressure, on the resistance of the MEA.

2. Experimental

2.1. Swift heavy ion radiation grafting: poly(PVDF-g-PS)

Prior to use, the 9 μm thick β PVDF films produced by Solvay (Belgium) were extracted in a Soxhlet apparatus with toluene, for 24 h. After drying at 60 °C under vacuum for 12 h, the samples were irradiated in an helium atmosphere at GANIL (Caen, France) with $_{78}\mathrm{Kr}^{31+}$ at a specific energy of 10 MeV amu^{-1}. The electronic stopping power $(\mathrm{d}E/\mathrm{d}x)_e$ of the Kr ions was 40 MeV $\mathrm{cm}^2.\mathrm{mg}^{-1}$. The fluence ($\Phi$) was 10^{10} ions cm^{-2}. For comparison purposes, other irradiation conditions were also used: gamma rays, and high energy oxygen and xenon beams. A SHI irradiation induces a heterogeneous dose distribution at the nanometric level. The doses quoted here correspond to the mean absorbed dose (D); $D\,(\mathrm{Gy}) = 1.6 \times 10^{-7}$. $\Phi\,(\mathrm{cm}^{-2})$. $(\mathrm{d}E/\mathrm{d}x)_e\,(\mathrm{MeV\,cm^2\,mg^{-1}})$.

The irradiated films were grafted with pure styrene for 1 h at 60 °C according to a process previously reported [48]. The grafting yield is given by $Y_w = (W_f - W_i)/W_i$ (%) where W_f and W_i are the sample weights after and before grafting, respectively.

2.2. Functionalisation: poly(PVDF-g-PSSA)

After swelling during 20 min in dichloromethane (CH_2Cl_2) at room temperature, the grafted fluoropolymers, noted poly(PVDF-g-PS) were immersed in a 10 vol.% chlorosulfonic acid solution for 30 min in order to add sulfonic acid groups (SO_3H) on the phenyl ring of the polystyrene. The chlorosulfonation proceeded by two successive reactions: the first one total and the second reversible, leading to the formation of sulfonate (SO_3H) and chlorosulfonate (SO_2Cl) groups. A basic hydrolysis (NaOH 1 M, RT, 2 h) was then performed to act on the reversible reaction to convert the SO_2Cl groups in SO_3Na ones. Na^+ are exchanged by H^+ by immersion in 1 M H_2SO_4 during 3 h at room temperature in order to recover the sulfonic acid groups. PVDF-g-PSSA membranes were rinsed three times in deionised water and dried gently at 50 °C under vacuum for 12 h. The hydrolysis was followed using Energy Dispersive Spectrometer (EDS) coupled to Field Emission Scanning Electron Microscope (FESEM). The hydrolysis was considered to be complete when the Cl ions K-ray signal was completely suppressed. The functionalisation rate was around 60%.

2.3. Infrared spectroscopy measurements

FTIR spectra of the polymer films were carried out with a Nicolet Magna-IR$^{\mathrm{TM}}$ 750 spectrometer equipped with a DTGS detector. Spectra were recorded in an Attenuated Total Reflection mode (ATR) using a diamond-crystal with single reflection. Experiments were carried out cumulating 32 scans at a resolution of 2 cm^{-1}.

2.4. High resolution magic angle spinning nuclear magnetic resonance (HR MAS NMR) spectroscopy

All experiments were performed with an Avance 500 spectrometer equipped with a triple resonance (^1H-^{13}C-^{31}P) HRMAS probe head. NMR rotors were standard ZrO_2 4 mm rotors without insert. Spinning speed corresponded to 5 kHz. Deuterated dimethylsulfoxide (dmso-d6) and dimethylformamide (dmf-d7) were purchased from Eurisotop (France). Each sample was prepared as follows: 80 μl of solvent was added to 8 mg of polymer and the mixture was heated at 100 °C for 1 h, so as to obtain a paste-like consistency. The resulting slurry was introduced into the HRMAS rotor using a simple pipette.

2.5. Ion exchange capacity

The ion exchange capacity (IEC) was measured following a conventional route. The membranes were first immersed in 1 M NaCl solution for 24 h at room temperature. The released protons were titrated against 0.01 M NaOH solution using phenolphthalein indicator. The IEC of the graft copolymer membranes was calculated using the following equation:

$$\text{IEC (mequiv. g}^{-1}) = \frac{V \cdot N_{\text{OH}}}{m}$$

where V is the volume of NaOH at the equivalence, N_{OH} is the normality of NaOH and m the total weight of polymer. The reported IEC values were the mean of five measurements and the average estimated error was ±8%.

2.6. Water uptake

Water uptake was determined by weighing the vacuum-dried membrane and the fully equilibrated membrane with water. The membrane sample was wiped with an adsorbent paper to remove excess water and the sample was weighted. The water uptake was determined as follows:

$$\text{Water uptake (wt\%)} = \frac{m_f - m_i}{m_i} \times 100$$

where m_f and m_i are the weights of wet and dried membranes respectively. The reported water uptake values were the mean of at least 3 measurements and the average estimated error was ±10%.

2.7. Proton conductivity

The membrane in-plane proton conductivity was determined by impedance spectroscopy using a Materials Mates 7260 impedancemeter and a home-made conductivity cell. A series of 1 mm thick gold lines inserted in a flat polymer support are used as electrodes and spaced from 0.2 cm to 1.75 cm. Pieces of membranes (1 cm × 2 cm) equilibrated at least 2 h in liquid water are placed between the two flat supports. The conductivity was measured with different combinations of electrodes in order to average measured values and to avoid any effect of local heterogeneities. The reported values were the mean of at least 4 measurements and the average estimated error was ±5%. The frequency was carried from 5 MHz to 100 Hz.

2.8. MEA preparation

Before starting the fuel cell test, the ion track grafted PVDF-g-PSSA membrane was fully hydrated by immersion in ultrapure water for 2 h. The membrane was then directly piled up into a 5 cm^2 single cell designed by Quintech between two commercial gas diffusion electrodes E-LAT LT 140EW-SI from BASF. These electrodes were made with 30 wt% Pt/C and the catalyst loading of each was 0.5 mg cm^{-2}. The stress on the membrane has been calculated taking into account the compressive behaviours of the electrode and the gasket and is about 1 MPa.

2.9. Fuel cell test

Fuel cell tests have been performed in co-flow configuration using a home-made fuel cell test bench feeding the cell with pure H_2 and O_2 at the anode and cathode sides, respectively. The relative humidity of each gas was controlled thanks to a bubbler and modified by the temperature of and by regulation of the temperature of the water. Relative humidity was calculated as the ratio of the theoretical partial pressures of water at the temperature of the bubbler and at the cell temperature.

Constant gas flows were used (40 ml min^{-1} for both hydrogen and oxygen up to 800 mA cm^{-2}). Therefore, the gas stoichiometries depend on the current density below this value and correspond to about 1.5 and 3 at 800 mA cm^{-2} for H_2 and O_2 respectively. Above 800 mA cm^{-2} hydrogen gas flow was increased to keep a constant stoichiometry of 1.5.

The cell temperature was controlled and progressively increased from 50 °C to 80 °C. During the test, the temperature of the bubblers was kept constant around 30 °C whatever the cell temperature inducing a decrease of the relative humidity as the cell temperature increased. A 2 absolute bars pressure was applied except for a specific experiment performed at 80 °C, 4 absolute bars and 100% relative humidity for each gas. Polarisation curves were recorded with a linear scan rate. The cell was operated continuously during 50 h.

2.10. In situ EIS measurements

Electrochemical Impedance Spectroscopy measurements have been performed in galvanodynamic mode with a Biologic potentiostat/impedancemeter VMP2 with a 20 A booster. The complex impedance was measured between 10 kHz and 0.3 Hz in each experimental condition at different current densities. For each frequency decade, 10 measurements were made and the amplitude was at a maximum at 10% of the value of the current. For each frequency, the values were recorded after waiting 4 periods and were average on 4 periods.

3. Results and discussion

3.1. Ion track grafted PVDF-g-PSSA membranes

Ion track grafting technique allows the creation of channels of grafted polyelectrolyte all along the linear ion tracks inside a thin PVDF film (Fig. 1). Structuring the matter is very interesting for generating privileged paths for proton conduction without inducing any further porosity. Consequently, such membranes have low gas permeation properties against H_2 and O_2. Similar PVDF-g-PSSA membranes have already been synthesized and characterized in our group for mainly biomedical purposes by FTIR [51,52], XPS [47,53], X-ray scattering and scanning electron studies [43,54]. The grafting heterogeneity of fluoropolymers irradiated by swift heavy ions in comparison to γ-ray was then well defined. In the present study, a high grafting yield of $Y_w = 140\%$ was chosen in order to radiograft not only inside the latent tracks but also to cover completely the membrane surface [43] in order to have the maximum interfacial exchange with the active layer of the PEMFC. At this grafting level, the initial 9 μm thick PVDF in beta phase reach 40 μm of total thickness. The translucent initial PVDF aspect turns to a white shiny colour in the grafted PS part (Fig. 2).

Fig. 2. Photograph of an ion track grafted PVDF-g-PSSA membrane (fluence 10^{10} cm^{-2}): white part corresponds to the radiografted part (grafting yield of 140 wt%), translucent part corresponds to the non-irradiated part (SHI beam width = 4 cm).

The FTIR spectra of the PVDF-g-PS and PVDF-g-PSSA obtained are in good agreement with that obtained previously [52] (Fig. 3). It was found under FTIR total reflexion mode a 100% covering of PS with the disappearance of PVDF CH_2 stretching vibration bands at 2985 cm^{-1} and 3025 cm^{-1} in favour to the typical PS bands in that region.

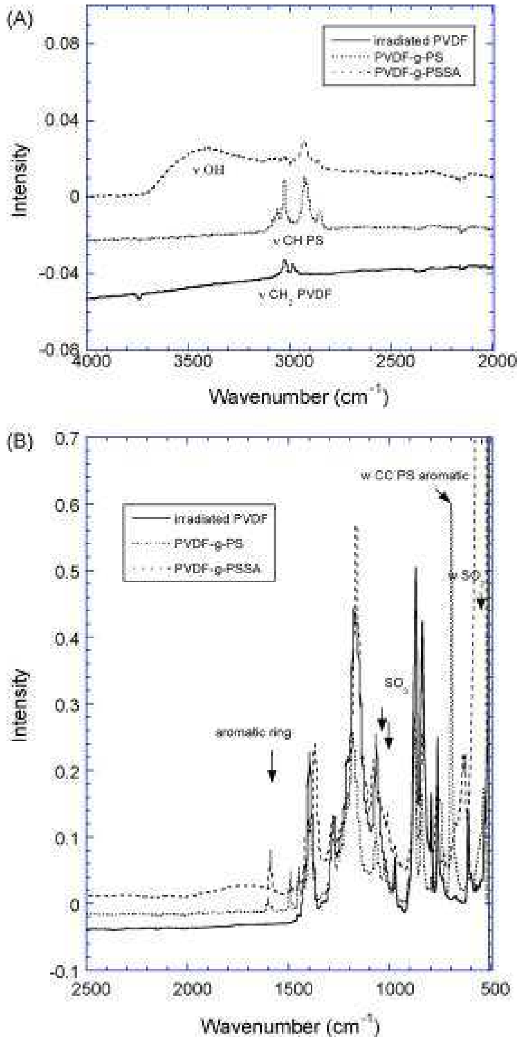

Fig. 3. FTIR spectra of the $^{78}Kr^{31+}$ irradiated PVDF, ion grafted PVDF with polystyrene (PVDF-g-PS) – Y_w = 140% – and subsequent sulfonation (PVDF-g-PSSA): (A) 4000–2000 cm^{-1}, region (B) 2500–500 cm^{-1} region.

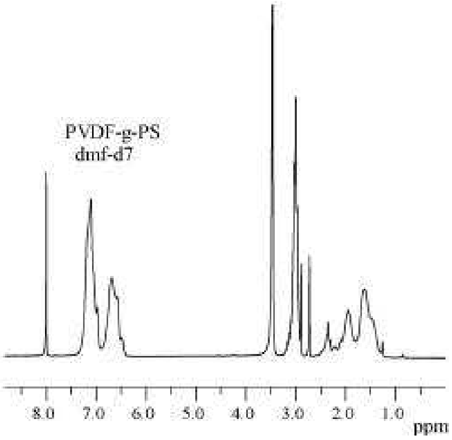

Fig. 4. HRMAS ^{1}H spectrum of ion track grafted PVDF-g-PS membrane (fluence 10^{10} cm^{-2}) swollen in deuteriated DMF.

To complete PVDF-g-PSSA membrane characterisation, in volume and time, we have used liquid NMR spectroscopy. After irradiation, some radicals on PVDF films may recombine together to form covalent bonds leading to cross-linked films. As a matter of fact, films are not soluble in DMF. Attempts to obtain solution spectra by classical liquid NMR probe were not satisfactory. Solid state spectra, in such a case, generally display poor resolution. A solution to this dilemma is to swell the films with the DMF and to acquire spectra while spinning at magic angle. Figs. 4 and 5 display the obtained ^{1}H spectra for ion track grafted PVDF-g-PS and PVDF-g-PSSA membranes respectively. In Fig. 4, ^{1}H spectrum displays 2 large peaks at 6.6 ppm and 7.1 ppm corresponding to the aromatic groups of PS. Two other peaks at 1.6 ppm and 2 ppm are attributed to CH_2 and CH of PS respectively. The triplet at 3 ppm corresponds to the PVDF. Peak integrations allow us to determine a grafting yield of 140 wt% in agreement with the gravimetric value. The PVDF-g-PS was well-swollen in DMF. After sulfonation, the solubility has changed and the swelling was no longer efficient in DMF. DMSO was found more appropriate. The need to change the solvent to acquire HRMAS NMR spectra shows a change in the hydrophilic property of the initial hydrophobic PVDF-g-PS membrane. Fig. 5 illustrates the ^{1}H spectrum of PDVF-g-PSSA in DMSO. A typical acidic proton peak appears at 13.1 ppm while the aromatic groups in the zone ranging from 6 ppm to 8 ppm seems to be less resolved and the CH and CH_2 of PSSA collapsed as it was previously described for PSSA in liq-

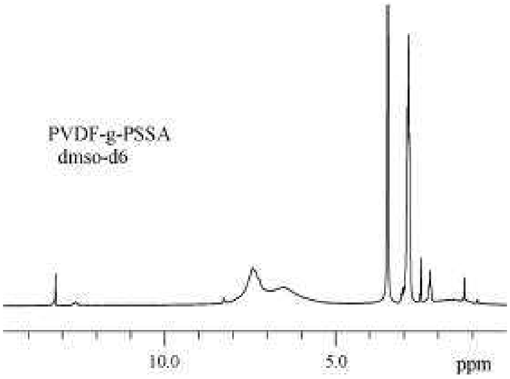

Fig. 5. HRMAS ^{1}H spectrum of ion track grafted PVDF-g-PSSA membrane (fluence 10^{10} cm^{-2}) swollen in deuteriated DMSO.

Table 1
IEC, water uptake and proton conductivities of ion track grafted PVDF-g-PSSA with 140 wt% PS content at various gas relative humidities, gas supplies and temperatures.

Polymer electrolyte membrane	IEC (mequiv. g^{-1})	Water uptake (wt%) at room temperature	λ ($[H_2O]/[SO_3H]$)	RH (%)	Gas feed rate (Bar)	T (°C)	σ (mS cm^{-1})
Ion track grafted PVDF-g-PSSA	2.97	17	3.7	35	2	50	36
				20	2	60	51
				15	2	70	55
				100	2	80	60
				100	4	80	61
Nafion®	0.95	40[a]	22[a]	100	4	80	80

[a] From literature [25,28,60].

uid ^{1}H NMR [55]. Unfortunately, in the latter case, the quantitative approach was not possible.

IEC values are indicative of the actual ion exchange sites available for proton conductivity. The higher values of IEC are then desirable to achieve higher proton conductivity in polymer electrolyte membranes. Ion track grafted PVDF-g-PSSA membrane with a Y_w of 140% exhibited a IEC of 2.97 mequiv. g^{-1}, which is three times higher than that of Nafion® 117 (Table 1). The water uptake of ion track grafted PVDF-g-PSSA is also presented in Table 1. The water uptake was found to be two times inferior to that of the value of Nafion® 117. From literature [25], the water uptake for PVDF-g-PSSA copolymer membrane obtained from homogeneous e-beam irradiation is higher than Nafion® 117; for example, a IEC of 1 in such a membrane corresponds to a water uptake of 52%. It means that our membrane structuration is very effective in constraining the water uptake inside the local hydrophilic channels. The high stiffness of the hydrophobic PVDF polymer matrix limits the swelling of the membrane to less than 20% in one direction only (membrane thickness).

3.2. Proton conductivities

Fig. 6 displays the proton conductivities of PVDF-g-PSSA membranes radiografted from different irradiation sources as a function of the grafting yield. Gamma irradiation provides a homogeneous irradiation through the solid. The induced radicals are consequently homogeneously distributed in the polymer bulk. The grafting occurs from the surface to the inner part of the PVDF film. It is then necessary to reach a threshold value of the grafting yield to connect each grafting fronts and to obtain percolation. For this reason the proton conductivities have been measured at low grafting yields. A series of SHI radiografted sulfonated membranes irradiated with Xe and O ions (fluence 7×10^9 ions cm^{-2} deposited dose 0.5 kGy and 10^9 ions cm^{-2} deposited dose 38 kGy respectively) were prepared and compared to Gamma irradiated (deposited dose 5 kGy). For the two types of SHI membranes with different ions, fluences and deposited doses the results are very similar indicating that these parameters are not first order parameters. Since in-plane conductivities are measured one could have expected a lower conductivities for SHI membranes compared to gamma irradiated materials. Since the conductivity is measured with electrodes located on each membrane side the limiting process is thus the through plane conductivity. A grafting yield of 10 wt% in 25 μm thick β-PVDF membrane corresponds to this threshold. For ion track grafted PVDF-g-PSSA membranes, proton conductivities were recorded even at very low grafting yields – below 10 wt% – because the grafting diffusion is favoured through the PVDF film all along the tracks. As a matter of fact, for SHI, the conductivity only depends on Y_w and not on D or $(dE/dx)_e$. Besides, at least, when Y_w is smaller than 30%, the conductivity obtained by SHI is higher than with gamma rays. This indicates that the cylindrical nanocomposite structure enhances the proton conductivity. The benefit of the specific structure induced with SHI is not restricted to the improvement of the mechanical and dimensional stability but also concerns proton conductivity. It is worth noting that the proton conductivities measured *ex situ* for large grafting yields (e.g. Fluence = 10^{10} tracks cm^{-2}; $Y = 140$ wt%; $\sigma = 120 \pm 6$ mS cm^{-1}) are closer to the value determined *in situ* by EIS in the fuel cell experiments.

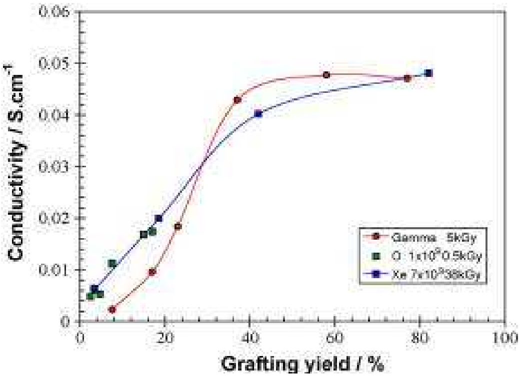

Fig. 6. Proton conductivities versus grafting yields for radiografted PVDF-g-PSSA membranes in latent tracks using two different type of ions, O and Xe and radiografted PVDFg-PSSA membranes using gamma irradiation.

3.3. Fuel cell performances

The conditioning of such new membranes was just a simple membrane immersion in acidic water. The test was started at rather low temperature (around 30 °C) in order to avoid membrane dehydration and to check for the absence of H_2 crossover. The pressure was progressively increased up to 2 absolute bars with a flow of 40 ml min^{-1} of fully humidified pure H_2 and O_2. The stabilised open circuit voltage (OCV) was quite low (860 mV) but no evidence of membrane leakage has been observed. The current was slowly increased up to 40 mA cm^{-2} and the voltage was around 610 mV. The cell temperature was then increased up to 50 °C (35% RH) and after 45 min, a polarisation curve was recorded (Fig. 7). At that stage, low performances were obtained (OCV 835 mV and 6.5 mA cm^{-2} at 700 mV). Three hypotheses are drawn to explain the low current density: poor quality of the membrane-electrode interface, a partial dehydration of the membrane or of the ionomer within the active layer. Indeed, because of the chemical composition of the membrane and the scale of proton conducting channel structures which covers about 74% of the surface, the interface between the membrane and the commercial electrode which contains perfluorosulfonic acid (PFSA) ionomer could be worst than with Nafion®. So, impedance spectroscopy measurements have been performed in order to better understand the imitating phenomena (Fig. 8).

Whatever the current density, the first semi-circle intercepts the abscise axis for a frequency of approximately 2 kHz when the imaginary part of the impedance is equal to zero revealing a pure ohmic

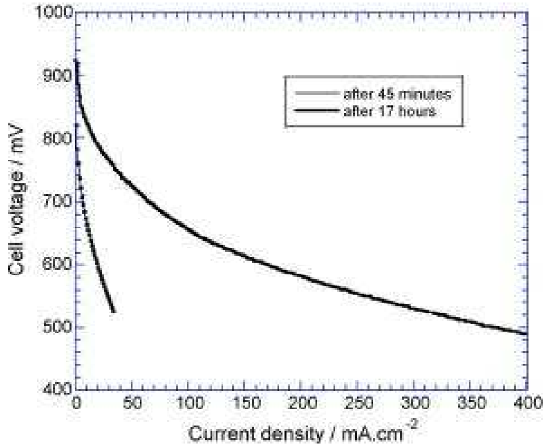

Fig. 7. Polarisation curves recorded during the conditioning step, after 45 min. and 17 h of operation at 50 °C with pure H_2 and O_2 at 2 bars and 35%RH.

behaviour. The corresponding specific resistance corresponds to the sum of all the ohmic phenomena, meaning ionic resistance of the membrane, electronic resistance of the electrodes and of the single cell test fixture components, interface resistance between all the electronic conducting cell components. Assuming that the electronic resistance of the cables, the single cell test fixture components and the interfaces between them are negligible compared to the resistances within the MEA (components and interfaces: R_{MEA}), it appears clearly that R_{MEA} does not depend on the current density and is about 56 mOhm or 280 mOhm cm^2 (Fig. 9). With 10 mOhm cm^2 [56] as electronic resistance for each electrode (R_{elec}) and about 5 mOhm cm^2 [57] as contact resistance between the electrodes and the monopolar plates (R_{contact}), the ionic resistance of the membrane and membrane/electrodes interfaces is about 250 mOhm cm^2. Assuming negligible interface ohmic losses, 5 cm^2 as active area and an homogeneous distribution of water content on the whole surface area and within the membrane thickness, a membrane conductivity of about 1.6×10^{-2} S cm^{-1} can be estimated. This is a quite high value with regard to the cell performance and to the low water uptake when expressed as the number of water molecules per sulfonic acid group ($\lambda \approx 3$). For the same water content, the proton conductivity of Nafion® is more or less similar, i.e. 2×10^{-2} S cm^{-1} at 80 °C [58]. This could probably be explained by the structure of these membranes with proton conducting channels through the whole thickness of the membrane. The discrepancy between the fairly high proton conductivity and the very low fuel cell performance can be understood considering the contributions of all the overpotentials through the analysis of the low frequency resistance in the EIS spectra. This total specific resistance (R_{T}) corresponds to the sum of the ohmic resistance (R_{MEA}) and the polarisation resistance (R_{Pol}): $R_{\mathrm{T}} = R_{\mathrm{MEA}} + R_{\mathrm{Pol}}$. For example, at 20 mA cm^{-2} the impedance value is 1 Ohm, that is to say that the specific resistance is about 5000 mOhm cm^2, which is

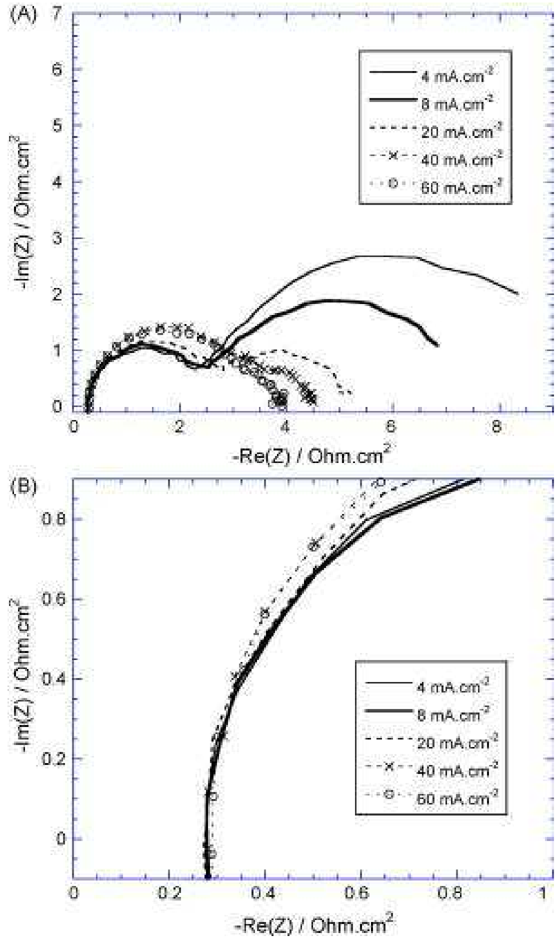

Fig. 8. Impedance spectroscopy measurements recorded during the conditioning step, after 45 min of operation at 50 °C with pure H_2 and O_2 at 2 bars and 35%RH (A. full recording; B. zoom of higher frequencies region).

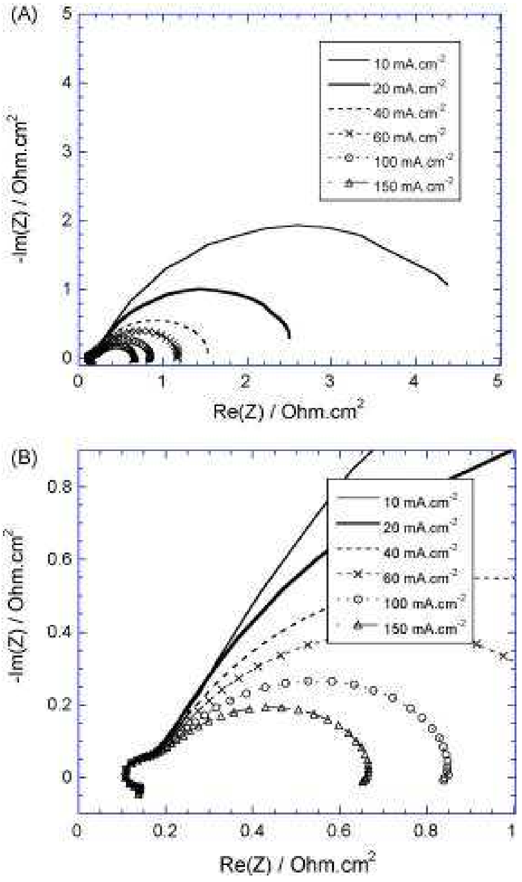

Fig. 9. Impedance spectroscopy measurements recorded during the conditioning step after 17 h of operation at 50 °C with pure H_2 and O_2 at 2 bars and 35%RH (A. full recording; B. zoom of higher frequencies region).

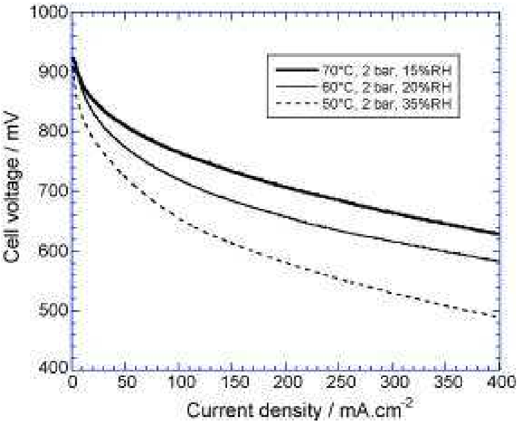

Fig. 10. Comparison of polarisation curves recorded at 50 °C, 60 °C and 70 °C with pure H_2 and O_2 at 2 bars.

in very good agreement with the one calculated from the slope of the polarisation curve.

In the Niquist plot, two main contributions are observed (Fig. 8). The first contribution with a characteristic frequency of about 200 Hz increases with the current density. It may be due either to a poor membrane-electrode interface or to the drying of the anode caused by the electroosmosis of water from the anode to the cathode and/or by a lack of water back-flow from the cathode to the anode side. Since the low current densities do not favour electroosmosis, the first hypothesis has thus to be considered. The second contribution with a characteristic frequency of a few Hz decreases as the current density increases. It is likely due to the activation overpotential of the oxygen reduction reaction (ORR) since the signal in this frequency range is characteristic of the charge transfer phenomena at the cathode side. It is a high value (about 1000 mOhm cm^2 at 60 mA cm^{-2}) probably because the low current density does not favour an efficient cathode hydration. The low performances at the beginning of the test are mainly due to charge transfer overpotentials on both the cathode and anode side originating from either a drying of the anode or a poor membrane-electrode interface which does not give an ohmic contribution at high frequency.

After 17 h of operation (50 °C, 2 absolute bars and 35% RH), the cell performances considerably increased and the OCV reached about 920 mV. A second polarisation curve was recorded (Fig. 7). While the cell voltage usually reaches the equilibrium in approximately 8 h with Nafion® in the same operating conditions and electrodes, the equilibrium is still not reached with SHI grafted membranes. A possible explanation of this delayed increase of performance is that the improvement of the membrane electrodes interfaces requires a sufficient MEA hydration especially at the anode and slowly favours a better water management. This is observed on impedance spectra by the disappearance of the contribution at 200 Hz. Only the contribution of the charge transfer at the cathode side which decreases as the current density increases remains (Fig. 9). The MEA specific resistance (110 mOhm cm^2) leads to a membrane proton conductivity of 5×10^{-2} S cm^{-1} (Fig. 9).

The performance progressively increased with the temperature up to 70 °C (Fig. 10) and the specific resistance decreases (110, 80 and 75 mOhm cm^2 at 50 °C, 60 °C and 70 °C respectively (Fig. 11). It worth noting that the cell temperature increase from 50 °C to 70 °C induces a decrease of the gas inlet relative humidity from 35% to 15% RH which should not favour the membrane hydration and consequently, an increase of both the membrane conductivity (8×10^{-2} S cm^{-1} and 9×10^{-2} S cm^{-1} at 60 °C and 70 °C, respectively) and the cell performance. Complementary experiments will be necessary to complete our understanding on the origin of the fuel cell performance (membrane and electrode hydration, electroosmosis, water back-diffusion, membrane reorganization, . . .).

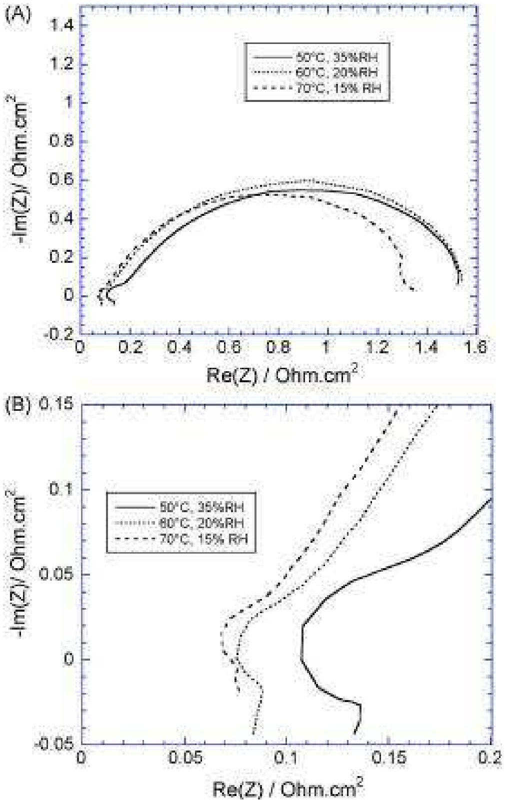

Fig. 11. Impedance spectroscopy measurements recorded at 40 mA cm^{-2} and 50 °C, 60 °C and 70 °C with pure H_2 and O_2 at 2 bars (A. full recording; B. zoom of higher frequencies region).

Both the OCV and the fuel cell performance increase with increasing cell temperature (OCV is respectively 920, 970, 1006 mV at 70 °C, 80 °C, 100% RH, 2 and 4 bars) (Fig. 12). There is no significant change in MEA specific resistance between 2 and 4 bars at 80 °C 100% RH but the ORR charge transfer resistance decreases as the pressure increases (Fig. 13) as expected for a higher reactant concentration on the electrodes. The conclusions extracted from EIS spectra of the polarisation curves are in good agreement. In addi-

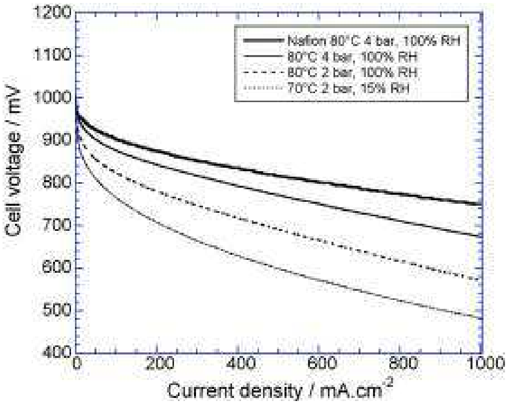

Fig. 12. Comparison of polarisation curves recorded at 80 °C with pure H_2 and O_2 and 100%RH at 2 and 4 bars.

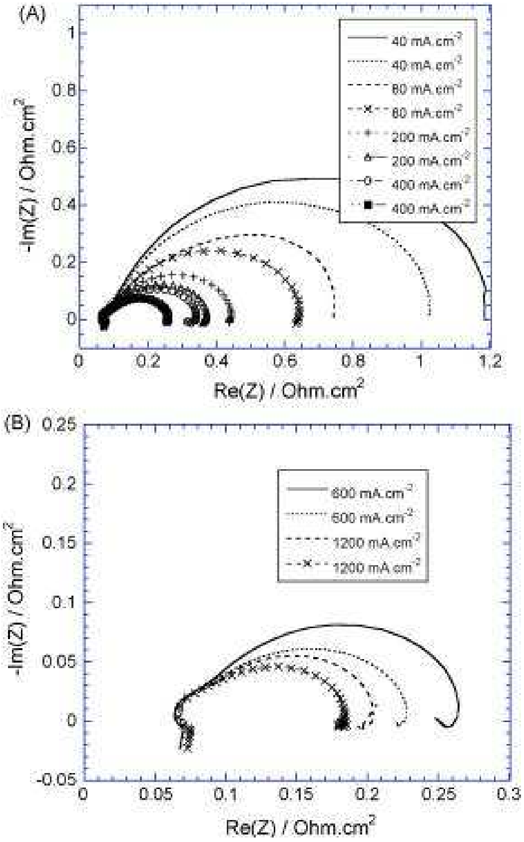

Fig. 13. Comparison of the impedance spectra recorded at 80 °C with pure fully humidified H_2 and O_2 at 2 bars (full symbol) and 4 bars (open symbols) (A. from 40 mA cm^{-2} to 400 mA cm^{-2}; B. from 600 mA cm^{-2} to 1200 mA cm^{-2}).

tion, the last point of the IES spectra at low frequencies related to polarisation curve is similar to the one of the left end side at high frequency. It means that the resistance of the membrane stays constant. At 80 °C, 4 bars with pure and fully humidified H_2 and O_2, the cell voltage is 670 mV at 1 A cm^{-2}. The performance is only a little lower than with a Nafion® NRE212 membrane (50 μm) with hot-pressed commercial electrodes which is a very encouraging result (Fig. 12).

4. Conclusion

PVDF-g-PSSA membrane obtained after SHI irradiation have been synthesized, characterized and tested in fuel cell continuously during 50 h in different operating conditions using pure H_2 and O_2. Despite poor performance during the starting procedure at low temperature, performance at 80 °C and 100% RH are finally similar to those obtained with Nafion® 212 membranes (50 μm). In these operating conditions, the proton conductivity calculated from the MEA specific resistance is the same as for Nafion®, e.g. 8×10^{-2} S cm^{-1}. This could be due to the unique structure of this membrane which have straight and large (~50 nm) proton conducting channels with high ion exchange capacity. The increase in performance at the beginning of the test and the behaviour of the MEA in the different operating conditions could be due to improvement of either interfaces and/or the water back-flow within the membrane. Work is in progress in order to understand more clearly the behaviour of the membrane since we obtain very promising results with these first tests. Notably, it will be interesting to study the mechanical support of the matrix before and after fuel cell test and compare the behaviour with other kind of PVDF-g-PSSA structures.

Indeed these membranes appear as very interesting materials since many parameters can now be optimized acting on the radiation and grafting conditions, the proton exchange functionalities (for example replacing the sulfonic acid (–SO_3H) groups by phosphonic acid (–PO_3H_2) groups known to be more efficient at high temperature) or on the grafted segment nature to increase both the stability and the acidity. Consequently, more chemistry is ongoing to test multi-functionalisations all along the proton conductive channels [59].

Acknowledgement

This work was supported by CEA-DRT/LITEN (Grenoble, France) in the framework of NTE French program.

References

[1] R.P.W.J. Struis, M. Quintilii, S. Stucki, J. Membr. Sci. 177 (2000) 215–223.
[2] S. Kim, M.M. Mench, J. Power Sources 174 (2007) 206–220.
[3] W. Liu, M. Crum, ElectroChem. Soc. Trans. 3 (2006) 531–540.
[4] B. Smitha, S. Sridhar, A.A. Khan, J. Membr. Sci. 259 (2005) 10–26.
[5] V. Saarinen, K.D. Kreuer, M. Schuster, R. Merkle, J. Maier, Solid State Ionics 178 (2007) 533–537.
[6] G. Maier, J. Meier-Haack, In Fuel Cells II; Springer-Verlag Berlin, Berlin, 216 (2008) pp. 1–62.
[7] X. Zhu, Y. Liang, H. Pan, X. Jian, Y. Zhang, J. Membr. Sci. 312 (2008) 59–65.
[8] D.J. Jones, J. Rozière, J. Membr. Sci. 185 (2001) 41–58.
[9] V. Ramani, S. Swier, M.T. Shaw, R.A. Weiss, H.R. Kunz, J.M. Fenton, J. Electrochem. Soc. 155 (2008) B532–B537.
[10] D.H. Choi, J. Lee, O. Kwon, J.Y. Kim, K. Kim, J. Power Sources 178 (2008) 677–682.
[11] C.H. Lee, C.H. Park, Y.M. Lee, J. Membr. Sci. 313 (2008) 199–206.
[12] C. Marestin, G. Gebel, O. Diat, R. Mercier, Fuel Cells Ii, vol. 216, Springer-Verlag Berlin, Berlin, 2008, pp. 185–258.
[13] J.S. Wainright, J.T. Wang, D. Weng, R.F. Savinell, J. Electrochem. Soc. 142 (1995) 121–123.
[14] J. Jouanneau, R. Mercier, L. Gonon, G. Gebel, Macromolecules 40 (2007) 983–990.
[15] J. Peron, E. Ruiz, D.J. Jones, J. Rozière, J. Membr. Sci. 314 (2008) 247–256.
[16] Y. Shen, J. Xi, X. Qiu, W. Zhu, Electrochim. Acta 52 (2007) 6956–6961.
[17] J.K. Choi, D.K. Lee, Y.W. Kim, B.R. Min, J.H. Kim, J. Polym. Sci. Part B - Polym. Phys. 46 (2008) 691–701.
[18] B.H. Liu, Z.P. Li, L.L. Chen, J. Power Sources 108 (2008) 530–534.
[19] D. Gomes, J. Roeder, M.L. Ponce, S.P. Nunes, J. Power Sources 175 (2008) 49–59.
[20] H.P. Brack, M. Wyler, G. Peter, G.G. Scherer, J. Membr. Sci. 214 (2003) 1–19.
[21] H.S. Huang, C.Y. Chen, S.C. Lo, C.J. Lin, S.J. Chen, L.J. Lin, Appl. Surf. Sci. 253 (2006) 2685–2689.
[22] J. Qiu, L. Zhao, M. Zhai, J. Ni, H. Zhou, J. Peng, J. Li, G. Wei, J. Power Sources 177 (2008) 617–623.
[23] Y.W. Kim, D.O. Lee, K.J. Lee, J.H. Kim, Eur. Polym. J. 44 (2008) 932–939.
[24] V. Saarinen, O. Himanen, T. Kallio, G. Sundholm, K. Kontturi, J. Power Sources 163 (2007) 768–776.
[25] S.D. Flint, R.C.T. Slade, Solid State Ionics 97 (1997) 299–307.
[26] T. Lehtinen, G. Sundholm, S. Holmberg, F. Sundholm, P. Björnbom, M. Bursell, Electrochem. Acta 43 (1998) 1881–1890.
[27] R. Souzy, B. Ameduri, B. Boutevin, G. Gébel, P. Capron, Solid State Ionics 176 (2005) 2839–2848.
[28] Y.W. Kim, J.K. Choi, J.T. Park, J.H. Kim, J. Membr. Sci. 313 (2008) 315–322.
[29] H.P. Brack, D. Ruegg, H. Buhrer, M. Slaski, S. Alkan, G.G. Scherer, J. Polym. Sci. Part B-Polym. Phys. 42 (2004) 2612–2624.
[30] B. Mattson, H. Ericson, L.M. Torell, F. Sundholm, Electrochim. Acta 45 (2000) 1405–1408.
[31] S. Kundu, K. Karan, M. Fowler, L.C. Simon, B. Peppley, E. Halliop, J. Power Sources 179 (2008) 693–699.
[32] M. Prasanna, E.A. Cho, T.-H. Lim, I.-H. Oh, Electrochem. Acta 53 (2008) 5434–5441.
[33] V.O. Mittal, H.R. Kunz, J. Fenton, J. Electrochem. Soc. 153 (2006) A1755–A1759.
[34] A. Anis, A.K. Banthia, S. Bandyopadhyay, J. Power Sources 179 (2008) 69–80.
[35] R. Souzy, B. Ameduri, Progr. Polym. Sci. 30 (2005) 644–687.
[36] H.G. Herz, K.D. Kreuer, J. Maier, G. Scharfenberger, M.F.H. Schuster, W.H. Meyer, Electrochim. Acta 48 (2003) 2165–2171.
[37] Y. Zhang, H. Zhang, C. Bi, X. Zhu, Electrochim. Acta 53 (2008) 4096–4103.
[38] P. Bebin, M. Caravanier, H. Galiano, J. Membr. Sci. 278 (2006) 35–42.
[39] K. Valle, P. Belleville, F. Pereira, C. Sanchez, Nat. Mater. 5 (2006) 107–111.
[40] A. Mokrini, M.A. Huneault, P. Gerard, J. Membr. Sci. 283 (2006) 74–83.
[41] S.A. Gursel, L. Gubler, B. Gupta, G.G. Scherer. Fuel Cells I, vol. 215, Springer-Verlag Berlin, Berlin, 2008, pp. 157–217.
[42] S. Hietala, E.M. Skou, F. Sundholm, Polymer 40 (1999) 5567–5573.

[43] C. Aymes-Chodur, N. Betz, M.-C. Porte-Durrieu, C. Baquey, A. Le Moël, Nucl. Instrum. Meth. Phys. Res. B 177 (1999) 377–385.
[44] M.M. Monnin, G.E. Blanford, Science 181 (1973) 743–744.
[45] N. Betz, C. Ducouret, A. Le Moël, Nucl. Instrum. Meth. Phys. Res. B 91 (1994) 151–156.
[46] N. Betz, Nucl. Instrum. Meth. Phys. Res. B 105 (1995) 55–62.
[47] N. Betz, S. Dapoz, M.-J. Guittet, Nucl. Instrum. Meth. Phys. Res. B 131 (1997) 252–259.
[48] N. Betz, A. Le Moël, J.-P. Duraud, E. Balanzat, C. Darnez, Macromolecules 25 (1992) 213–219.
[49] N. Betz, E. Balanzat, A. Le Moël, J.-P. Duraud, Radiation Effects Defects Solids 126 (1993) 221–224.
[50] M.-C. Clochard, T. Berthelot, CEA, France, 2007, p. FR0757875.
[51] C. Ducouret, E. Petersohn, N. Betz, A. Le Moël, Spectrochim. Acta 51A (1995) 567–572.
[52] S. Dapoz, N. Betz, A. Le Moël, J. Chim. Phys. 93 (1996) 58–63.
[53] S. Dapoz, N. Betz, M.-J. Guittet, A. Le Moël, Nucl. Instrum. Meth. Phys. Res. B 105 (1995) 120–125.
[54] G. Gébel, E. Ottomani, J.-J. Allegraud, N. Betz, A. Le Moël, Nucl. Instrum. Meth. Phys. Res. B 105 (1995) 145–149.
[55] C.M. Fernyhough, R.N. Young, A.J. Ryan, L.R. Hutchings, Polymer 47 (2006) 3455–3463.
[56] S. Escribano, J.F. Blachot, J. Etheve, A. Morin, R. Mosdale, J. Power Sources 156 (2006) 8–13.
[57] I. Nitta, T. Hottinen, O. Himanen, M. Mikkola, J. Power Sources 171 (2007) 26–36.
[58] Y. Sone, P. Ekdunge, D. Simonsson, J. Electrochem. Soc. 143 (1996) 1254–1259.
[59] T. Berthelot, M.-C. Clochard, CEA, France, 2007, p. FR0757873.
[60] T.E. Springer, T.A. Zawodzinski, S. Gottesfeld, J. Electrochem. Soc. 138 (1991) 2334–2342.

2.4.6 Polymer (2004)

Available online at www.sciencedirect.com
SCIENCE DIRECT®

Polymer 45 (2004) 8683–8694

polymer

www.elsevier.com/locate/polymer

Tailoring bulk and surface grafting of poly(acrylic acid) in electron-irradiated PVDF

M.-Cl. Clochard[a], J. Bègue[a], A. Lafon[a], D. Caldemaison[b], C. Bittencourt[c], J.-J. Pireaux[c], N. Betz[a,*]

[a]*CEA-Saclay, DSM/DRECAM/LSI/LPI-Bat.466, F-91191 Gif-sur-Yvette Cédex, France*
[b]*LMS, Ecole Polytechnique, Route de Saclay, F-91128 Palaiseau Cédex, France*
[c]*LISE, FUNDP, 61 Rue de Bruxelles, B-5000 Namur, Belgique*

Received 15 March 2004; received in revised form 1 October 2004; accepted 20 October 2004
Available online 5 November 2004

Abstract

Endowing conventional hydrophobic poly(vinylidene fluoride) (PVDF) films with hydrophilic properties was conducted using electron beam irradiation. Grafting of acrylic acid (AA) in/onto pre-irradiated PVDF films was investigated. Reaction parameters, monomer concentration and inhibitor concentration were examined. Radiation grafted films (PVDF-*g*-PAA) were synthesized with various grafting yields ranging from 12 to 130 wt % in presence of Mohr's salt (25 wt %). Below 80 wt % of monomer concentration, the degree of swelling was found to increase with the grafting yield. The PAA was arranged randomly in all PVDF matrix (grafting through). Above 80 wt % of monomer concentration, the PAA was grafted only onto the surface of PVDF films leading to a highly dense layer of PAA. Grafting through or surface grafting processes were achieved by varying the water fraction in the initial monomer solution. Water molecule acts not only as a carrier for the monomer but also as a plasticizer expanding the film in the three dimensions. Evidences of grafting through and surface grafting were produced using FTIR in ATR mode, SEM coupled to X-ray detection and XPS. An accurate quantification of AA units was possible up to the micromole via a Cu^{2+}–EDTA complex analyzed by UV–vis spectroscopy.

Keywords: PVDF; Radiation grafting; Acrylic acid

1. Introduction

Because of its excellent mechanical and physico-chemical properties, poly(vinylidene fluoride) (PVDF) has found wide-spread industrial applications and research interest since the 1960s. Especially, PVDF membranes are produced for separation and filtration. Often, these membranes are chemically and/or physically modified in order to match specific applications, e.g. ion-exchange membranes. As such, hydrophilic PVDF membranes have been studied [1,2] and applied for non-conventional field such as drug delivery [3,4]. Introducing hydrophilic groups on hydrophobic PVDF films surface is also of biological great interest. Indeed, the covalent immobilization of proteins on the surface of polymers is generally considered as a promising approach to enhance blood or tissue compatibility of biomaterials [5].

Several approaches have been developed to endow hydrophobic membranes with hydrophilic properties. These approaches have included coating and grafting. In the latter approach, various techniques were used for hydrophilic monomer (e.g. acrylic acid) grafting onto various hydrophobic polymers: pulsed plasma [6–8], corona discharge [9], ozone treatment [2], gamma radiation [8,10–12], electron-beam irradiation [13,14]. In semicrystalline polymers, ionizing radiation has the advantage of inducing the formation of stable radicals able to initiate the monomer grafting in a second step. The absorbed dose which is

---

[*] Corresponding author. Tel.: +33 1 69 08 48 34; fax: +33 1 69 08 96 00.

E-mail address: betz@drecam.cea.fr (N. Betz).

0032-3861/$ - see front matter © 2004 Elsevier Ltd. All rights reserved.
doi:10.1016/j.polymer.2004.10.052

proportional to the number of active radical sites inducing further grafting allows a precise control of radical initiator concentration. This elegant and easy technique is known as post-radiation grafting, or radiation-induced graft polymerization.

When the irradiated films are in contact with air—during or after irradiation—, radicals can react with oxygen leading to the formation of peroxy radicals ($POO^{\cdot}$) which can recombine and lead to the formation of peroxides (POOP), hydroperoxides (POOH), acids, alcohols or ketones. As described by Chapiro [15] grafting reactions on peroxidized polymers (so-called peroxide method) usually proceeds via thermal decomposition of peroxides and hydroperoxides which leads to alkoxy ($PO^{\cdot}$) radicals able to initiate radical addition polymerization of monomers. Still the exact nature of the initiators is not so clearly established and seems to depend on the chemical composition and the crystalline structure of the polymer. In fluorinated polymers such as poly(tetrafluoroethylene) (PTFE) or tetrafluoroethylene/hexafluoropropylene copolymer (FEP), it was concluded that graft polymerization initiation occurred from alkyl radicals resulting from deoxygenation of stable peroxy radicals [16–19]. In PVDF films, stable alkyl and peroxy radicals are stabilized by the crystalline zones [20–23]. These radicals exhibit considerable long lifetime at room temperature so that films can be stored for several years before grafting. A significant consumption of both alkyl and peroxy radicals was observed in electron-irradiated PVDF grafted with N-vinylpyrrolidone [24] and in γ-ray-irradiated PVDF grafted with styrene [25]. The nature of the initiating sites is addressed in this paper.

Post-radiation grafting to polymeric films proceeds from the substrate surface and as the films swell, the grafting progressively occurs throughout the films until the whole bulk is grafted (grafting-through). This mechanism is known as the *grafting front mechanism*. It was first described in Chapiro's pioneer work in the early 60s [15]. Such a grafting front mechanism was evidenced in poly(vinyl fluoride) electron-grafted with N-vinylpyrrolidone using differential interference contrast microscopy by Ellinghorst et al., [26]. Ellinghorst et al., also performed electron-grafting of PVDF with various monomers [27]. In the case of AA, grafting-through could not be obtained in pure monomer at any temperature ranging from 50 to 80 °C. This progression of the grafting front inside the film depends on various parameters among which the solubility properties of monomer and graft polymer. The existence of this mechanism in PAA grafting of PVDF is discussed using, SEM coupled to X-ray detection, XPS and FTIR in transmission and ATR mode.

The present paper also reports on the effect of inhibitor, temperature, monomer concentration on the grafting yield and quantification of AA units by UV–vis spectroscopy via toluidine blue and Cu^{2+}–EDTA complexes in PVDF-grafted-PAA (PVDF-*g*-PAA) films.

2. Experimental section

2.1. Materials and reagents

The following chemicals were purchased from Sigma-Aldrich and used as received: acrylic acid (AA) stabilized with 200 ppm hydroquinone, Mohr's salt [$FeH_8N_2O_8S_2\cdot 6\text{-}6H_2O$], potassium *tert*-butoxide C_4H_9OK 95%, sulfuric acid H_2SO_4, copper II chloride, toluidine blue powder. From Merck, Titrisol® of 0.1 M NaOH and 0.1 M HCl were used for titration purpose. Hydrophobic PVDF films (PVDF α Atochem, 25 μm thick) were Soxhlet-extracted in toluene and dried at 50 °C under vacuum. EPON® resin (Fluka) was prepared following Fluka's instructions with two polymerization temperature steps. Ion-exchange water was used throughout.

2.2. Radiation grafting of PVDF with acrylic acid

Post-irradiation grafting was accomplished by first irradiating the PVDF films at room temperature under a helium atmosphere using a 2.5 MeV Van de Graaf accelerator. Films were irradiated at an absorbed dose *D* of 150 kGy (dose-rate: 500 kGy/h). Immediately after irradiation, films were stored under nitrogen atmosphere at room temperature. Before grafting, films were cut ($\sim 20\times 20\ mm^2$), measured (surface area and thickness) weighted and characterized by FTIR spectroscopy. Then, the films were immersed at room temperature into a grafting solution containing AA and Mohr's salt (0.25 wt % for most experiments). Under these conditions, more than 99% of acrylic acid monomer will be present in the non-ionized form. These solutions were deaerated by bubbling nitrogen during 15 min in glass tubes. Tubes were hermetically closed and put into a thermostated silicon oil bath at 60 °C for 1 h otherwise stipulated. Films were first washed in fresh water and then Sohxlet-extracted in boiled water overnight. Films were dried at 50 °C in vacuum to constant weight. The grafting yield *Y* was determined gravimetrically according to the following formula:

$$Y(\mathrm{wt}\%) = \frac{m_\mathrm{f} - m_\mathrm{i}}{m_\mathrm{i}} \times 100$$

where m_f and m_i are the weights of grafted and initial film, respectively.

2.3. Infrared spectroscopy measurements

FTIR spectra of the polymer films were carried out with a Nicolet Magna-IR™ 750 spectrometer equipped with a DTGS detector. The sample compartment is continuously purged with by a nitrogen flux. In order to improve the quality of the spectra in transmission mode, measurements were recorded positioning the samples at the Brewster's angle to eliminate interference fringes. Background acquisition was performed before each sample acquisition. To analyze the first micrometers of the film, spectra were recorded in an Attenuated Total Reflection mode (ATR) using a diamond-crystal with single reflection. Both spectra were collected by cumulating 32 scans at a resolution of 2 cm^{-1}.

2.4. UV–vis spectroscopy

A UNICAM model UV 300 spectrophotometer was used to measure the maximum absorbance at 633 nm for toluidine blue solutions and 740 nm for Cu^{2+}–EDTA complex. Toluidine blue protocol was described by Kang et al., [28]. Quantification by cupric ions was developed in our laboratory. PVDF-*g*-PAA films were put in 20 ml of 0.1 M NaOH solution during 30 min. Films were then rapidly dried on filter paper and checked by FTIR to determine the complete carboxyl ionization. Films were transferred to 10 ml of 0.1 M $CuCl_2$ (or $CuSO_4$) solutions and stirred for at least 1 h. After a quick rinsing in deionized water, films were immersed in a 0.1 M EDTA solution for an additional hour. All the cupric ions were desorbed in a Cu^{2+}–EDTA complex form analyzed by UV–vis spectroscopy. Assuming that a Cu^{2+} ion reacts with two carboxylate groups, it is then easy to deduce the number of carboxyl groups present in a PVDF-*g*-PAA film. The best limit of this dosing method was found to be the micromole.

2.5. Scanning electron microscopy

Scanning electron microscopy (SEM) has been carried out with a Phillips apparatus equipped with a LaB_6 tip, and coupled with a PGT-Princeton Gamma Tech. X-ray detector and a PRISM Digital spectrometer (LMS, Ecole Polytechnique). The used technology is based on Energy Dispersive System (EDS). Samples were firstly immersed in a potassium *tert*-butoxide solution (8:8 w/w). A vivid violet colored the films. Then, films were embedded in EPON resin before being cut by a Leica microtome. The cut edge was coated with Au using a sputtering device and analyzed.

2.6. X-ray photelectron spectroscopy (XPS)

X-ray photoelectron spectra were recorded on a HP5950A spectrometer using a monochromatic Al Kα X-ray source (1486.6 eV). The concentric hemispherical electron energy analyzer is equipped with a multichannel detector operating at a constant energy analyzer mode at electron take-off angle of 51.5°. The use of a flood gun permits to reduce charge effects. Pass energy of 50 eV is used for both the survey and core level scans. The resolution was between 0.8 and 1 eV.

Binding energies were determined by reference to the C_{1S} component due to carbon bond only to carbon and hydrogen, set at 285 eV. Linear baseline for background subtraction and Gaussian functions were used for peak fitting. Atomic percentages were determined from peak areas by using Scofield factors [29] ($C_{1s}=1$, $F_{1s}=4.43$, $O_{1s}=2.93$, $N_{1s}=1.8$).

3. Results and discussion

3.1. Initiation of grafting

As underlined in Section 1, the nature of the active sites able to initiate polymerization (alkyl $P^{\cdot}$ and peroxy $POO^{\cdot}$ radicals, peroxides POOP and hydroperoxides POOH) seem to depend strongly on the chemical composition of the polymer. In PVDF, we identify the active sites able to initiate a polymerization as: alkyl radicals (mid-chain $–CF_2–C^{\cdot}H–CF_2–$ and end-chain $–CF_2–C^{\cdot}H_2$), end-chain peroxy radicals ($POO^{\cdot}$), primary hydroperoxides ($–CF_2–CH_2–OOH$) [20,22]. As it is known that radicals initiate graft polymerization, we wanted to evaluate the contribution to grafting of the hydroperoxides.

In Fig. 1a,a′ are shown the transmission spectra of a 150 kGy—the maximum absorbed dose used in the work—electron irradiated PVDF sample compared to that of a virgin sample. Indeed, as emphasized on the subtraction spectrum, irradiation and post-irradiation induced defects are observed which consist mainly in oxidation defects and dehydrofluorination (–CH=CF– at 1716 cm^{-1}) [30]. In the OH valence absorption region, a narrow band at 3650 cm^{-1} and three large bands at 3620, 3580 and 3540 cm^{-1} are observed and assigned to free end-chain alcohols ($–CF_2–CH_2OH$), associated and free in-chain alcohols ($–CF_2–CHOH–CF_2–$) and primary hydroperoxides ($–CF_2–CH_2–OOH$), respectively [31]. The formation of acid fluoride (COF at 1852 cm^{-1}) is observed. Chain scission ($–CH=CF_2$) scarcely occurs as witnesses the small increase of the 1754.6 cm^{-1} absorption band. Despite irradiation and oxidation defects are feebly generated at 150 kGy in the PVDF samples, the formed hydroperoxides could give rise to grafted chains and homopolymer as described by Chapiro [15]. The hydroperoxide concentration in PVDF is estimated to be 0.4 μmol kg^{-1} if an absorption coefficient value of 310 kg mol^{-1} cm^{-1} is assumed [32]. Compared to the total radicals concentration (3 and 9 mmol kg^{-1} for absorbed doses of 100 and 200 kGy, respectively [25]), the hydroperoxides concentration is extremely low. In addition, thermal stability of fluorinated hydroperoxides was observed up to 80 °C [32]. Therefore, in order to evaluate the thermal stability of hydroperoxides during grafting, annealing of 150 kGy electron irradiated films was performed at 60 °C during 24 h under N_2 atmosphere. As observed from Fig. 1b,b′, they are stable at the temperature used for grafting, as all the other radiolysis and oxidation products. Only a small increase of the free end-chain alcohol (presumably due to peroxy radical conversion induced by heating) occurs.

Peroxides could also be induced by irradiation but infrared is a poor technique to observe peroxide bonds

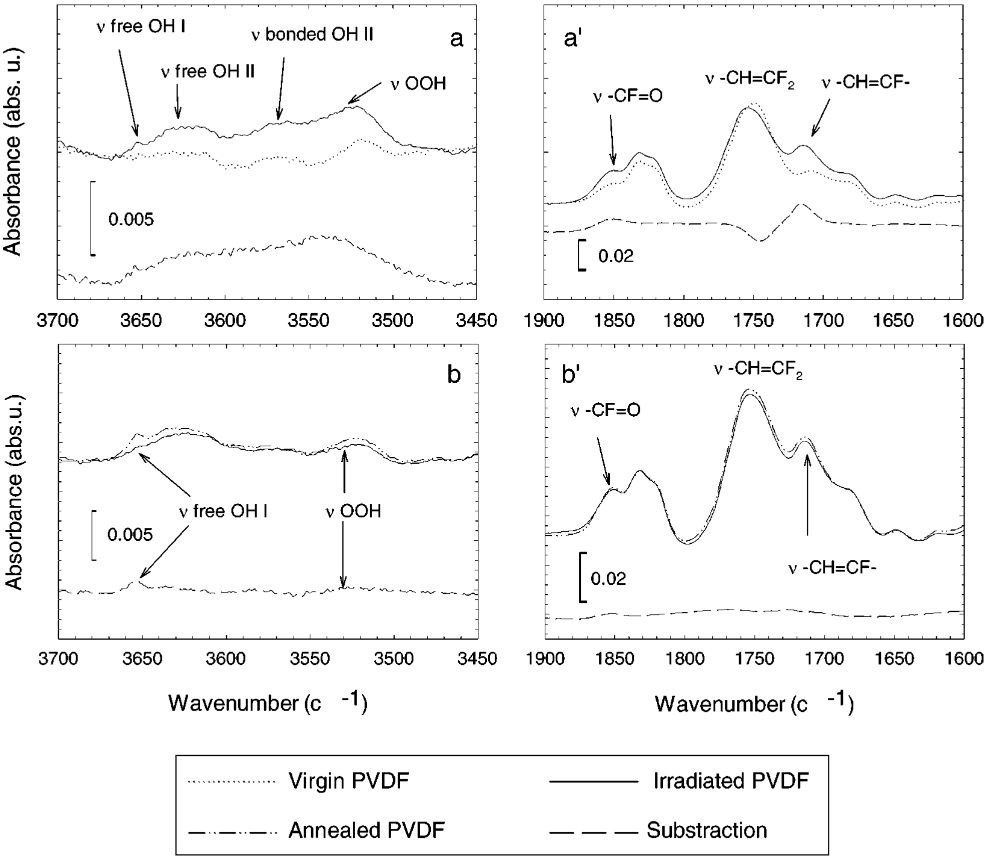

Fig. 1. FTIR transmission PVDF spectra illustrating the effect of a 150 kGy electron irradiation (a, a′) and 24 h annealing at 60 °C under N_2 (b, b′) atmosphere.

which have a weak IR absorption. Moreover, the OO bond valence absorption of peroxides is difficult to observe in fluoropolymers because it is screened by the high intensity CF valence absorptions. Chemical methods can be used though they are difficult to implement in insoluble polymers such as can be irradiated PVDF (gel dose at ca 30 kGy). In a 500 kGy electron irradiated ETFE, the concentration of peroxides was found to be very low when compared to that of hydroperoxides, alcohols and radicals [32]. Anyhow, peroxides are expected to have higher stability than hydroperoxides and therefore should not contribute to grafting initiation.

From the results and discussion above, it can be considered that mainly the stable alkyl and peroxy radicals initiate the grafting reaction.

3.2. Optimization of grafting conditions

The irradiated films containing the initiating radicals (Section 3.1) are immersed in the acrylic acid water solution. Grafting experiments are performed at 60 °C during 1 h. At this temperature, two chemical reactions occur: i) thermal homopolymerization of acrylic acid in solution, and ii) grafting reaction on the solid substrate. Water is a solvent for both the grafted chains and the homopolymer. Therefore, when the homopolymer is formed in high quantity in solution, it can diffuse in the graft copolymer. If not entirely extracted from the PAA grafted films, erroneous grafting yield is measured [13]. Consequently, addition of inhibitor to the AA solution is needed to minimize homopolymerization. At the same time, hindering of the grafting reaction cannot be excluded, the minor consequence being a lowering of the grafting yield. A well known acrylic acid polymerization inhibitor, Mohr's salt, was tested in a 75% monomer solution. At this concentration, homopolymerization takes place in the grafting solution, films are highly grafted and grafting occurs in the bulk of the film which exhibits a 3D increase of its dimensions. These conditions were deliberately chosen in order to highlight as much as possible the inhibitor effect on the grafting yield of the film and the homopolymerization in solution. Results are presented in Fig. 2. As expected, no homopolymerization occurs in the grafting solution. With increasing inhibitor concentration, the grafting yield of the film falls from 130% to 0.01% wt % [Mohr's salt] to 70% where it remains stable. As the inhibitor is able to diffuse in the film, it speeds up the termination reaction of the grafting polymerization thus yielding to lower grafting yields.

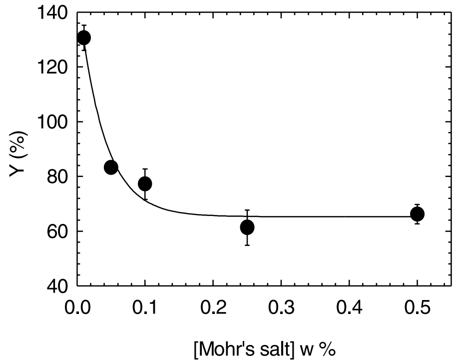

Fig. 2. Variation of the grafting yield versus Mohr's salt concentration in the grafting solution. Grafting parameters: $D=150$ kGy, [AA] = 75 vol %, grafting temperature and time is of 60 °C and 1 h, respectively.

Inhibitor's influence on the grafting yield decrease reaches a maximum at a concentration of 0.25 wt % presumably due to diffusion limited effects.

In order to determine optimal grafting time, grafting kinetics were performed that are shown in Fig. 3 for two different doses, 30 and 100 kGy. Grafting yield sharply increases in the first hour. Beyond 1 h, the grafting rate slows down leading to an asymptotic saturation of the grafting yield. Large standard deviations on grafting yields are observed after 4 h especially on the 30 kGy irradiated films.

The absorbed dose *D* also influences the grafting reaction. When the absorbed dose increases, the number of excitation and ionization events increases as a consequence of the electronic interactions of the incident electrons with the polymer leading to an increase of the grafting initiators. If so, then increasing the number of radicals is expected to induce a continuous rise of the grafting yield. As shown in Fig. 4 the grafting yield obtained in pure monomer passes through a maximum of approximately 14% at 10 kGy and levels off just under 10% with further increasing dose. The influence of storage time as long as 5 years is also shown in Fig. 4. It has no effect on the grafting yield at 10 kGy, but slightly decreases the grafting yield values for higher doses so that leveling off occurs more or less at ca 8%. Consequently, reproducible pre-irradiated PVDF films are obtained leading to proper and easy-going grafting results even after a long-term period.

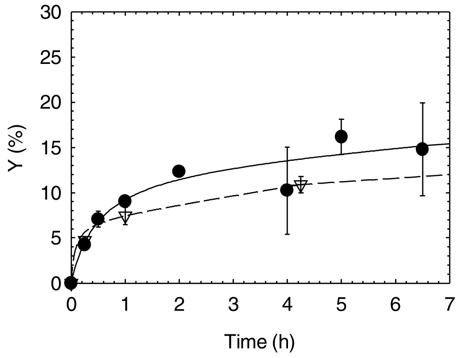

Fig. 3. Grafting kinetics: (▼) 100 kGy; (●) 30 kGy, [AA] = 100 vol %, [Mohr's salt] = 0.25 wt %, 60 °C.

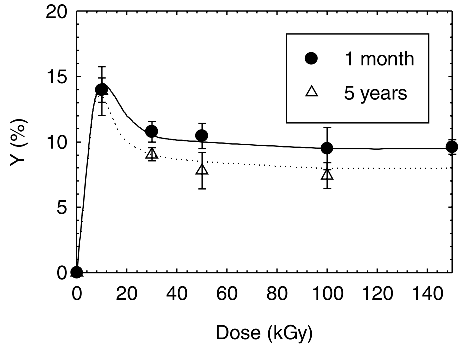

Fig. 4. Grafting yield versus absorbed dose, [AA] = 100 vol %, [Mohr's salt] = 0.25 wt %, grafting temperature and time is of 60 °C and 1 h, respectively.

In addition to the presence of a maximum grafting yield, differences are also observed in the behavior of the films dimensions. At 10 kGy the grafted film expands and remains transparent while at higher doses, no expansion occurs and the films are opaque. As the absorbed dose increases, in most polymers part of primary radicals recombines leading to the formation of crosslinks. As the density of crosslinks increases, the polymer tends toward the formation of an insoluble network. The dose at which the film becomes insoluble (*gel dose*) can be estimated by sol–gel experiments in suitable solvents. The gel dose of PVDF is known to occur in the 20–30 kGy range ([33] and references therein). Consecutively, at lower dose (10 kGy) PVDF polymer chains mobility allows a good accessibility of the monomer to bulk radicals thus increasing the grafting yield. The grafting occurs in the bulk; the PVDF film expands. At doses higher than the gel dose, only a fraction of primary radicals is reached by the monomer to start and propagate the grafting reaction because of the crosslinks induced by irradiation in the PVDF film. When the absorbed dose increases, the number of crosslinks increases which renders the penetration of the monomer progressively uneasy. Therefore, the grafting yield decreases and finally reaches a constant value in the dose-range examined. Similar behavior of the grafting yield with increasing dose was observed with vinyl fluoride (VF)/vinylidene fluoride copolymers electron grafted with NVP [34]. The copolymer with the lowest VF content (20 mol%) shows a maximum close to 10 kGy with a grafting yield of ca 20 wt %. It was assumed that the occurrence of the maximum was the point at which the grafting reaction became diffusion controlled: the monomer is consumed in the surface layers before it can reach the inside of the films.

Under these conditions, it was decided to perform grafting for 1 h at 60 °C in the presence of 0.25 wt % of Mohr's salt on 150 kGy irradiated films.

3.3. Grafting yield and monomer concentration dependence

Fig. 5 shows the variation of the grafting yield as a function of the AA concentration. It can be seen that by increasing monomer concentration, the grafting yield increases steadily up to approximately 40% at 50 vol % of AA due to an increase of the polymerization rate. Then a rapid rise up to more than 120% at 80 vol % of AA where the grafting yield is at a peak is observed. For higher AA concentrations (90 and 100 vol %), a sharp decrease of the grafting yield occurs.

The macroscopic examination of the grafted films shows different results whether the monomer concentration is lower or higher than that of the peak at 80 vol % of AA. For monomer concentrations below 80 vol %, the films were expanded and transparent. This was not the case for monomer concentrations higher than 80 vol %. The films did not exhibit any change of their surface area (very slightly for 90 vol %) and became white and non-transparent. As is shown in Fig. 6 which plots the surface area expansion ($Y_E = (Sf - Si)/Si \times 100$) as a function of the grafting yield, the surface area expansion is directly linked to the degree of swelling when the monomer concentration is below 80 vol %. It is linearly proportional to the grafting yield. For higher concentrations, the surface area expansion is close to zero. Also plotted in Fig. 6 is the volume expansion ($Y_E = (Vf - Vi)/Vi \times 100$) versus the grafting yield. The volume expansion increases linearly with the grafting yield (correlation factor of 0.94) over the whole concentration-range. This illustrates that, at monomer concentrations higher than 80 vol %, all the PAA is grafted onto PVDF film surface and the thickness variation of the film gives directly the grafting yield.

As the PAA is insoluble in its monomer, grafting with pure AA prevents the diffusion of monomers to the inner part of the film due to its exclusion from graft PAA onto PVDF surface. Therefore, these films with a white PAA layer grafting are only ‘surface’-grafted. Our results are consistent with Ellinghorst et al., study [27].

The addition of water molecules that solubilize both the PAA and the AA, allows the AA diffusion in the water soaked PAA top-layer. Water molecules act not only as a carrier for the monomer AA but also as a plasticizer of the soaked PVDF-*g*-PAA. Progressively, as the presence of water expands PVDF chain network, the AA penetration into PVDF bulk is favored. This physical effect is predominant from 99 up to 80 vol % of aqueous AA solution. At 80 vol % of AA aqueous solution, an exact equimolarity exists between water molecules and AA units. Hydration is at its maximum. Radical sites induced by electron irradiation in the films bulk become all very accessible and PAA copolymerization can occur everywhere in the PVDF film, swelling it and expanding it in a homogeneous way. The isotropic PAA distribution in the PVDF matrix is attested by film transparency. Then, as more water molecules are added, the monomer concentration decrease reduces the polymerization rate and the grafting yield decreases, but grafting occurs in the bulk due to the plasticizing effects of the water molecules.

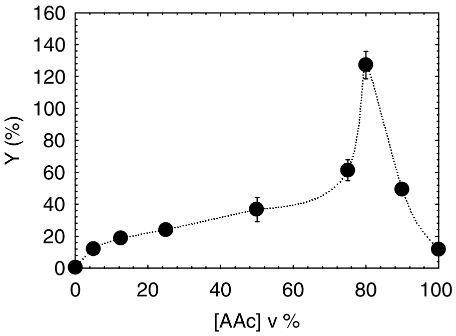

Fig. 5. Grafting yield versus monomer concentration, $D = 150$ kGy, [Mohr’s salt] = 0.25 wt %, grafting temperature and time is of 60 °C and 1 h, respectively.

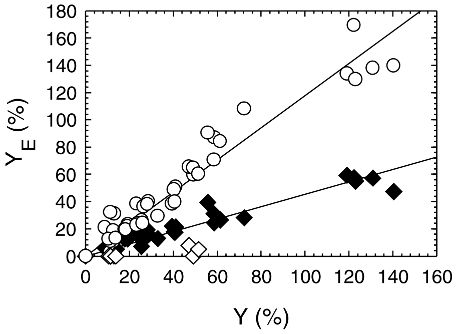

Fig. 6. Film expansion versus grafting yield, ○ volume, ◆ surface; ◇ surface expansion of surface grafting samples; $D = 150$ kGy, [Mohr’s salt] = 0.25 wt %, grafting temperature and time is of 60 °C and 1 h, respectively.

The grafting yield drops rapidly from 130 to 40 wt %, then slowly until 10 wt %. This is principally due to two additional effects that overcome the water plasticizing effect. Firstly, the dilution induces less monomer and less probability for AA to encounter another AA leading to a lower polymerization rate. Secondly, the increase in polymer chains mobility favors termination reactions on growing PAA chains.

At peak, despite the presence of the inhibitor in the solution, a contribution of the Trommsdorff effect to the dramatic increase of the grafting yield at 80 vol % cannot be totally excluded. This gel effect is the result of a sudden self-acceleration of polymerization reaction enhanced by the decrease of the termination rate due to an increased polymerization medium viscosity.

3.4. Morphology and structure of PVDF-g-PAA copolymers films

To gain a better understanding of the grafting process, it is necessary to determine the graft distribution over the film thickness. Four different grafted films have been chosen:

two transparent ones at 10 and 40 wt % of grafting yield and two white films at 10 and 40 wt % of grafting yield corresponding to initial monomer concentrations of 5, 50, 100 and 90 vol %, respectively. Films were immersed in a potassium *tert*-butoxide aqueous solution (8:8 w/w) in order to deprotonate the PAA chains. Potassium PAA salts are obtained in 1 h. After embedding in an epoxy resin, thin sections of the films were cut and observed perpendicular to the film surface by SEM coupled with X-ray detector. X-ray detection permits to obtain atomic distribution profiles across the film thickness by selecting potassium and fluorine X-ray energies. Potassium reveals the AA distribution while fluorine, PVDF location. In this way, it is possible to visualize the grafting front location.

Mechanical behavior is very different when comparing these four films. Highly grafted and expanded films are brittle while surface grafted ones (either highly or poorly grafted) remain as supple as the original PVDF. During microtoming, each one of them exhibited different cutting qualities (Fig. 7) revealing various mechanical properties. The most brittle film corresponding to [AA] 50 vol % is the most homogeneous. The other ones show stretches and rips depending on their grafting yield.

At low grafting yield in pure AA (Fig. 7a), potassium profile gives around 25% of graft on both edges and 50% of pure PVDF in the middle: AA was not able to reach the inner part of PVDF film. At similar grafting yield but in presence of water ([AA] = 5 wt %, Fig. 7c), the grafting front is more advanced due to water plasticizing effect as discussed previously. Indeed, only a thickness of 4 μm is potassium free on [AA] 5 vol % film compared to 10 μm potassium free on [AA] 100 vol % film. At higher grafting yield (Fig. 7d), grafting-through is achieved homogeneously in the bulk for [AA] 50 vol % film. The penetration depth at similar grafting yield on [AA] 90 vol % film is lower (Fig. 7b). At [AA] 90 vol %, [AA] has twofold molar excess compared to water molecules and the film is heterogeneous. EDAXS profiles confirm our assumption on the water plasticizing effect and its important role in the grafting-through process. It should be noted though, that at this scale fluorine atoms are detected throughout the entire analyzed film section giving indication of no real PAA layer, even on the 'surface'-grafted films.

In order to get more data about surface chemical composition, XPS experiments were performed which give information on the top ~5 nm polymer film. XPS survey spectra of virgin PVDF and PVDF-*g*-PAA 'surface'-grafted samples are presented in Fig. 8. The virgin PVDF shows a typical PVDF surface with an intense F_{1s} peak (Fig. 8a). The ratio of the F_{1s} to C_{1s} peaks is characteristic of the PVDF (Table 1). After grafting, an additional peak of oxygen appears due to the presence of the grafted PAA. As illustrated (Fig. 8) and calculated (Table 1), there is a significant decrease in relative *F* content when the samples are grafted. Compared to a grafting performed in pure AA monomer (Fig. 8b), more fluorine is observed when grafting is performed in an aqueous solution ([AA] = 5 vol %, Fig. 8c). Indeed, in the former case, no F_{1s} peak is seen on the survey spectrum (Fig. 8b). In this case, no surface expansion of the sample is observed upon grafting while a small expansion of the surface occurs in the case of grafting in water. As the same surface area is analyzed and as the two samples exhibit comparable grafting yield, the expansion of the surface could be responsible of the huge difference in the *F* content between the two grafted samples.

Table 1
Atomic percentages of C, F, O from XPS for virgin PVDF, 'surface' grafted PVDF-*g*-PAA ([AA] = 100 vol %) and grafted-through PVDF-*g*-PAA ([AA] = 5 vol %)

Sample	C_{1S} (%)	F_{1S} (%)	O_{1S} (%)
Virgin	49.3	47.5	3.2
Surface grafting	61.4	0.4	37.7
Grafting-through	70.5	12.2	15.4

The values of atomic percentages were obtained from the core line spectra of the atom concerned (survey spectra are shown in Fig. 8).

More detailed chemical analysis of PVDF surface modification is obtained from the C_{1s} core level spectra depicted in Fig. 9. Virgin PVDF C_{1s} shows two peaks at 286.6 and 291.1 eV for CH_2 and CF_2, respectively, separated by 4.5 eV. A slight oxidation of 3.2% is detected due to oxidation during storage. The O_{1s} corresponding signal was decomposed into two Gaussian peaks at 532.8 and 534.6 eV for C=O and C–O, respectively (not shown). These oxidation defaults are mainly carboxylic acid type. After grafting, three additional peaks corresponding to PAA groups are observed at 285, 285.7 and 289.4 eV for CH_2, CH and COOH, respectively. An oxidation peak at 287.3 eV that represents approximately 5% of total C_{1S} peaks area has to be added to the decomposition in order to fit properly the experimental data in accordance with the initial oxidation found on virgin PVDF (Table 1). The corresponding O_{1s} core level spectrum also confirms oxidation presence by a 5% increase of C=O component (spectrum not shown). This oxidation may come from initial PVDF film storage and/or little post-irradiation oxidation.

The graft PAA is mainly located in the surface as it was pointed out on SEM micrograph (Fig. 7). An estimation of the covering degree can be obtained by calculating the rate of PAA unit from the C_{1s} line as:

$$\text{Covering Degree (\%)} = \frac{\frac{n_{\text{PAA}}}{3}}{\frac{n_{\text{PVDF}}}{2} + \frac{n_{\text{PAA}}}{3}} \times 100$$

where n_{PAA} equals to the sum of PAA peaks area divided by Scofield factor and n_{PVDF}, PVDF peaks area sum divided by its corresponding Scofield factor.

In presence of water ([AA] = 5 vol %), the PAA covering degree is equal to 57% for PVDF-*g*-PAA. For the PVDF grafted in pure monomer, the covering degree cannot be calculated because of a too low *F* content. The higher PVDF peaks contribution (Fig. 9) together with surface area expansion give evidence of increased diffusion of AA in the

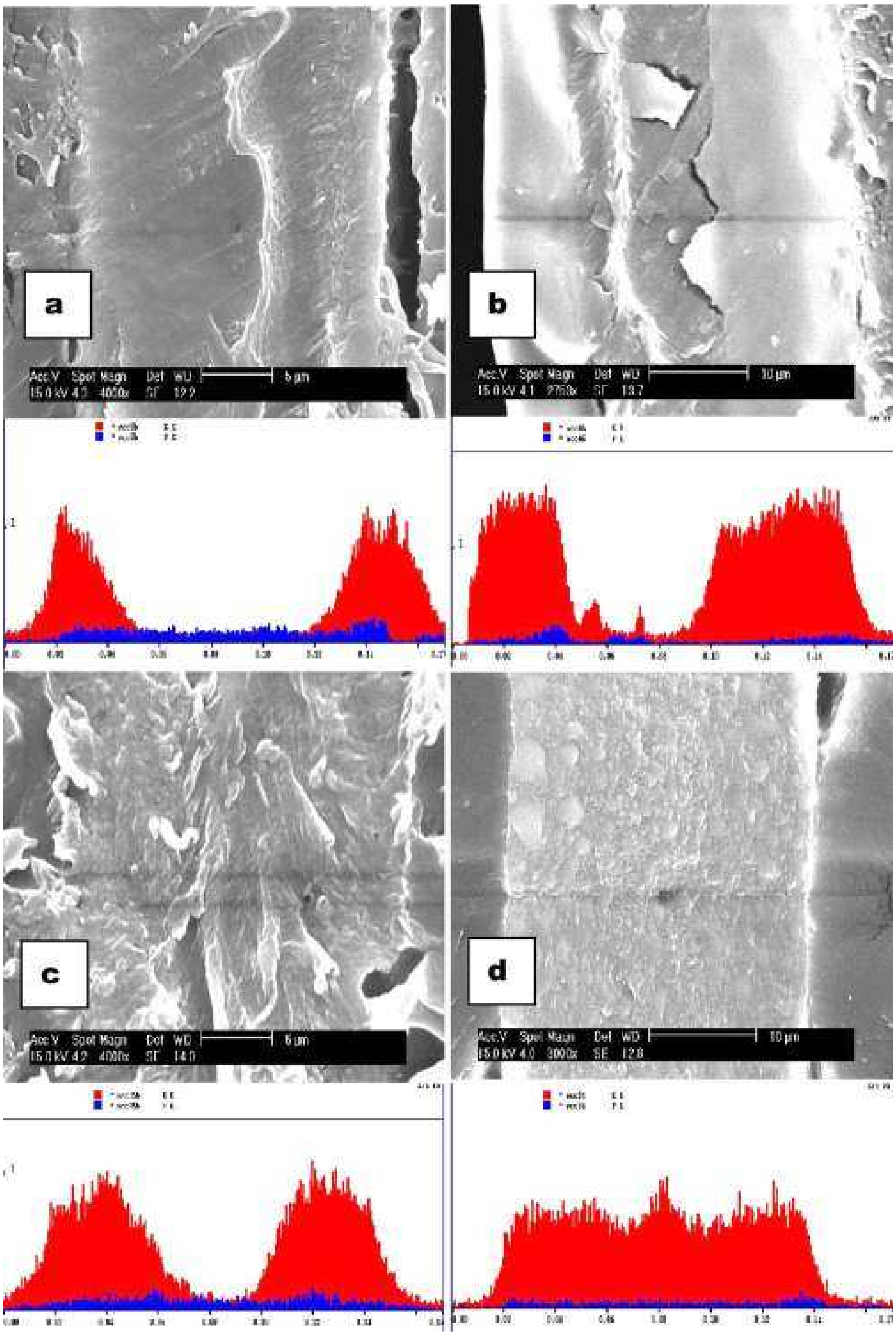

Fig. 7. SEM micrographs and profiles of PVDF-*g*-PAA films initially irradiated at 150 kGy, grafted at 60 °C, 1 h with [Mohr's salt] = 0.25 wt % and treated in a solution of *t*BuOK (8:8 w/w). (a) $Y = 8.8$ wt %, [AA] = 5 vol %, (b) $Y = 40.8$ wt %, [AA] = 50 vol %, (c) $Y = 11.3$ wt %, [AA] = 100 vol %; (d) $Y = 47.21$ wt %, [AA] = 90 vol %. In profiles, red corresponds to potassium and blue, to fluorine atoms.

PVDF during the grafting when it is performed in aqueous solution.

The PAA layer should then be rather represented by a PAA gradient from the PVDF film surface to the inner part with various penetration front location and densities depending on initial grafting conditions.

3.5. PAA quantification

The chemical composition of PVDF-*g*-PAA copolymers films was determined by FTIR in transmission and ATR mode. Transmission spectra give information on the bulk of the films while the ATR experiments analyze roughly the

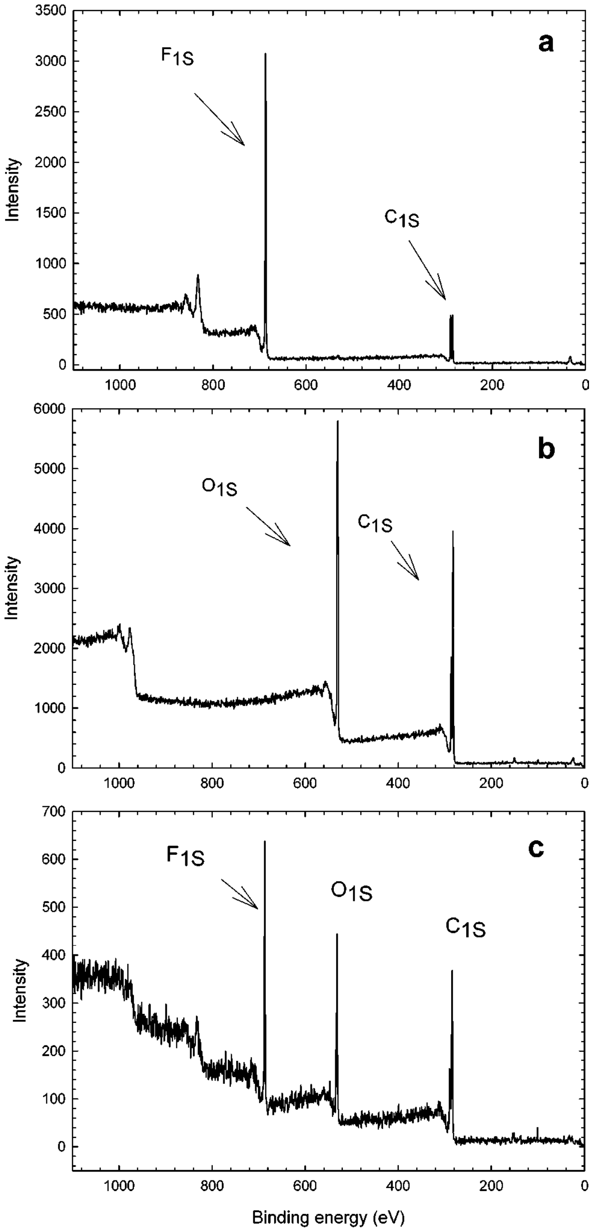

Fig. 8. XPS survey spectra of (a) virgin PVDF, (b) PVDF-*g*-PAA, [AA] = 100 vol %, Y = 13%, (c) PVDF-*g*-PAA, [AA] = 5 vol %, Y = 13%.

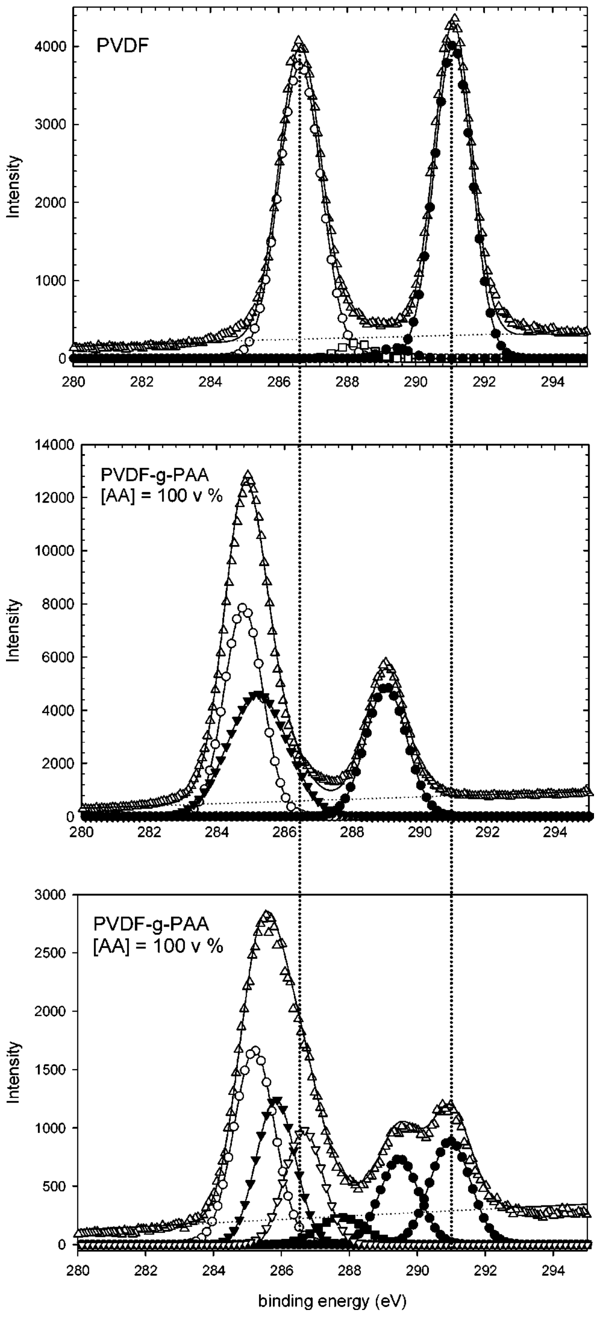

Fig. 9. XPS C_{1S} spectra (Δ) and C_{1S} decomposition: (○) $\mathit{CH_2}$–CH (PAA); (▼) CH_2–CH (PAA); (▽) $\mathit{CH_2}$–CF_2 (PVDF); (□) oxidation; (●) C–O (PAA); (■) CH_2–$\mathit{CF_2}$ (PVDF); ···. base line; — fit.

first micrometer of the films at 2000 cm^{-1}. All spectra of the PVDF-*g*-PAA films were similar and previously described in detail [13]. A characteristic band for the O–C=O stretching (ν = 1710 cm^{-1}) related to the COOH groups of the grafted PAA chains (Figs. 10–12) is observed. The corresponding OH vibration gives rise to a broad band in the 2500–3500 cm^{-1} region on which are superimposed the CH_2 asymmetric and symmetric stretching absorption bands of PVDF at 3025 and 2985 cm^{-1}, respectively. The 1500–400 cm^{-1} range gives no useful information in transmission because of the high intensity absorption bands of PVDF. Since the concentration of a functional group is directly proportional to its absorption peak area, the absorption intensity of every absorption band related to PAA increases as the grafting yield increases (Fig. 10). The PAA carbonyl absorption band of very high intensity due to a high absorption coefficient is close to the saturation even at ca 10% grafting yield.

Figs. 11 and 12 were obtained in ATR mode and compare

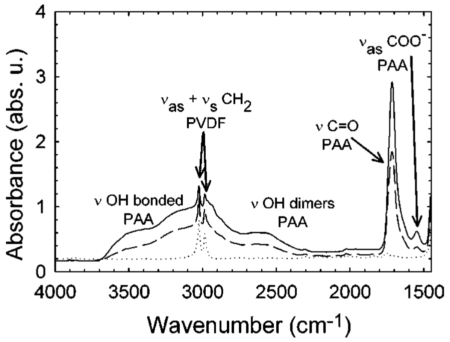

Fig. 10. FTIR transmission spectra of 150 kGy electron irradiated PVDF (···) and PVDF-*g*-PAA films copolymers at 10% grafting yield (– – – [AA] = 100 vol %) and 40% grafting yield (— [AA] = 50 vol %). [Mohr's salt] = 0.25 wt %, grafting temperature and time is of 60 °C and 1 h, respectively.

the surface of grafted samples with different structure for two comparable grafting yields. Contrarily to transmission mode, ATR analysis investigates the first 0.55 μm of the film surface at 3000 cm^{-1}. In ATR mode, surface grafted films spectra ([AA] of 90 and 100 vol %) have stronger absorption intensity for PAA signals than bulk grafted films.

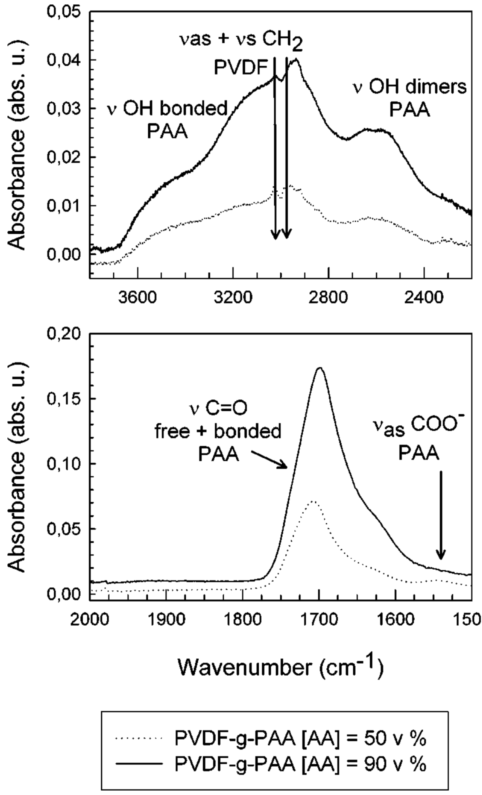

Fig. 11. FTIR spectra in ATR mode—comparison between PVDF-*g*-PAA synthesized from [AA] = 50 vol % and [AA] = 90 vol %. *D* = 150 kGy, [Mohr's salt] = 0.25 wt %, grafting temperature and time is of 60 °C and 1 h, respectively.

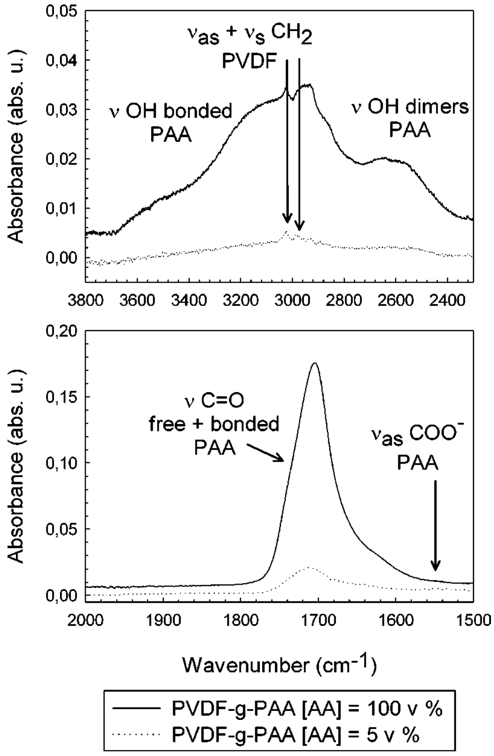

Fig. 12. FTIR spectra in ATR mode—comparison between PVDF-*g*-PAA synthesized from [AA] = 5 vol % and [AA] = 100 vol %. *D* = 150 kGy, [Mohr's salt] = 0.25 wt %, grafting temperature and time is of 60 °C and 1 h, respectively.

Conversely, the CH_2 PVDF stretching vibration doublet remains observable for bulk grafted PVDF-*g*-PAA films and almost completely disappears for surface grafted PVDF-*g*-PAA films. This is in agreement with XPS results where a higher density of PAA is observed in the surface in the case of 'surface'-grafted film.

An unexpected peak at 1555 cm^{-1} was also observed. It was more or less expressed from a sample to another. By immersing films into an acidic H_2SO_4 solution (pH 2) at different times, it was demonstrated that the decrease of this peak contributes to the increase of the COOH peak at 1710 cm^{-1} (Fig. 13). This suggests that the peak at 1555 cm^{-1} corresponds to carboxylates (asymmetric stretching vibration of CO_2^-) that progressively converse in acids upon acidification of the films. This conversion is reversible though the films loose mechanical properties progressively.

Quantification of carboxylic functions by IR was therefore difficult due to different molar absorption coefficient of carboxyl functions. Therefore quantification was performed using analytical methods. Firstly pH-titration was achieved. PVDF-*g*-PAA films were immersed in a titrated sodium hydroxide solution for one hour. Aliquots of this solution were then titrated by hydrochloric acid. This back-titration

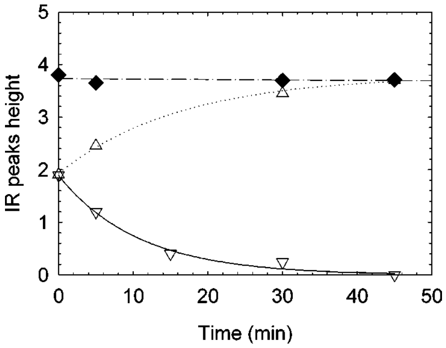

Fig. 13. Carboxyl peaks height of 30% bulk grafted PVDF-*g*-PAA film versus time in aqueous solution of H_2SO_4 (pH 1): (●) 1555 cm^{-1}; (▼) 1710 cm^{-1}; (♦) sum of heights. $D=150$ kGy, [AA] = 25 vol %, [Mohr's salt] = 0.25 wt %, grafting temperature and time is of 60 °C and 1 h, respectively.

permits to dose accurately millimoles of AA. The accuracy requires controlled conditions such as the use of boiled deionized water to avoid undesired carbonatation, titrated solutions (Titrisol®) and automatic burette. For low yield grafted films, this technique was inadequate and a UV–vis back-titration was necessary to dose the micromole of AA. Quantification using toluidine blue (TB) was adapted from Kang et al., [28]. For 'surface' grafted films with roughly 7% grafting yield ([AA] = 100 vol %), molar TB/AA ratios are very low and equal to 0.066 ± 0.017 corresponding to 0.15 ± 0.07 μmol/cm^2. With higher 'bulk' grafted films obtained with [AA] = 50 vol % (ca 27%), molar TB/AA ratio decreases to 0.020 ± 0.009. However, as the surface area is expanded in this latter case the toluidine blue molar number per area unit equal to 0.12 ± 0.09 μmol/cm^2 remains unchanged. This means that toluidine blue doses only AA units present on the uppermost surface. Thus, this value corresponds to the saturation limit. Steric hindrance avoids toluidine blue to access to all AA units.

Cupric ions are smaller and have a high affinity for EDTA (ethylene diamine tetra-acetic acid). A protocol was then elaborated to back-titrate low yield grafted films immersed in a cupric ion solution and desorbed in EDTA solution. The EDTA–cupric ion complexes are dosed by UV–vis spectroscopy. Two salts have been tested: copper II sulphate and copper II chloride. With copper II sulphate 100% of AA units are accurately dosed with a Cu^{2+}/AA molar ratio equal to 1.02 ± 0.13 while with copper II chloride only 75% of the AA units are dosed with a Cu^{2+}/AA molar ratio equal to 0.74 ± 0.11. This is due to the difference of pH between the two solutions, for the used conditions, pH_{CuSO_4} is greater than pH_{CuCl_2}. A small fraction of the pendant acid groups along the PAA chain is ionized in contact with $CuCl_2$ solution. The difference of reactivity which is less for carboxylates than for carboxylic acid explains the observed difference.

4. Conclusion

Several parameters governing the structure and morphology of PVDF-*g*-PAA films have been determined. Initial grafting conditions are important for the final mechanical properties of the materials. Grafting-through or 'surface'-grafting can be achieved by varying the water fraction in the initial monomer solution. Evidence of the plasticizing effect of water molecules was pointed out and confirmed by SEM coupled to X-ray analysis. For 'surface'-grafting, a highly dense PAA layer covers PVDF films surface. As far as it is dense, it is rather a gradient than a pure PAA layer as grafted chains are intimately mixed with PVDF chains. When adding water, the PAA density becomes less important and the grafting through process occurs more easily. The two grafting fronts diffuse with increasing grafting yield from both surfaces to the inner part of PVDF film until they join to obtain a complete homogeneous PVDF-*g*-PAA copolymer film.

The development of accurate back-titration technique was performed to quantify the micromole of AA trapped in PVDF bulk using UV–vis spectroscopy. They reveal that the accessibility of AA carboxylic functions depends greatly on the molecular size of the probes. Therefore, the choice of the dosing method can be chosen depending on the functionalization goals. Also, biology and interface chemistry would certainly push us to displace the detection limits to nanomole determination. In this purpose, we are planning to adapt biochemistry dosing techniques.

The possibility to design the grafted film structure can be of interest for various application fields such as membranes where grafting-through is required or biomaterials where often the surface properties need to be different than that of the bulk.

Acknowledgements

This work was performed in the frame of the LRC DSM 98-15. The authors gratefully acknowledge the financial support by a grant from *Lefoulon-Delalande* Foundation (Institut de France, Paris).

References

[1] du Pasquier A, Warren PC, Culver D, Gozdz AS, Amatucci GG. Solid State Ionics 2000;135:249–57.
[2] Ying L, Wang P, Kang ET, Neoh KG. Macromolecules 2002;35: 673–9.
[3] Jarvinen K, Akerman S, Svarfvar B, Tarvainen T, Viinkka P, Paronen P. Pharm Res 1998;15(5):802–5.
[4] Tarvainen T, Svarfvar B, Akerman S, Savolainen J, Karhu M, Paronen P, Järvinen K. Biomaterials 1999;20:2177–83.
[5] Steffens G, Nothdurft L, Buse G. Biomaterials 2002;23(16):3523–31.
[6] Suh TS, Joo CK, Kim YC, Lee MS, Lee HK, Choe BY, Chun HJ. J Appl Polym Sci 2002;85(11):2361–6.

[7] Gancarz I, Pozniak G, Bryjak M, Frankiewicz A. Acta Polym 1999; 50:317–26.

[8] Dogué IL, Mermilliod N, Foerch R. Nucl Instr Meth B 1995;105(1–4): 164–7.

[9] Lei J, Liao X. Eur Polym J 2001;37:771–9.

[10] El-Sawy NM, Sagheer FA. Polym Int 1998;47:324–30.

[11] Mokhtar SM. Polym Int 1997;42:335–9.

[12] Aouadj S, Chapiro A. Die Angew Makromol Chem 1996;235:73–80.

[13] Betz N, Bègue J, Goncalves M, Gionnet K, Déléris G, Le Moël A. Nucl Instr Meth B 2003;208:73–80.

[14] Zouahri A, Elmidaoui A. J Polym Sci Part A: Polym Chem 1996;34: 1793–8.

[15] Chapiro A. Radiation chemistry of polymeric systems. New York: Interscience; 1962.

[16] Chapiro A. J Polym Sci: Symp 1975;50:181–8.

[17] Rånby B, Rabek JF. ESR spectroscopy in polymer research. Berlin: Springer; 1977.

[18] Bozzi A, Chapiro A. Eur Polym J 1987;23:255–7.

[19] Dmitrenko AV, Serushkin MI, Mesh AM, Agnivtseva TG, Ivanchev SS. Polym Sci USSR 1992;34(4):319–23.

[20] Tamura N, Shinohara K. Prep Prog Polym Phys Japan 1963;6:265–8.

[21] Helbert JN, Wagner BE, Pointdexter EH, Kevan L. J Polym Sci, Polym Phys Edn 1975;13:825–34.

[22] Suryanarayana D, Kevan L. J Am Chem Soc 1982;104:6251–4.

[23] Betz N, Petersohn E, le Moël A. Radiat Phys Chem 1996;47:411–4.

[24] Niemöller A, Ellinghorst G. Die Angew Makromol Chem 1987;148: 1–18.

[25] Aymes-Chodur, C. University Pierre et Marie Curie, Paris, France; 1998.

[26] Ellinghorst G, Fuehrer J, Vierkotten D. Radiat Phys Chem 1981;18(5-6):889–97.

[27] Ellinghorst G, Niemöller A, Vierkotten D. Radiat Phys Chem 1983; 22(3/5):635–42.

[28] Kang ET, Tan KL. Macromolecules 1996;29:6872–9.

[29] Scofield JHJ. Electron Spectrosc Relat Phenom 1976;8:129.

[30] Betz N, Moël AL, Balanzat E, Ramillon JM, Lamotte J, Gallas JP, Jaskierowicz G. J Polym Sci: Part B Polym Phys 1994;32:1493–502.

[31] Boullier I, Esnouf S, Moël AL. J Polym Sci B: Polym Phys 2003;41: 1509–17.

[32] Guilmeau I. In Université Pierre et Marie Curie (Paris VI); University Pierre et Marie Curie (Paris VI): Paris; 1998, p 184.

[33] Betz N, Le Moël A. Nucl Instr Meth B 1996;116:207–11.

[34] Vierkotten D, Ellinghorst G. Die Angew Makromol Chem 1983;113: 153–68.

2.4.7 Langmuir (2001)

Langmuir **2001,** *17,* 5901−5910

Adsorption of Polyisobutenylsuccinimide Derivatives at a Solid−Hydrocarbon Interface[†]

M.-Cl. Dubois-Clochard, J.-P. Durand, B. Delfort, P. Gateau,* L. Barré, and I. Blanchard

Institut Français du Pétrole, BP 311, 1-4 av. de Bois-Préau, 92506 Rueil-Malmaison, France

Y. Chevalier

Laboratoire des Matériaux Organiques à Propriétés Spécifiques, UMR 5041 CNRS,
Université de Savoie, BP 24, 69390 Vernaison, France

R. Gallo

ENSSPICAM, Faculté Saint-Jérôme, 13397 Marseille Cedex 20, France

Received January 12, 2001. In Final Form: June 5, 2001

The adsorption of polymer dispersants of the polyisobutenylsuccinimide series has been studied at the solid/xylene interface. Carbon black was studied as a model solid. Adsorption isotherms were determined, the enthalpy of adsorption was measured by calorimetry, and the thickness of the adsorbed layer was obtained from small-angle neutron scattering. The paper emphasizes the structure−properties relationships with the help of a series of polyisobutenylsuccinimides having different polyamine groups and different polymer architectures, simple diblock (PIBSI) and comblike structure (polyPIBSI). The polyamine part ensured a strong adsorption on the solid surface, which increased in strength with the number of amine groups. In the same way, changing the diblock structure for a comblike one led to an enhanced affinity of the polymer for the solid surface. The adsorption was enthalpic but the Gibbs free energy of adsorption remained moderate because of a large entropy loss during adsorption. There was an enthalpy−entropy compensation phenomenon. Below a concentration of 70 mmol/m^3, the polymers adsorbed as a 30 Å thick monolayer and the adsorption phenomenon was irreversible, due to the polymeric nature of the polar part. A drastic increase of adsorbed amount took place for higher concentrations. The formation of reverse hemimicelles was assumed as the origin of this phenomenon. The supplementary adsorption was reversible, showing that the polymer−polymer interactions were weaker than the polymer−surface interactions.

1. Introduction

Carbonaceous deposits coming from fuel and lubricants are known to be formed over time at critical locations in an engine. These deposits can degrade vehicle performance and driveability, increase fuel consumption and pollutant emissions, and may lead to the destruction of the engine. To remedy these problems, detergent−dispersant additives are used in fuels and lubricants in order to avoid or decrease deposit adhesion on metallic surfaces and prevent deposit aggregation.[1] These compounds are mainly polymer surfactants such as polyisobutenylsuccinimide (PIBSI) derivatives, which are extensively used as fuel detergents[2] and ashless dispersant additives for lubricants.[3] It is presumed that the efficiency of these structures is coming from the strong adsorption of the polyamine block onto the deposits or metallic surfaces.[4] The polyisobutenyl block forms a steric barrier preventing adhesion and/or aggregation.

The present work was a comparative study of the adsorption on solid surfaces for two families of polymers: a linear diblock polyisobutenylsuccinimide (PIBSI) and a comblike poly(polyisobutenylsuccinimide) (polyPIBSI) (Figure 1). They have been compared in terms of performance and action mechanisms.[5] To model carbonaceous deposits, carbon black particles having their surface oxidized have been chosen.

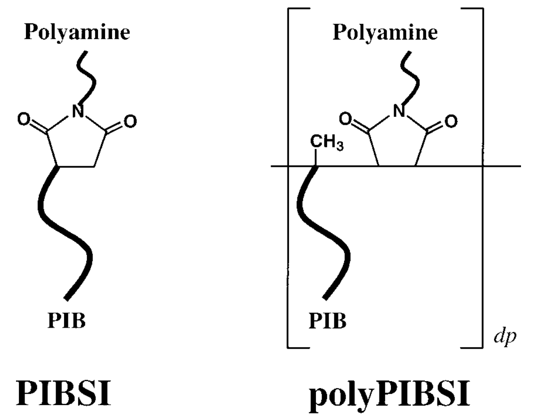

Figure 1. Linear diblock and comblike polyisobutenylsuccinimides.

In this paper, emphasis is given to the adsorption process. The thermodynamics of the adsorption have been studied using adsorption isotherms and by calorimetry

---

* To whom correspondence should be addressed.

[†] This work is a part of PhD thesis of M.-Cl. Dubois-Clochard.

(1) Guibet, J.-C. *Carburants et moteurs*; Publications de l'Institut Français du Pétrole; Technip: Paris, 1997.

(2) Owen, K.; Landells, R. G. M. In *Gasoline and diesel fuel additives*; Owen, K., ed., Wiley: London, 1989; Chapter 1, p 23.

(3) Forbes, E. S.; Neustadter, E. L. *Tribology* **1972**, *5*, 72.

(4) Udelhofen, J. H.; Zahalka, T. L. *Additives requirement for today's smaller engines*; SAE 851644; SAE Publications: Warrendale, 1986.

(5) Dubois-Clochard, M.-Cl. Ph.D. Thesis, University Paris VI, and Publications de l'Institut Français du Pétrole, Technip: Paris, 1998.

10.1021/la010076o CCC: $20.00

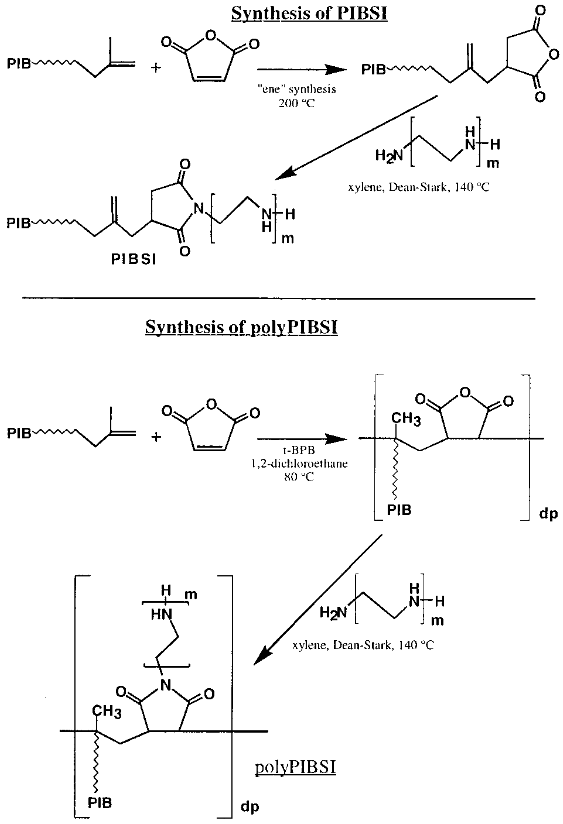

Figure 2. General synthesis schemes of PIBSI and polyPIBSI.

measurements. The structure of the adsorbed layer has been investigated by means of small-angle neutron scattering. The synthesis of the two classes of detergent–dispersant additives is first presented. A set of each class of polymers was prepared varying the nature of the polyamine part. Then, adsorption studies onto carbon black will be presented and discussed.

2. Experimental Section

2.1. Synthesis of Polyisobutenylsuccinimide of Different Structures. The polyisobutene (PIB) used for the synthesis of all amphiphilic polymers was a linear polymer purchased from BASF (GLISSOPAL 1000) having an average molecular weight $M_n = 1000$ g·mol^{-1}. The macromolecules were terminated by a double bond at one of the chain ends; 90% of the chain ends were vinylic exo double bonds, while the remaining 10% were endo double bonds. These polymers having such a high degree of reactive vinylic end groups could be efficiently functionalized. Polyamines (from DELAMINE) used for synthesis of PIBSI and polyPIBSI were either linear, tetraethylenepentamine (TEPA), triethylenetetramine (TETA), and diethylenetriamine (DETA), or cyclic, aminoethylpiperazine (AEP).

General reaction schemes for the syntheses of PIBSI and polyPIBSI are presented in Figure 2. The PIBSI and polyPIBSI are abbreviated in the following as PIBSI–TEPA, PIBSI–TETA, PIBSI–DETA, and PIBSI–AEP or polyPIBSI–DETA and polyPIBSI–AEP, according to the name of the polyamine used.

2.1.1. Synthesis of Diblock PIBSI. A 100-mL three-necked round-bottom flask, equipped with a magnetic stir bar and fitted with a condenser, a nitrogen/vacuum inlet, and a dropping funnel was charged with 5 g (0.005 mol) of PIB and an equimolar amount of maleic anhydride (0.50 g, 0.005 mol). The mixture was stirred under nitrogen atmosphere for 6 h at 200 °C without any solvent. The unreacted maleic anhydride was removed under reduced pressure during 1 day at 150 °C in a rotary evaporator. The full disappearance of free maleic anhydride was followed by size exclusion chromatography (SEC). IR spectroscopy showed the appearance of two characteristic bands at 1862 and 1781 cm^{-1} corresponding to the stretching of the C—O—C and C=O bonds of the anhydride, respectively. The same flask was then fitted with a Dean–Stark apparatus topped by a condenser, a nitrogen/vacuum inlet, and a dropping funnel. An equimolar amount of polyamine (TEPA, TETA, DETA, or AEP) was added to a solution of the polyisobutenylanhydride in xylene (50 wt %) and reacted at 140 °C during 6 h. IR spectroscopy showed the characteristic absorption band of the imide at 1700 cm^{-1} and the full disappearance of the anhydride bands, showing that the reaction has reached completion. ^{13}C NMR (ppm from TMS): 32 (CH_3 of PIB), 36 (CH_2 of PIB), 59 (–C– of PIB), 180 (carbonyls), and lines corresponding to ethylene groups of polyamines between 40 and 58 ppm: 45 and 54 ppm for AEP; 46–48 and 50–53 ppm for EDA, DETA, TETA, and TEPA.

2.1.2. Synthesis of Comblike PolyPIBSI. The free radical copolymerization of maleic anhydride and PIB used as a macromonomer was carried out using *tert*-butylperoxybenzoate (*t*-BPB) as a radical initiator.[6] In a 100-mL three-necked round-bottom flask equipped with a magnetic stir bar and fitted with a condenser, a nitrogen/vacuum inlet, and a dropping funnel, *t*-BPB (1.875 g, 0.0097 mol) was added dropwise to a solution of PIB (93.87 g, 0.1 mol) and maleic anhydride (9.48 g, 0.097 mol) in 60 mL of 1,2-dichloroethane at 45 °C. The reaction mixture was then stirred at 80 °C during 30 h. Monitoring the course of the polymerization by SEC indicated the end of the chain growth after 30 h. The solvent was removed under reduced pressure, and the unreacted maleic anhydride was removed by heating at 150 °C at 0.1 mmHg during 1 day. The copolymer was then fractionated by precipitation with acetone into three fractions of different chain lengths corresponding to number-averaged polymerization degrees of 9, 13.5, and 18. This radical copolymerization gave an alternate copolymer with low molar masses because of transfer reactions to the solvent. The polydispersity index $I_P = M_w/M_n$ was 1.2 for each fraction. ^{13}C NMR (ppm from TMS): 30 (CH_3 of PIB), 37 (CH_2 of PIB), 59 (–C– of PIB), 180 (carbonyls). IR: 1860 and 1770 cm^{-1} (anhydride bands).

These fractions were functionalized with DETA or AEP by the same method as used for the PIBSI. ^{13}C NMR (ppm from TMS): 30 (CH_3 of PIB), 37 (CH_2 of PIB), 59 (–C– of PIB), 180 (carbonyls) and peaks corresponding to ethylene groups of polyamines between 40 and 58 ppm: 45 and 54 ppm for AEP; 46–48 and 50–53 ppm for DETA. IR: 1700 cm^{-1} (succinimide band).

2.2. Carbon Black Solid. Acidic carbon black REGAL 400R was purchased from CABOT SA. The specific area as measured by nitrogen adsorption according to the BET method was 96 m^2/g. The nitrogen adsorption measurements did not display any hysteresis, showing that the carbon particles were not porous. The acidic oxygenated surface groups were titrated according to the method proposed by Boehm[7] and Custodéro[8] using $NaHCO_3$, Na_2CO_3, NaOH, and $NaOC_2H_5$ as bases for the titration of carboxylic acids, lactones, phenols, and any carbonyl functions, respectively. This titration led to 9×10^{-5} mol of carboxylic acids and 2×10^{-4} mol of total acids per gram of carbon black. These values correspond to surface densities of 0.9 μmol/m^2 for the carboxylic acids and 2.0 μmol/m^2 for any acidic group or to mean surface areas per acidic group of 1.8 and 0.83 nm^2, respectively. These values are to be compared to the densities of adsorbed polymer obtained from adsorption isotherms.

2.3. Adsorption Isotherms. The adsorbed amounts of PIBSI on carbon black surface were determined by a titration of the PIBSI concentration before and after adsorption using an acidic indicator, the 3,3′,5,5′,tetrabromophenolphthalein methyl ester.[9,10] All the absorption spectra of the indicator in the presence

---

[6] Chevron, US patent, 5,175,225, 1992.

[7] (a) Boehm, H. P.; Diehl, E.; Heck, W. *Rev. Gén. Caout.* **1964**, *41*, 461. (b) Boehm, H. P.; Diehl, E.; Heck, W.; Sappok, R. *Angew. Chem.* **1964**, *3*, 669. (c) Boehm, H. P.; Diehl, E.; Heck, W. *Proc. Carbon Conf.* **1966**, 369.

[8] (a) Custodéro, E. PhD thesis, Université de Haute Alsace, 1992. (b) Donnet, J.-B.; Custodéro, E. *Carbon* **1992**, *30*, 813.

[9] Pugh, R. J.; Matsunaga, T.; Fowkes, F. M. *Colloids Surf.* **1983**, *7*, 183.

[10] Pugh, R. J.; Fowkes, F. M. *Colloids Surf.* **1984**, *9*, 33.

of PIBSI were joined in one isosbestic point showing that only two species were present in the solution. The complex formed was easily followed by UV−visible spectroscopy at $\lambda_{max} = 570$ nm.

2.3.1. Adsorption. The adsorption isotherms were obtained starting from solid−PIBSI−xylene dispersions with different weights of adsorbent for a same amount of PIBSI. Fifty milliliters of a PIBSI solution (120 mg/L) in xylene was added at each solid fraction (carbon black, $0.01 \text{ g} \le m \le 0.2 \text{ g}$). These suspensions were stirred at 500 rpm during 15 min (equilibrium state completely reached according to the kinetic results). Aliquots (1.5 mL) of the supernatant were taken after 1 h of settling and titrated by UV−visible spectroscopy (Lambda 3B, Perkin-Elmer) in the presence of the acidic indicator. The supernatant was filtered (0.2 μm Millipore Fluoropore filters) before being titrated. Adsorption isotherms were measured at 20 and 60 °C. Measurements of the kinetics of adsorption were carried out in order to ensure completion of the adsorption process: several identical dispersions were stirred at 500 rpm for different times when 1.5 mL of supernatant was titrated. The adsorption kinetic was very fast, and the equilibrium was reached within 5 min.

The adsorbed amounts at equilibrium Γ were calculated from the equation

$$\Gamma = \frac{(C_0 - C_{eq})\,V}{mA_{BET}M_n}\ (\text{mol}\cdot\text{m}^{-2}) \qquad (1)$$

where C_0 was the initial concentration of the PIBSI solution, C_{eq} was the supernatant equilibrium concentration (thereafter referred to as C), V was the volume of the solution, and m and A_{BET} were the solid adsorbent weight and specific area.

2.3.2. Desorption Experiments. Dispersions with the same rate PIBSI/adsorbent were first equilibrated for adsorption, and various volumes of pure xylene were added corresponding to dilution factors of 1.2, 1.5, 2, 3, and 6. The dispersions were stirred again 45 min at 1000 rpm, allowed to settle for 1 h, and filtered. The supernatants were titrated by UV−visible spectrometry in the presence of the acidic indicator. The desorption studies were made at 20 and 60 °C. Kinetic measurements were also carried out. Dispersions with the same rate PIBSI/adsorbent were diluted with the same volume of xylene. Each identical dilute dispersion was stirred at 1000 rpm, and aliquots were taken and titrated at different times.

2.4. Calorimetry. The measurements were made with a Setaram C80 II calorimeter at 30 °C, slightly above room temperature for allowing a correct control of the temperature. This microcalorimeter was equipped with a mixing cell having two compartments. The contents of the two compartments were mixed by rotating the cell. A correct stirring of the solid and liquid was achieving by several rotations of the mixing cell. The apparatus has been calibrated by Joule effect at room temperature. One of the compartments was filled with the carbon black which was already wetted by a small amount of the solvent. That way, the heat of immersion of the dry solid does not contribute to the measured heat flow. The second compartment was filled with the dispersant solution in the remaining amount of solvent. The heats of adsorption were measured for mixing 10 cm^3 of solution with various amounts of carbon black so as to investigate the full adsorption isotherm. Since a dilution of the polymer takes place during the adsorption process, the corresponding heat of dilution has to be subtracted.[11] The measured heats of dilution of the polymers in xylene were very low as compared to the heats of adsorption, so that their contribution was neglected and the heats of dilution were not measured systematically.

2.5. Small-Angle Neutron Scattering SANS. The SANS experiments were performed with the PACE spectrometer[12] at the Laboratoire Léon Brillouin, an experimental facility of the CNRS and CEA at Saclay (France). The sample-to-detector distance of 2.00 m and selected wavelength of 6.0 Å allowed measurements in a domain of scattering vector, $q = (4\pi/\lambda)\sin(\theta/2)$, ranging from 1.5×10^{-2} to 1.6×10^{-1} Å^{-1}. Samples were contained in Hellma quartz cells of 2 mm thickness for contrast variation studies and determination of the thickness of the adsorbed polymer layer.

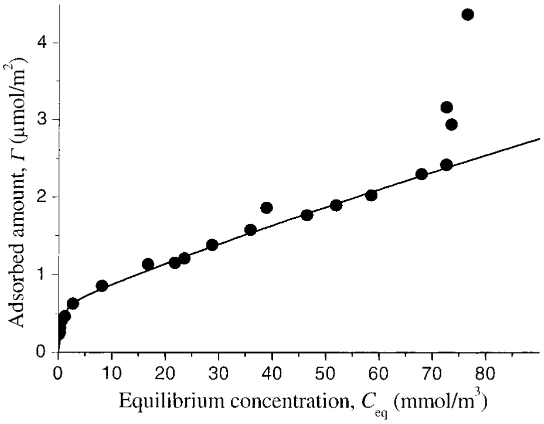

Figure 3. Adsorption isotherm of PIBSI−TETA on carbon black REGAL 400R at 60 °C. The solid line is the best fit for a di-Langmuir isotherm (see text).

3. Results and Discussion

The adsorption isotherms on carbon black displayed some similarities, and several distinct concentration regimes could be clearly identified. After a first steep increase of the adsorbed amount at low concentrations, the adsorption isotherms displayed a break of the slope followed by a domain of lower slope for polymer concentrations in range 5−70 mmol/m³. In some instances, the adsorption isotherm reached an horizontal plateau in this concentration regime. A sudden and sharp increase of the adsorbed polymer amount occurred for concentrations around 70−80 mmol/m³. A typical example of such an adsorption isotherm is shown on a wide range of concentrations in Figure 3.

Because of such a complexity of adsorption phenomena of PIBSI and polyPIBSI at the carbon black−xylene interface, the presentation is split into two parts where the results pertaining to high equilibrium concentrations ($C_{eq} > 70$ mmol/m³) are moved to the end of the paper. Most of the data concern the low equilibrium concentration part of the adsorption isotherms ($C_{eq} < 70$ mmol/m³) which are discussed in detail with emphasis on structure−properties relationships. To be able to compare the adsorption isotherms of different polymers, a suitable model of adsorption has to be selected. The use of a model allows number comparison instead of the general features of the adsorption isotherms. Different factors have been studied: the contribution of the hydrophilic part, the effect of the polymer structure, and the temperature. The thermodynamic study of the adsorption has been complemented by investigations of the desorption (reversibility) and of the structure of the adsorbed layer.

In the case of PIBSI−DETA and PIBSI−AEP, the adsorption isotherms started with a finite slope at the origin and reached a plateau at high concentrations of polymer. The simple Langmuir model could fit quite well to such experimental data. But this was no longer the case for PIBSI−TETA or PIBSI−TEPA in which the polar part was more important (Figure 4) and with the comblike copolymers (Figure 6). The unsuitability of the Langmuir isotherm was obvious since significant adsorbed amounts

---

[11] (a) Korn, M.; Killmann, E.; Eisenlauer, J. *J. Colloid Interface Sci.* **1980**, *76*, 7. (b) Korn, M.; Killmann, E. *J. Colloid Interface Sci.* **1980**, *76*, 19.

[12] Équipements expérimentaux du Laboratoire Léon Brillouin. Available from LLB, CEN Saclay, 91191 Gif-sur-Yvette cedex, France. The LLB is a CEA−CNRS laboratory.

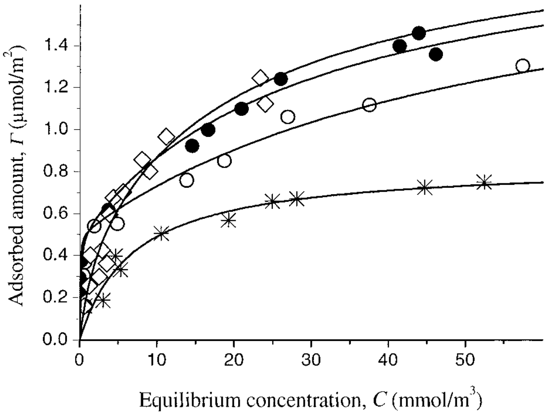

Figure 4. Adsorption isotherms of different PIBSI on carbon black REGAL 400R at 20 °C: (∗) PIBSI−AEP; (◇) PIBSI−DETA, (●) PIBSI−TETA, (○) PIBSI−TEPA. The solid lines are the best fit of the models using the parameters of Table 1 (see text).

were still measured at vanishing equilibrium concentrations (the adsorption isotherm started with a vertical slope).

3.1. Modeling the Adsorption Isotherms. The obvious advantage of the Langmuir model of adsorption rests in its simplicity and the clear physical meaning of the parameters. Thus, for a model surface where the adsorption sites are identical and independent

$$\Gamma = \frac{\Gamma_{\max} KC}{1 + KC} \tag{2}$$

where $\Gamma_{\max}$ is the surface excess (adsorbed amount per unit area) at saturation of the surface sites and K is the equilibrium constant of the adsorption process ($\Delta_{\text{ads}}G^\circ = -RT\ln(K)$). The same advantages were kept using a di-Langmuir model for the adsorption isotherms where the adsorption took place on two types of sites with surface concentrations at saturation, Γ_1 and Γ_2, and equilibrium constants K_1 and K_2

$$\Gamma = \frac{\Gamma_1 K_1 C}{1 + K_1 C} + \frac{\Gamma_2 K_2 C}{1 + K_2 C} \tag{3}$$

The physical reality of two distinct types of adsorption sites is not proven, but this model could fit to the whole experimental data. There are several acidic sites at the surface of carbon black particles, and two types of acidic sites were indeed titrated. This model was used as an easy way to extract parameters to which a physical meaning could be ascribed and compare them for the different polymers. The relevant parameters are the total adsorption excesses at saturation $\Gamma_{\max} = \Gamma_1$ or Γ_2, and the equilibrium constants K_1 and K_2. In the case of comblike copolymers where the adsorption isotherm is vertical at $C = 0$, K_1 is very large ($K_1 = \infty$) and eq 3 reduces to

$$\Gamma = \Gamma_1 + \frac{\Gamma_2 K_2 C}{1 + K_2 C} \tag{4}$$

3.2. Determination of the Molar Thermodynamic Parameters. A combination of the results of the adsorption isotherms and calorimetric data gave complementary information about the thermodynamics of the adsorption process. Indeed, the integration of the adsorption isotherm yields the molar integral Gibbs energy variation pertaining to the adsorption process[13]

$$\Delta_{\text{ads}}G_{\text{M}} = -\frac{RT}{\Gamma}\int_0^C \frac{\Gamma}{C}\,\mathrm{d}C \tag{5}$$

The integration for the Langmuir (and di-Langmuir) isotherm gives the analytical equation

$$\Delta_{\text{ads}}G_{\text{M}} = -\frac{RT\Gamma_{\max}}{\Gamma}\ln(1 + KC) \tag{6}$$

It should be stressed that the values of $\Delta_{\text{ads}}G_{\text{M}}$ as calculated from eq 6 do not depend so much on the di-Langmuir model of the adsorption isotherms. The use of the model allows an easy integration of eq 5, but any different mathematical model which would fit to the experimental data would give comparable values of the integral. For the purpose of integration, the use of the model provides a smooth function which passes correctly through the experimental data in the same way as any other mathematical function having no physical meaning such as a polynomial or a cubic spline. From the molar Gibbs free energy $\Delta_{\text{ads}}G_{\text{M}}$ and the molar enthalpy $\Delta_{\text{ads}}H_{\text{M}}$ as directly measured by calorimetry, the molar entropy of adsorption $\Delta_{\text{ads}}S_{\text{M}}$ was calculated. These thermodynamic parameters represent the variation for the adsorption of 1 mol of polymer at constant temperature and constant pressure on a surface wetted by the solvent.

The values of the molar integral Gibbs free energies were negative (the adsorption was spontaneous) and the measured enthalpies were negative (exothermic) too. $\Delta_{\text{ads}}G_{\text{M}}$ is a measure of the relative affinity of the polymer for the interface.

3.3. Influence of the Hydrophilic Polyamine Part. The first observation was that the longer the hydrophilic part, the higher the affinity of the PIBSI for the solid surface. But the adsorption isotherms were not simple, and several different phenomena contributed depending to the type of polyamine. The surface of carbon black particles was not homogeneous since both strong and weak acidic sites were detected by the titration method of Boehm (see Experimental Section). The polymeric nature of both blocks also contributes to the complexity: the polyamine part which adsorbs on the acidic sites may bind to several surface sites and the effects of steric hindrance of the PIB part appear as the adsorbed density increases. A unified description of the adsorption process is proposed in the following, using a phenomenological two-step adsorption model in which the physical origins of adsorption was ignored.

For polymers that adsorb by means of one of their chain end, two distinct regimes have been identified.[14] In the "mushroom" regime at low coverage where the adsorbed macromolecules are dilute enough for being independent, the adsorption follows the same laws at for small molecules and the configuration of the adsorbed macromolecules is the same as in dilute solution. In particular, the adsorbed polymer coils have the same gyration radius R_{G} as obtained in dilute solution; the thickness of the polymer layer is twice R_{G}. The "brush" regime occurs at high coverage where the macromolecules are constrained to stretch because of the presence of the neighboring adsorbed macromolecules. The hindrance of the already adsorbed

---

[13] Briant, J.; Belot, D., *C. R. Acad. Sci. Paris, Ser. C* **1975**, *280*, 1335.

[14] (a) Alexander, S. *J. Phys.* (*Paris*) **1977**, *38*, 983. (b) de Gennes, P. G. *Macromolecules* **1980**, *13*, 1069. (c) de Gennes, P. G. *Adv. Colloid Interface Sci.* **1987**, *27*, 189.

Table 1. Thermodynamic Parameters of the Adsorption Isotherms of the PIBSI As Estimated from the Model

	PIBSI–AEP	PIBSI–DETA	PIBSI–TETA	PIBSI–TEPA
type of isotherm	Langmuir	di-Langmuir	di-Langmuir	di-Langmuir
Γ_1 (μmol/m^2)	0.84	0.5	0.5	0.5
K_1 (m^3·mol^{-1})	140	500	11000	30000
Γ_2 (μmol/m^2)		1.5	1.5	1.5
K_2 (m^3·mol^{-1})		44	33	18
Γ_{max} (μmol/m^2)	0.84	2.0	2.0	2.0

macromolecules impedes further adsorption. The crossover from the "mushroom" to the "brush" regime is observed when unperturbed polymer coils are able to ensure a complete coverage of the surface, which is when the adsorbed amount per unit area reaches $\Gamma^* = 1/(\pi R_G^2 N_{Av})$.[15] Xylene and similar aromatic solvents (toluene, benzene) are close to Θ-solvent at room temperature.[16] For poly(isobutene) of molar mass 1000, an estimate of the gyration radius from viscosity measurements in benzene at 24 °C ($T = \Theta$) was $R_G = 10$ Å,[16] giving $\Gamma^* = 0.53$ μmol/m^2. On another hand, the gyration radius has been measured by means of X-ray scattering in *n*-heptane good solvent as $R_G = 9$ Å,[17] giving $\Gamma^* = 0.65$ μmol/m^2. This value of Γ^* is close to the surface density of strong acidic sites (0.9 μmol/m^2) as determined by the titration method of Boehm (see experimental part).

Adsorption first took place at the more acidic sites. For PIBSI–TETA and PIBSI–TEPA, the affinity for the strongly acidic sites was very high, so that the experimental adsorption isotherms were vertical at their origin (the residual concentration was so low that it could not be detected by the titration). The adsorption of PIBSI–AEP was weaker since the slope at the origin was lower and the adsorbed amount at the plateau at higher concentrations was also less. PIBSI–DETA showed an intermediate behavior.

In the case of the weak adsorption of PIBSI–AEP, the Langmuir model was better. The maximum adsorbed amount was 0.84 μmol/m^2, in agreement with the surface density of strong acidic sites of 0.9 μmol/m^2. The adsorption of PIBSI–AEP on the carbon black surface occurred on the strong acidic sites only, with a 1:1 stoichiometry. The PIBSI–AEP bears two basic amino groups however, one secondary amine at the chain end and one tertiary amine. Only one of these amines could interact with the acidic groups of the surface. It was inferred that the terminal secondary amine was able to adsorb, whereas the weakly basic tertiary amine which was buried into the center of the molecule could not contribute to the adsorption. Despite its complex chemical structure, the PIBSI–AEP behaved as a simple fatty amine as regards to adsorption.

For the other PIBSI, the two-step model obviously held. In the case of both PIBSI–TETA and PIBSI–TEPA, K_1 was very large ($K_1 \approx \infty$) and the maximum adsorbed amount at the first step Γ_1 was 0.4–0.5 μmol/m^2. For PIBSI–DETA, the slope at the origin is finite and a Langmuir adsorption isotherm fitted correctly to the experimental data, but the di-Langmuir one fitted better and was retained for having a unified description of the adsorption process.

Γ^* stood right in the domain where the adsorption isotherms of PIBSI–TETA and PIBSI–TEPA showed a slope discontinuity. Thus, the two steps of the di-Langmuir model might then be ascribed to the two adsorption regimes ($\Gamma^* = \Gamma_1 \approx 0.5$ μmol/m^2). But this value of Γ_1 was also close to the surface density of strong acidic sites so that the assignment of the first adsorption step to a precise physical origin was ambiguous. The adsorption on the strong acidic sites with a 2:1 stoichiometry would have given $\Gamma_1 = 0.45$ μmol/m^2 as well. Whatever the origin of the transition, the first step was in the mushroom regime and the adsorption took place on the strong acidic sites. The stoichiometry of the surface acid–base interaction was 2:1 since Γ_1 was half the density of strong acidic sites. This stoichiometry was allowed because at least two amine groups of the same molecule were available to two acidic sites; these molecules bore one terminal primary amine and one, two, or three secondary amine groups which were also available for the adsorption. The maximum adsorbed amount $\Gamma_1 + \Gamma_2$ could not exceed the total surface density of acidic sites of 2.0 μmol/m^2. For the best fit of the di-Langmuir model to the experimental adsorption isotherms, Γ_1 and Γ_2 were set at the same fixed values for all compounds: $\Gamma_1 = 0.5$ μmol/m^2 and $\Gamma_2 = 1.5$ μmol/m^2. The parameters giving the best fit to the experimental data according to these constraints are shown in Table 1. The fits were good, giving confidence in the assumptions.

Of course, the affinity of the polyamine head was larger when several amines were present. Thus, the adsorption strength was in the order PIBSI–AEP ($K_1 = 140$ m^3·mol^{-1}) < PIBSI–DETA ($K_1 = 500$ m^3·mol^{-1}) < PIBSI–TETA ($K_1 = \infty$) ≤ PIBSI–TEPA ($K_1 = \infty$). The second adsorption process was known to be much more complex, but it was modeled with the help of a second Langmuir process described by the two phenomenological parameters Γ_2 and K_2. This second adsorption process took place at the less acidic surface sites which were widely distributed in strength, and the effects of steric hindrance of the polymer tails contributed at high polymer coverages.

Except for PIBSI–AEP, the adsorption reached completion, and all the acidic sites were occupied with a 1:1 stoichiometry at full coverage since $\Gamma_1 + \Gamma_2 = 2.0$ μmol/m^2. Surprisingly, the values of K_2 decreased from PIBSI–DETA to PIBSI–TEPA. Since two strong acidic sites were occupied by one macromolecule at the end of the first adsorption process, the adsorption with a 1:1 stoichiometry required the release from one of these sites. The energy balance of the second process included the desorption of some of the amine groups which have been adsorbed during the first process. This phenomenon provided a rationale for the decrease of K_2 while the affinity of the molecule was increasing. A dynamic rearrangement took place in the polymer layer in the course of the adsorption process.

The adsorption enthalpy has been measured by means of immersion calorimetry. The enthalpies were negative (exothermic) in all cases (Figure 5a). The adsorption enthalpies were larger for the longer polyamines, as expected. The molar integral adsorption enthalpy $\Delta_{ads}H_M$ was calculated from the measured enthalpy and the adsorption isotherm in the low equilibrium concentration domain as

$$\Delta_{ads}H_M = \frac{\Delta H_{meas}}{MA_{sp}\Gamma} \qquad (6)$$

---

(15) Mosquet, M.; Chevalier, Y.; Brunel, S.; Guicquero, J.-P.; Le Perchec, P. *J. Appl. Polym. Sci.* **1997**, *65*, 2545.

(16) Fox, T. G., Jr.; Flory, P. J. *J. Am. Chem. Soc.* **1951**, *73*, 1909.

(17) Yamada, M.; Osa, M.; Yoshizaki, T.; Yamakawa, H. *Macromolecules* **1997**, *30*, 7166.

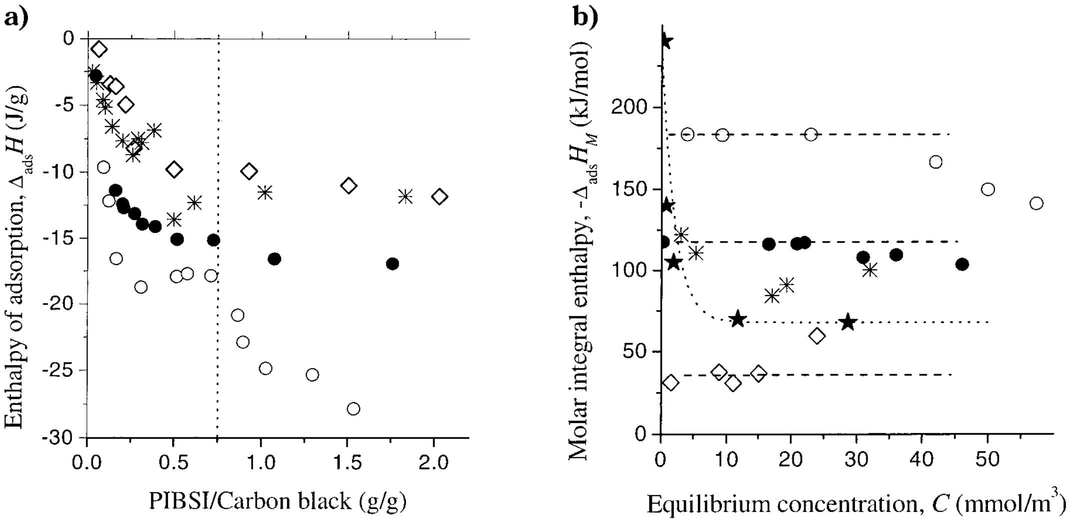

Figure 5. (a) Measured enthalpy per gram of carbon black immersed into a PIBSI solution. The dotted vertical line marks the limit between the low and high equilibrium concentration domains. (b) Molar integral adsorption enthalpy $\Delta_{ads}H_M$ as a function of the equilibrium concentration. For both sides: (∗) PIBSI–AEP; (◇) PIBSI–DETA, (●) PIBSI–TETA, (○) PIBSI–TEPA; (★) polyPIBSIDETA (dp = 9).

For a given polymer, $\Delta_{ads}H_M$ was constant at coverages lower than 0.8–1.0 μmol/m^2 (C_{eq} < 20 mmol/m^3) where the first adsorption process was predominant (Figure 5b). A decrease of $|\Delta_{ads}H_M|$ was observed at higher coverage for PIBSI–TEPA and PIBSI–TETA, showing that the second adsorption process had a lower enthalpy. This effect was clear for PIBSI–TEPA, and less pronounced but still significant for PIBSI–TETA. It was not observed in the data for PIBSI–DETA and PIBSI–AEP which displayed much scatter because smaller values of enthalpy were measured. A constant value of $\Delta_{ads}H_M$ for PIBSI–AEP was expected since only the first process of the model was operating, but this was actually not obvious in the calorimetric data. $|\Delta_{ads}H_M|$ was also larger than expected as compared with the other polymers studied. $|\Delta_{ads}H_M|$ increased in the order PIBSI–DETA < PIBSI–TETA < PIBSI–TEPA. An enthalpy increment per amino group of −60 kJ/mol could be determined in this later series. This value was in the expected range for the molar heat of the reaction of an amine with a carboxylic acid.

The molar entropy of adsorption was calculated from the calorimetric data and $\Delta_{ads}G_M$. $\Delta_{ads}S_M$ was negative in all cases. $\Delta_{ads}S_M$ did not depend much on the concentration. The reduction of the entropy for an adsorption process was expected because of the loss of degrees of freedom of the adsorbed polyamine part. It was then larger for the longer polyamines. Thus, the molar entropy losses $|\Delta_{ads}S_M|$ were of the order of 100, 350, and 550 J/(mol·K) for PIBSI–DETA, PIBSI–TETA, and PIBSI–TEPA, respectively.

The main feature of the thermodynamic parameters was a large negative enthalpy with a large negative entropy variation. The resulting Gibbs energy variation was weak and negative; $\Delta_{ads}G_M$ was lower than $\Delta_{ads}H_M$ by a factor of 10 or more. Thus, the adsorption was enthalpic in origin, and the moderate values of $\Delta_{ads}G_M$ resulting from an enthalpy–entropy compensation were $|\Delta_{ads}H_M| \approx T|\Delta_{ads}S_M|$.

3.4. Influence of the Structure of the Polymer. Two different structures of polymers having the same chemical functions were compared: comblike and simple diblock structures. This comparison was illustrated for the polymers functionalized with AEP and DETA in Figure 6. For both polymers, the effect of changing the polymer architecture from diblock to comblike was to enhance the affinity of the polymer. The consequence could be seen in the adsorption isotherms which started with a vertical slope at the origin ($K_1 = \infty$). The maximum adsorbed amount Γ_{max} increased strongly from PIBSI–AEP to polyPIBSI–AEP. On the contrary, for the PIBSI–DETA which could adsorb up to the saturation of the acidic surface sites of the carbon black, the polymerization into a comblike architecture did not allow a supplementary adsorption at saturation but a decrease of Γ_{max} was observed. This effect might be ascribed to the irreversible nature of the adsorption for polymers of high molar masses. Thus, the rearrangement inside the adsorbed layer, which allowed the complete coverage of the acidic site with the PIBSI, could not operate in the case of the polymerized (comblike) PIBSI.

The fits of the models to the experimental data were poor (Table 2). The very large values of K_1 reflect the infinite slope of the adsorption isotherms at the origin. Within experimental accuracy, Γ_1 was the same for all comblike polymers and was equal to the density of strongly acidic sites (0.9 μmol/m^2). The influence of the polymerization degree (dp between 9 and 18) was insignificant. The values of K_2 and Γ_2 were not accurate because they were much too sensitive to slight variations of the experimental values, and they could not be used for any discussion. For concentrations above 20 mmol/m^3, the slopes of the isotherms were small as compared to that of the corresponding PIBSI. The effects of steric hindrance by the adsorbed macromolecules in the "brush" regime were not important because the PIB chains were already close to each other along the backbone of the comblike copolymer. The effect of distribution of the strength of the acidic sites at the surface was also smeared out since amino groups were brought about the weak acidic sites when neighboring groups bound to strong acidic sites.

The molar integral adsorption enthalpy $\Delta_{ads}H_M$ of polyPIBSI-DETA (dp = 9) was still negative, but its magnitude decreased as the coverage increased (Figure 5b). $|\Delta_{ads}H_M|$ was very high, larger than for PIBSI–TEPA, for low coverages (low equilibrium concentrations). It decreased steeply and finally reached a nearly constant value (65–70 kJ/mol), close to that of PIBSI–DETA, as

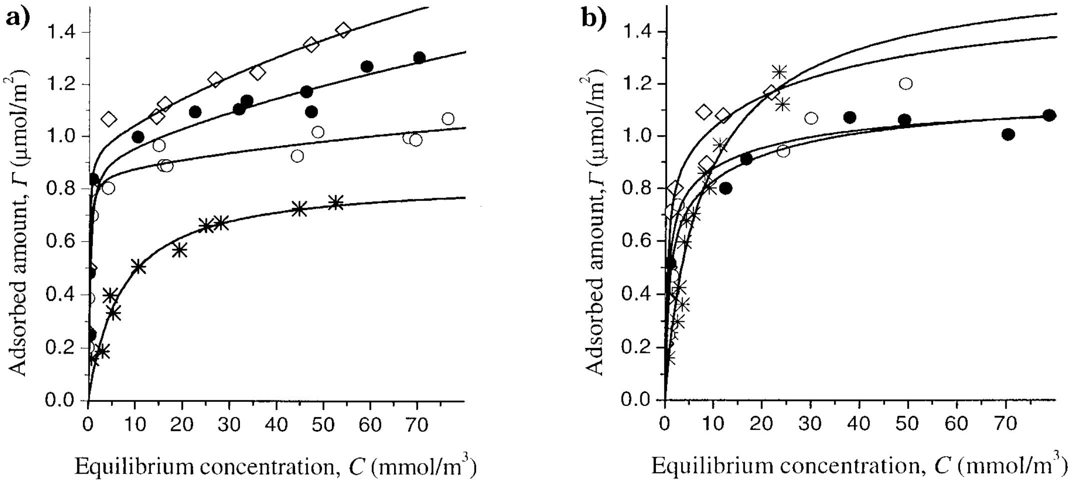

Figure 6. Adsorption isotherms on carbon black REGAL 400R at 20 °C for PIBSI (∗) and polyPIBSI of 9 (◇), 13.5 (●), and 18 (○) PIBSI repeat units: (a) PIBSI–AEP and polyPIBSI–AEP; (b) PIBSI–DETA and polyPIBSI–DETA. The solid lines are the best fit of the models using the parameters of Table 2 (see text).

Table 2. Thermodynamic Parameters of the Adsorption Isotherms of the PIBSI and PolyPIBSI As Estimated from the Model

	PIBSI–AEP				PIBSI–DETA			
	dp = 1	dp = 9	dp = 13.5	dp = 18	dp = 1	dp = 9	dp = 13.5	dp = 18
Γ_1 (μmol/m^2)	0.84	0.95	0.91	0.86	0.50	0.90	0.72	0.80
K_1 (m^3·mol^{-1})	140	9900	3600	5900	500	2700	1700	2000
Γ_2 (μmol/m^2)		1.67	1.54	0.59	1.50	0.66	0.45	0.35
K_2 (m^3·mol^{-1})		7	5	5	44	35	50	50

the saturation of the surface sites completed. The steep variation of $\Delta_{ads}H_M$ as a function of coverage was unexpected and remains difficult to rationalize. The calorimetric data showed the same trends as the adsorption isotherms: a dramatic effect of the polymeric nature of the comblike structure at low concentrations but no significant effect at high coverages. The molar adsorption entropy also varied with coverage. The large entropy loss at low coverages could be associated with the restriction of conformational freedom of the polymer backbone as the polyamine pendant groups were tightly immobilized at surface sites. The lesser entropy loss at higher coverage reflected the looser binding to the surface, allowing more dynamic fluctuations inside the adsorbed layer. Last, the entropy loss coming from the PIB chain stretching in the brush regime was reduced in the case of the comblike copolymer because the PIB chains were already squeezed together in the polymer in solution.

The advantage of the comblike architecture was to enhance the affinity for the surface. This effect was expected, this was the same as the effect of the length of the polyamine. A polymer always adsorb more strongly than its monomeric analogue. The effect on the adsorbed amount at saturation only manifested in the case of AEP where the functional group was not able to ensure a strong adsorption.

3.5. Influence of the Temperature. When the temperature increased from 20 to 60 °C, most of the features of the adsorption isotherms were retained. The most characteristic difference was an increase of the adsorbed amounts (compare the data of PIBSI–TEPA in Figures 3 and 4). This was unexpected since an increase of the temperature generally led to a decrease of the adsorption when the adsorption process is exothermic. The same results have been reported by Pugh et al.[10] with PIBSI at the carbon black/hydrocarbon interface. Their explanation was based on the capillary condensation of the PIBSI into the carbon black micropores. In our case, the BET nitrogen adsorption data have shown that the REGAL 400R carbon black had no microporosity, so this explanation was not suitable. A large variation of the adsorption enthalpy or entropy as a function of temperature might account for such phenomena as well.

The coverage at which the transition from the first adsorption regime to the second one was observed for $\Gamma^* = 0.65$ μmol/m^2 at 60 °C, which was larger than the value of 0.50 μmol/m^2 estimated at 20 °C. This observation can again be rationalized in terms of a transition from a mushroom to a brush regime since the PIB coils collapse as the temperature rises above the Θ temperature, increasing the value of Γ^*.

3.6. Desorption Study. The desorption did not occur upon dilution with the pure solvent (see Experimental Section) at 20 or at 60 °C. As shown in Figure 7, the adsorption phenomenon was totally irreversible in the present dilute concentration domain ($C_{eq} < 70$ mmol/m^3). The irreversible adsorption is quite common with polymers.[18] Indeed, the desorption process would imply the simultaneous desorption of several bound functional groups, which is an event of very low probability.

Since the adsorption was irreversible, the equilibrium state of the adsorption isotherms might be questionable. For a thermodynamic point of view, adsorption isotherms for an irreversible adsorption process are vertical at the origin. The amount irreversibly adsorbed corresponds to the point where the adsorption isotherm intersects the y axis (Γ_1 when $K_1 = \infty$). When carbon black particles were immersed into a PIBSI solution, there was no barrier against the adsorption and complete adsorption was

---

[18] (a) Napper, D. H. *Polymeric stabilization of colloidal dispersions*: Academic Press: London, 1983. (b) Fleer, G. J.; Cohen Stuart, M. A.; Scheutjens, J. M. H. M.; Cosgrove, T.; Vincent, B. *Polymer at interfaces*: Chapman & Hall: London, 1993.

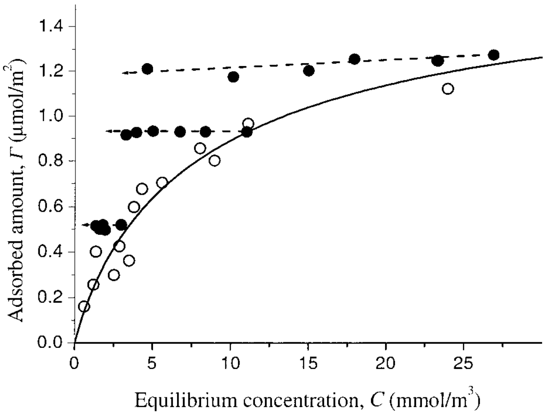

Figure 7. Desorption of PIBSI−DETA by successive additions of pure solvent to an equilibrated suspension of carbon black: (○) adsorption isotherm; (●) results after additions of increasing amounts of xylene (from the initial suspension on the right side to the left side).

possible if it was thermodynamically allowed. The adsorption process was very fast, as mentioned in the Experimental Section. In the present case, the adsorbed amount remained constant upon dilution, while it was coexisting with nonzero equilibrium concentration. The desorption was observed to be irreversible because it was very slow. The suspensions were kept 15 days without any modification of the adsorbed amount, even at 60 °C. Thus, the adsorbed amounts presented in this paper were considered as being at thermodynamic equilibrium.

It should be noticed that the desorption of a full macromolecule was irreversible, but the desorption of some of the amine groups was possible. As a matter of fact, this process was put forward as a mechanism for the rearrangement of the macromolecules inside the adsorbed polymer layer, allowing the adsorption to continue toward high coverages. The adsorption was then reversible at a microscopic point of view, each amine in a same polyamine chain being able to desorb and adsorb again onto a different site.

3.7. Thickness of the Monolayer. The adsorbed polymer layer could be observed in carbon black dispersions by means of small-angle neutron scattering (SANS). In a contrast variation experiment where the carbon black particles could be matched with the solvent, the observed scattering was due to the sole polymer.[19,20]

Most adsorption experiments have been carried out with xylene as a solvent, but the carbon black particles could not be contrast-matched with deuterated xylene. Contrast matching conditions could be attained with *n*-heptane. As shown in the contrast variation experiment (Figure 8a), successful contrast matching between carbon black particles and heptane was obtained with a mixture of 3.5% of hydrogenated heptane and 96.5% of deuterated heptane. It corresponded to a scattering length density of the carbon black particles of 6.06×10^{10} cm^{-2}. However, a small residual scattered intensity was still observed at the contrast matching point, which was ascribed to structural inhomogeneities in the carbon black particles. The following experiments were performed at this matching point in *n*-heptane solvent.

The irreversibility of the adsorption allowed us to determine the thickness of the monolayer by SANS without being disturbed by the free polymer in solution. These measurements were carried out with the poly-PIBSI−DETA (dp = 9) having a comblike structure for which the adsorption was fully irreversible. It has been checked for this polymer that the adsorption isotherms in *n*-heptane and in xylene were identical within experimental accuracy. The polymer was adsorbed onto the carbon black from a solution in heptane and the liquid phase containing free polymer could be replaced by pure heptane without loss of adsorbed polymer by washing the filtered solid with heptane.

It has been possible to evaluate the thickness of the polymer layer at the matching point composition for polyPIBSI−DETA (dp = 9) adsorbed on carbon black at the "plateau" ($\Gamma = 1.2-1.3$ μmol/m²). The scattered intensity essentially decayed as q^{-2} for $q < 0.1$ Å^{-1}, which showed that the structure of a thin layer was observed. Small deviations from the q^{-2} decay provide a measurement of the thickness of the adsorbed layer. For small thickness h such that $hq \ll 1$, the scattered intensity reads[20]

$$I(q) \propto \frac{1}{q^2}\, e^{-(q^2h^2)/12} \tag{7}$$

The plot of $\ln(I \times q^2)$ as a function of q^2 was linear (Figure 8b), and the slope gave the thickness $h = 31.0$ Å. This value is close to the length of a fully stretched PIB chain of $M_n = 1000$, which is around 37 Å. Thus, a monolayer was adsorbed, the polymer chains were stretched, and the structure of the adsorbed layer resembled that of a polymer brush.[14] This is in agreement with the adsorption isotherm results and with previous studies on similar systems using a surface force apparatus.[21]

It was not possible to extract more information on the internal structure of the adsorbed polymer layer because the polymer layer was thin; these structural details were below the resolution of the measurements. As discussed in the extreme case of short macromolecules adsorbed or grafted on latex particles,[22] even the determination of the thickness can be difficult for thin layers because the data can be extremely sensitive to the incoherent background subtraction.

3.8. High Equilibrium Concentrations. At higher concentrations, the adsorbed PIBSI amount increased dramatically for $C_{eq} < 70-80$ mmol/m³ (Figure 3). An increase of the enthalpy was also observed at this equilibrium concentration for PIBSI−TEPA and PIBSI−TETA (Figure 5a). The sharp increase of Γ in the adsorption isotherm was not caused by a bias in the titration method because it occurred suddenly in a narrow concentration domain; a systematic error of titration would cause a smoother deviation from the plateau.

Small-angle X-ray scattering of PIBSI solution in xylene up to concentrations of 60 wt % did not show any lamellar organization. The formation of multilayers at the surface was then excluded. Capillary condensation in pores was also ruled out since the carbon black particles were not porous. A possible origin of such a sharp increase of the adsorbed amount might be the formation of surface aggregates often referred to as hemimicelles. This phenomenon is well documented for aqueous solutions.[23] In the present case where xylene was the solvent, hemimicelles of the reverse type would form: the polar polyamine parts would aggregate at the surface and the

---

(19) Williams, C. E. In *Neutron, X-Ray and Light Scattering*; Lindner, P., Zemb, Th., Eds., North-Holland: Amsterdam, 1991; p 101.

(20) Auvray, L.; Auroy, P. In *Neutron, X-Ray and Light Scattering*; Lindner, P., Zemb, Th., Eds., North-Holland: Amsterdam, 1991; p 199.

(21) Georges, E.; Georges, J.-M.; Hollinger, S. *Langmuir* **1997**, *13*, 3454.

(22) Elaïssari, A.; Chevalier, Y.; Ganachaud, F.; Delair, T.; Pichot, C. *Langmuir* **2000**, *16*, 1261.

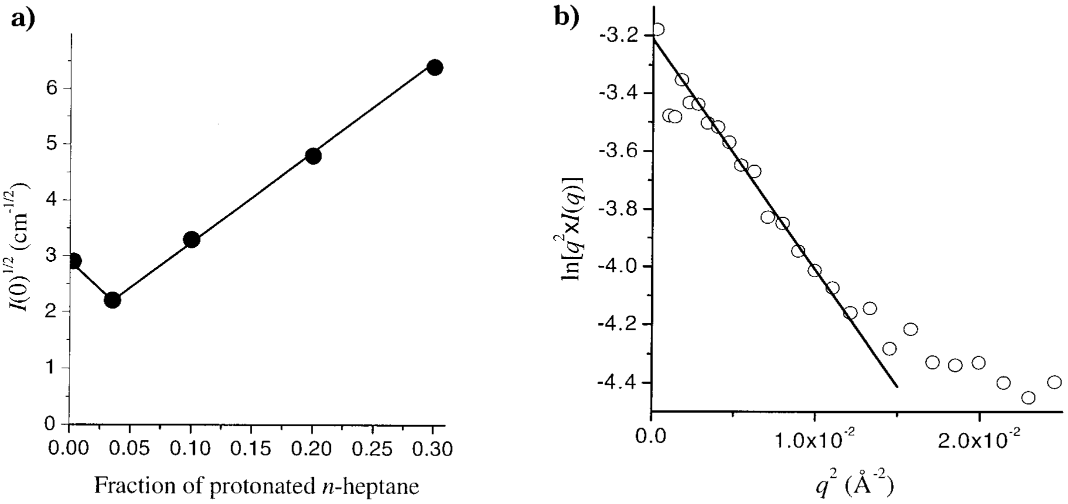

Figure 8. SANS data for the estimation of the polymer layer thickness: (a) determination of the contrast matching conditions; (b) SANS data at the matching point for adsorbed polyPIBSI−DETA (dp = 9) and linear regression according to eq 7.

PIB chains would protrude toward the solvent. Only one report of such a reverse hemimicelle formation by Zhu et al.[24] could be found in the literature.

It was difficult to conclude from the present data about surface hemimicelles formation or a sudden condensation of the polymer at the solid surface. This second explanation was also attractive and quite realistic. However, experiments we have made using dynamic light scattering and rheological measurements on carbon black dispersions[25] showed a good stabilization of the dispersions at high polymer concentrations, which would not agree with the condensation assumption. As a matter of fact, just the explanation of hemimicelles or surface aggregates remained. Because of the high concentration of polymer, the present data was of poor accuracy and could not be extended toward higher concentrations. Thus, according to the method used for the determination of the adsorption isotherms, the adsorbed amount was estimated from the difference between the initial concentration and the concentration remaining in solution after the adsorption process. The accuracy of this method falls down when the magnitude of the small concentration decrease upon adsorption reaches the accuracy of the titration method. This situation was encountered in the high concentration regime ($C_{\mathrm{eq}} > 100$ mmol/m^3). Because of these limitations, it was not reasonable to compare the experimental data with any theoretical model like that of the hemimicelles.[23,24]

At higher concentrations, the adsorption phenomenon was reversible. Thus, in a desorption experiment of PIBSI−DETA initially adsorbed at a level $\Gamma = 3.0$ μmol/m^2 at 20 °C, the dilution with xylene decreased Γ to 1.0 μmol/m^2 within 15 min and remained at this level for at least 200 min. The kinetics of desorption was exponential with a decay time of 8.5 min. The formation of reverse hemimicelles was reversible, but the binding of the underlying monolayer was irreversible. Polymer−polymer interactions were then weaker than acido-basic interactions between the polymer and the carbon black surface.

4. Conclusions

The different polymers adsorbed by their hydrophilic polyamine part on the acidic functions of the carbon black surface were chosen as an engine deposit model. The adsorption took place via a complex mechanism which could be modeled with two steps: a low coverage regime where macromolecules adsorbed on independent strong acidic sites and a second regime at higher coverages where weaker acidic sites could be reached and where the steric hindrance by the macromolecular tails contribute to the thermodynamics of adsorption. Such a two-step sequence of adsorption was reminiscent of the two regimes of adsorption described by Alexander and de Gennes as the "mushroom" and "brush" regimes.[14] The adsorption was strongly exothermic. The adsorption enthalpy was in the range of −60 kJ/mol of amine group in the PIBSI, in the range of the postulated acid−base interactions at the surface. The adsorption enthalpy was less in the second regime where a dynamic reorganization of the bound amino groups inside the adsorbed layer was postulated. The large negative enthalpic contribution to the Gibbs free energy of adsorption was compensated by a large entropic contribution coming from the entropy loss upon adsorption. At low concentrations, it has been shown that the adsorption phenomenon was irreversible, due to the multifunctional nature of the polar part.

The affinity for the solid surface increased with the number of amino groups in the polar part. Both the adsorption enthalpy and Gibbs free energy were enhanced by lengthening the polyamine part of the polymers. Similarly, changing the diblock for a comblike structure led to a much stronger adsorption. The adsorption of a comblike structure was stronger than a diblock one as the hydrophilic parts were forced to huddle together, decreasing the stretching of hydrophobic parts during adsorption. The monolayer was then more dense and more stable, according to the entropic evolution of the system.

Some compounds having amine groups behave quite differently, however. Thus, PIBSI−AEP bound rather weakly and was unable to bind to all available acidic sites. PIBSI−AEP adsorbed to strongly acidic sites only with a 1:1 stoichiometry. The two amino groups were not operative for the binding to the surface. The large steric

---

[23] a) Cases, J.-M.; Mutaftschiev, B. *Surf. Sci.* **1968**, *9*, 57. (b) Cases, J.-M.; Villieras, F. *Langmuir* **1992**, *8*, 1251. (c) Zhu, B.-Y.; Gu, T. *Adv. Colloid Interface Sci.* **1991**, *37*, 1. (d) Zhu, B.-Y.; Gu, T.; Rupprecht, H. *Prog. Colloid Polym. Sci.* **1992**, *88*, 74.

[24] Zhu, B.-H.; Gu, T. *Colloids Surf.* **1990**, *46*, 339.

[25] Dubois-Clochard, M.-Cl.; et al. Manuscript in preparation.

hindrance of the piperazine ring, especially about the tertiary amine, may be the origin of this weak binding.

The macromolecules adsorbed as a monolayer for concentrations below 70 mmol/m^3. The thickness was 30 Å, close to the length of a fully stretched PIB chain. Above 70−80 mmol/m^3, a large increase of the amount of adsorbed polymer was observed. This was tentatively ascribed to the formation of hemimicelles of the reverse type at the carbon black surface. The surface aggregation phenomenon was reversible, showing that the polymer−polymer interactions were weak.

The results of this study has been complemented and supported by works on aggregation kinetics and rheology measurements of carbon black suspensions stabilized by the same polyisobutenylsuccinimide derivatives.[5,25]

Acknowledgment. The authors wish to thank Dr. J.-M. Letoffé of the Applied Thermodynamics Laboratory of the INSA at Lyon (France) for his help in calorimetry experiments.

LA010076O